OPTIMIZATION OF THE SINTERING PROCESS: METAL MATRIX COMPOSITES AND ZINC OXIDE VARISTORS

This thesis is submitted to
Dublin City University
in fulfilment of the requirements
for the award of the degree of
Doctor of Philosophy

BY

Mohammad Durul Huda B. Sc. Eng., M. Sc. Eng.
School of Mechanical and Manufacturing Engineering
Dublin City University, Dublin 9
Ireland

Name of supervisors: Dr. M.A. El Baradie

Professor M.S.J. Hashmi

Dr. Ramon Puyane (Industrial supervisor)

Collaborating organisation- Harris Ireland, Dundalk, Ireland

September, 1994

IN THE NAME OF ALLAH,
MOST GRACIOUS,
MOST MERCIFUL.

Dedicated to

My Parents and Family

DECLARATION

I hereby certify that this material, which I now submit for assessment on the programme of study leading to the award of Doctor of Philosophy is entirely my own work and has not been taken from the work of others save and to the extent that such work has been cited and acknowledged within the text of my work.

Signed: Md. Durul Huda ID No.: 90700970

Date: 29-9-94

ACKNOWLEDGEMENT

The author is indebted to his supervisors, Dr. M.A. El Baradie and Professor M.S.J. Hashmi for their guidance, constructive suggestions and comments and encouragements at all stages of this work.

The author would also like to express his gratitude to his industrial supervisor, Dr. Ramon Puyane, for his guidance, advice and support while carrying out the project at Harris Ireland.

Sincere thanks are due to Mr. Liam Domican and Mr. Tom Walsh of the school of Mechanical and Manufacturing Engineering, Mr. Geoard Dardis and Mr. George Kenny from FORBAIRT and my fellow students Mr. A.M.S. Hamouda and Mr. I.A. Choudhury for their co-operation in different stages of this work.

The author is grateful to Liam Craven, Peter O'Connell, Peader Finnegan, Seamus Cassey, Anne Harmon, Brendan Mulholland, Darina Mukiam and P. Belew of Harris Ireland, for their co-operation and assistance to carry out all electrical tests and special thanks to M. Lambe for the SEM Photograph.

The author acknowledges the financial support received from Materials Ireland (Forbairt) and BRITE/EURAM II project (DOCERPO- contract no. BRE2.CT90.0148 in which School of Mechanical and Manufacturing Engineering, Dublin City University is one of the partners).

Finally, the author would like to express his special thanks to his wife, Sopna Huda for her perseverance and encouragement to complete this project.

ABOUT THE AUTHOR

The author graduated and received his B.Sc. Engg. (Mechanical) degree from the Bangladesh University of Engineering and Technology (BUET), Dhaka, Bangladesh, in 1984. He received his M.Sc. Engg. (Mechanical) degree in 1987 from the same Institution. He was a teaching assistant in the Department of Mechanical Engineering of BUET from 1984 to 1986. He joined in the Department of Mechanical Engineering of BUET in March, 1986 as a lecturer and became an assistant professor in June, 1988. In 1991, he received a studentship from the School of Mechanical and Manufacturing Engineering of Dublin City University to pursue this Ph.D study. He carried out his research work on Metal Matrix Composites at Advanced Materials Processing Centre of Dublin City University and on varistors at Harris Ireland, Dundalk, Ireland.

Optimization of the Sintering Process:
Metal Matrix Composites and Zinc Oxide Varistors

Mohammad Durul Huda B.Sc. Eng., M. Sc. Eng.

ABSTRACT

The sintering process of Metal Matrix Composites and Ceramic Varistors has been studied in this project. Metal Matrix Composites of Al/Al_2O_3 and Al-6061/SiC and ceramic ZnO varistors were manufactured through compaction and sintering process. The compressibility of Al/Al_2O_3 was studied with respect to lubrication and volume fraction of reinforcement. The effect of sintering temperature, sintering time and volume fraction of reinforcement on the compressive strength and hardness of Al/Al_2O_3 composites has been investigated. Mathematical models for hardness of Al/Al_2O_3 composites and compressive strength and hardness of Al-6061/SiC have been developed utilizing design of experiments and response surface methodology.

A theoretical model for the flow stress behaviour of Metal Matrix Composites has been developed which considers the effect of the size and shape of the particles and the volume fraction of the reinforcement.

For the sintering operation of zinc oxide varistors, two apparatus, one for controlling the weight loss and other for controlling the shrinkage were developed and used to obtain constant weight loss and shrinkage rates.

An optimized firing profile has been established which gives higher energy capability of the product and simultaneously reduces the firing time.

A mathematical model has been developed for the failure analysis of the varistors in relation to the weight loss rate and shrinkage rate. The microstructure of the samples fired by rate controlled sintering has been studied by SEM.

CONTENTS

INTRODUCTION

Sintering is one of the main manufacturing processes to produce ceramic products, namely those which are highly refractory or very high melting points. In this project, both metal matrix composites (MMCs) and doped zinc oxide ceramics have been produced by this technique.

Nowadays, there is an increasing demand for high-strength, high temperature materials. Metals are not suitable for use at high temperature because their strength drops down dramatically with increasing temperature. Ceramic materials withstand high temperature but their brittleness limits their use. So, to meet this criteria, the composite material has come to the front line by combining the strength of the ceramic with the ductility of the metal.

The advantage of using MMC materials are the property combinations that can result in a number of service benefits. Among these are increased strength, decreased weight, higher service temperature, improved wear resistance and higher elastic modulus . The excellent mechanical properties of these materials, together with the weight saving and the relative low cost in production makes them very attractive for a variety of engineering applications in the automotive and aerospace industries.

MMC materials are in the immature stage in respect of the development of their manufacturing system. There is also limited data for strength characteristics of MMC at different reinforcement levels. The optimized sintering process of MMC has not been yet established. Since MMC is a mixture of more than one material, the sintering operation becomes complex.

Zinc oxide ceramics have several applications in the electronic industry such as resistors for Cathode tube displays, sensors and varistors amongst others. Varistors, are used to protect the electrical equipment from power surges and lightning strikes. Zinc oxide is an intrinsic n-type semiconductor. By doping zinc oxide with bismuth oxide and other suitable additives, it is possible to get a non-ohmic material, the resistance of which changes dramatically with the applied voltage. At low voltage, the varistor material behaves like an insulator with resistivities of the order of 10^{10} to 10^{12} Ω/cm. At a certain voltage, known as the varistors nominal voltage (V_{nom}), the material becomes a good conductor that can have 1 to 10 Ω/cm. This represents practically a change of about 12 order of magnitude. This electrical behaviour arises because of the remarkable characteristics of the zinc oxide ceramic which are developed during sintering.

The sintering operation of varistors can be further optimized to enhance the properties the properties of the final ceramic microstructure. During sintering, binder burn out and volumetric shrinkage take place at low and high temperature respectively. Both parameters must be controlled to obtain defect free products that in turn will exhibit high electrical energy absorption capability.

The work programme of this project can be outlined as follows:

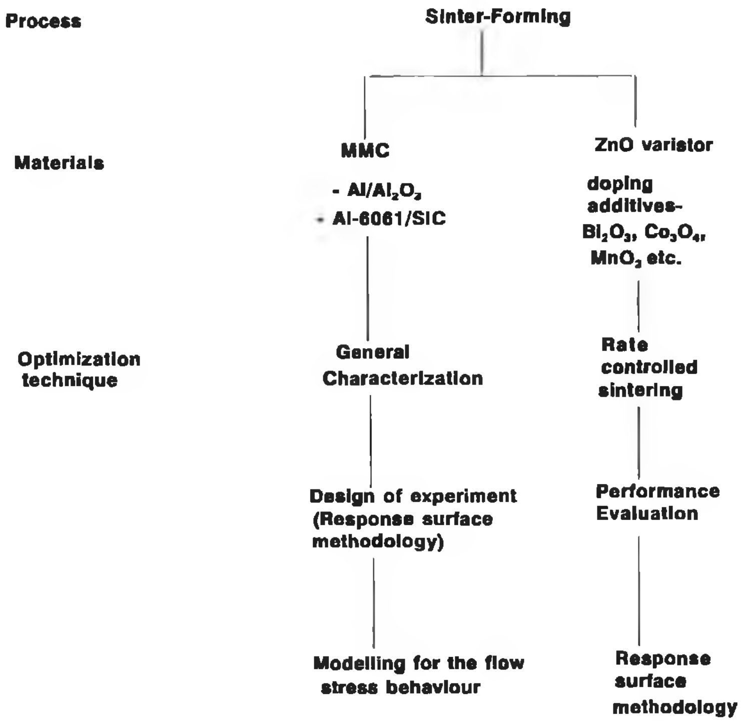

There are three main objectives for the work of MMC:

(1) to study the effect of sintering parameters and volume fraction of reinforcements on the strength of the composite.

(2) to develop the mathematical model for the strength in relation to the sintering parameters and volume fraction of reinforcements applying design of experiments and response surface methodology and establish the optimum sintering conditions.

(3) to develop an analytical model for the flow stress behaviour of metal matrix composite.

The main objective of the work for zinc oxide varistors is as follows:

(1) to establish an optimum firing profile through rate controlled sintering which will give a higher energy capability product and simultaneously preferably reduce the

sintering cycle time.

(2) to develop a mathematical model based on design of experiment and response surface methodology for establishing the combined effect of binder burnout and shrinkage on the electrical energy absorption capability of the products.

(3) to study the effect of rate controlled sintering on V-I characteristics of varistors.

(4) to study the effect of rate controlled sintering on the microstructure of the zinc oxide varistors.

To get the above objectives, two instruments which were developed before, one for controlling the binder burn out and another for controlling the shrinkage have been modified for the purpose of the present work.

This thesis contains eight chapters:

The first chapter deals with the literature survey of metal matrix composites, zinc oxide ceramic powders and rate controlled sintering of ZnO varistors.

Chapter 2 gives a general discussion on sinter forming process covering the areas of powder characteristics, blending and compaction. Also it includes description of composite materials and zinc oxide varistors.

Chapter 3 describes the equipments which are used in this project and the experimental technique. The compressibility of Al/Al_2O_3 with respect to lubricant and volume fraction of reinforcement has been carried out. The effect of sintering temperature and sintering time with volume fraction of reinforcement on mechanical properties of Al/Al_2O_3 are also discussed.

In chapter 4, rate controlled sintering of zinc oxide is presented. Two computer programmes are described, one for weight loss control and the other for shrinkage control. A relationship between heating rate and weight loss rate has been introduced to obtain a linear weight loss to eliminate the organic additives in varistor materials. Several temperature profiles are generated for the constant weight loss rate limit using a computer programme developed for this purpose. Similarly several temperature and shrinkage profiles are generated for the different shrinkage rate.

Chapter 5 describes the characteristics of varistors and performance evaluation through electrical testing. The energy capabilities of discs sintered by the rate controlled firing profiles are presented together with watt[1] loss, leakage and IR values. The results obtained through rate controlled sintering (RCS) are compared with the standard firing profile. A microstructure analysis using scanning electron microcopy is also carried out for the RCS samples.

Chapter 6 explains the modelling of the mechanical strength of MMC and electrical energy capability of zinc oxide varistors. The models have been developed utilizing the design of experiments and response surface methodology. The mathematical models for hardness for Al/Al_2O_3 composites and compressive strength and hardness (2nd order model) for Al-6061/SiC have been developed. The failure modelling for zinc oxide varistors with respect to weight loss rate and shrinkage rate is also presented in this chapter.

Chapter 7 describes the analytical modelling for the flow stress behaviour which is developed considering the volume fraction of reinforcements, shape and size of the material. This model is based on the stress-strain curve of the matrix material and the reinforcement. Chapter 8 contains the conclusions of the sintering process of metal matrix composite and zinc oxide ceramics and provides suggestions for future work for MMC and ZnO varistors.

---

[1] energy rate

CHAPTER ONE

LITERATURE SURVEY

1.1 INTRODUCTION

A review of literature pertaining to sintering process of metal matrix composite and zinc oxide varistors has been enumerated in this chapter. This work can be divided into three main sections as follows:

(1) Metal matrix composites
(2) Zinc oxide ceramic powders
(3) Rate controlled sintering of ZnO varistors

1.2 METAL MATRIX COMPOSITES

Metal matrix composites are advanced materials, used mainly as high temperature, high strength and light weight materials in aerospace and automotive industry. The literature survey on MMCs can be divided as:

(1) Manufacturing techniques
(2) Materials
(3) Compaction
(4) Sintering
(5) Strength and

(6) Modelling

1.2.1 Manufacturing techniques

There are several fabrication techniques available to manufacture the MMC materials: there is no unique route in this respect. Due to the choice of material and reinforcement and the types of reinforcement, the fabrication techniques can vary considerably from case to case.

To manufacture fibre reinforced MMC with sheets or foils of matrix material diffusion bonding method is normally used. Chou T.W. et al [1] showed the different steps in fabricating MMC by diffusion bonding. Normally filaments of stainless steel, boron and silicon carbide have been used with aluminium and titanium alloys matrices [2-5].

The fabrication process of MMC by vacuum metal infiltration was used by Champion et al [6]. These authors used aluminium oxide fibre FP (Polycrystalline fibre) of Du Pont Company. In this technique, as the first step, FP yarn is made into a handleable FP tape with a fugitive organic binder in a manner similar to producing a resin matrix composite prepeg. Fibre FP tapes are then inserted into a casting mould of steel or other suitable material. The fugitive organic binder is burned away, and the mould is infiltrated with molten metal and allowed to solidify. Metals such as aluminium, magnesium, silver and copper have been used as the matrix materials in the liquid infiltration process because of their relatively lower melting points. This method is desirable in producing relative small-size composite specimens having unidirectional properties [2].

Bhagat [7] fabricated stainless steel wire reinforced aluminium matrix composites by high-pressure squeeze casting and showed that these composites at a 40% fibre volume fraction have a tensile strength that is more than three times greater than that of an aluminium matrix cast under the same fabrication technique.

Fukunaga and Goda [8] fabricated composites of silicon carbide fibre reinforced Al and Mg metals by squeeze casting and showed the existence of eutectic surroundings that are independent of the squeeze pressure and depend on the alloy quantity and on the fibres which lowered the tensile strength of the composite. However a machine part with a complex shape can be constructed in a short time by this method [9].

Alcan has installed laboratory scale deposition (spray-co-deposition) units at its Banbury Laboratories to investigate the possibilities of manufacturing MMCs on an economic scale, concentrated primarily on SiC as the reinforcing element. According to this process, the shape of the final product depends on the atomizing condition and the shape and the motion of the collector.

Singer and Ozbek [10] formulated this technique (spray co-deposition) to manufacture a composite. They used various second-phase particles, namely sand, alumina, SiC, chilled iron, graphite etc. Up to 36% of SiC, Al_2O_3, chilled iron, graphite and sand particles and a mixture of these, 75-120 μm in size, can be incorporated successfully in aluminium at AL-5Si alloy matrices. Structural examination showed that a homogeneous distribution of particles is obtained even with mixture of particles having widely differing morphology and density, moreover the particles were surrounded completely by the matrix material. No significant diffusion was obtained across the particle/matrix interfaces because of the very short matrix solidification time.

White and Wills [11] used this technique to manufacture SiC reinforced Al composites. Full density is not achieved during this process and hot or cold rolling are used to densify the material prior to mechanical testing.

Hosking et al [12] used compocasting technique to fabricate the composites. This method is useful to fabricate a composite with discontinuous fibres. The compocasting apparatus consists of an induction power supply, a water-cooled vacuum chamber with its associated mechanical and diffusion pumps and a crucible and mixing assembly for agitation of the composites. Primarily the melt is formed by heating and continuous stirring and then transferred into the lower die-half of the press and the top die is brought down to shape and solidify the composite by applying the pressure. Abis [13] and Kohara [14] used hot pressing and Miliere and Suery [15] used squeeze casting after stirring to make a high density material.

The Powder Metallurgy (PM) route is the most commonly used method for the preparation of discontinuous reinforced MMCs [11, 16-20]. Figure (1.1) shows the flow chart of the general PM route. Several companies are using this technique to manufacture MMC using either particulates or whiskers as the reinforcement materials. Among them DWA, Silag and Novamet are well known leading MMCs manufacturers. In this process powders of matrix materials and reinforcement are first blended and fed into a mould of the desired shape. Pressure is then applied to further compact the powder (cold pressing). In order to facilitate the bonding between the powder particles, the compact is then heated to a temperature that is below the melting point but sufficiently high to develop significant solid state diffusion (sintering). Alternatively, after blending the mixture can be pressed directly by hot pressing: however HIP is helpful for securing high density material. The consolidated product is then used as a MMC material after some secondary operation.

DWA and Silag use the proprietary blending process to combine reinforcement with metal powder whereas Novamet employs the mechanical alloying techniques to combine the reinforcement and matrix constituents.

Metallic materials such as copper, nickel, aluminium, cobalt, titanium, molybdenum based alloy and steel are often used in the powder process as matrix materials [2] with reinforcing elements SiC, graphite, Ni, Ti and Mo [21-22]. Since no melting and casting is involved, the powder process is more economical than many other fabrication techniques. This technique offers several advantages over fusion metallurgy of diffusion bonding [23], some of these advantages being as follows:

1- Lower temperature can be used during preparation of a PM based composite. This results in less interaction between the matrix and the reinforcement, consequently minimizing undesirable interfacial reactions, which leads to improved mechanical properties.

2- In some cases PM techniques will permit the preparation of composites that can not be prepared by fusion metallurgy. It has been reported [24] that SiC whiskers will dissolve in a molten Ti-alloy matrix, while dissolution can be minimized by using the PM route. Again it has been shown that SiC fibres are highly compatible with solid aluminium but only fairly compatible with liquid aluminium [14].

3- The preparation of particulate or whisker-reinforced composites is generally speaking easier using the PM blending technique than it is using the casting technique.

4- Particulate reinforcement is much less expensive than continuous filament of similar composition.

In reference [25], the details of the fabrication methods were described. Table (1.1) shows the comparison of different fabricating techniques. In the present study, PM route has been used to manufacture the samples. The operation consists of **mixing,**

blending, cold pressing and sintering. After sintering the samples have been tested for mechanical strength.

1.2.2 Materials

In metal matrix composite, metals are used as the matrix materials. Nowadays the main focus is given to aluminium as a matrix material [26] because of its unique combination of good corrosion resistance, low density and excellent mechanical properties. Titanium [27] has been used in aero-engines mainly for compressor blades and discs, due to its higher elevated temperature resistance property. Magnesium is the potential material to fabricate composite for making reciprocating components in motors and for making pistons, gudgeon pins, spring caps [28]. It is also used in aerospace due to its low coefficient of thermal expansion and high stiffness properties with low density.

Much work had been carried out on fibre as a reinforcing element. But for isotropic property, nowadays discontinuous fibres are a main focus of interest. Among the many ceramic reinforcements considered for making aluminium matrix composite, Al_2O_3 and SiC have been found to have excellent compatibility with the aluminium matrix [13,29]

1.2.3 Compaction

The processing of metal matrix composites (MMCs) with discontinuous reinforcement involves mixing the powder with the reinforcing phase, cold compaction and sintering [30]. So compaction is one of the important stages in sinter-forming route which gives the powder an initial shape and gives the compact the necessary strength for handling at further processes.

To optimize the powder processing system and for proper handling of the compact, the appropriate amount and type of lubricant must be admixed with the metal and reinforcing element powder which facilitate the compaction and ejection process. To minimize segregation during blending, lubricant particle size should be smaller than the largest metal and reinforcing powder particles [31].

Frey and Halloran [32], Dynys and Halloran [33] studied the behaviour of spray dried alumina and aggregated alumina powders respectively. They found that the density of the green compact increases with decrease in the binder content, whereas it increases with the increase in the moisture content.

Al-Tounsi A. et al [34] studied the compaction of agglomerated zinc oxide powder. They concluded that the smaller average size gives better compressibility and a decrease in the binder content gives better compressibility. Lubaba et al [35] studied the compaction of MgO-flake graphite mixtures to the fabrication of composite refractory materials. They showed that the porosities of compacted specimens containing graphite are much lower than those of compacts containing MgO alone but having a considerable oxide size distribution. Kim T.W. et al [36] studied the compaction behaviour of thick composite laminates during cure. They concluded that the cure pressure played a dominant role to the ultimate compaction rather than the temperature.

Reilly J.J. and Kamel I.L [37] studied the characterization and cold compaction of polyether-etherketone powders. They concluded that compaction was successful at room temperature using the 150 grade powders with low viscosity grade but not with the 450 grade powders which possesses high viscosity.

Huda D. et al [38] stated that the addition of 1% lubricant to AMC powder is good practice in order to give the compact enough strength for handling and to lubricate the die walls to facilitate pressing as well as ejecting the compacted part. However the presence of lubricant in the finished part is not desirable, hence it should be burnt of before sintering takes place. The burnt off temperature for lubricant is between 430 ° to 540 ° C depending on lubricant type and sintering atmosphere [39]. The primary requirement for a good composite structure is a homogeneous distribution of the reinforcement in the matrix. This is achieved by a proper choice of blending time and rotation of the mixture [40]. It is difficult to make the composite at higher volume fraction of reinforcement by PM method [41]. However repressing and re-sintering may improve the strength of the composite.

1.2.4 Sintering

Bassani J.L. and Taggart D.G. [42] developed constitutive equations for analyzing sintering of a powder compact around a rigid spherical inclusion. They showed that the presence of the inclusion caused a build up of stress that retarded sintering while creep would eventually relax this stress.

Kanetake N. [43] studied the alumina reinforced composite for the flow stress analysis. The metal matrix composite was fabricated by sintering with sintering atmosphere, air and subsequently extruding. He concluded that the flow stress increased by composing alumina particles and extruding after sintering. The strain hardening rate had been increased also by composing alumina particles and hot extruding.

Maclean M. and Dower R. [44] produced the aluminium alloy short fibre MMC using the PM route. They used short alumina fibre, Saffil with 2014 and 6061 aluminium alloy. They sintered the samples at 580 °C and 630 °C for 2014 and 6061 alloy respectively in vacuum with sintering time 45 minutes. After sintering, the samples were hot extruded and heat treated separately. They concluded that in the extruded condition the mechanical properties of both MMC systems increased with fibre content but for heat treated condition, 10 wt. percent fibre addition showed the higher mechanical value.

Jha A. K. et al [45] studied the sintering behaviour of 6061 aluminium alloy composite. They used each of graphite, talc, alumina and TiC as dispersoid up to 14 vol%. After pressing, the green compacts were sintered in a tubular furnace at temperature 615 °C for 30 min. with sintering atmosphere, argon, vacuum and nitrogen. They concluded that nitrogen atmosphere imparted minimum densification whereas argon atmosphere resulted in maximum densification. Densification parameter of the sintered composites increased with addition of hard dispersoid (alumina and TiC) whereas addition of graphite particles resulted in a decrease.

1.2.5 Strength

Thellman et al [46] produced SiC_p/Al composite from powder (SiC_p=Silicon carbide particles). Firstly powder was blended and then finished parts were produced by hot pressing. The product was then solution heat treated followed by artificial ageing (T_6 :heat treatment and artificial ageing). They concluded that 30 v/o SiC_p/Al-6061-T6, exhibited an 80% increase in modulus and a 35% increase in yield strength with only a 5% increase in density.

In reference [16], the composites were first normally casted and then remelted and compressed over a porous ceramic plate in order to form a random mat of Al_2O_3 whiskers and SiC_w (SiC_w=Silicon carbide whisker). Here it was shown that the compressive strength for Al/SiC_w was higher than that of Al/Al_2O_3 composites.

Al/Cu and Al/Li metal matrix composites were produced commercially using SiC as the reinforcement [47]. But the manufacturing route was not known. The composites were tested by uniaxial compression. The tensile data supplied by the company was higher than that of the tested compression data. In reference [48], the operations of producing SiC_w/Al composites were consisted of blending, hot pressing and extrusion or rolling. Here it was shown that the strength values largely depended on the volume fraction of reinforcement. Table (1.2) and (1.3) show the strength data for aluminium matrix composite.

Table 1.2 Compressive strength data for aluminium matrix composite

Materials	UCS Mpa	References
25 v/o SiC_p/Al -6061 T6 30 v/o SiC_p/Al-6061 T6	581 716	46
23 v/o Al_2O_3/Al 20 v/o SiC_w/Al 25 v/o SiC_w/Al	254 455-524 552-641	16
17 v/o SiC/Al-Cu 13 v/o SiC/Al-Li	408 (Measured)[1] 610 (supplied) 359 (Measured) 550 (supplied)	47
Hi SiC/Al 2024 rolling Low SiC/Al 6061 rolling	619 500	48

---

[1] by author

Table 1.3 Hardness data for aluminium matrix composite

Materials	Hardness	References
30 v/0 SiC_p/Al CT90-T6	94 (Rb)	46
15 v/o SiC_f/Al heat treated	78 (Rb)	15
15 v/o SiC_f/Al-7 wt% Si, Squeeze casting	72 (Rb)	
17 v/o SiC/Al-cu	123 (Hv) (Measured)	47

1.2.6 Modelling

The property and strength of the composite depends on the type and amount of matrix and reinforcement. The general criteria of these materials is shown in figure (1.2). Normally the reinforcement deforms elastically and matrix deforms both elastically and plastically. The important required mechanical properties of composites are yield stress (σ_y) and work hardening rate (h), than other mechanical properties such as stiffness E and fracture toughness K. The higher the yield stress and work hardening rate of a MMC are the greater the compatibility of the MMC in sustaining a higher applied load. This criteria of MMC increases the design flexibility of a component made of such a MMC.

The yield strength of a ductile material can be greatly enhanced by homogeneous dispersion of hard particles. These particles, such as oxides and carbides, often can deform only elastically. So the plastic strain moreover is only contributed by the matrix alone and its magnitude further reduced according to the volume fraction of these phases. These double effect may significantly increase the yield stress and work hardening modulus of the composite system. Relatively much work has been carried out on the elasto-plastic behaviour of fibre-reinforced composite. References [49-50] review the different models used for the strengthening mechanisms of metal matrix composites. Among them, the law of mixtures is used to predict the composite stiffness where the strain in both matrix and reinforcement phases considered same. It is mainly used for the fibre reinforced composite. The general equation of the law of mixture is

$$\sigma_c = \sum_{i=0}^{N} V_i \, \sigma_i \tag{1.1}$$

In the case of two-phase systems, matrix and one kind of reinforcing phase, the above equation can be simplified as:

$$\begin{aligned} \sigma_c &= V_0\sigma_0 + V_1\sigma_1 \\ &= V_m\sigma_m + V_f\sigma_f \end{aligned} \tag{1.2}$$

where the matrix and reinforcing phases are denoted by subscript m and f respectively and c denoted by composite.

The shear lag model is best applied to an aligned short fibre composite loaded along the fibre axis. Figure (1.3) shows the model for shear lag analysis. Primarily it was based by Cox [51] considering deformation of fibre and matrix elastically and considers load transfer at the matrix-fibre interface to calculate the composite stiffness but later it was extended by Nardone and Prewo [52] to predict the yield stress of a MMC assuming deformation of matrix plastically and the fibre remaining elastic. Since for the particulate composite, the load transfer in terms of shear stress at the matrix-fibre interface becomes limited due to the shorter interfacial length, it can not be used for the particle reinforced composite.

Since recently discontinuous fibre or particle dispersed composites having isotropic property are expected as a new structural material, much attention has been given on this new class of material. The beauty of this material is that it can be produced by the conventional manufacturing system. Tandon and Weng recently studied the spherical particle reinforced elasticity [53] and plasticity [54] for the load carrying capacity of particle reinforced composites. Their theories were based on Eshelby's [55] solution of an ellipsoidal inclusion and Mori-Tanaka's concept of average stress in the matrix [56]. Kanetake N. and Ohira H. [57] considered the dislocation theory proposed by Ashby [58] for the work hardening in a non-homogeneous material and used the theoretical calculation method proposed by Tandon and Weng [54)] for the ellipsoidal particles.

1.3 ZINC OXIDE POWDERS

For varistors application, some oxides are added to the zinc oxide powder. The common doping powders are oxide of bismuth, antimony, manganese and cobalt. All powders are mixed by milling to give the sufficient energy for sintering and then spray drying. The spray dried powders are then pressed in different sizes. After forming, the green-parts are placed in a kiln and sintered at high temperature. At higher temperatures, grain growth occurs, forming a structure with controlled grain size. The rate of sintering is strongly influenced by the particle size and densification rate increases with decreasing particle size. Lange F. and Kellett B. [59] showed that a small particle size was preferable for the sintering operation. Yeh T. and Sacks M. [60]

showed that there should be uneven shrinkage if the green density was not uniform. So a green body being dense and as uniform as possible is desired for the sintering.

Much work had been carried out on the effect of doping materials on sintering specially with bismuth oxide. Bijoy Sarma and Rama Mohan T.R. [61] developed a mathematical model for the study of sintering kinetics of zinc oxide. They suggested that the region where rapid diffusion takes place not only for zinc oxide but several oxides as well, can be changed by a suitable calcination of the powders whereby surface defect characteristics of individual particles are modified.

Senda and Bradt [62] studied the grain growth for ZnO and ZnO with Bi_2O_3 addition from 0.5 to 4 wt% for sintering from 900°C to 1400°C in air. For the pure ZnO the average grain size increased proportionally to the one third power of the time, the grain growth exponent or n value was observed to be 3 while the apparent activation energy was 224 ± 16 kj/mol. Additions of Bi_2O_3 to promote liquid phase sintering increased the ZnO grain size and the grain growth exponent to about 5 but reduced the apparent activation energy to about 150 kj/mol.

Dey and Bradt [63] studied the grain growth of ZnO for Bi_2O_3 contents from 3 to 12 wt% in sintering from 900°C to 1400°C. Here it was found that the rate of ZnO grain growth was found to decrease with increasing Bi_2O_3.

Kim et al [64] studied the densification and microstructure development in Bi_2O_3 doped ZnO on the effect of Bi_2O_3 content for sintering temperature 800°C to 1200° C. A small amount of Bi_2O_3 in ZnO ($\leq$ 0.1 mol%) retard densification, but the addition of Bi_2O_3 to more than 0.5 mol% promoted densification by the formation of a liquid phase above the eutectic temperature ($\approx$740°C). The amount of Bi_2O_3 influenced the microstructure of sintered body also. When the Bi_2O_3 was small ($\leq$ .5 mol%), a liquid phase penetrated into the boundaries between grains. At this doping level, an increase in the amount of the liquid phase enhanced grain growth. Large grain boundary mobility resulted in the formation of intragrain pores. The skeleton structure formation was more pronounced with increasing Bi_2O_3 content, resulting in a reduction in grain growth rate. Pores accumulated on the boundaries between ZnO grains and the liquid phase, which decreased the sintered density.

Trontelj and Kojar [65] investigated the sintering on binary system (ZnO-TiO_2, ZnO-K_2O, pure ZnO, ZnO-Li_2O and ZnO-Sb_2O_3). They showed that sintering temperature changes with the variation of the doping element. The shrinkage starts almost at 600°C for ZnO-TiO_2, pure ZnO and ZnO-Li_2O but for ZnO-K_2O and ZnO-Sb_2O_3 systems, it starts at 800 and 1000°C respectively. Among them, the rate of shrinkage is very rapid in ZnO-Li_2O binary system. The concentration of interstitial Zinc ions in ordinary Zinc oxide is very small. The incorporation of Li into the ZnO lattice produces Zn interstitial by displacement of lattice Zinc ions by interstitial lithium. A concentration gradient of Zn-interstitial is set up between the surface and the interior of ZnO particles, which could accelerate sintering. The K^+ ion is large as compared to Li^+ and it is not likely to be incorporated into the ZnO lattice. The influence of K_2O on the sintering of ZnO is slightly retarding.

1.4 RATE CONTROLLED SINTERING OF ZINC OXIDE VARISTORS

Normally after pressing the green disc has been sintered according to a firing profile which is based on historical trial and error basis. In the firing process, two important things happen. Firstly, organic binders are burnt out at low temperature and secondly shrinkage occurs at high temperature.

Binders are added to ceramic powders to improve their flowability, handling and compressibility characteristics as well as to enhance the mechanical properties of the green compact. The burning temperature of the binder should be less than the temperature at which the compact shrinkage starts. This assists the binder inside the compact to escape when shrinkage takes place.

If the binder burns at an inconsistent rate, it can adversely affect the quality of the finished ceramic component due to the creation of micro cracks which will develop into bigger cracks at a later stage of the firing process or other defects such as explosive spalling or bubble formation. The higher heating rate for the binder burn out also produces void and pores in the final product [66].

During firing densifications take place and the density of the fired compact could reach the solid density depending on several parameters. Earlier densification rates are excessive which create trapped pores. It is also seen that the constant heating rate firing curves produce rapid initial densification, pore entrapment and excessive grain growth which in there will have a detrimental effect on the electrical properties of the blocks. So for getting defect free samples with no microcracks, no bubble formation, no excessive grain growth, no rapid densification and no pore entrapment, these two parameters, binder burnout and shrinkage should be controlled.

Very little work had been carried out on this area. Chu et al [67] studied the heating rate on densification of ZnO powder. They found that the higher the heating rate the higher the temperature at which densification starts. They also observed that the final densities obtained were independent on the heating rate. Kaysser and Lenhart [68] sintered ZnO agglomerates at 1360°C in O_2. They observed that directly heated samples showed large residual pores after sintering whereas presintered samples reached full density.

Dong and Bowen [69] showed that bubble formation occurs during sintering through polymer decomposition and developed a technique for observing bubble formation during binder burn out in ceramic processing using hot-stage microscope. They studied the effect of initially trapped gas bubbles, amount of residual solvent, ceramic powder surface and heating rate on ceramic processing. They concluded that (a) bubbles resulting from polymer decomposition products tend to form cluster and coalesce. (b) The final bubble size appears to increase as the thickness of the binder solution increases. (c) Initial trapped gas bubbles and solvent bubbles shrink as the temp. increases. (d) Bubble nucleation and bubble shrinkage temp. increase as the heating rate increases.

Huckabee and Palmour III [70] studied the rate controlled sintering on MnO (.1%) doped Alumina. The sintering particle was $\approx$ 0.1 to 0.2 μm with a specific surface area of 6 to 11 m^2/g. They studied the linear-linear rate-controlled densification and linear-linear-log decreasing rate controlled densification with conventional isothermal firing schedule and concluded that linear-linear-logarithmic rate controlled sintering gave sintered parts with higher final density. The linear-linear-logarithmic decreasing densification rate regime produces near-optimum firing condition readily attaining density $\rho = 3.96$ g/cm^3 (99.3% of ρth) with average grain size by a factor of 3 or more when compared with conventional firing and produces a more uniform grain size distribution.

Al-Tounsi A. et al [71] studied the binder burn out using different temperature profile for the firing cycle. It was considered that weight loss during the firing process can be controlled to a good degree by using a computer. It was also seen that the ratio of surface area to volume seems to have an effect on the binder burn out stage in the firing process. The higher ratio favours the elimination of binder at higher rates. The time for bigger disc needed more time than that of smaller disc of the same weight.

Al-Tounsi A. et al [72] investigated the weight loss by controlling the heating rate for the furnace using a specifically developed software package. The binder burn out stage was controlled using a proportional method. It was shown that a temperature profile for linear weight loss could be achieved through this close loop control.

Strauss J.T. and German R.M. [73] constructed a high temperature batch furnace for real-time analysis of sample weight loss (thermo-gravimetric analysis-TGA), compact temperature profile (differential thermal analysis-DTA) and evolved gas composition using various gas analytical method. All those analytical capabilities were controlled by a microprocessor coupled to a computerized controller. Their long-range goal was to develop an expert systems software to fully govern the thermal and atmosphere cycle in a closed-feedback loop. They generated a preliminary data for the expert system and indicated a complex series of interactions between powder compacts and the atmosphere during heating.

Lockey et al [74] successfully controlled ceramic drying and calcining operation. It ensured uniform gas evolution to prevent cracking on sudden release of gas. Instead of increasing temperature according to a preset schedule, the output signal from a thermogravimetric analysis apparatus was used as an input to a computer system which varies the temperature as required to cause mass loss to follow a preselected schedule.

Palmour H. et al [75] studied the microstructural development of chemically prepared alumina by optimizing rate controlled sintering. They used a feed-back controlled dilatometer for the experiments. They claimed, it was evident that RCS profile has resulted in a substantially finer, more uniform grain size, with remnant small pores located as boundaries and at triple points, rather than being trapped within grains.

Verweij and Bruggiink [76] investigated the reaction-controlled binder burnout of ceramic multilayer capacitors. They used the maximum weight loss rate to design a weight-time program for a reaction controlled process. The sample temperature set-point control was performed by using a controller with proportional, integrative and derivative action. The total burnout time can be reduced considerably and tuning and control loop activation can be made such that the reaction rate varies gradually with time and never exceeds a certain limit.

Al-Tounsi A. et al [77] established a linear relationship between the current shrinkage rate and the heating rate for the sintering of ZnO varistors. The shrinkage had been controlled during the firing process at a constant rate using a feed back loop to control the heating rate by using the above relation.

Winkler S. et al [78] studied the sintering operation of SiC and ZrO_2 with high-temperature dilatometer having rate controlled capability. They concluded that the same densities were obtained at the same temperatures when comparing the measurements with and without RCS. Speyer R.F. et al [79] studied the rate controlled shrinkage by dilatometry. They used PID (proportional-integral-derivative) control system to see the linear and curvilinear shrinkage of discs made from zinc oxide powders. They concluded that an exponentially increasing temperature-time profile was required to maintain the linear specimen shrinkage rate.

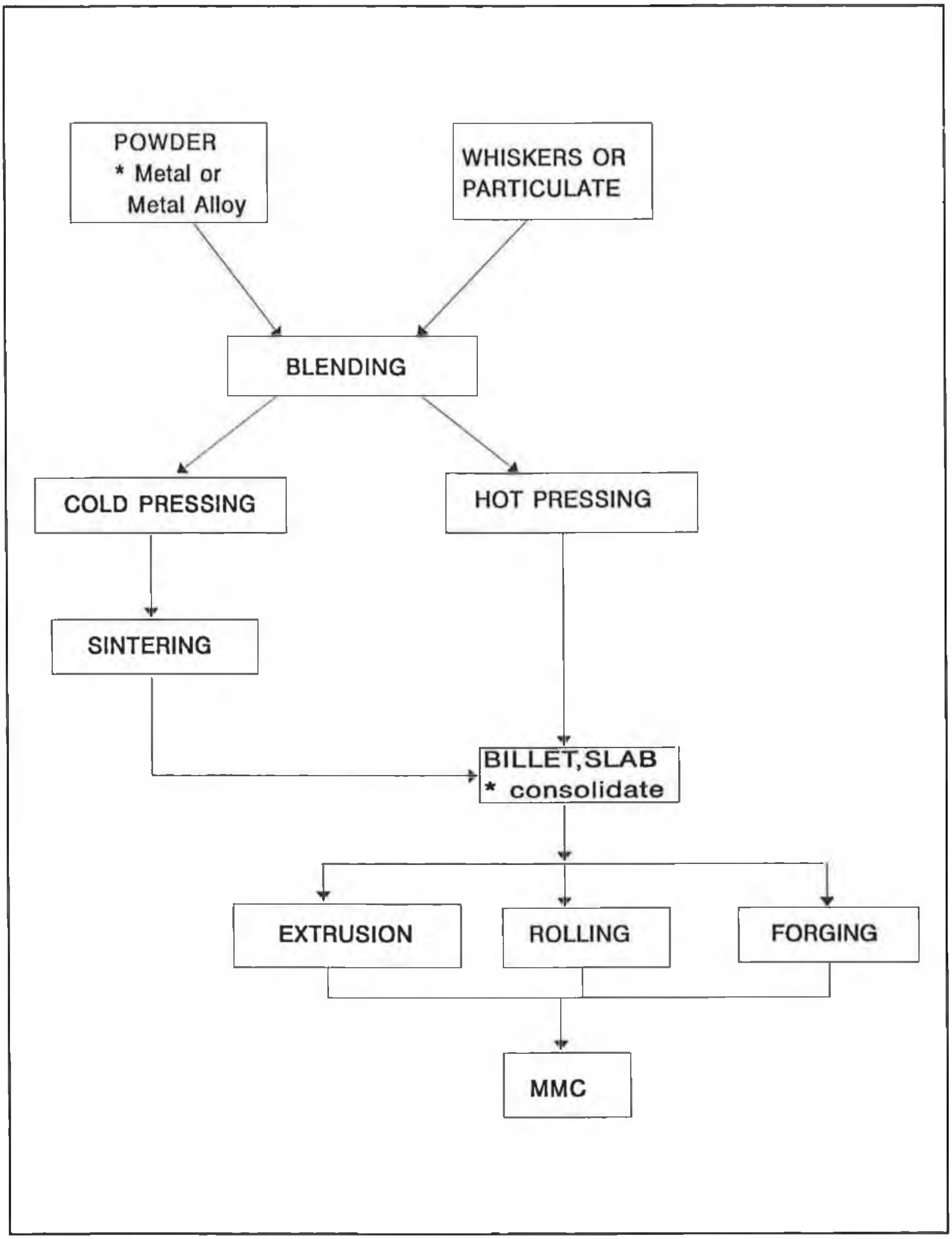

Figure 1.1 Flow chart for composite fabrication by powder metallurgy.

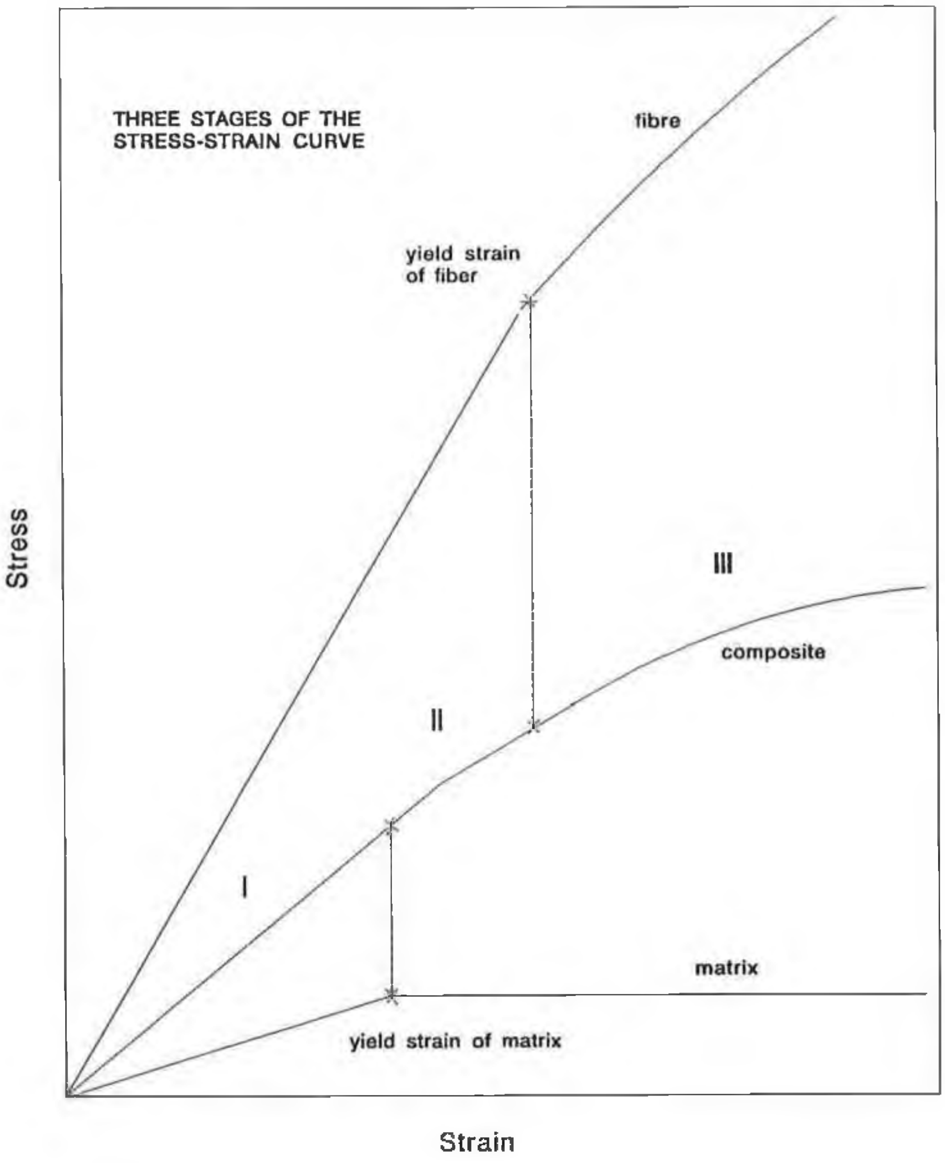

Stage I : both matrix and fibre elastic

Stage II : matrix deforms plastically and fibre remains elastic

Stage III : both matrix and fibre deform plastically

Figure 1.2 Stress-strain curves of a MMC, the unreinforced matrix metal and reinforcing fibre [50]

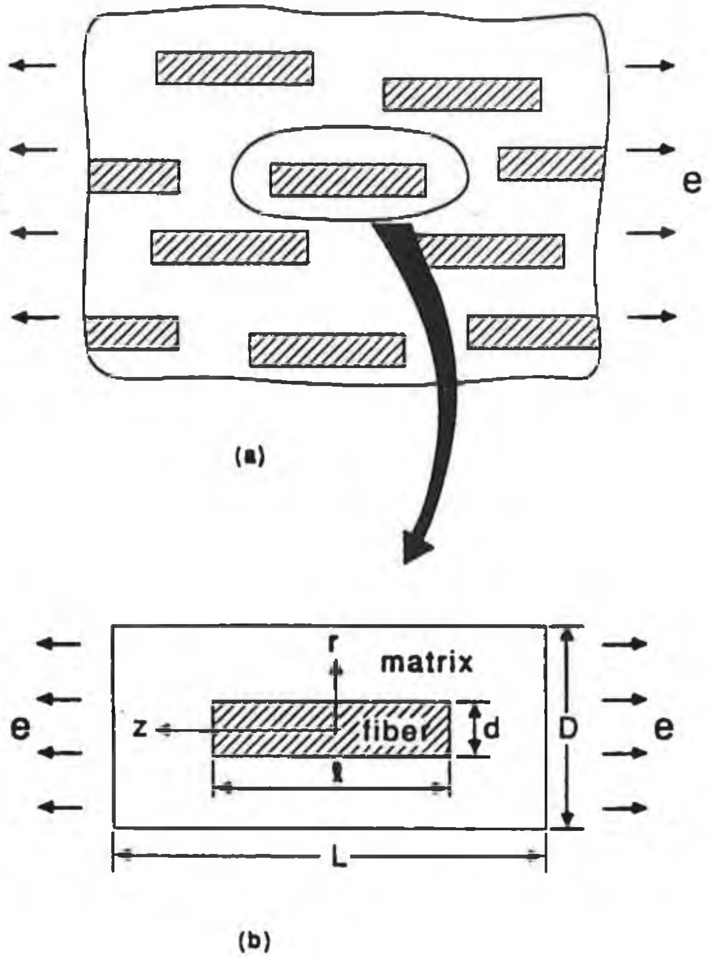

Figure 1.3 Shear drag model for aligned short fibre composite; (a) representative short fibre, (b) unit cell for shear drag analysis [21].

Table 1.1 Comparison of Different Techniques

Route	Cost	Application	Comments
Diffusion Bonding	High	used to make sheets, blade, vane, shaft, structural component	handles foils or sheets of matrix and filaments of the reinforcing element
Powder Metallurgy Technique	Medium	mainly used to produce small objects (especially round), bolts, pistons, valves, the high strength and heat resistant materials	Both matrix & reinforcements are used in powder form, best for using particulate reinforcement. Since no melting is involved, there is no reaction zone developed, showing high strength composite.
Liquid Metal Infiltration	Low-Medium	used to produce structural shapes, such as rods, tubes, beams with maximum properties in a uniaxial direction	filaments of reinforcement are used.
Squeeze Casting	Medium	widely used in Automotive industry for producing different components such as piston, connecting rod, rocker arm, cylinder head, suitable for making complex objects.	generally applicable to any type of reinforcement and may be used for large scale manufacturing
Spray Casting	Medium	used to produce friction materials, electrical brushes & contacts, cutting & grinding tools.	Particulate reinforcement is used. Full density materials can be produced.
Compo-casting	Low	It is widely used in automotive, aerospace, industrial equipment and sporting good industries, used to manufacture bearing materials.	suitable for discontinuous fibres especially particulate reinforcement.

CHAPTER TWO

SINTER FORMING OF METAL MATRIX COMPOSITES AND ZINC OXIDE CERAMICS

2.1 INTRODUCTION

The sinter forming route has been used in this research project for the manufacture of both the metal matrix composites and zinc oxide varistors. Hence, this chapter has been mainly devoted to a general description of the following three main areas:

(1) Sinter forming process
(2) Composite materials and
(3) Zinc oxide varistors

2.2 SINTER FORMING PROCESS

The sintering process is the most important step of PM route where the compact made from powder becomes consolidated and strengthened by the heat energy. The general process for making a product by powder metallurgy route is to mix the powder called mixing, then blending and making a compact by pressing, called compaction and then firing the product at high temperature called sintering. So the following material and processing steps are described first as the performance of the sintering process depends on them .

(1) Powder characteristics

(2) Blending and

(3) Compaction

2.2.1 Powder Characteristics

Relevant powder characteristics influencing the sintering process are the particle size distribution, particle shape and interparticle friction. Particles are considered to be below 1000 μm in size (below 1 mm). Both the particle size distribution and the particle shape affect the compact packing. Usually, high packing densities are sought to ensure strength and uniformity in the final product. Specific surface area indicates the nature of powder size distribution with its shape. Normally higher surface area is desirable for the sintering. Fine powders have more interparticle friction than coarse powders having low flowability. But the finer particles give higher final density. Lubricants or flow agents can be added to fine powders to lower the interparticle friction. There are four main approaches to fabricating metal powders-mechanical, chemical, electrolyte and atomization. Ceramic powders are produced by mechanical technique such as milling. Most alloy powders are fabricated by atomization techniques. Figure (2.1) shows the different shapes of the particle. Normally powders of spherical shape are taken for analyzing the effect of particle size on strength and average particle size is used to designate the particle size. Zinc oxide varistors powders are pressed in aggregate form.

2.2.2 Blending

Mixing is needed if there is more than one powder. If mixing is performed for prolonged times, the particle shape and hardness can be changed and there could be size segregation of the components. So care must be exercised at this step. Most metal powder mixing and blending are performed using rotating containers. Distribution of mixing becomes uniform if mixing can be done three dimensionally.

2.2.3 Powder Compaction

Compaction is an important step for the manufacturing of composites using the PM route. The most important effects of compaction are:

1. Increased density by reduction of the voids between powder particles.
2. Cold welding, mechanical locking and adhesion of the particles to produce sufficient "green strength" to permit handling of the powder.
3. Plastic deformation of the powder particles to induce recrystallization during sintering and
4. Increased contact area between the particles by plastically deforming the powder.

There are many parameters which affect the compressibility of composite powder. Figure (2.2) shows the variable parameters for the compaction process. The variable parameters related to powder characteristics are particle size, particle size distribution, particle shape, binder and lubrication addition while for compaction process, the variables are compaction speed, compaction pressure, pressing action (single or double action) friction between powder particle and die walls. The amount and type of reinforcement also affect the compressibility.

Normally higher grain size particles are better for compaction because of the less friction between the particles but smaller grain size particles are better for sintering. Narrow particle size distribution gives better compressibility. Usually high compaction pressure is needed for solid phase sintering and lower compaction pressure is needed for liquid phase sintering. Excessive compacting pressures may produce cleavage fractures or slip cracks, especially in parts with thick and thin sections in the direction of pressing. Insufficient pressure, on the other hand , produces fragile parts that will not hold together during handling.

Powder compaction is divided into four steps:

(1) The first step is termed rearrangement wherein at low pressures the powders achieve a denser packing by sliding past one another. Rearrangement is aided by coarse particle sizes, hard particles and smooth surfaces.

(2) With increased pressure, powders form point contacts which grow in size by a combination of elastic and plastic deformation. The growth of the interparticle contact zones is dependent on several material parameters including the elastic modulus, yield strength and work hardening rate. Significant porosity reduction occurs during plastic deformation.

(3) Depending on the nature of the material, eventually with high compaction pressures the material becomes fully work hardened. Consequently any further increase in density becomes dependent on particle fragmentation. With fragmentation, the remaining void space slowly becomes filled with the resulting debris.

(4) Finally, at ultrahigh pressures a powder mass achieves a stable, high density. Application of increased pressure results in bulk elastic type compression which tends

to be non-permanent deformation. Very infrequently are such pressures encountered in practical compaction.

Material hardness hinders compaction but coarse particle size or the addition of a lubricant can aid compaction, however coarse particle size and lubrication both slow sintering and reduce the green strength. Compaction is easier with mixed elemental powders. In general, both the green and sintered strength are improved by higher compaction pressures but the ejection force and die wear are both increased by high pressures.

2.2.4 Sintering

Packed particles heated above half the absolute melting temperature under a protective or reducing atmosphere will stick together by a process known as sintering. Most sintering treatments are conducted at temperatures around 75% of the absolute melting temperature. This solid state welding together of particles leads to a decrease in the surface area, an increase in compact strength, and in many cases a shrinkage in the compact. With prolonged high temperature sintering there will be a decrease in the number of pores, the pore shape will become smooth and grain growth can be expected. The process of sintering is generally the result of atomic motion stimulated by the high temperatures. The initial strains, surface area and curvatures existing in a pressed powder compact drive and bias the atomic motions responsible for sintering. Several different paths of atomic motion can contribute to the effect including volume diffusion, plastic flow, grain boundary diffusion and surface diffusion. In most cases the sintering kinetics are determined by several parameters including pressed density, material, particle size, sintering atmosphere, temperature and even degree of sintering. As mass flow takes place, the geometric progression can be divided into three stages representative of driving forces.

(1) During the initial stage of sintering, the particles are forming bonds between each other with rapid mass flow localized to the interparticle neck (bond) region. Local curvature gradients are the main driving force for mass flow. With longer sintering time, the pore structure becomes smoothed, leading to an elimination of the major curvature gradients, giving the intermediate stage of sintering.

(2) The intermediate stage is driven by the inter-facial energy; surface tension and grain boundary energy. These are weak forces hence the sintering rate is low and sensitive to the pore-grain boundary morphology.

(3) Finally, grain growth occurs and the pores become isolated and near spherical shape. Elimination of these isolated pores can be difficult and is dependent on the presence of grain boundaries. Unfortunately, grain growth typically hinders final stage sintering. Figure (2.3) shows the three stages of sintering. Here it is shown that pore volume shrinks and the pore become smoother as sintering proceeds. As pore spheriodization occurs, the pores are replaced by grain boundary.

The mass transport during sintering can be taken place by two ways, bulk and surface transport. The bulk transport sintering process gives compact densification whereas a surface transport process gives the same structural change without densification. In general a finer particle size increases the shrinkage, similarly a higher sintering temperature or longer sintering time tends to promote shrinkage. Alternatively, pressing reduces the shrinkage and improves strength, thus high compaction pressures are used to give good dimensional control in the sintered component. The electrical, magnetic, mechanical and physical properties are enhanced by high temperature sintering. However, the sintering force (surface tension) is rather weak. To enhance the overall process it is common to impose an external force through pressure or to provide a highly active kinetic path through the addition of a second phase. Hot isostatic pressing has been the most rapidly expanding commercial form of pressure enhanced sintering. Besides pressure assisted sintering, there are two other procedures in use to enhance densification during sintering-activated (solid state) and liquid phase techniques. These both rely on second phase additions to promote rapid mass transport or to enhance the operative driving forces. For metal matrix composite since aluminium is used, so it acts as an activated materials itself and for zinc oxide varistors, bismuth oxide accelerates the densification due to its melting at the sintering temperature.

2.3 COMPOSITE MATERIALS

Composites are new types of material called advanced materials because of their use at elevated temperature where existing materials are not suitable to use. The following sections gives the general idea about composites especially metal matrix composites.

2.3.1 Definition of Composite

The following criteria designate a composite:

(a) It must be man made.

(b) It must be a combination of at least two chemically distinct materials with a distinct interface separating the constituents.

(c) The separate materials forming the composite must be combined three dimensionally.

(d) It should be created to obtain properties which would not otherwise be achieved by any of the individual constituents [21].

So it is defined as:

A composite material is a materials system composed of a mixture or combination of two or more micro-constituents differing in form and /or material composition and that are essentially insoluble in each other unlike metal alloys. The mother material is the matrix whereas the other is called reinforcement.

2.3.2 Types of Composites

Several classification systems have been used to identify the composite [80], such as

(a) by basic material combinations, e.g., metal-organic or metal-inorganic,

(b) by bulk-form characteristics, e.g., matrix systems or laminates,

(c) by distribution of the constituents, e.g., continuous or discontinuous,

(d) and by function, e.g., electrical or structural.

As example, when the classification is based on the form of structural constituents, it is classified into five groups :

(1) Fibre composites, composed of fibres with or without matrix

(2) Flake composite, composed of flat flakes with or without a matrix

(3) Particulate composites, composed of particles with or without a matrix

(4) Filled (skeletal) composites, composed of continuous skeletal matrix filled by a second material

(5) Laminar composites, composed of layer or laminar constituents.

Figure (2.4) shows the above five composites. But nowadays composite is widely recognised according to its matrix. So they are classified into three groups as

MMC- metal matrix composite, where metal is used as a matrix material.

CMC- ceramic matrix composite, where ceramic materials are used as matrix materials.

and PMC- polymer matrix composite, where polymer is used as the matrix material.

2.3.3 History of Metal Matrix Composites

Composites are not new. Serious development began in the 1960s with the introduction of boron, graphite and aramid fibres. Work on metal matrix composite in the late 1960s resulted in numerous boron/aluminium metal matrix composite parts. However interest in MMCs diminished in the early 1970s as polymer matrix composites became the dominant materials. The introduction of new fibre reinforcement materials provided impetus for a MMC revival late in the last decade. Polymer matrix materials are still the most mature of composite technologies. Ceramic matrix composites are the least developed. Metal matrix composite systems lie somewhere between the two.

2.3.4 Matrix Materials and the Reinforcement

Metal acts as the matrix i.e., bonding element. Its main function is to transfer and distribute the load to the reinforcements or fibres. This transfer of load depends on the bonding interface between the matrix and the reinforcement: however bonding depends on the type of matrix and reinforcement and the fabrication technique.

The matrix can be selected on the basis of oxidation and corrosion resistance or other properties [21]. Generally Al, Ti, Mg, Ni, Cu, Pb, Fe, Ag, Zn, Sn and Si are used as the matrix materials, but Al, Ti and Mg are used widely.

For the reinforcement, characteristics such as chemistry, morphology, microstructure, mechanical and physical properties and cost have been considered, whilst for matrix factors such as density, strength potential, strength retention at elevated temperature and ductility/toughness are considered important. Again, matrix selection involves not only desired properties but also which material is the best suited for composite manufacturing. For example 7xxx[1] aluminium alloy rather than 2xxx aluminium alloy exhibits best combination of strength and toughness for aerospace application, but despite this, 2xxx aluminium alloy composite is used widely for the aerospace application. This is because if 7xxx aluminium alloy composite is used, an interface is developed between the 7xxx aluminium alloy and the reinforcement, which degrades the strength of the composites [81].

The 2xxx (Copper aluminium alloys), 6xxx (Silicon, magnesium aluminium alloys), and 7xxx (Zinc aluminium alloys) have been widely used as the matrix material for making composites. Recently aluminium-lithium alloy (8xxx) has been attracting the attention of the researcher due to its good wettability characteristics. For the good bonding and strength in the composite, metal alloys are used as the matrix element instead of pure metal.

---

[1] designated by Aluminium Federation Company

Reinforcement: Reinforcement increases the strength, stiffness, temperature resistance capacity but lowers the density of MMC. The prime role of the fibres (reinforcements) is to carry the load. The reinforcements can be divided into two major groups, continuous and discontinuous. The MMCs produced by them are called as continuously (fibre) reinforced composite and discontinuously reinforced composites. However, they can be subdivided broadly into five major categories: continuous fibres, short fibres (chopped fibres, not necessarily the same length), whiskers, particulate (or platelet) and wire (only for metal)

With the exception of wires, reinforcements are generally ceramics, typically these ceramics being oxides, carbides and nitrides. These are used because of their combinations of high strength and stiffness at both room and elevated temperatures. Common reinforcement elements are SiC, Al_2O_3, TiB_2, boron and graphite.

Continuous fibres in composite are usually called filaments, the main continuous fibres including boron, graphite, alumina and silicon carbide. The fibre is unique for unidirectional load when it is oriented in the same direction of loading, but it has low strength in the direction perpendicular to the fibre orientation.

Short fibres are "long" compared to the critical length l_c ($l_c = d.S_f/S_m$ where d is the fibre diameter, S_f is the reinforcement strength, and S_m is the matrix strength) and hence show high strength in composites, considering aligned fibres. Short fibres namely Saffil and Kaowool are used widely for the reinforcement of automobile engine components.

Whiskers are characterised by their fibrous, single-crystal structures which have almost no crystalline defects. Numerous materials, including metals, oxides, carbides, halides and organic compounds, have been prepared under controlled conditions in the form of whiskers. Presently, silicon carbide whisker reinforcement is produced from rice husk which is a low-cost material.

Particulates are the most common and cheapest reinforcement materials. These produce the isotropic property of MMCs which shows a promising application in structural fields. Initially, attempts were made to produce reinforced aluminium alloys with graphite powder [82-84], but only low volume fractions of reinforcement had been incorporated ($\langle 10\%$). Presently higher volume fractions of reinforcements have been achieved for various kinds of ceramic particles (oxide, carbide, nitride). Currently Kohara [85] has worked on SiC_p-Al and SiC_w-Al composite materials, showing that the SiC-particulate-reinforced aluminium matrix composites are not strong as the SiC whisker reinforced composites.

Metallic filaments are called wire, and they are characterized by their high elastic moduli. Among them, molybdenum and tungsten are the most outstanding. Presently stainless steel wire is creating interest. However the main disadvantage of metal filaments is that their density is higher than that of ceramic whiskers, with the probable exception of Beryllium. The details of reinforcement was given in reference [86].

The properties of MMC materials depend on the following.

(1) The properties of the individual components: for example, since the strength of metal alloy is greater than pure metal, it is now used instead of pure metal.

(2) The relative amounts of the components: with increasing volume fraction of reinforcement element, strength increases.

(3) The size, shape and distribution of the reinforcement: continuous fibres exhibit the highest strength when oriented unidirectionally, whisker and particulate giving better strength when distributed uniformly in the matrix.

(4) The degree of bonding between components : this is the most important parameter

for updating the strength. It is advisable to choose the proper metal and reinforcement with their suitable combination of CTE (coefficient of thermal expansion).

(5) The selection of an appropriate fabrication method.

2.3.5 Fabrication Route

Generally there are two types of fabrication methods:

(1) Solid-phase fabrication methods: diffusion bonding, hot rolling, extrusion, drawing, explosive welding, PM route, pneumatic impaction, etc. and

(2) Liquid-phase fabrication methods: liquid metal infiltration, squeeze casting, compocasting, pressure casting and spray codeposition amongst others.

Normally the liquid-phase fabrication method is more efficient than [85] solid-phase fabrication method because the solid-phase processing requires a longer time.

There are currently six manufacturing processes that have reached industrial status: these are diffusion bonding, the powder metallurgy route, liquid-metal infiltration, squeeze casting, spray co-deposition and compocasting. All those routes are discussed briefly in chapter one.

2.3.6 Applications

Presently, MMCs are not only used in aerospace industry but are also widely used in the automotive industry, in leisure items, in sports goods and in structural design. Aluminium oxide reinforced aluminium has been used in automotive connecting rods to provide stiffness and fatigue resistance with lighter weight. Aluminium reinforced with SiC whiskers has been fabricated into aircraft wing panels, producing 20% - 40% weight savings. In air frames, by using MMCs, the weight savings can be upto 60% [87]. SiC_P reinforced aluminium is now widely used as a microwave packaging unit. Compressor discs, blades, vanes, rotors of jet engines and guideline components for Trident missiles have been successfully made by MMC. In the near future, MMC and CMC will occupy the position of conventional metal alloys in manufacturing jet engines [88] and in air-frames [89]. SiC_p/Al composites now are used to make tennis rackets and the heads of golf clubs [90] and engine components and pistons are made by SiC_w/Al composite [91]. Carbon fibre reinforced composite is used to fabricate fishing rods and squash rackets. MMCs are attractive for satellite construction due to their higher mechanical damping properties [92] than those of other common structural materials.

2.4 ZINC OXIDE VARISTORS

Zinc oxide varistors are ceramic materials, mainly made from zinc oxide powders. Zinc oxides have moderate hardness and known as electronic ceramics due to their application. The following sections deal with the function and actions of varistors and discussed as:

(1) ceramic

(2) Voltage suppression device and

(3) Characteristics of zinc oxide varistors

2.4.1 Ceramic

Ceramics are the "Art and Science of non-organic non-metallic materials". These are brittle and do not have significant amounts of plastic deformation at room temperature. They are chemically inert and have low thermal and usually electrical conductivities. Ceramic includes a very wide range of materials like heavy clayware, refractories, cement, glass, abrasives and pure oxides. Oxides are the largest group of ceramics. These include the majority of the traditional materials which are generally based on silica, alumina, magnesia or two or more of these. The following table (2.1) [93] shows the different class of ceramic with their composition and function.

2.4.2 Voltage Suppression Device

A voltage suppression device is needed where deleterious transient overvoltages can occur. Zinc oxide varistors are used as transient overvoltage suppression devices. These are used to protect the electrical devices from transient overvoltage created by lighting strikes or power surges through diverting the overvoltage transient from the sensitive load in order to limit the residual voltage. There are two major categories of transient suppression:

(a) those that attenuate transients, thus preventing their propagation into the sensitive circuit and

(b) those that diverts transients away from sensitive loads and so limits the residual voltage.

The filter, generally of the low-pass type, connected in series within a circuit acts as the attenuator which attenuates the transient (high frequency) and allows the signal or power flow (low-frequency) to continue undisturbed.

Voltage clamping device and crowbar are used for diverting the transient. Unlike voltage suppression device, the crowbar device has limitation such as delay time. The delay time is typically microseconds, during which the load is unprotected for the case of crowbar. The voltage clamping device is a component having a variable impedance depending on the current flowing through the device or on the voltage across its terminal. These devices exhibit a nonlinear impedance characteristics-that is, Ohm's law is applicable but the equation has a variable R.

An important advantage of this type of device is that the functional characteristics of an electronic or electrical circuit are not affected by the insertion of such a device either before or after the transient for any steady state voltage below the maximum clamping voltage of the device. Figure (2.5) shows the transient voltage and the location of crowbar and the clamping device in the circuit. Voltage clamping devices are selenium cells, zener diodes and varistors which are either silicon carbide or metal oxide.

Selenium cells: Selenium transient suppressors apply the technology of selenium rectifiers in conjunction with a special process allowing reverse breakdown current at high-energy levels without damage to the polycrystalline structure. They do not have the clamping ability of the more modern metal-oxide varistors or avalanche diodes. So their field of application has been considerably diminished.

Zener diodes: Silicon rectifier technology has improved the performance of regulator-type zener diodes in the direction of design of surge suppression type avalanche diodes. The major advantage of these diodes is their very effective clamping system but they have low energy absorption capability, therefore at high voltage line, zener diodes are not used.

Varistors: The varistor functions as a nonlinear variable impedance. The relationship between the current in the device I and the voltage across the terminals V, is typically described by a power law:

$$I=K\ V^{\alpha} \tag{2.1}$$

Where

$$\alpha=\frac{\log I_2-\log I_1}{\log V_2-\log V_1} \tag{2.2}$$

and K is a proportional constant relate to the non-ohmical behaviour. The α exponent in the equation represents the degree of nonlinearity of the conduction. A linear resistance has an $\alpha=1$. The higher the value of α, the better the clamp and so better the performance. Therefore higher alpha values are desired for the varistor application. Silicon carbide varistors have relatively low α values which are mainly used in high-power, high-voltage surge arresters. Metal oxide varistors are primarily zinc oxide varistors which have α values considerably greater than those of silicon carbide varistor. Figure (2.6) shows the V-I characteristics of the above four transient suppression devices and table (2.2) shows the characteristic and different features of transient suppression [94]

2.4.3 Characteristics of Zinc Oxide Varistors

Zinc oxide varistors are ceramic, semiconducting N-type element manufactured through sinter-forming route. Small additions of bismuth, cobalt, manganese and other metal oxides are responsible for the nonlinearity characteristics of ZnO varistors. Their non linear current voltage behaviour (V-I) is shown in figure (2.7) [94]. This curve shows the leakage, nominal varistors's operation and upturn region. By varying the overall chemical composition and the processing conditions during manufacturing of the varistors, this V-I curve can be shifted up, down or the left or right and the values of α may be changed.

The structure of the body of varistors consists of a matrix of conductive zinc oxide grains separated by grain boundaries providing P-N junction semiconductor characteristics. These boundaries are responsible for blocking condition at low voltages and are the source of the non-linear electrical conduction at higher voltages. When exposed to high voltage transients, the varistor impedance changes many orders of magnitude from a near open circuit to a highly conductive level, thus clamping the transient voltage to a safe level. The potentially destructive energy of the incoming transient pulse is absorbed by the varistor, thereby protecting vulnerable circuit components.

Each ZnO grain of the ceramic acts as if it has a semiconducting junction at the grain boundary. Figure (2.8) shows the typical varistor microstructure. Since the non-linear electrical behaviour occurs at the boundary of each semiconducting ZnO grain, the varistor can be considered as a "multi-junction" device composed of many series and parallel connection of grain boundaries. The nominal varistor voltage V_n depends basically on the thickness of the device which has a number of grains "**n**" are in series between electrodes. The voltage drops varies 2-3 V (barrier voltage is normally 3 V per grain boundary) per grain boundary junction and does not vary for grains of different sizes. Therefore mean grain size and grain size distribution play a major role in electrical behaviour. So smaller grain size with uniform distribution are always desirable for the high performance of the varistors. Rate controlled sintering may play an effective role on this.

The relationship of varistors voltage with grain size is very simple and stated as follows:

$$V_n = (3\ V)\ n$$

where n is the average number of grain boundaries between electrodes and 3 V is barrier voltage per grain boundary. If D is the varistor thickness and d is the average grain size then

$$\begin{aligned} D &= (n+1)\ d \\ &\approx V_n\ d/3 \end{aligned}$$

So for increasing the V_n with the same thickness, the grain size should be small. The varistor voltage V_n, is defined as the voltage across a varistor at the point on its V-I characteristics where the transition is complete from the low-level linear region to the highly nonlinear region. If the grain sizes become uniform, during pulse, all the grains "switch on" together having uniform heat generation through the whole body of the varistors and no cracks occur for the pulse. On the other hand porosity is a bad thermal conductor, so the heat generation in the body becomes uneven due to the presence of porosity and varistor cracks or fail due to the thermal shocks. Therefore product of minimal porosity is desired. Rate controlled sintering also may improve the distribution of the phase material and reduce the porosity.

Figure (2.9) shows the different steps for producing the varistors. Bismuth oxide is molten above 825 °C, assisting in the initial densification of the polycrystalline ceramic. This polycrystallinity is the key to varistor action in ZnO. The addition of Bi_2O_3 has been found to be essential for forming non-ohmic behaviour. However, addition of transition oxides such as Co_3O_4 and MnO_2 also enhance nonlinearity. Similarly, multiple dopants such as a combination of Bi_2O_3, Sb_2O_3, MnO_2, SiO_2, Co_3O_4 and others can produce greater nonlinearity than a single dopant [95]

The nonlinearity in the ZnO varistor is a grain boundary phenomenon. There are different models to describe the nonlinearity, among them, the Schotty barrier model is widely accepted which can explain the non ohmic properties, the temperature dependence of the I-V curve, effect of additives, dielectric properties, bias voltage dependence of capacitance, transient conduction phenomena and degradation of the I-V curve [96].

According to this, the grain boundaries contain defect states which trap free electrons from the n-type semiconducting ZnO grains, thus forming a space charge depletion layer in the ZnO grains in the region adjacent to the grain boundaries [97]. The figure (2.10) shows an energy band diagram for a ZnO-grain boundary-ZnO junction which explains how the varistor action changes from leakage region to normal varistor region. In this figure (2.10), the left hand grain is forward biased, V_L and the right side is reverse biased to V_R. The depletion layer widths are X_L and X_R, and the respective barrier heights are ϕ_L and ϕ_R. The zero biased barrier height is ϕ_0. As the voltage bias is increased, ϕ_L is decreased and ϕ_R is increased, leading to a lowering of the barrier and increase in conductance.

The low current linear region is controlled by the impedance of the ZnO grain boundaries and the High-Current Upturn region is controlled by the impedance of the grain in the ZnO microstructure.

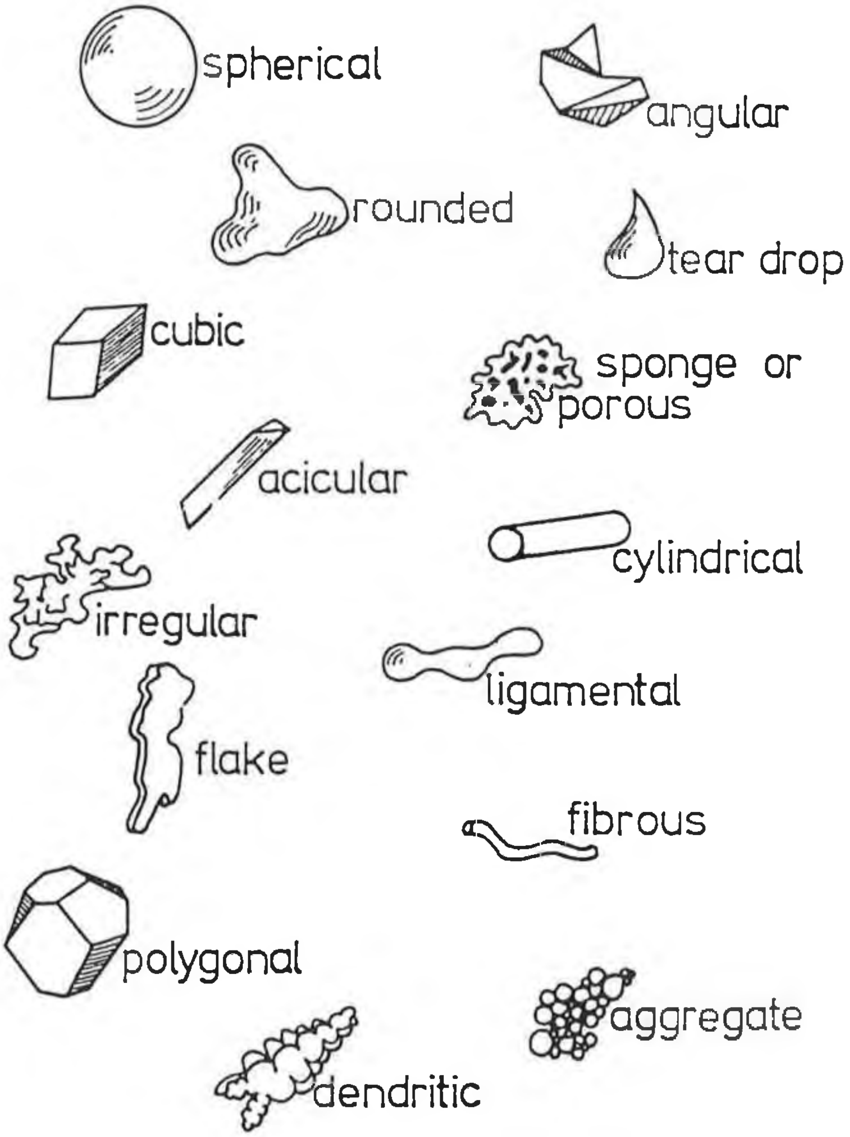

Figure 2.1 Different shapes of powder [98].

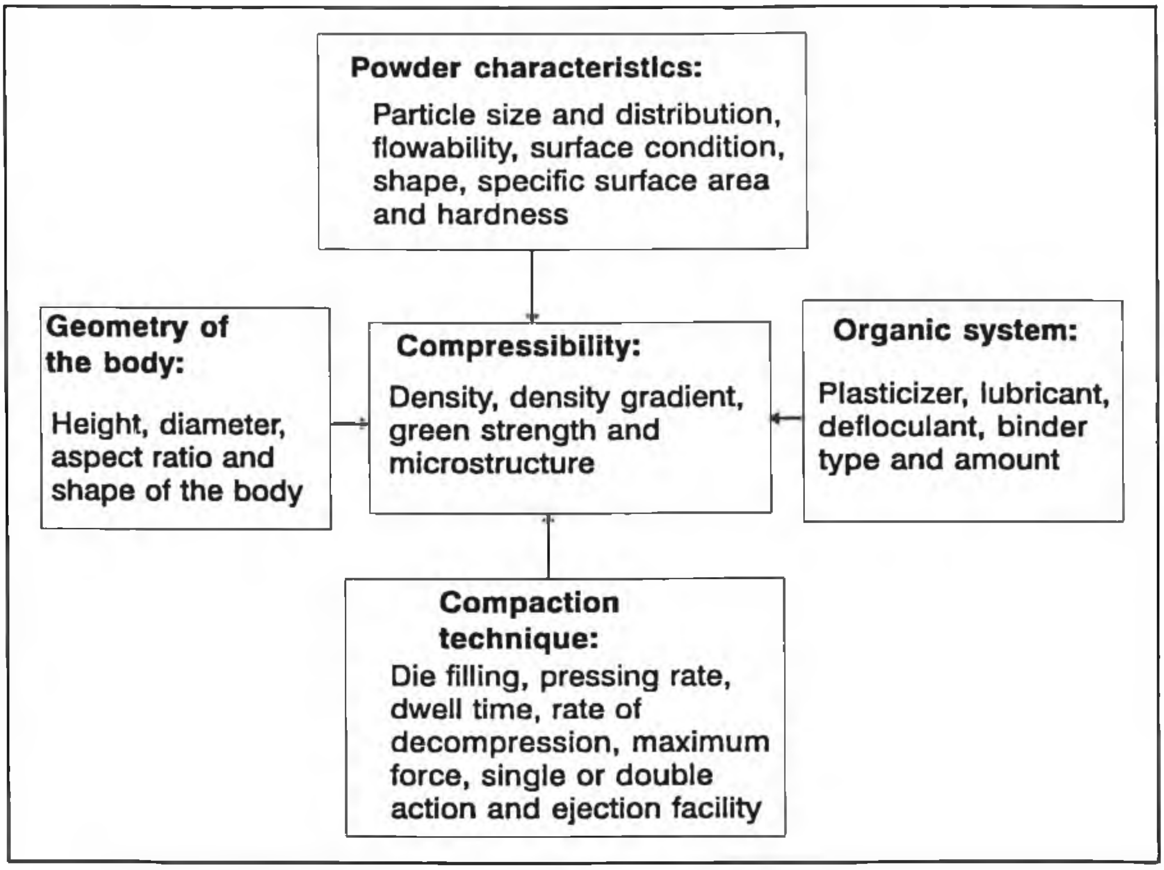

Figure 2.2 Variable parameters for compressibility.

(after A.N.M. Karim)

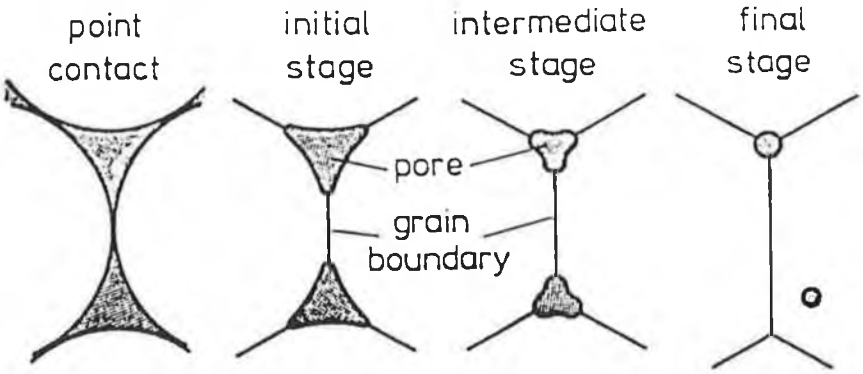

Figure 2.3 The steps of the sintering operation with formation of grain boundaries [98].

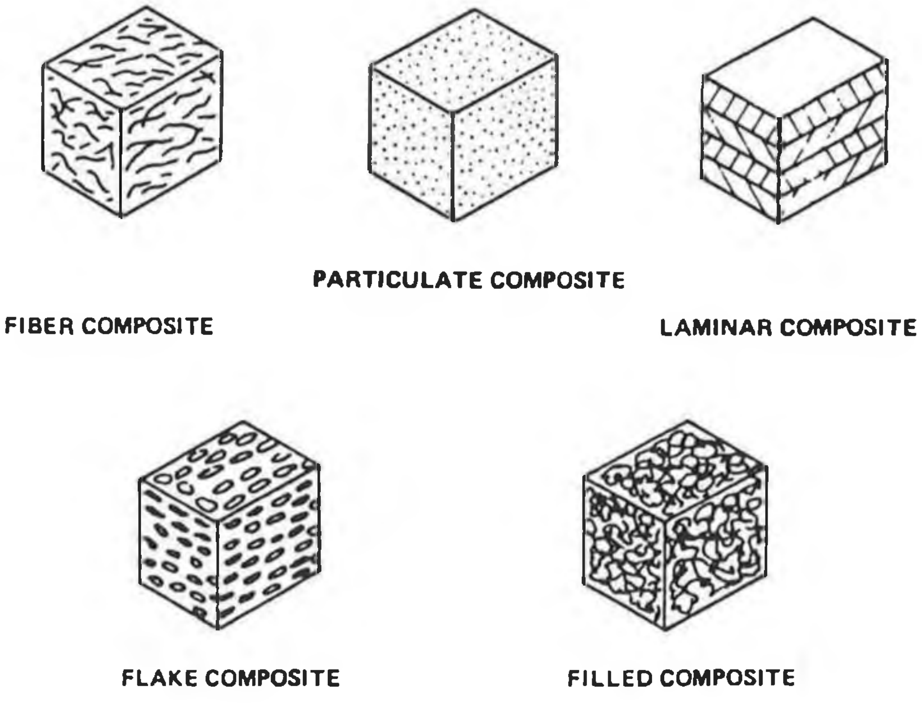

Figure 2.4 Classes of composites [80]

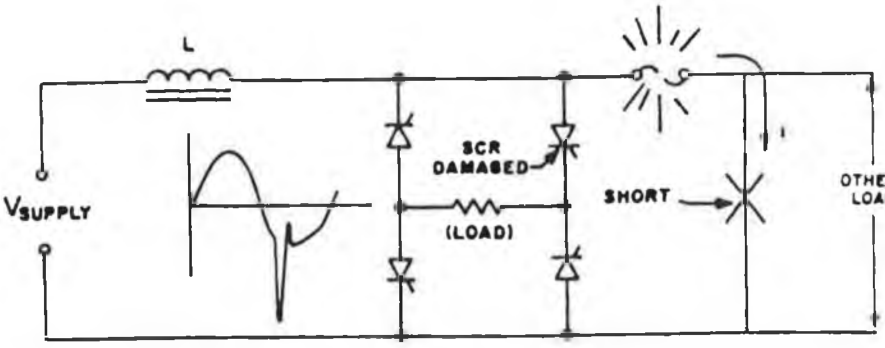

Figure 2.5 (a) Voltage transient cause by fuse blowing during power fault [94].

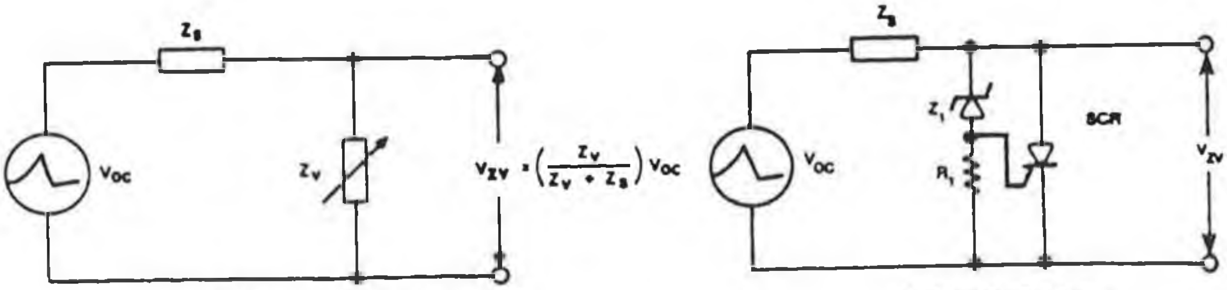

a) Voltage Clamping Device

b) Crowbar Device

Figure 2.5 (b) Location of voltage clamping device and crowbar showing division of voltage with variable impedance suppressor [94].

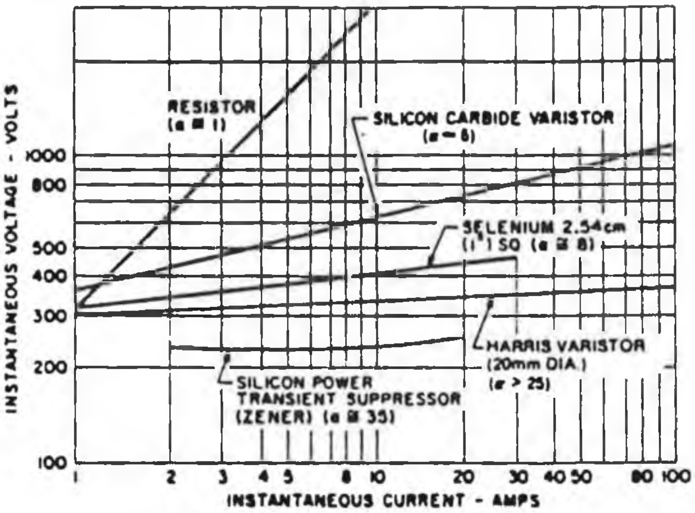

Figure 2.6 V-I characteristics of four transient suppressor devices [94]

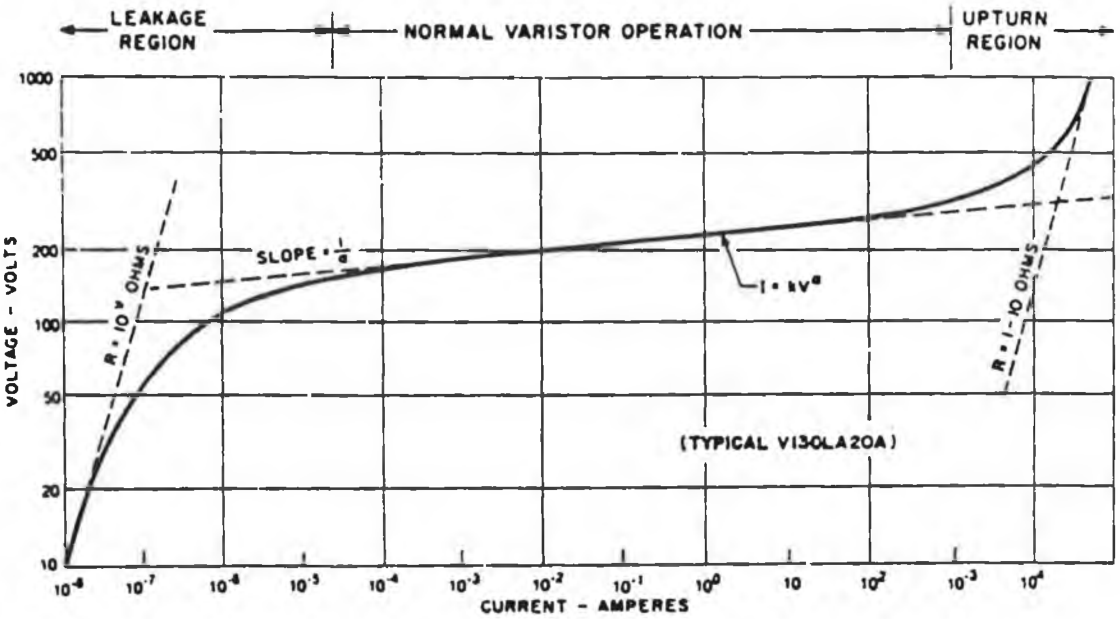

Figure 2.7 Typical varistor V-I curve [94].

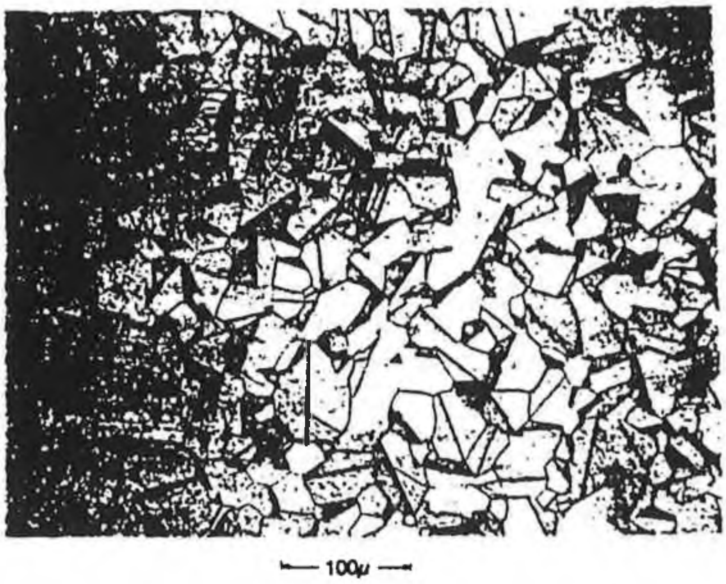

Figure 2.8 (a) Optical photograph of a polished and etched section of a varistor [94].

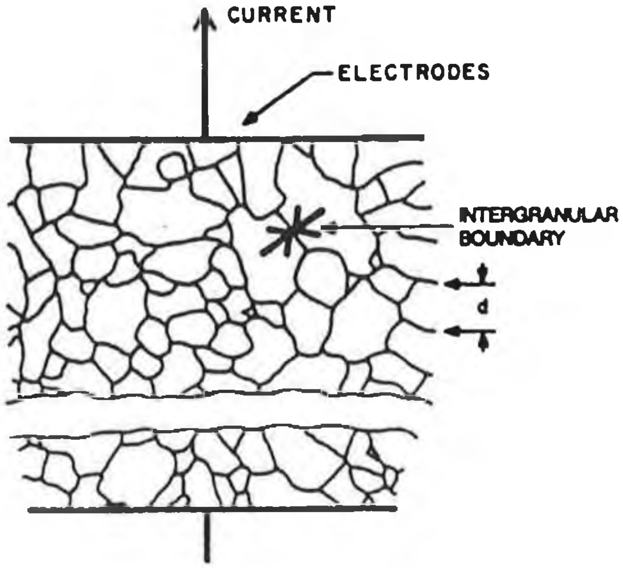

Figure 2.8 (b) Schematic depiction of the microstructure of a metal-oxide varistor. Grains of conducting ZnO (average size d) are separated by intergranular boundaries [94].

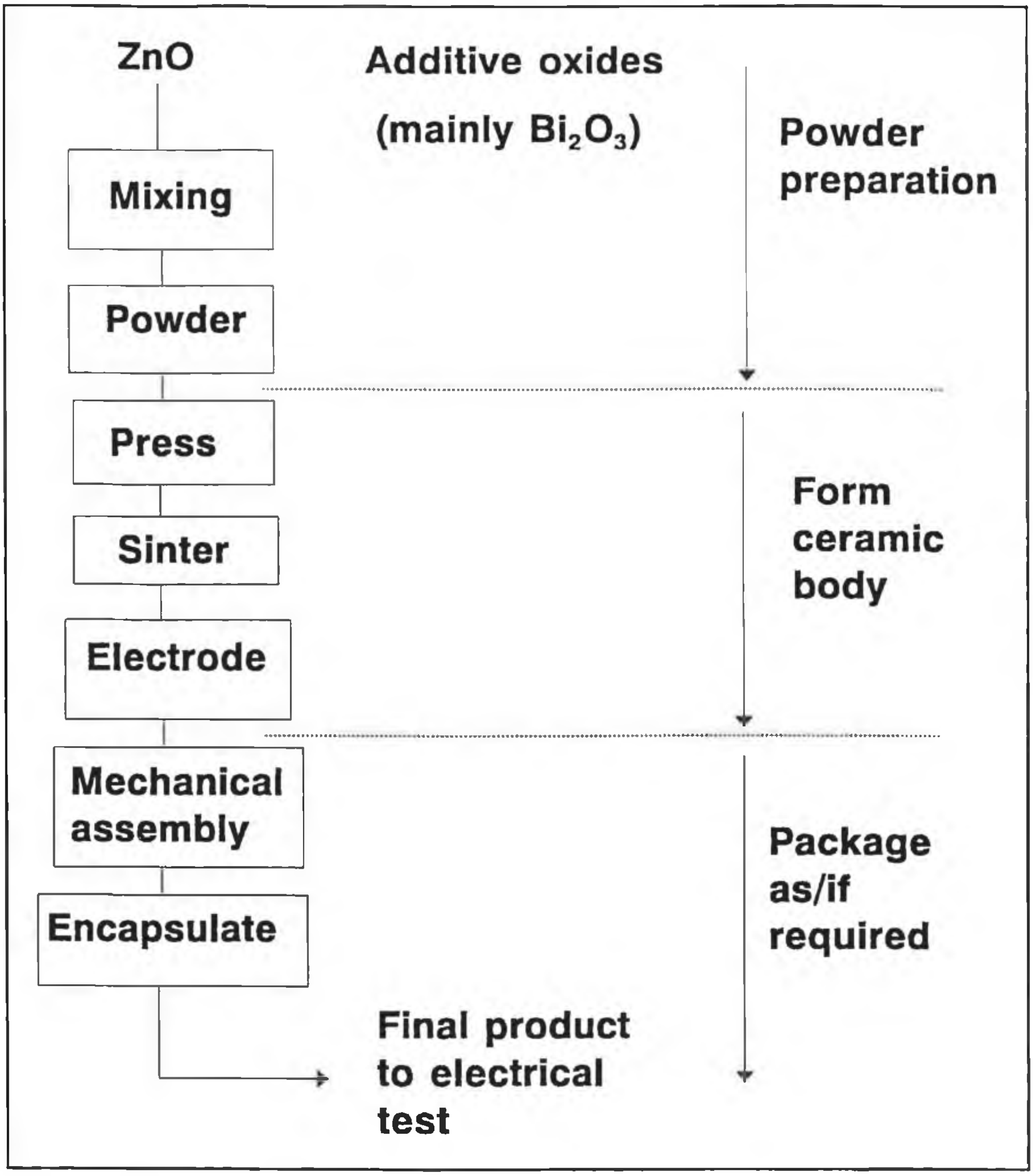

Figure 2.9 Schematic flow diagram of varistor fabrication [94].

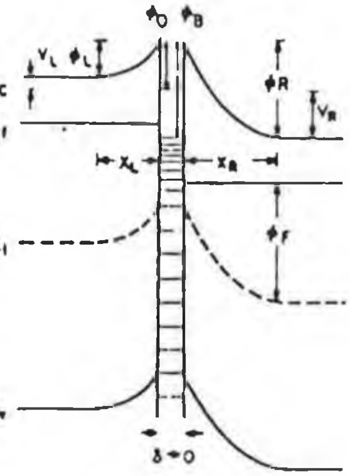

Figure 2.10 Energy band diagram of a ZnO-grain boundary-ZnO junction [94].

Function	Class	Nominal Composition*
Electrical	Insulation	α-Al_2O_3, MgO, porcelain
	Ferroelectrics	$BaTiO_3$, $SrTiO_3$
	Piezoelectric	$PbZr_{0.5}Ti_{0.5}O_3$
	Fast ion conduction	β-Al_2O_3, doped ZrO_2
	Superconductors	$Ba_2YCu_3O_{7-x}$
Magnetic	Soft ferrite	$Mn_{0.4}Zn_{0.6}Fe_2O_4$
	Hard ferrite	$BaFe_{12}O_{19}$, $SrFe_{12}O_{19}$
Nuclear	Fuel	UO_2, UO_2–PuO_2
	Cladding/shielding	SiC, B_4C
Optical	Transparent envelope	α-Al_2O_3, $MgAl_2O_4$
	Light memory	doped $PbZr_{0.5}Ti_{0.5}O_3$
	Colors	doped $ZrSiO_4$, doped ZrO_2, doped Al_2O_3
Mechanical	Structural refractory	α-Al_2O_3, MgO, SiC, Si_3N_4 $Al_6Si_2O_{13}$
	Wear resistance	α-Al_2O_3, ZrO_2, SiC, Si_3N_4, toughened Al_2O_3
	Cutting	α-Al_2O_3, ZrO_2, TiC, Si_3N_4, SIALON
	Abrasive	α-Al_2O_3, SiC, toughened Al_2O_3, SIALON
	Construction	Al_2O_3–SiO_2, CaO–Al_2O_3–SiO porcelain
Thermal	Insulation	α-Al_2O_3, ZrO_2, $Al_6Si_2O_{13}$, SiO_2
	Radiator	ZrO_2, TiO_2
Chemical	Gas sensor	ZnO, ZrO_2, SnO_2, Fe_2O_3
	Catalyst carrier	$Mg_2Al_4Si_5O_{18}$, Al_2O_3
	Electrodes	TiO_2, TiB_2, SnO_2, ZnO
	Filters	SiO_2, α-Al_2O_3
	Coatings	NaO–CaO–Al_2O_3–SiO_2
Biological	Structural prostheses	α-Al_2O_3, porcelain
	Cements	$CaHPO_4 \cdot 2H_2O$
Aesthetic	Pottery, artware	Whiteware, porcelain
	Tile, concrete	Whiteware, CaO–SiO_2–H_2O

Table 2.1 Classification of ceramics by function [93]

V-I Characteristics	Device Type	Leakage	Follow on I	Clamping Voltage	Energy Capability	Capacitance	Response Time	Cost
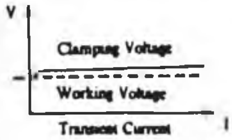	Ideal Device	Zero To Low	No	Low	High	Low Or High	Fast	Low
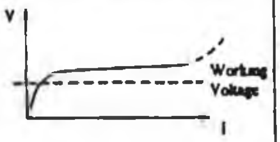	Zinc Oxide Varistor	Low	No	Moderate To Low	High	Moderate To High	Fast	Low
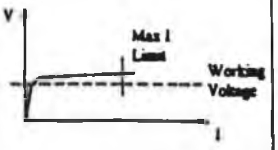	Zener	Low	No	Low	Low	Low	Fast	High
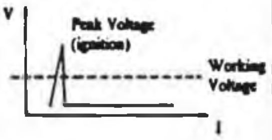	Crowbar (Zener - SCR Combination)	Low	Yes (Latching Holding I)	Low	Medium	Low	Fast	Moderate
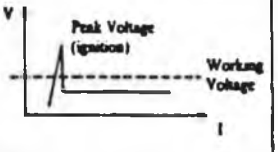	Spark Gap	Zero	Yes	High Ignition Voltage Low Clamp	High	Low	Slow	Low To High
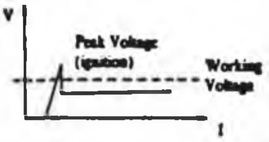	Triggered Spark Gap	Zero	Yes	Lower Ignition Voltage Low Clamp	High	Low	Moderate	High
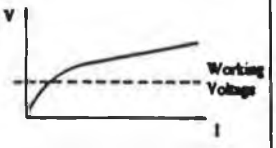	Selenium	Very High	No	Moderate To High	Moderate To High	High	Fast	High
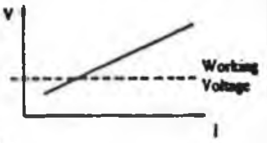	Silicon Carbide Varistor	High	No	High	High	High	Fast	Relative Low

Table 2.2 Characteristics and features of transient voltage suppressor technology [94].

CHAPTER THREE

EXPERIMENTAL TECHNIQUES AND RESULTS

3.1 INTRODUCTION

In this chapter, the descriptions of the materials and equipment which were used in this project are given. The experimental procedure has been enumerated and the compressibility of MMC has been discussed. Also some results of MMC showing the relationship between the mechanical properties and the sintering parameter have been presented here. So the writing is divided as follows:

(1) Materials

(2) Tools and Equipment

(3) Experimental Procedure and

(4) Results and Discussion

3.2 MATERIALS

3.2.1 Metal Matrix Composites

Two kinds of matrix powders were used, pure aluminium powder and aluminium alloy powder. Their grades are Al-1000 and Al-6061. The physical characteristics and chemical composition of these powders are shown in table (3.1) and table (3.2). Alumina and SiC powders were used as the reinforcement. The physical characteristics of these powders are shown in table (3.3) and table (3.4). The reinforcement powders are mixed in different proportion with matrix powders. After mixing of matrix and reinforcement with lubricant, these powders were analyzed for their particle size distribution. The analysis sheet (1) shows the particle size distribution for 20% of volume fraction of alumina in aluminium matrix composite powders whereas analysis sheet (2) shows the particle size distribution of the Al-6061/SiC composite powders for 23% volume fractions of SiC. From analysis sheet, the 50% value give the mean particle size. The mean particle size of Al-6061/SiC composites is lower than that of Al/Al_2O_3 composites.

3.2.2 ZnO Powders

Standard powders were used for the zinc oxide varistors. The general criteria of this powder is shown in table (3.5).

Table 3.1 Physical characteristics and chemical composition of aluminium powder

Powder	Conditions
Pure Al	Atomised, Max^{m} particle size 400 μm, purity 99.5% and density 2.70 g/cc

Table 3.2 Physical characteristics and chemical composition of aluminium alloy powder

Powder	Compositions %					
Al alloy 6061, Max^{m} particle size 45 μm	Silicon	Iron	Copper	Magnesium	Chromium	Aluminium
	0.75	0.16	0.30	1.01	0.18	balance

Table 3.3 Physical characteristics and chemical composition of alumina powder

powder	Conditions
Alumina	Atomized, Mean particle size 45 μm and density 3.90 g/cc

Table 3.4 Physical characteristics and chemical composition of SiC powder

Powder	Conditions
Silicon carbide	Electrical, Mean particle size 75 μm, purity 98.7% and density 3.2 g/cc

Table 3.5 Ceramic powder characteristics

Powder	Average particle size-μm	Density		Binder content g/kg	Moisture content g/kg	Binder type
		Bulk g/cc	Tap g/cc			
Standard	15-20	1.785	2.02	15	0.90	B

3.2.3 Lubricants

To facilitate compaction and ejection, zinc stearate was used in solid form. For compression test of the compacts, a thin sheet of teflon (0.125 mm) smothered with a film of petroleum jelly was used as the lubricant. The physical characteristics of zinc stearate lubricant is given in table (3.6).

Table 3.6 Physical characteristics of zinc stearate powder

Lubricant	Characteristics
Zinc stearate	Boiling temperature-120 °C, density-0.1 g/cc, particle size-0.5 μm

3.3 TOOLS AND EQUIPMENTS

3.3.1 Powder Mixing Tool

Metal powder mixing was carried out using a double cone mixture of 1.25 ltr. capacity made of stainless steel. Plate (3.1) shows the photograph of the mixer.

3.3.2 Powder Compaction Tool

A die set was used to produce discs of 17 mm diameter with different thickness. The punch tips and the die wall were made of tungsten carbide while the rest of the die parts (base, die body, guide rods, lower punch and upper punch) were made from high carbon high chromium steel (D2 material). The die was designed as a floating die set where the die body was supported by springs, to produce double sided compression with an option for a single action pressing. Figure (3.1) shows an assembly drawing of the die set and plate (3.2) shows the photograph of the die assembly.

3.3.3 Compaction Rig

A 50 kN INSTRON testing machine of model 4204 was used for making the green compact from the powders using the above die set. The same machine was also used for compression testing as described in section 3.3.5.

3.3.4 Sintering Unit

A box furnace (LENTON THERMAL DESIGN LTD) was modified to carry out the sintering operation of MMC. The maximum operating temperature of this furnace was 1200 °C. Figure (3.2) shows the box furnace and plate (3.3) shows a photograph of the sintering unit.

For the sintering of ceramic powder compacts, a pot furnace (TLB 34) was used. This will be described in chapter four.

3.3.5 Compression Testing Machine

A 50 kN INSTRON universal testing machine of model 4204 was used for the compression test of Al/Al_2O_3 composites. The compression test of Al-6061/SiC composite was carried out by 100 kN AVERY DENISON universal testing machine.

The INSTRON machine consists of a loading frame and a control console as a separate assembly accompanied with a plotter. The basic operation of the instrument consists of selecting a load cell for a particular testing application, mounted the load cell in the moving crosshead within the loading frame, then setting a specimen in position so that the load applied can be measured. Appendix A gives the full specification of the machine and plate (3.4) shows a photograph of the machine.

3.3.6 Hardness Tester

A micro hardness tester of type LEITZ MINILOAD 2 was used to measure the hardness of the specimens. This tester is capable of measuring three kinds of hardness- Vickers, Knoop and Scratch hardness by changing the diamond head. In this project, Vickers hardness method was employed to measure the hardness. The tester was calibrated first by the calibration tool. Then the load was applied to the specimen for a certain period. According to the indentation diameter of diamond indenter (pyramidal shape), the hardness was calculated or chosen from the tables. Always load 1.961 N was used for this work.

3.3.7 Grinding and Polishing Equipment

DAP-V (Struers) was used for the grinding and polishing operation to prepare a sample for hardness testing and for microstructure analysis. DAP is a complete programme of relatively small motor-driven machines for wet grinding and for alumina and diamond polishing of metallographic, ceramic and mineralogical specimens. For automatic polishing Pedimin-2 (Struers) was used which hold the polishing disc, mounted on DAP-V. Prestopress-3 (Struers) was used for making the polishing disc of the samples. Plate (3.5) shows the grinding and polishing equipment.

3.3.8 Optical Microscope

The optical microscope metallograph Reichert MeF3 was used for the microstructure analysis of Al/Al_2O_3 composite. A camera with providing polaroid film was attached with this microscope.

3.3.9 Scanning Electron Microscope (SEM)

Fine scale structural, topographic and dimensional measurements, beyond the scope of optical microscopy, were carried out using a Scanning Electron Microscope. The microstructure of the rate controlled sintering samples were taken by SEM manufactured by JEOL Ltd., model 840 A .

3.3.10 Weight Loss Equipment

The weight loss equipment consists of a balance, a PC, furnace, programmable furnace controller and serial communication interface adapter. It is described in the following chapter four.

- A balance of METTLER PM 6100 was used to monitor continuously the weight loss as a function of the furnace temperature. It was connected to an Amstrad computer through a RS 232 interface in COM1 port. It has a handshake mode facility and data can be sent bidirectionally by both the computer and the balance. The balance can weigh up to 6.1 kg with a resolution of 0.001 g.

- A personal computer (AMSTRAD 1512, 614 kB) equipped with a communication card SIO-2 was used. It has two ports with 25 pins and 9 pins. The 25 pins port was used as COM2 for the communication with the furnace controller and 9 pin port was kept idle.

- A pot furnace type Surefire TS 25, K+F was equipped with WEST 2054 controller programmer to execute the temperature profile in the furnace. The controller programmer has 8 temperature control modules and each module has 4 stages. Each stage consists of a ramp and dwell. The modules can be linked together to form a recipe or recipe and modules together can form a macro which gives a complex temperature profile. For the operation, it has two modes, slave and master with option X02 and X10 respectively. By slave mode, it can be controlled externally. For the communication with a personal computer, it is equipped with RS 422/RS 485 interface. For this project a RS 422 interface was used. To drive the controller programmer by computer, the **com** option of the controller was kept **EN**.

- The SCIA-30 serial communication interface adapter was used to convert the signal from the computer to a suitable form for the controller and vice versa. It was connected with the computer through a RS 232 interface by COM2 port and with the controller through RS 422 interface using a terminal block of 8 contact point.

3.3.11 Shrinkage Monitoring Equipment

The shrinkage monitoring equipment consists of a PC, furnace, controller, transducer, transducer conditioner and SCIA-30. This setup is fully described in chapter four.

- The personal computer AMSTRAD 1512, 614 kB was the same one as used for the weight loss equipment.

- The Pot furnace type Surefire TS25, K+F equipped with WEST 2054 controller programmer was the same one as used for the weight loss equipment.

- A displacement transducer with a spring return armature (LVDT type ACT/500/A, RDP Group) was used to measure the shrinkage of the sample during sintering. The transducer can measure displacements of up to ± 12.5 mm. It was calibrated and fixed +20 mm for measuring the contraction and -5 mm for the expansion. It was mounted through the top of the furnace using a vertical stand.

- A digital transducer indicator and conditioner (model 400/LVDT, RDP Group) was used to convert the electrical signal from the transducer, from analog to digital suitable for computer logging. The indicator has a resolution of 1 μm.

- The interface SCIA-30 and the RS 232/RS 422 signal converter were the same ones as described earlier for the weight loss equipment.

3.4 EXPERIMENTAL PROCEDURE

3.4.1 Powder Mixing

A powder volume between 20 and 40% of the mixer capacity is usually optimal for powder mixing [98]. So 500 g of matrix material with different volume fractions of reinforcement (alumina and SiC) was loaded separately into the double cone type mixture. Zinc stearate was added in the ratio of 1% by weight as a lubricant to reduce friction between the powder particles and the die wall during compaction and ejection. To test the effect of amount and type of lubricant, zinc stearate and calcium stearate in different proportion 1, 2, 3, 4 and 5% by weight were used with the alumina composite powders. The loaded powder was held in a lathe and rotated at 40 rpm for 60 min. for the Al-6061/SiC composite powder and 90 min. for Al/A_2O_3 composite powder. After each operation, the powders were unloaded and the mixer was cleaned for the subsequent run.

3.4.2 Powder Compaction

The die set unit was first placed on the anvil of the INSTRON machine. Then a predetermined quantity of powders was weighed to an accuracy of ± 0.01 g with the help of a boatlike plastic container and poured into the die cavity. The upper punch was then replaced manually into the die cavity. The load was applied gradually until the level of the required density was reached. Since different volume fractions of reinforcement were used, the applied load were varied to keep the green density the same. For Al/Al_2O_3 composite powders, the density of the green compact was 2.38 g/cc and for Al-6061/SiC composite powders, a 78% theoretical relative density was maintained for the green compact. For this, initial compaction tests were carried out before producing the compacts to find the compressibility curves of these powders. Figure (3.3) shows the compressibility curve for Al/Al_2O_3 composites whereas figures (3.4 to 3.8) show the compressibility curve for Al-6061/SiC composites of 8, 10, 15, 23 and 28% volume fraction of reinforcement respectively. From these curves, the load was determined which was set as a limit to stop the compaction load to get the same density. 50 kN load was used for the compaction of powder of the highest volume fraction of reinforcement. After reaching the maximum load, the load was held for 5 seconds and then released.

Ejection was done by removing the upper punch and placing the ejection tool at the top of the die body and reapplying the load to eject the compact. The compaction speed was used 2 mm/min. throughout the experiment and 10 mm/min. for the ejection. After each operation, die cavity wall and the punch tips were cleaned if needed.

3.4.3 Sintering

Before starting the sintering operation, the furnace was calibrated to get the actual temperature. The base dimension of the furnace was 8 x 12". The temperature varies on the bottom surface of the furnace and the centre region of 4 x 4" shows the constant temperature region but it always 10-20 °C lower than that of set limit temperature. So for setting the sintering temperature always 15° C was added to the required temperature. The temperature inside the furnace was stabilised after 15 min. Therefore, soaking times were considered after that. To maintain the sintering atmosphere a small hole was drilling at the bottom and at the top position of the rear side of the furnace and each hole was fitted with a small hollow tube. Argon gas with 5% hydrogen was used as a protective atmosphere.The gas was fed through the bottom tube. After charging each batch of compacts to be sintered, the gas was allowed to pass at a high flow rate (about 12 cf/min) for certain period between 10 to 15 min. to purge the air inside the chamber. The flow rate of gas was then kept low and maintained throughout the sintering cycle. The compacts were placed on a ceramic plate and kept at the centre of the furnace. These were sintered in batches of 6 at set sintering temperatures. The heating rate should be low. Plate (3.6) shows the defects of the samples for high heating rate due to the high rate of lubricant burnout. It was seen that below the melting temperature of Al, the sintering operation was not effective since no liquid phase sintering took place. The sintering temperature for Al/Al_2O_3 were 650°, 700°, 750° and 800°C and four different sintering time of 30, 60, 90 and 120 min. But the Al-6061/SiC compacts were sintered at 570°, 600°, 675°, 760° and 800°C for sintering time of 2.43, 3, 5, 8.3 and 10.3 hrs. For both cases the controlled atmosphere was created by Argon gas with 5% hydrogen. The compacts passed through a burnout stage at 540 °C for 30 minutes to burnout the fugitive lubricant. The compacts were then allowed to cool to room temperature inside the furnace. The flow of argon gas maintained during the whole cycle of heating, soaking and cooling.

3.4.4 Measurements

All dimensional measurements were taken using a micrometer with an accuracy of ± 1 μm. The weight of the powder and the sample after pressing and firing were carried out using an analytical balance with an accuracy of 0.01 g.

3.5 RESULTS AND DISCUSSION

3.5.1 Compressibility

To study the compressibility of the composite powders, Al/Al_2O_3 and Al/SiC composite powders were used. The compressibility curves were generated from the load displacement curve. Single action pressing were used to assess the compressibility while double action pressing was used to study the strength of green and fired compacts.
Figure (3.9) shows the compressibility curves for the 10% volume fraction of Al_2O_3 reinforcement with varying 1, 2, 3, 4, and 5% by wt. of zinc stearate lubricant. The curves show that there is very little effect of the amount of lubricant on the density. It is shown in figure (3.10) the compressibility curves for 2% by wt. of zinc stearate lubricant for varying volume fractions of Al_2O_3 reinforcement. This figure shows that with increasing reinforcement, the density decreases. It can be seen that for a given compaction stress, compacts made with 10% reinforcement have a higher density than those made with 20, 30

and 40% reinforcement.

Figure (3.11) shows compressibility curves for 20% alumina reinforcement with calcium stearate lubricant of 1, 2, 3, 4 and 5% by wt.. These curves also show that there is little effect of the amount of lubricant on compressibility. The compressibility curves for 1% by wt. of calcium stearate with 10, 20, 30, and 40% alumina reinforcement are shown in figure (3.12). Here, it is seen that the density decreases with the increase of reinforcement at a given compaction stress.

Figure (3.13) shows compressibility curves for 30% alumina reinforcement of 1% by wt. of zinc stearate and calcium stearate. It is seen that there is no effect of lubrication type on the compressibility. The compressibility curves for 20% SiC reinforcement with varying zinc stearate is shown in figure (3.14). It is seen that there is little effect of lubrication amount on the compressibility.

Compressibility curves for 5% zinc stearate with varying SiC reinforcement are shown in figure (3.15). These curves illustrate that with increasing reinforcement, the density decreases at a given compaction stress. Figure (3.16) shows compressibility curves for different reinforcements. It is seen that at zero stress, the density of compact made by SiC is higher than that of the compact made with Al_2O_3 due to the rearrangement of the particles. Its density at the middle is lower than that of the compact made with Al_2O_3. But at higher stress, the density of compacts made from SiC and Al_2O_3 becomes the same showing that the relative density of specimen made from SiC is higher than that of specimen made from alumina, since the theoretical density of SiC is lower than that of Al_2O_3.

Generally it is seen from all of the compressibility curves that there is a sharp increase in the density at the beginning of the compaction process then it starts to slow down at high pressures. This sharp increase in the curve is due to the particles rearrangement where particles try to occupy the smallest place. As the pressure increases, the particles start to deform and fracture and leads to further densification by the fact that the newly formed small pieces can move into the remaining pore spaces between the larger particles. Moreover after releasing the load it can be noticed from the load-displacement curve that there is a reduction in the density. This is due to the spring back effect where the compact recovers elastically and it increases with the increase of reinforcement and compaction pressure. TiC was also used to see the compressibility. Titanium is a hard dispersoid and not suitable for cold compaction, since a heavy friction force developed resulting ejection force is greater than compaction load. So it was rejected though it imparts high strength and wear resistance to the base material.

3.5.2 Mechanical Strength

The mechanical strength of the green body is an important factor. Firstly, because unreliable green compacts lead to unreliable final product and secondly, it is important that the compact has sufficient strength for handling purposes. It has been observed that the distribution of large flaws in the green body remained unchanged through sintering. Furthermore, additional flaws can be introduced by grain growth (99) which in turn weaks the fired sample. Normally green bodies of 50% theoretical relative density are produced during standard manufacturing conditions. It has been suggested that the strength for most ceramic green bodies varies from 1 to 2 MPa (99). With the increase of volume fraction of reinforcement, the compaction pressure increases producing the green compact of same density for further operation.

Griffith's flaw theory (100) can be used to predict the strength of brittle materials. It assumes

the presence of intrinsic flaws of a specific shape, and there is always one with the least favourable location and orientation and that the crack growth from this flaw causes failure. This theory ignores the statistical nature of the problem. The statistical approach is widely used for predicting the strength but in this case, it does not specify the nature of the flaw. Normally Weibull's distribution is used for the statistical analysis of strength of materials due to brittle fracture, of crack initiation toughness or fatigue life. The Weibull distribution function $P(\sigma)$ is defined as:

$$P(\sigma)=1-e^{-[\frac{(\sigma-\sigma_0)}{b}]^m} \quad for \quad \sigma \rangle \sigma_0 \qquad (3.1)$$
$$P(\sigma)=0 \quad for\ \sigma \langle \sigma_0$$

Where σ_0, b, and m are the three Weibull parameters which define this distribution function. For the strength study, $P(\sigma)$ is taken as the probability of failure when a stress σ is placed on the specimen. The parameter σ_0 is the zero strength since $P(\sigma)=0$ for $\sigma<\sigma_0$. The constants b and m are known as the scale parameter and the Weibull slope parameter (modulus) respectively. The probability of failure $P(\sigma)$ at a load σ is determined from

$$P=\frac{k}{n+1} \qquad (3.2)$$

where k= the order number of the sequenced data

and n= the total sample size

From equation (3.1) it can be written

$$e^{(\frac{\sigma-\sigma_0}{b})^m}=[1-P(\sigma)]^{-1} \qquad (3.3)$$

Taking the natural log of both sides of equation (3.3) yields

$$\left(\frac{\sigma-\sigma_0}{b}\right)^m=\ln[1-P(\sigma)]^{-1} \tag{3.4}$$

Taking $\log_{10}$ of both sides of equation (3.4) gives a relation for the slope parameter m. Thus

$$m\ (\log_{10}(\sigma-\sigma_0)-\log_{10}b)=\log_{10}\ln[1-P(\sigma)]^{-1} \tag{3.5}$$

considering σ_0 and b are zero, the equation (3.5) becomes

$$m[\log(\sigma)]=\log\ \ln[1-p(\sigma)]^{-1} \tag{3.6}$$

$$m=\frac{\log\ln[1-P(\sigma)]^{-1}}{\log(strength)} \tag{3.7}$$

where m is slope of the straight line. So higher the value of slope, higher the reliability of the sample.

The Weibull approach [101] for predicting the probability of failure of a structure involves dividing the total volume into many volume elements, each element having a small probability of failure. The probability of survival of the part as a whole is then found by multiplying together the probabilities of survival of all the elements. The elements are considered to be similar to the links of chain, with the weakest link determining the strength of the chain. Thus the properties of a volume element, as inferred from the statistics of fracture in simple tension or bending, played a central role in Weibull's theory. The theory states [102] that the probability that rupture will occur within a given volume subjected to any uniform stress is assumed to be completely determined by a quantity σ which may be calculated from the three principal stresses.

3.5.3 Diametral Compression Test

The green strength of the compacts was measured using the diametral compression test. This test had been performed by placing the compact between two flat surfaces as shown in figure (3.17). The force was applied along a diametral plane of the compact. The loading produces a biaxial stress distribution within the specimen which constant all along the cylindrical axis Z of the specimen. This stress distribution consists of a tensile stress at the plane where the force is applied and a compressive stress which acts along the loaded diameter [103]. Compacts were tested in both the green and fired states using this test. The recorded load was used to calculate the tensile strength of the compact using the following equation according to reference [104].

$$\sigma = \frac{2P}{\pi h D} \tag{3.8}$$

where σ is the tensile stress, h is the compact height, D is the compact diameter and P is the recorded fracture load.

The diametral test was carried out on 10 green specimens for each powder compact. The results of the test were used to calculate the probability of failure for brittle materials using Weibull's theory for strength of brittle materials [105]. Plate (3.7) shows the fracture of the samples in diametral compression test.

Figure (3.18) shows probability curves for the green compacts of 10% volume fraction of

Al_2O_3 reinforcement with 1% by wt. of zinc stearate and calcium stearate lubricant. It is seen from these curves that the strength of the compact using zinc stearate is higher than that of the compact using calcium stearate. However, the slope of the curve for the calcium stearate is higher. It means that the strength of the compact is more reliable than that of the compact made from zinc stearate. The probability curves for the green compacts of 20% volume fraction of Al_2O_3 with 1, 2, and 3% by wt. of zinc stearate lubricant are shown in figure (3.19). It is seen from these curves that there is not much difference in strength for the different amounts of lubricant. But for 1% lubrication, the strength is little bit higher than those for the others. Also the slope of the curve is the highest showing that the strength of this compact with 1% lubrication is more reliable than the others.

Figure (3.20) shows probability curves for the green compacts of 10, 20, and 30% Al_2O_3 reinforcement with 1% by wt. of zinc stearate. These curves show that the strength of compact made from 10% reinforcement is the highest and most reliable than the others. The probability curves for the fired compacts of 20% Al_2O_3 reinforcement with 1, 2 and 3% by wt. of zinc stearate lubricant is shown in figure (3.21). This figure shows that compacts have higher strength than those of green compacts but less reliability, where it can be seen that the slope of the curves deteriorate in respect of the curve

3.5.4 Compressive Strength Test of Al/Al_2O_3 Composites

After firing, the compressive strength test is also carried out. With the increase of reinforcement, ductility of the samples decreases and the samples were broken down suddenly without preliminary cracks during testing for higher reinforcements. The load at breaking point of the specimen for higher volume fraction of reinforcement are taken to calculate the compressive strength. Plate (3.8) shows the sintered samples of different volume fraction of Al_2O_3.

The effect of time on compressive strength has been analyzed for different volume fraction of reinforcement (10, 20, 30 and 40%). These are shown in figures (3.22) to (3.25) respectively. It is shown from both figures (3.22) and (3.23) that the strength increases with increasing sintering temperature and time. This could be due to the uniform distribution of the particles and higher soaking time which allows uniform grain growth. In addition the slopes of the curves increase with increase of sintering temperature greater than 700° C.

For 30% and 40% reinforcement figures (3.24) and (3.25) show respectively that generally the strength increases with increasing sintering temperature but the trends of the curves for 30 and 60 min. sintering time are different from those of the curves for 90 and 120 min. sintering time when the temperature is greater than 750° C. This could be due to the longer soaking time at higher temperatures which changes the density simultaneously with the microstructure of the material.

The relationship between compressive strength and volume fraction of reinforcement has been presented for different temperatures 650, 700, 750 and 800 °C in figures (3.26) to (3.29) respectively. Figure (3.26) shows for temperature 650° C that the compressive stress decreases with the increase of reinforcement. The value of compressive stress for different time at certain reinforcement becomes same but at time 60 min. gives higher values. It is shown in figure (3.27) for temperature 700° C that compressive stress decreases with the increase of reinforcement. At lower reinforcement, the value of compressive stress at 120 min. is higher than that of other time but it decreases with increase of reinforcement and becomes same at higher reinforcement. The compressive stress in figure (3.28) for temperature 750 °C shows that it decreases with increase of reinforcement but the value of compressive stress increases with increase of time. Figure (3.29) shows for temp. 800° C that the compressive stress decreases with increase of reinforcement. There is significant difference of compressive stress at 20% reinforcement for sintering time 120 and 30 min. respectively and has higher value in time 120 min. but at higher volume fraction the compressive stress for different time becomes same.

In all cases the compressive stress decreases with increase of reinforcement. It could be due to the achievement of small relative density of the green compact for higher reinforcement. Since no shrinkage takes place and in some cases swelling occurs, density actually decreases. At higher reinforcement, the bonding between the matrix and the reinforcement deteriorates. Therefore the material has the lower resistance to deformation. As a preliminary experiment, the particle size was taken very high. The larger particles retard shrinkage and thus causing less bonding between the particle and keep the strength low.

3.5.5 Hardness of Al/Al_2O_3 composites

Hardness is defined as the resistance of the material to indentation or scratching. Microhardness tester was used and Vicker's hardness was measured. For each sample, 15 readings were taken and the average values were represented the hardness of the sample. For the measurement of hardness, at first the top face of the samples was ground and polished by the polishing machine.

The effect of time on hardness has been analyzed for different volume fraction of reinforcement (10, 20, 30 and 40%). These are shown in figures (3.30) to (3.33) respectively. Figure (3.30) shows at 10% reinforcement that for sintering time of 30, 60 and 90 min. the Hardness increases for up to 750 °C sintering temperature and then decreases showing that at 750 °C, the bonding between the matrix and the reinforcement is the optimum. However for sintering time of 120 min., the hardness increases with sintering temperature of up to 800 °C . This could be due to the improvement of bonding with the soaking time. It is shown in figure (3.31) that at 20% of reinforcement the hardness becomes greatest at 750 °C except for 30 min. sintering time which shows an irregular pattern. This could be explained by the fact that the distribution of the particles and the bonding between the matrix and reinforcement can not reach uniformity during this short period of sintering time. For 30% reinforcement it is seen that the hardness becomes maximum at sintering temperature of 700 °C. It implies that the bonding between the matrix and the reinforcement is better at this temperature than compared to other temperatures. Figure (3.33) shows that at 40% reinforcement for 30 and 60 min. sintering time, the hardness is maximum at about 770 °C and 730 °C respectively but for 90 and 120 min. sintering time, it is about 800 °C. The irregular nature of the curve corresponding to the higher sintering times is most likely to be due to different grain growth mechanisms.

The relationship between hardness and volume fraction of reinforcement for different temperature 650°, 700°, 750° and 800 °C has been presented in figures (3.34) to (3.37) respectively. At 650° C it is seen that the hardness increases with the increase of reinforcement only at higher sintering times. This could be, due to the improvement of bonding with the soaking time. It is shown in figure (3.35) for temp. 700° C that the hardness increases with increase of reinforcement for all of the sintering time which is expected. But the irregular nature of the curves corresponding to the lower sintering time (30 and 60 min.) is most likely to be due to different grain growth mechanisms. Figure (3.36) shows for temp. 750° C that the hardness becomes maximum at the highest reinforcement but minimum at 30 percent reinforcement for 30 and 60 min. sintering time. This could be due to the degradation of bonding at this reinforcement. It is shown in figure (3.37) for temp. 800° C that the hardness becomes maximum at the highest percentage of reinforcement. But the pattern of the curves from 10 to 30 percent of reinforcement is irregular. This could be due to the different grain growth mechanism.

The values of hardness and the compressive stress are generally lower than the available data in the literature. Since after sintering, no shrinkage takes place, the density decreases giving lower strength. To improve the sintering operation, alloying aluminium with sintering catalyst such as Fe, B, must be introduced.

3.5.6 Microstructure

A brief study was carried out on the microstructure of Al/Al_2O_3 composite. The study was carried out by optical microscopy. The microstructures are taken for only 10% and 20% reinforcement to see the distribution of reinforcement in the matrix and grain growth. The temperatures are taken as 750° C and 800° C, since these temperatures played a vital role for the hardness and compressive stress values. Different times are taken to study the effect of soaking temperature on the microstructure. It is evident from figures (3.38 a) and (3.38 b) for 10% reinforcement and for time 60 min. at temp. 750° C and 800°C respectively that the structure of the sample sintered at 750 °C is rather dense showing small porosity than that for temp. 800° C. This results in greater hardness as shown in figure (3.30). For 10% reinforcement at temperature 800° C and time 120 min. shown in figure (3.38 d), the grains grow but they are of smaller size than that of specimen produced at 750 °C for time 120 min. (fig. 3.38 c) giving also higher hardness as shown in figure (3.30).

In figure (3.39 a) and (3.39 b) for 20% reinforcement and for time 60 min. at temp. 750°

C and 800° C respectively, it is seen that the distribution of alumina is uniform with less porosity at 750° C. This results in greater hardness as shown in figure (3.31). In figures (3.39 c) and (3.39 d) for 20% reinforcement and for time 30 min. at 750° C and 800° C respectively it is shown that the distribution of alumina in the sample at 800 °C is also uniform with less porosity giving greater hardness than that of the specimen sintered at 750 °C (see figure 3.31).

02 Jun 1994 11:38 am

MALVERN Instruments SB.0B

Matrix- Pure Aluminium
Reinforcement- 20% volume fraction of alumina

0000006252

1978 pil 1JP337

High Size	Under %	High Size	Under %	High Size	Under %	High Size	Under %	High Size	Under %	High Size	Under %
564	100	254	21.2	114	3.9	51.3	0.5	23.1	0.3	10.4	0.3
524	90.9	236	18.4	106	2.9	47.7	0.4	21.4	0.3	9.64	0.3
488	81.8	219	16.3	98.6	2.2	44.4	0.4	19.9	0.3	8.97	0.3
454	73.0	204	14.8	91.7	1.7	41.2	0.4	18.5	0.3	8.34	0.3
422	64.5	190	13.7	85.3	1.4	38.4	0.4	17.2	0.3	7.76	0.3
392	56.3	176	12.6	79.3	1.2	35.7	0.4	16.0	0.3	7.21	0.3
365	48.7	164	11.5	73.8	1.1	33.2	0.4	14.9	0.3	6.71	0.3
339	41.6	153	10.1	68.6	0.9	30.8	0.4	13.9	0.3	6.24	0.2
315	35.3	142	8.6	63.8	0.8	28.7	0.4	12.9	0.3	5.80	0.2
293	29.7	132	6.9	59.3	0.7	26.7	0.4	12.0	0.3		
273	24.9	123	5.3	55.2	0.6	24.8	0.4	11.2	0.3		

Span 1.00

D[4,3] 355.89µm

D[3,2] 231.18µm

D[v,0.9] 520.81µm

D[v,0.1] 151.53µm

D[v,0.5] 369.42µm

Source = :Sample
Focal length = 300 mm
Presentation = pil

Beam length = 14.3 mm
Log. Diff. = 3.119
Obscuration = 0.0051
Volume distribution

Model indp
Volume Conc. = 0.0027%
Sp.S.A 0.0260 m^2/cc.

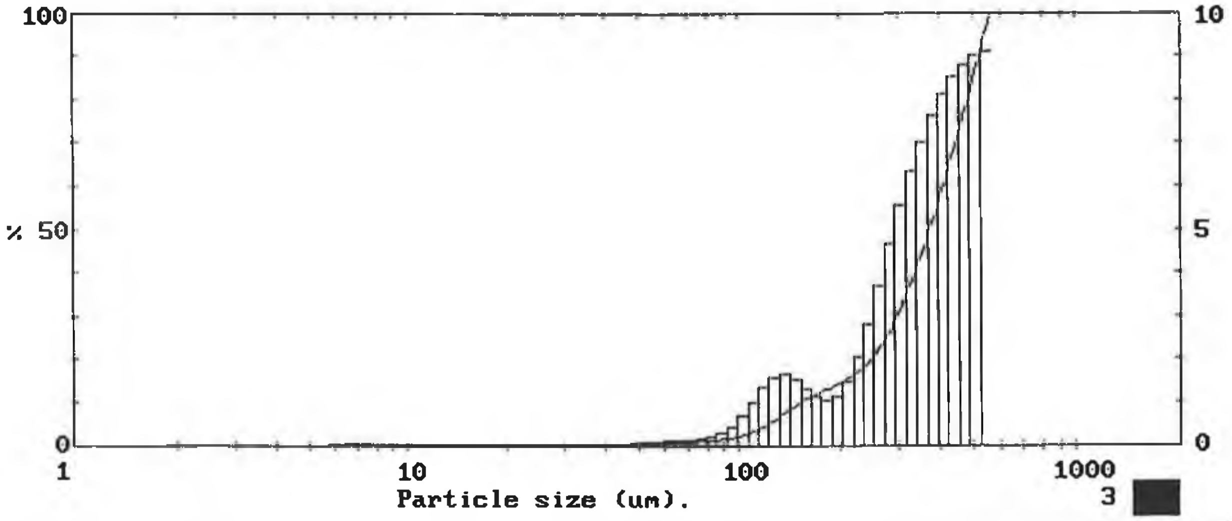

HARRIS IRELAND

Analysis sheet 1 Particle size distribution of 20% volume fraction of reinforcement for Al/Al_2O_3 composites.

11 Aug 1994 1:50 pm

MALVERN Instruments SB.0B

23 % volume fraction of reinforcement
Al-6061/SiC composites 000000006564

1978 pil 1JP337

High Size	Under %	High Size	Under %	High Size	Under %	High Size	Under %	High Size	Under %	High Size	Under %
118	100	53.3	96.7	24.0	36.1	10.8	4.1	4.84	0.0	2.18	0.0
110	100	49.5	93.2	22.3	31.3	10.0	2.9	4.50	0.0	2.03	0.0
102	100	46.1	89.0	20.7	27.1	9.31	2.2	4.19	0.0	1.88	0.0
95.2	100	42.8	84.3	19.3	23.6	8.66	1.7	3.89	0.0	1.75	0.0
88.6	100	39.8	79.0	17.9	20.4	8.05	1.4	3.62	0.0	1.63	0.0
82.4	100	37.0	73.3	16.7	17.7	7.49	1.0	3.37	0.0	1.51	0.0
76.6	99.9	34.4	67.2	15.5	15.1	6.97	0.7	3.13	0.0	1.41	0.0
71.2	99.8	32.0	60.8	14.4	12.7	6.48	0.4	2.91	0.0	1.31	0.0
66.2	99.8	29.8	54.3	13.4	10.3	6.02	0.2	2.71	0.0	1.22	0.0
61.6	99.7	27.7	47.8	12.5	8.0	5.60	0.1	2.52	0.0		
57.3	98.9	25.8	41.7	11.6	5.9	5.21	0.0	2.34	0.0		

Span 1.18

D[4,3] 29.40µm

D[3,2] 23.51µm

D[v,0.9] 46.83µm

D[v,0.1] 13.27µm

D[v,0.5] 28.40µm

Source = :Sample
Focal length = 63 mm
Presentation = pil

Beam length = 14.3 mm
Log. Diff. = 6.407
Obscuration = 0.6883
Volume distribution

Model indp
Volume Conc. = 0.0642%
Sp.S.A 0.2552 m²/cc.

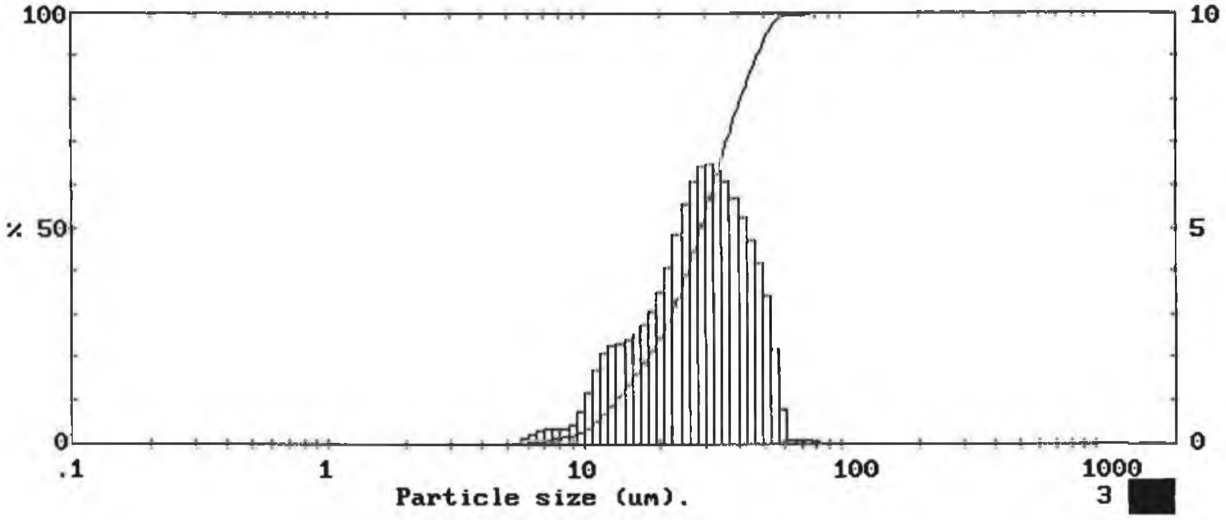

HARRIS IRELAND

Analysis sheet 2 Particle size distribution of 23% volume fraction of reinforcement for Al-6061/SiC composites.

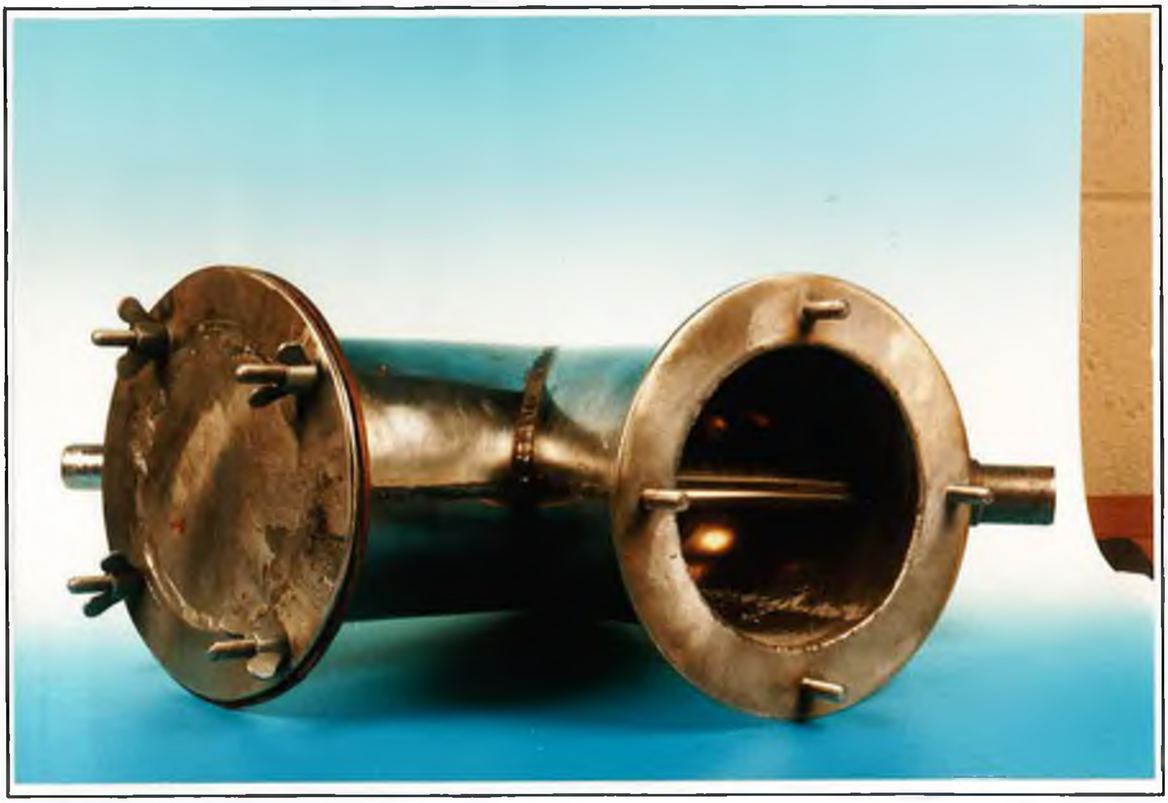

Plate 3.1 Photogarph of the V-mixer.

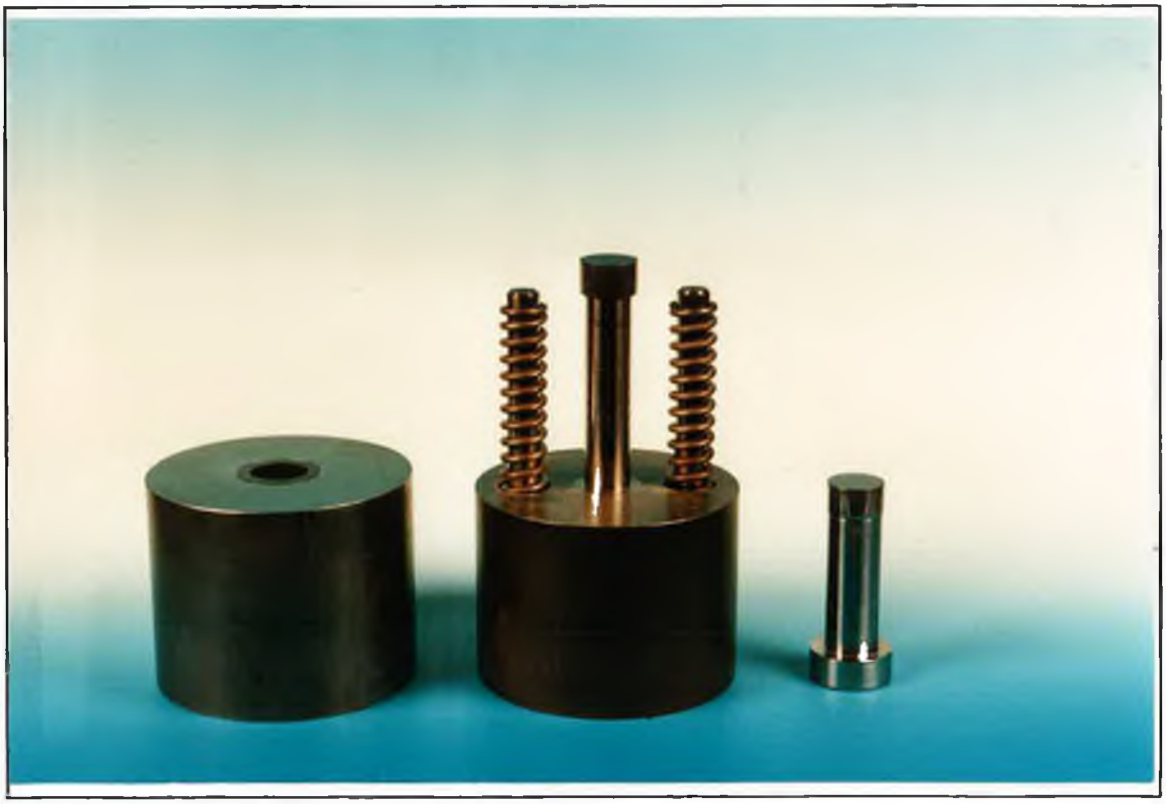

Plate 3.2 Photograph of the 17 mm diameter die set.

Plate 3.3 Photograph of the box furnace.

Plate 3.4 Photograph of the INSTRON machine.


Plate 3.5 Photograph of the grinding and polishing machine with Presto-press.

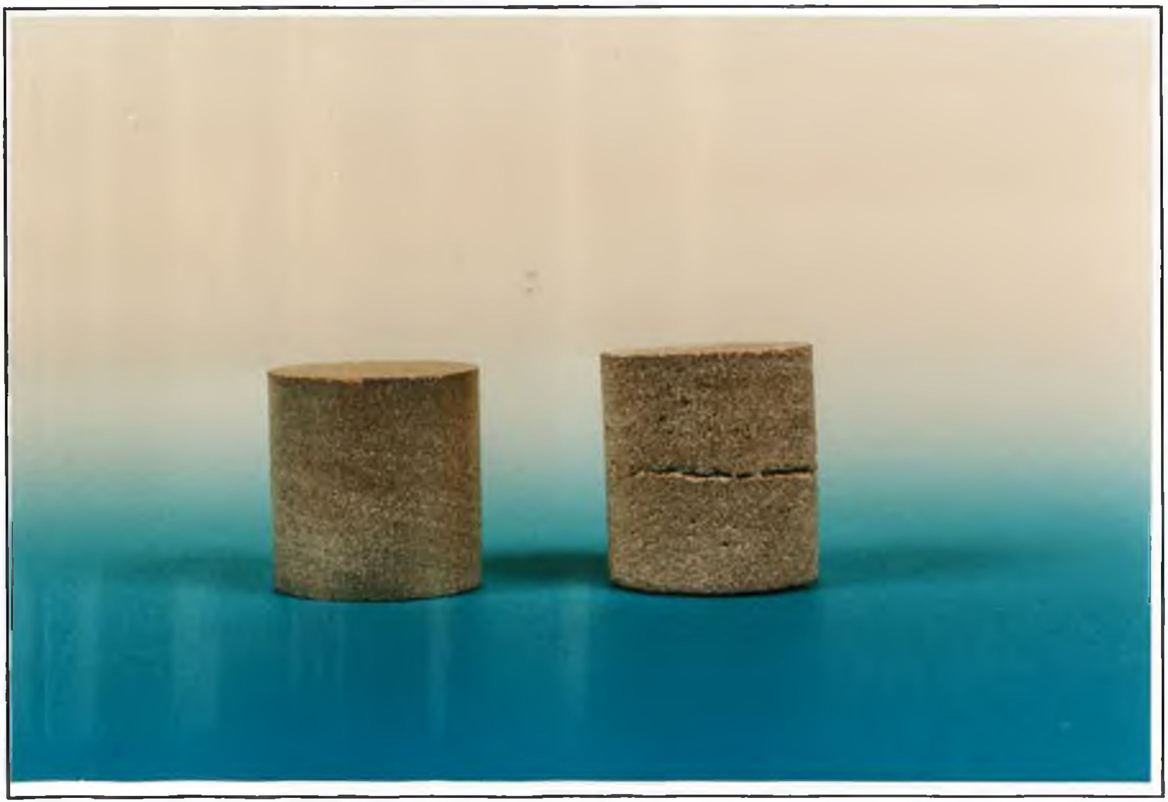
Plate 3.6 Defects of the sample, right one (left one is defect free) due to high heating rate.

Plate 3.7 Fracture of the samples in diametral compression test.

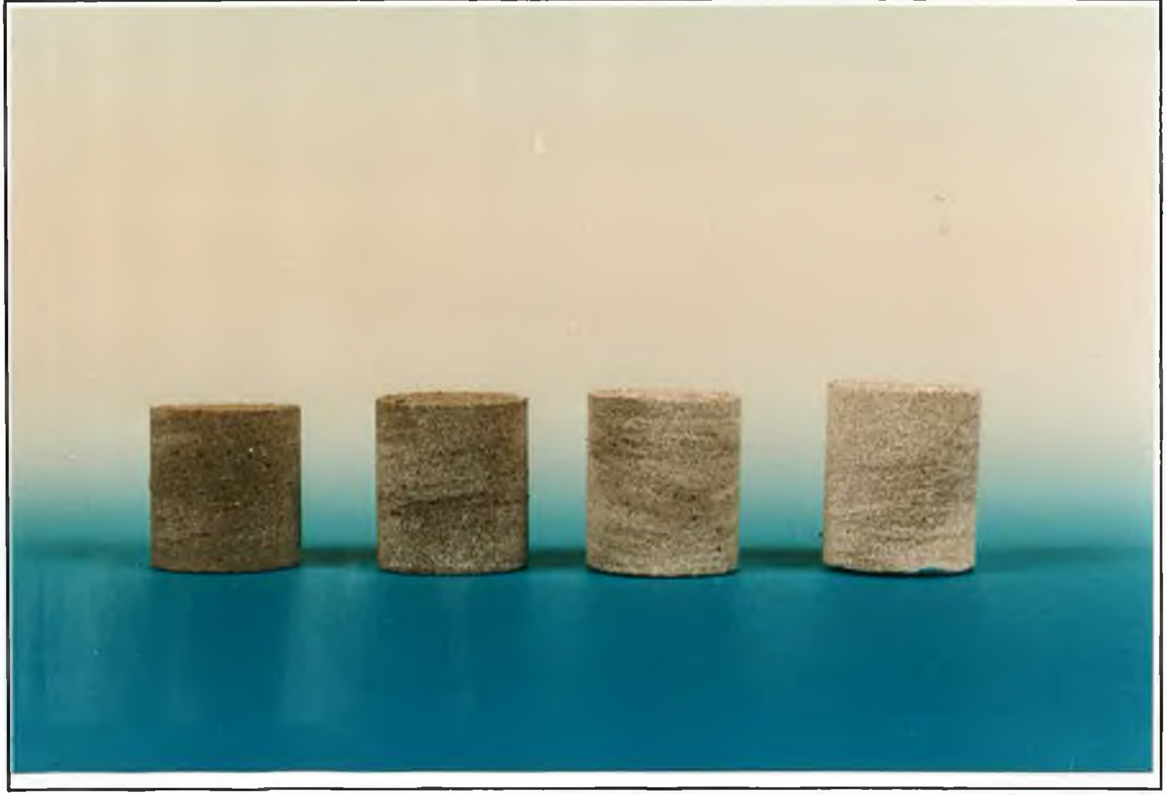

Plate 3.8 Defect free samples of the Al/Al_2O_3 composites.

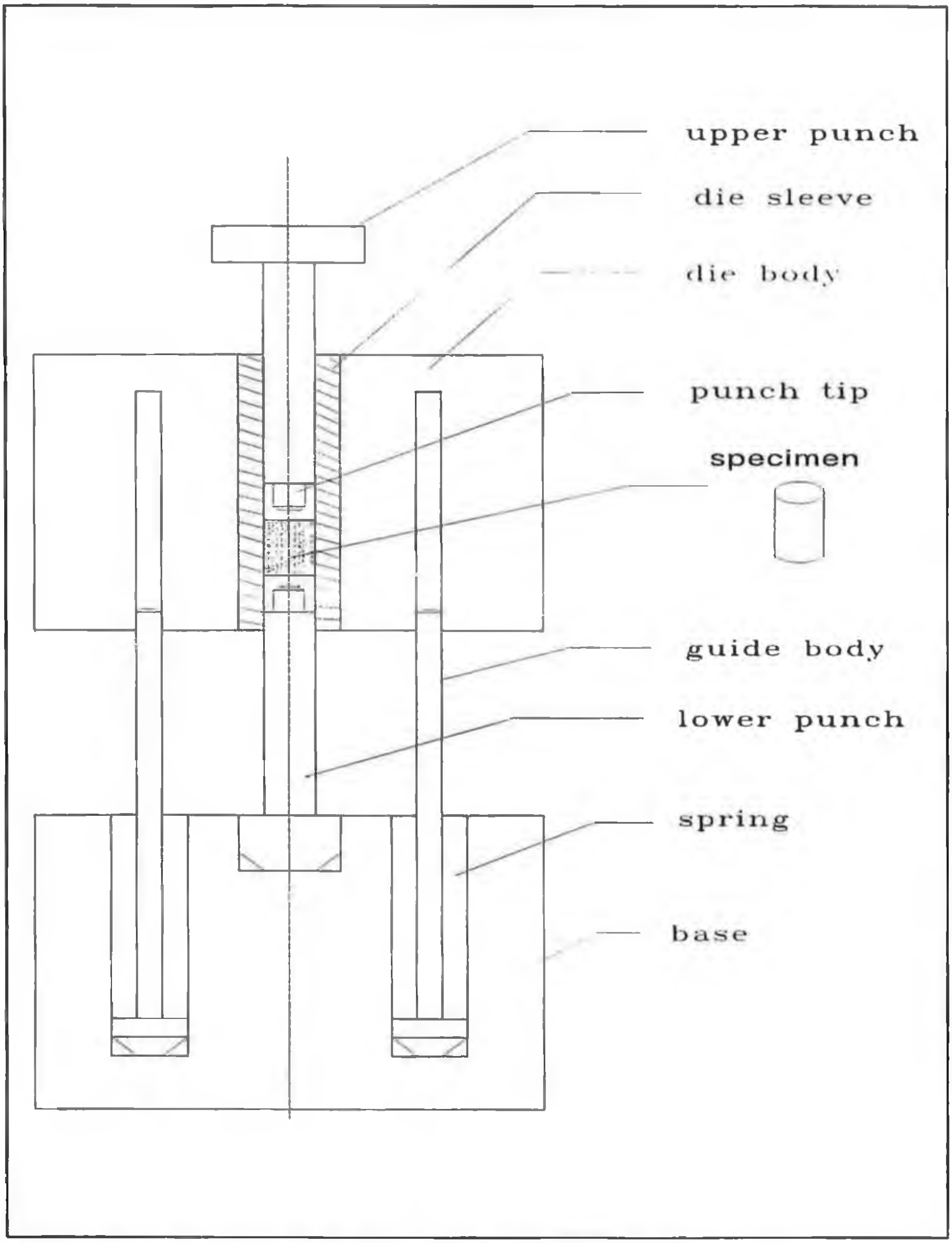

Figure 3.1 Assembly drawing of the die set

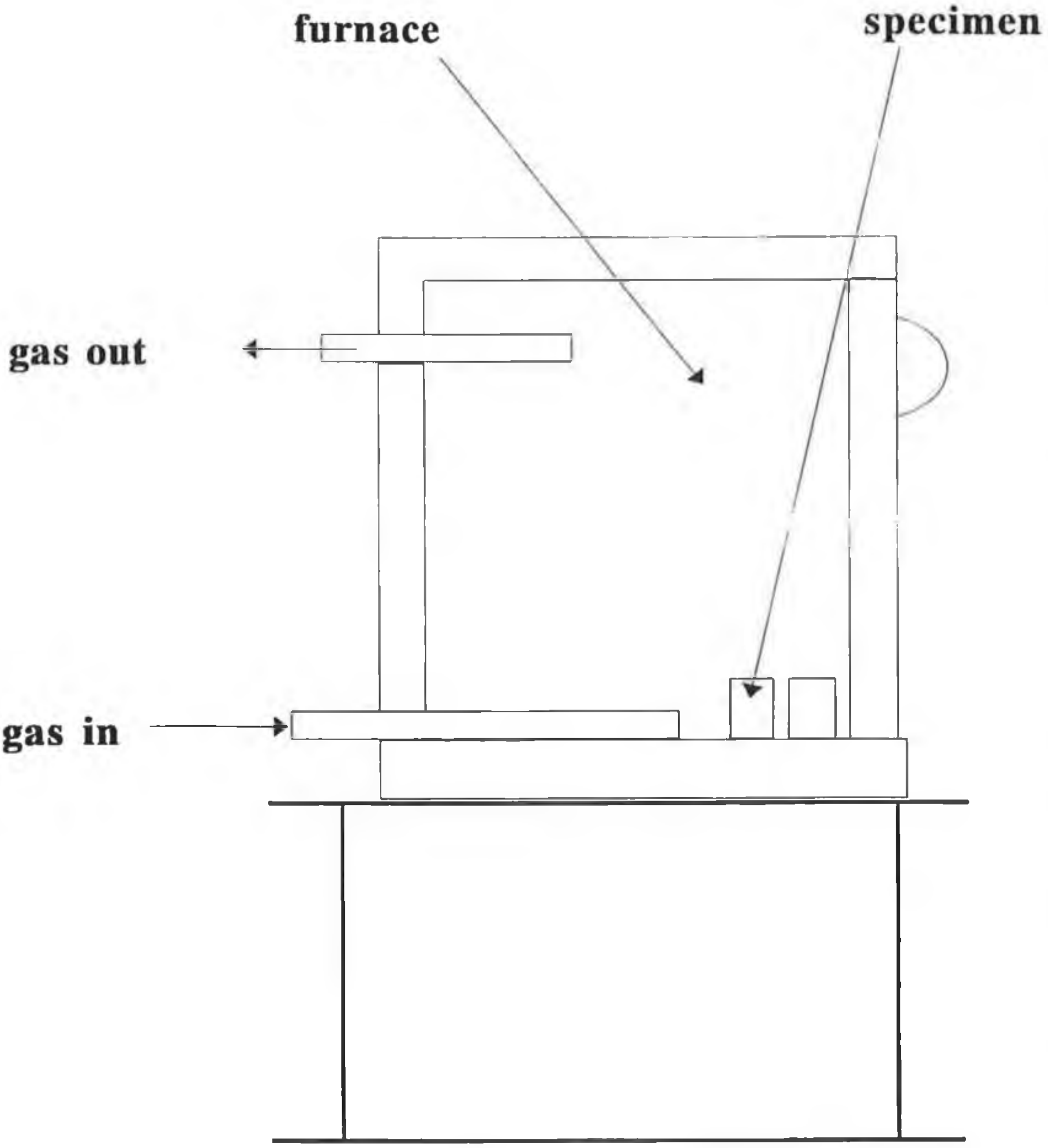

Figure 3.2 Assembly drawing of the sintering unit.

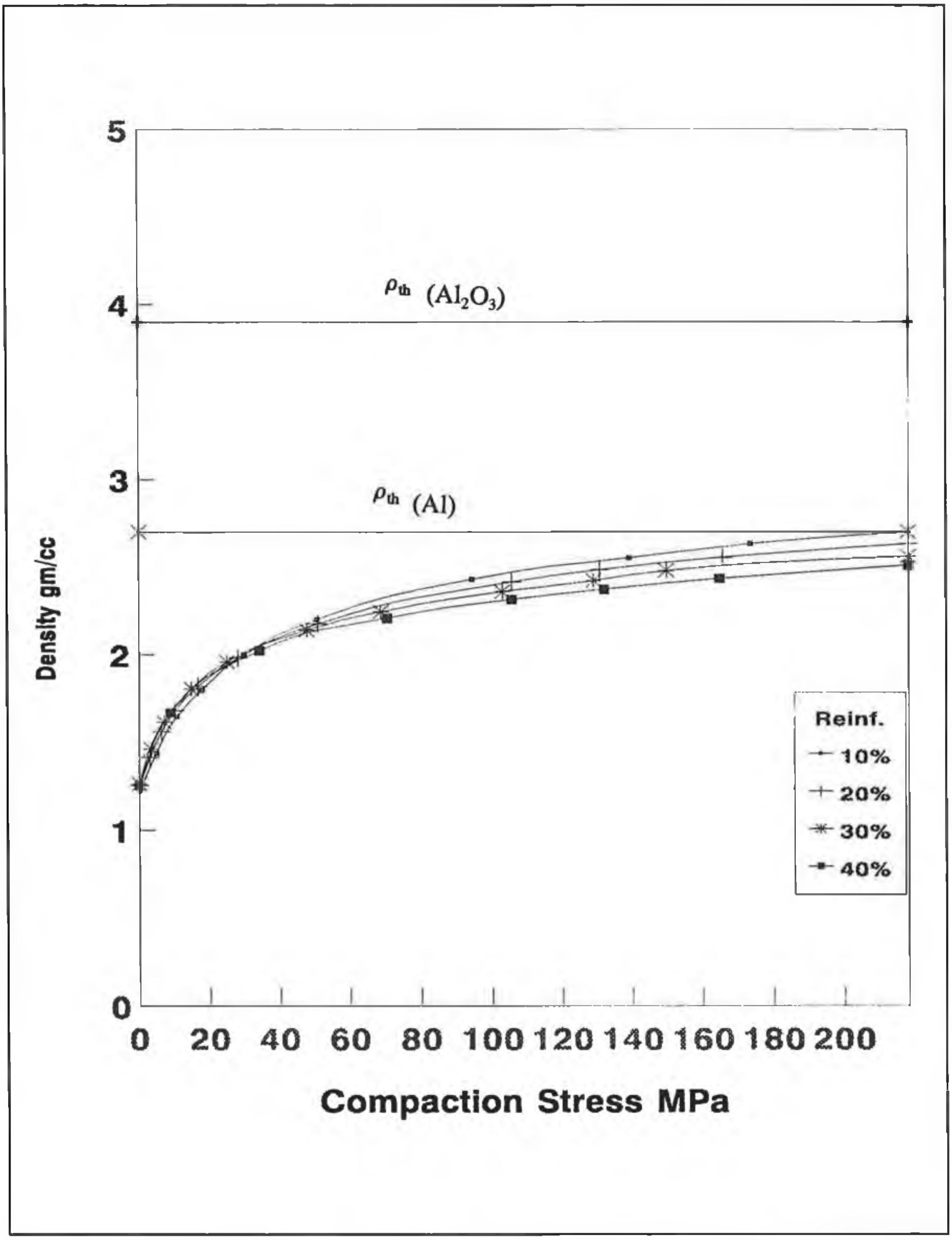

Figure 3.3 Compressibility curve for 10, 20, 30 and 40% volume fraction of reinforcement of Al/Al_2O_3 composites

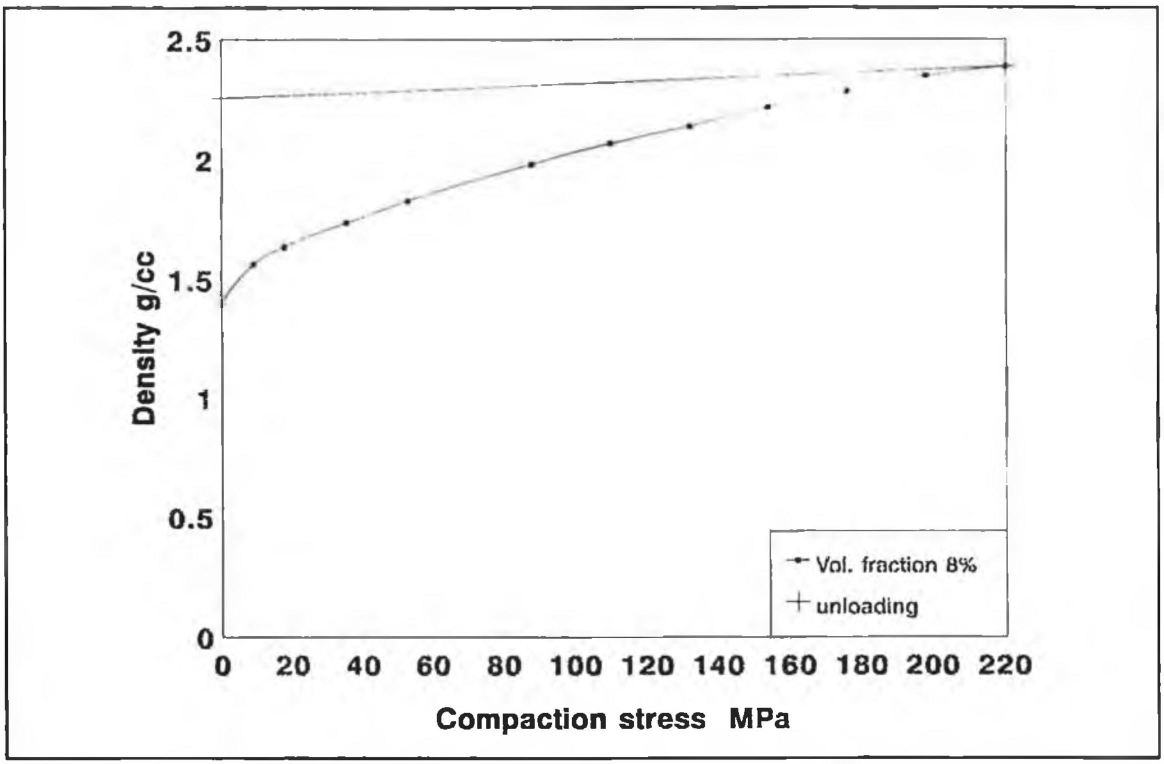

Figure 3.4 Compressibility curve for 8% volume fraction of reinforcement of Al-6061/SiC composite.

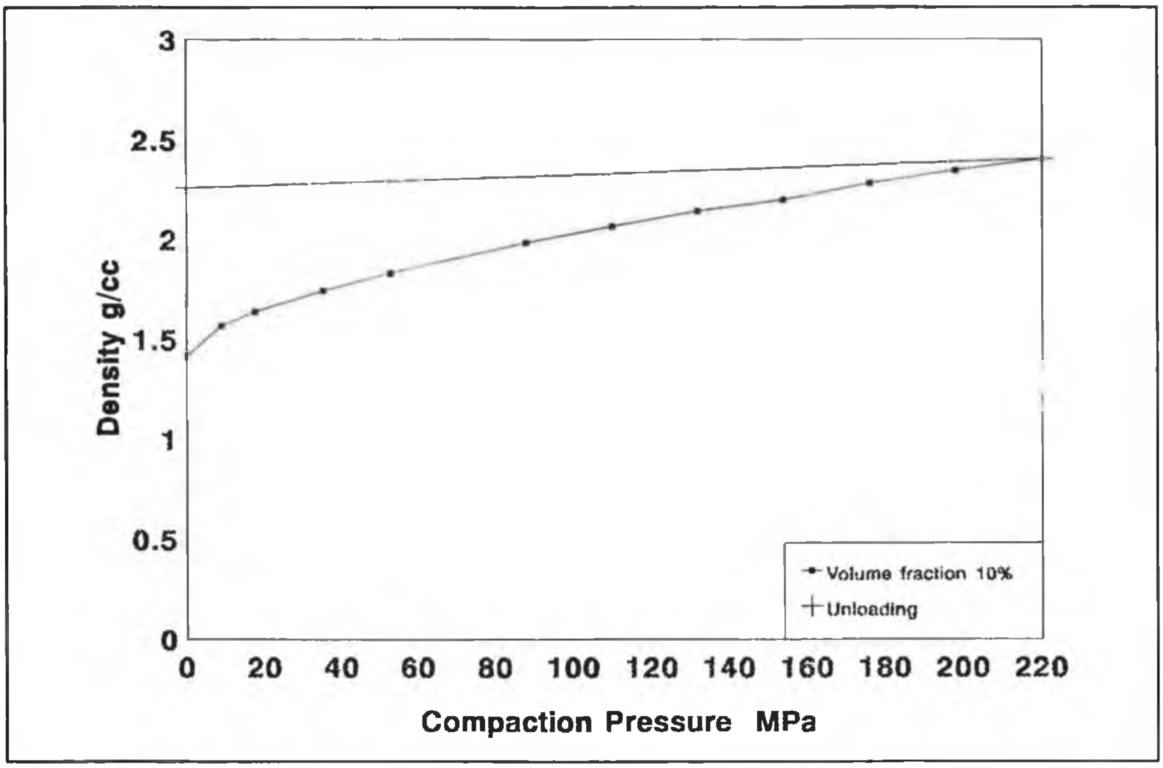

Figure 3.5 Compressibility curve for 10% volume fraction of reinforcement of Al-6061/SiC composite.

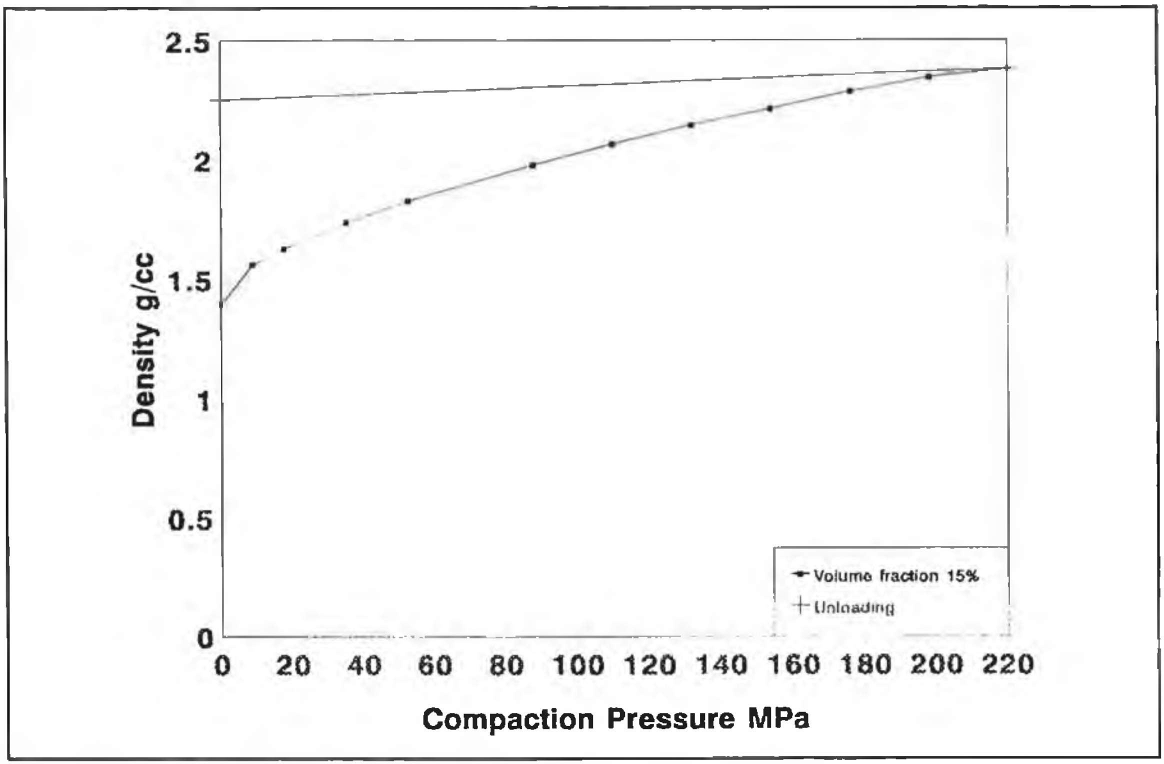

Figure 3.6 Compressibility curve for 15% volume fraction of reinforcement of Al-6061/SiC composite.

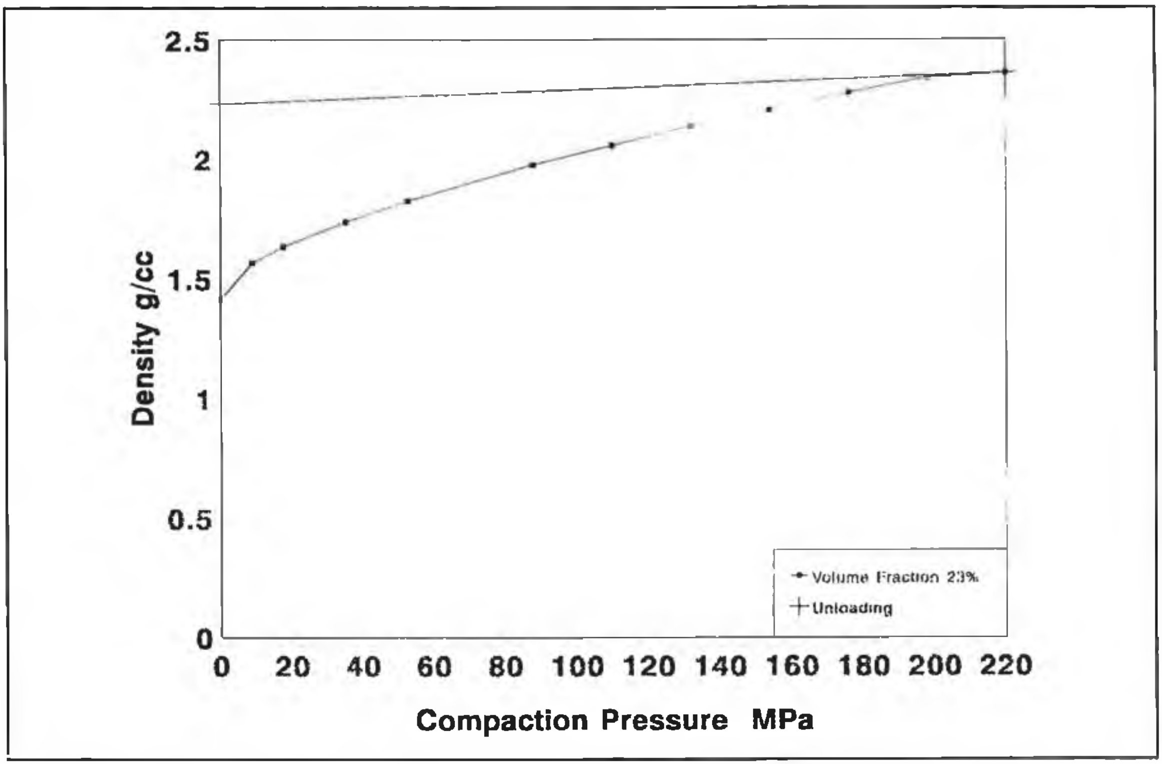

Figure 3.7 Compressibility curve for 23% volume fraction of reinforcement of Al-6061/SiC composite.

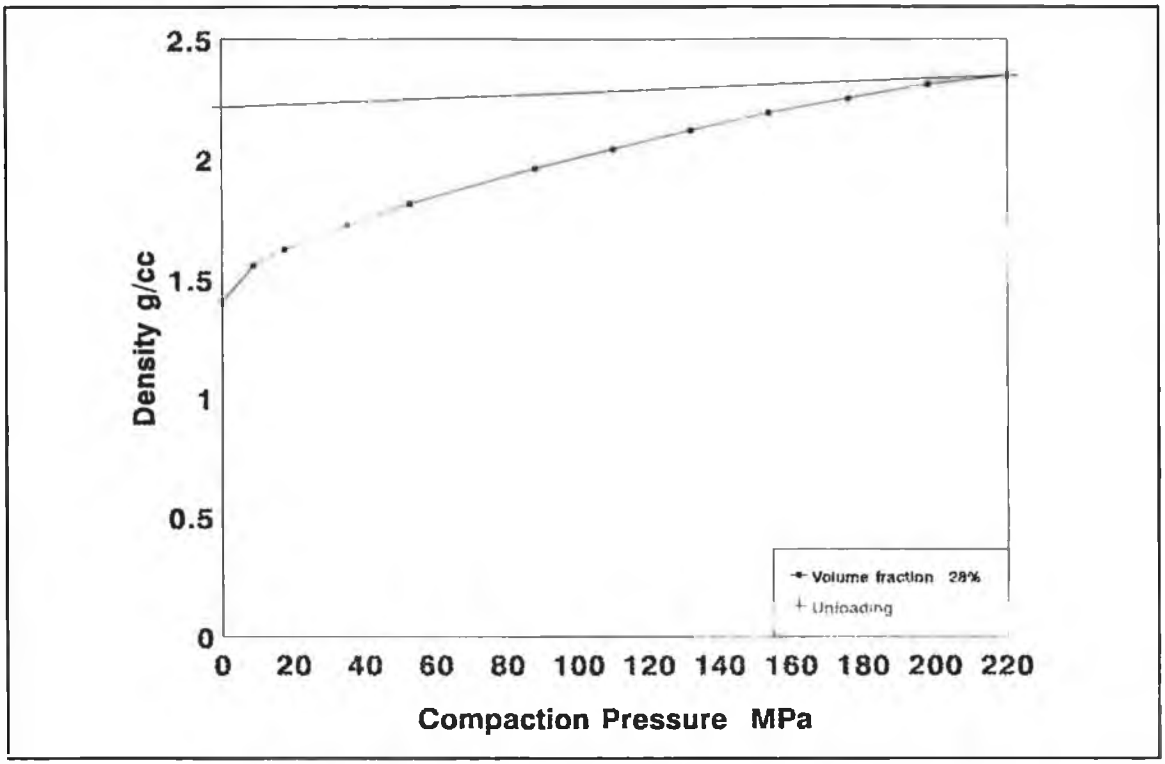

Figure 3.8 Compressibility curve for 28% volume fraction of reinforcement of Al-6061/SiC composite.

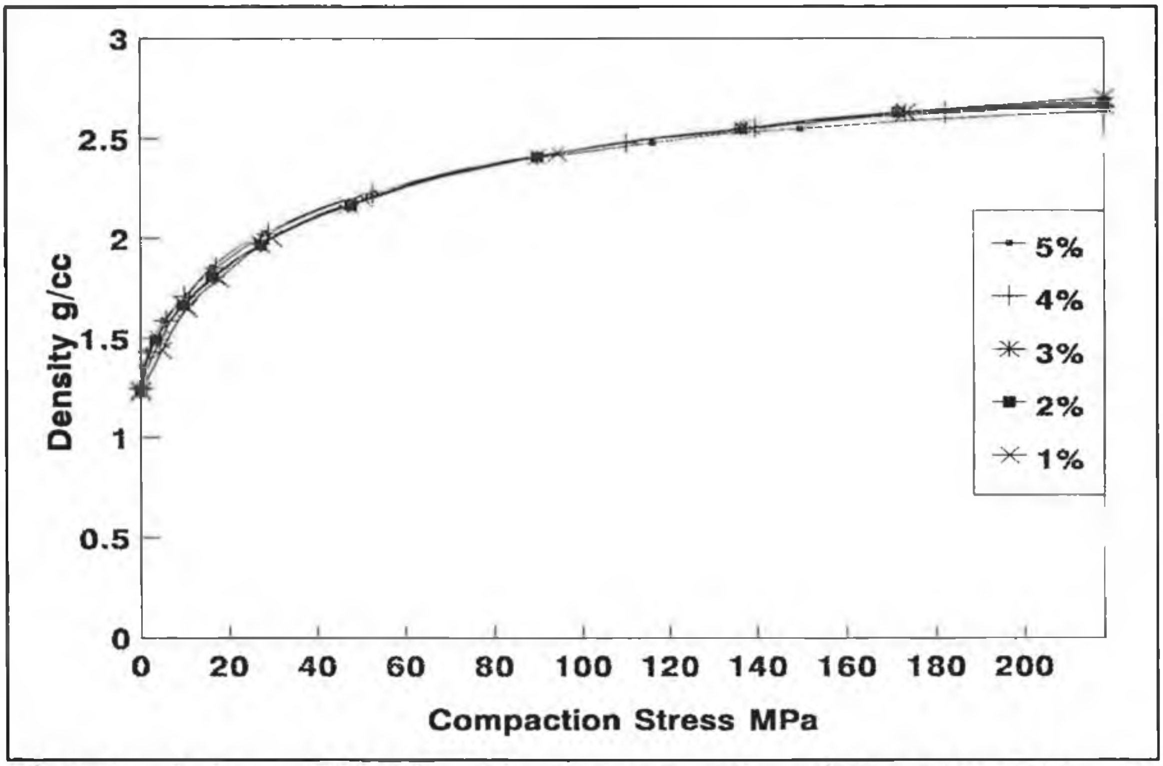

Figure 3.9 Effect of amount of zinc stearate on compressibility of Al/Al_2O_3 composites for 10% volume fraction of reinforcement.

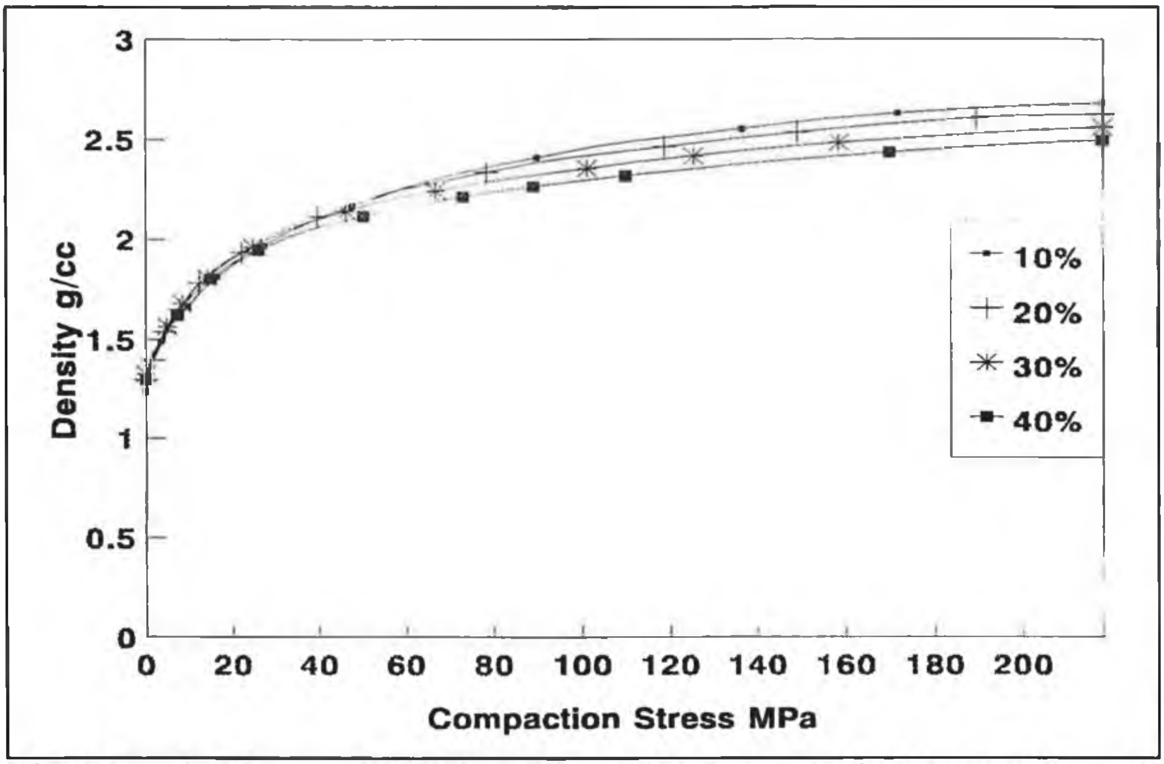

Figure 3.10 Effect of alumina reinforcement on compressibility of Al/Al_2O_3 composite for 2% zinc stearate.

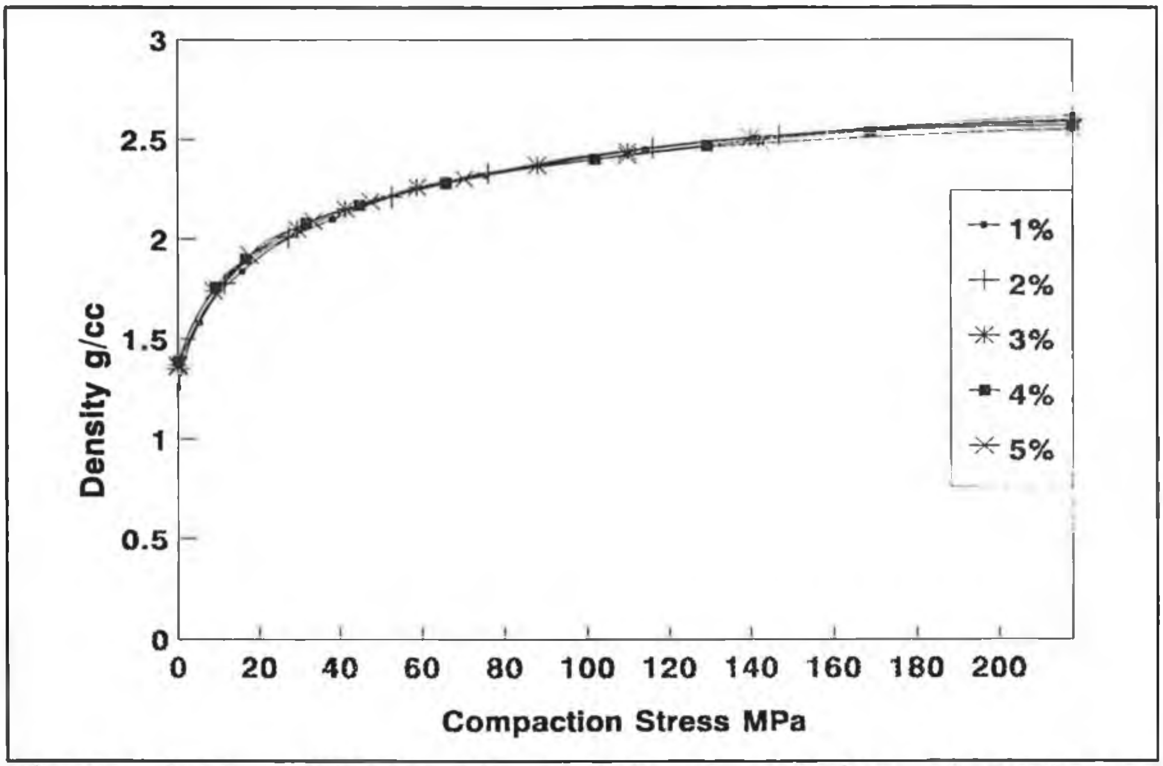

Figure 3.11 Effect of amount of calcium stearate on compressibility of Al/Al_2O_3 composite for 20% alumina.

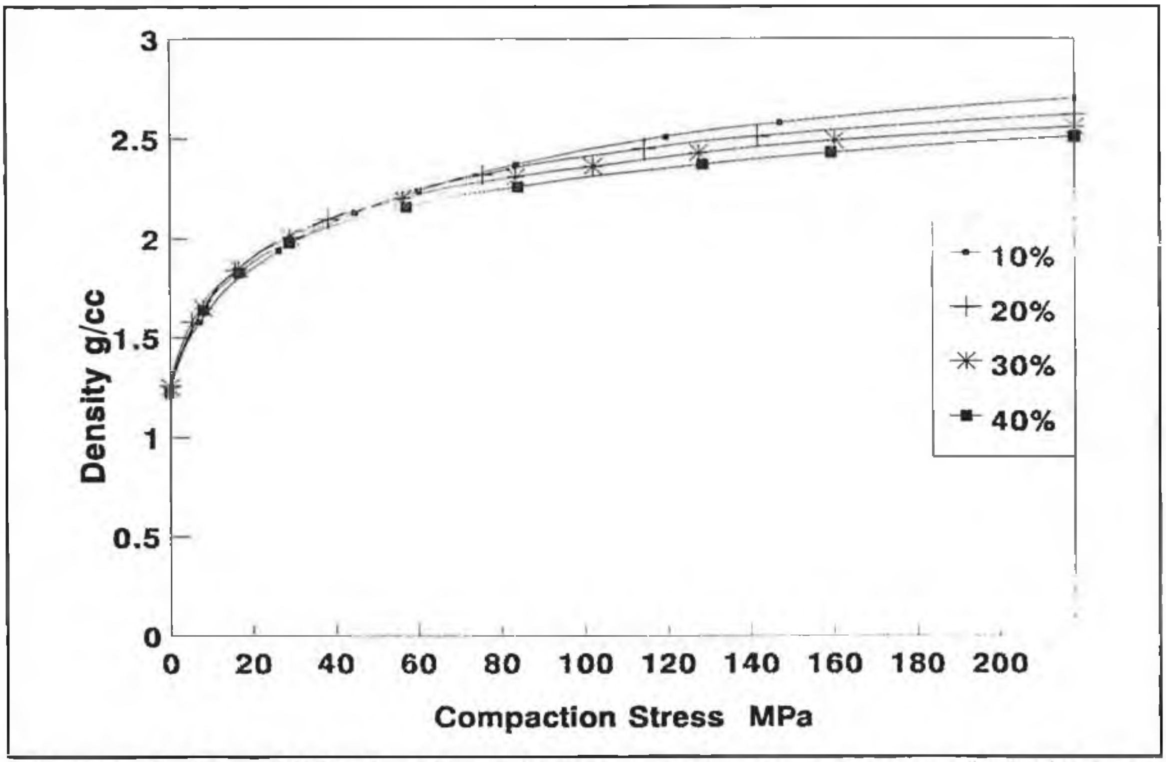

Figure 3.12 Effect of reinforcement on compressibility of Al/Al_2O_3 composite for 1% calcium stearate.

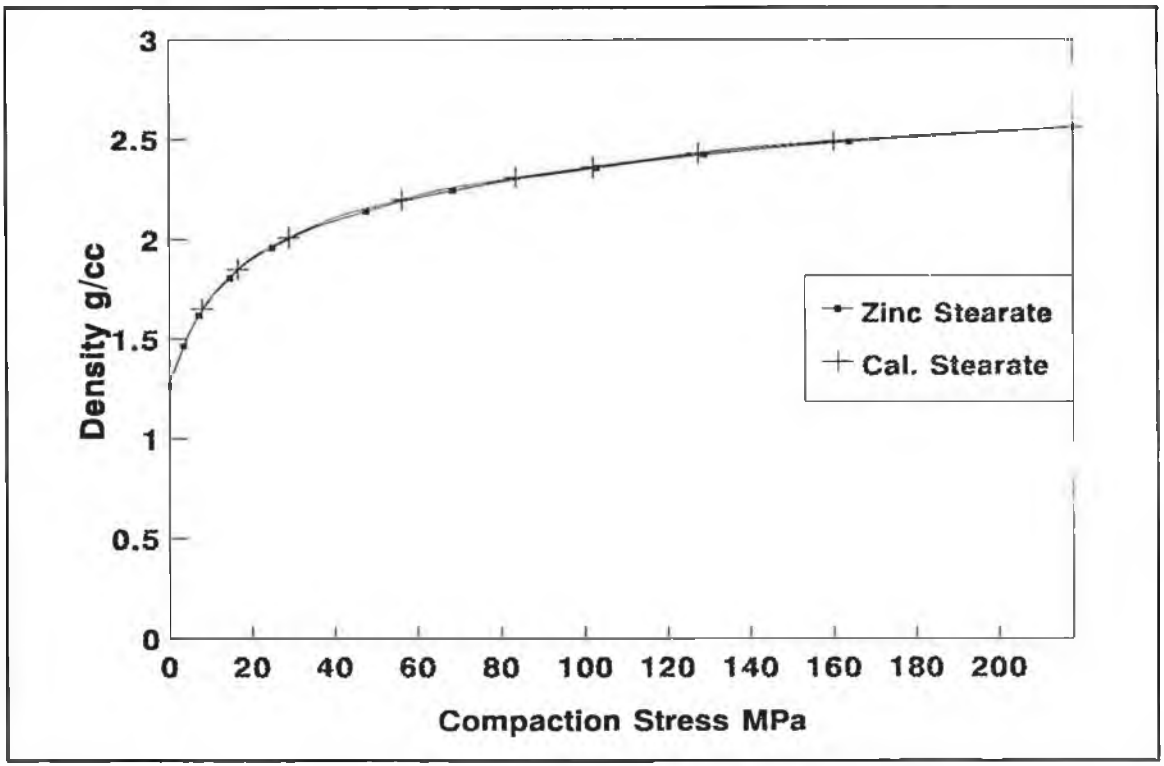

Figure 3.13 Effect of lubrication type on compressibility of Al/Al_2O_3 composite for 30% alumina.

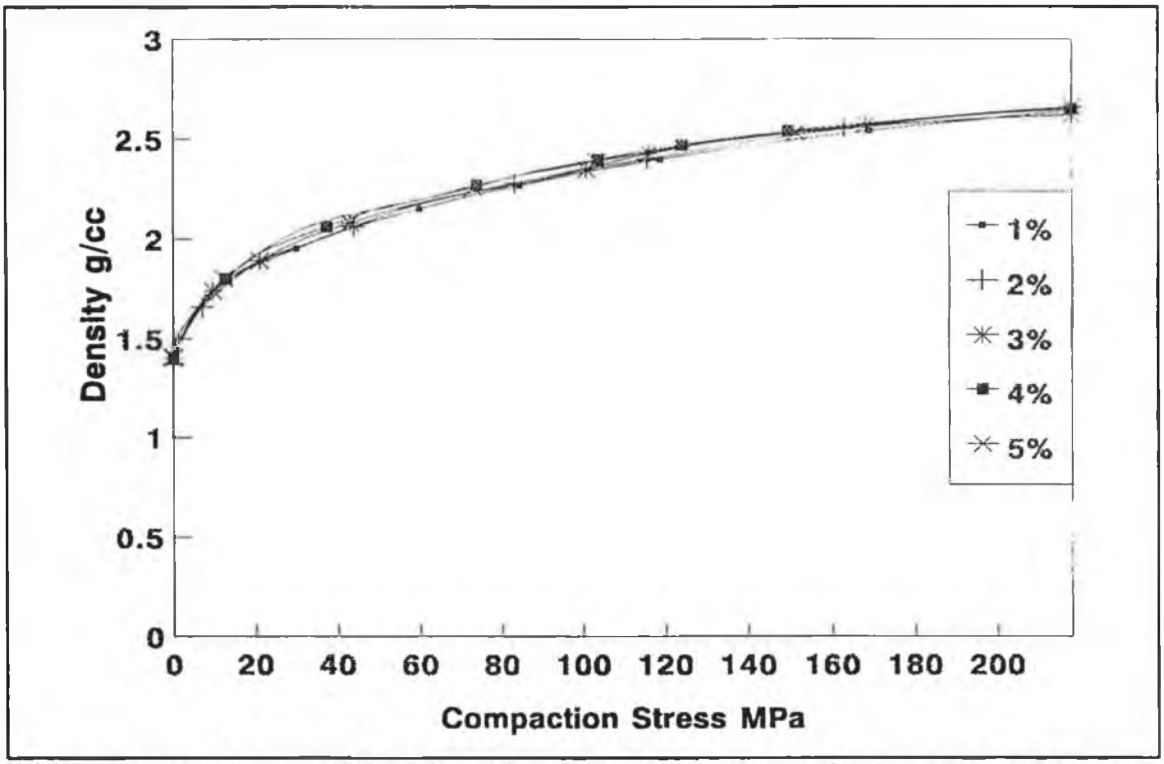

Figure 3.14 Effect of amount of zinc stearate on compressibility of Al/SiC composite for 20% SiC.

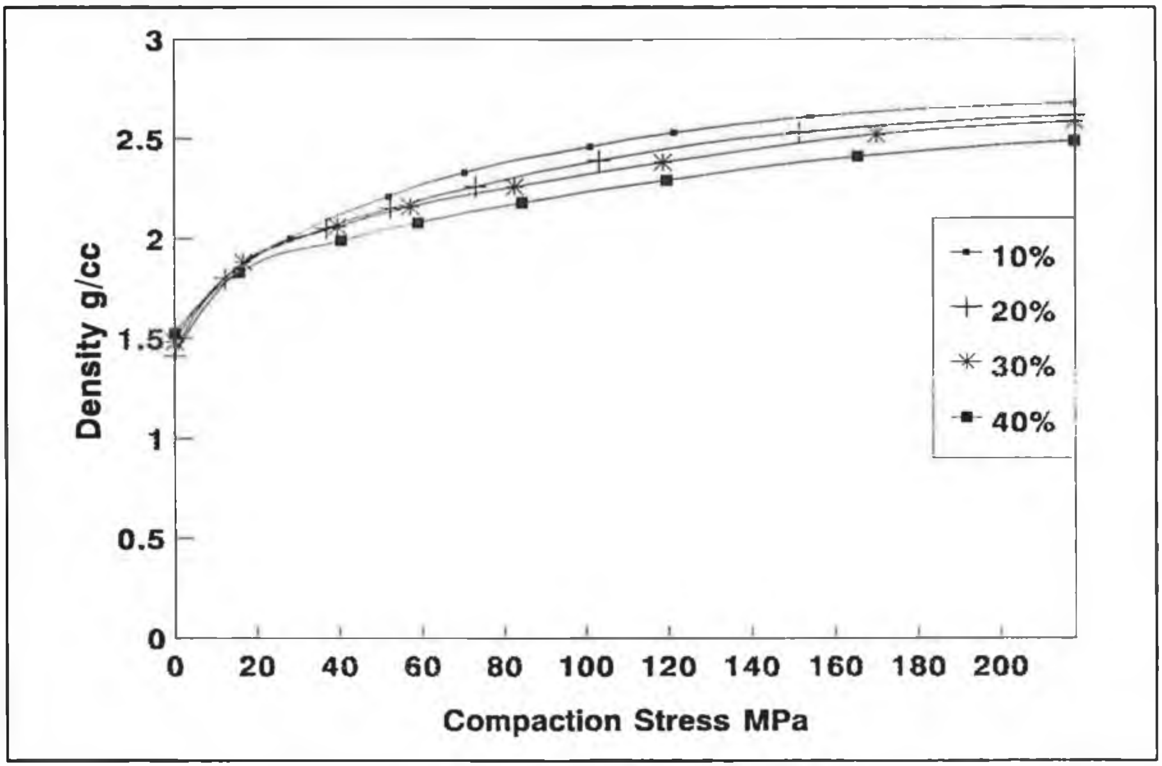

Figure 3.15 Effect of SiC reinforcement on compressibility of Al/SiC composite for 5% zinc stearate.

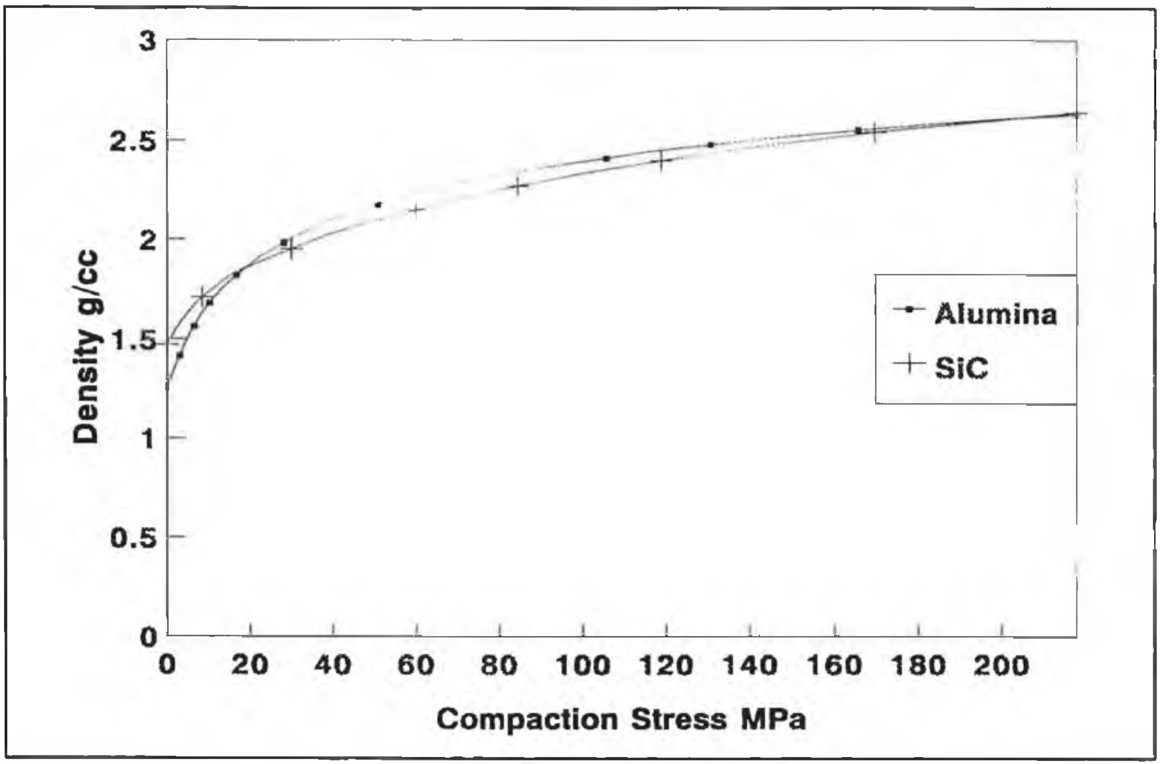

Figure 3.16 Effect of type of reinforcement on compressibility of MMCs for 1% zinc stearate.

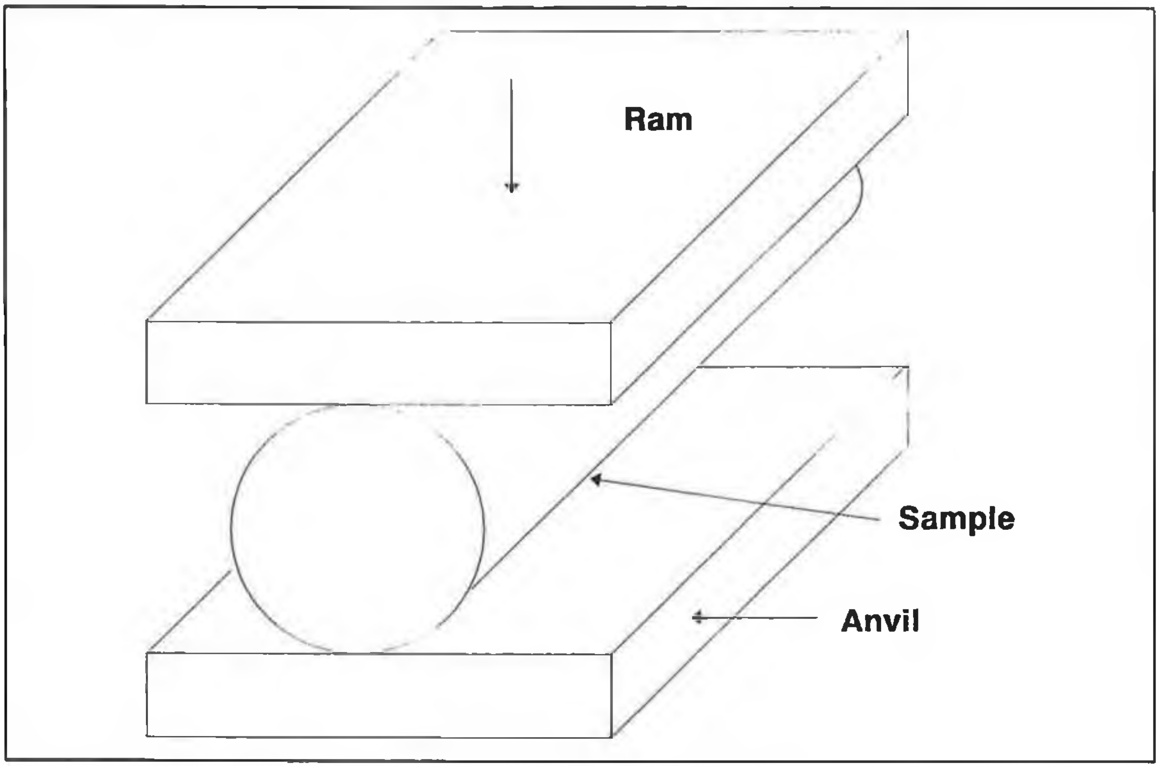

Figure 3.17 Set up for diametral compression test.

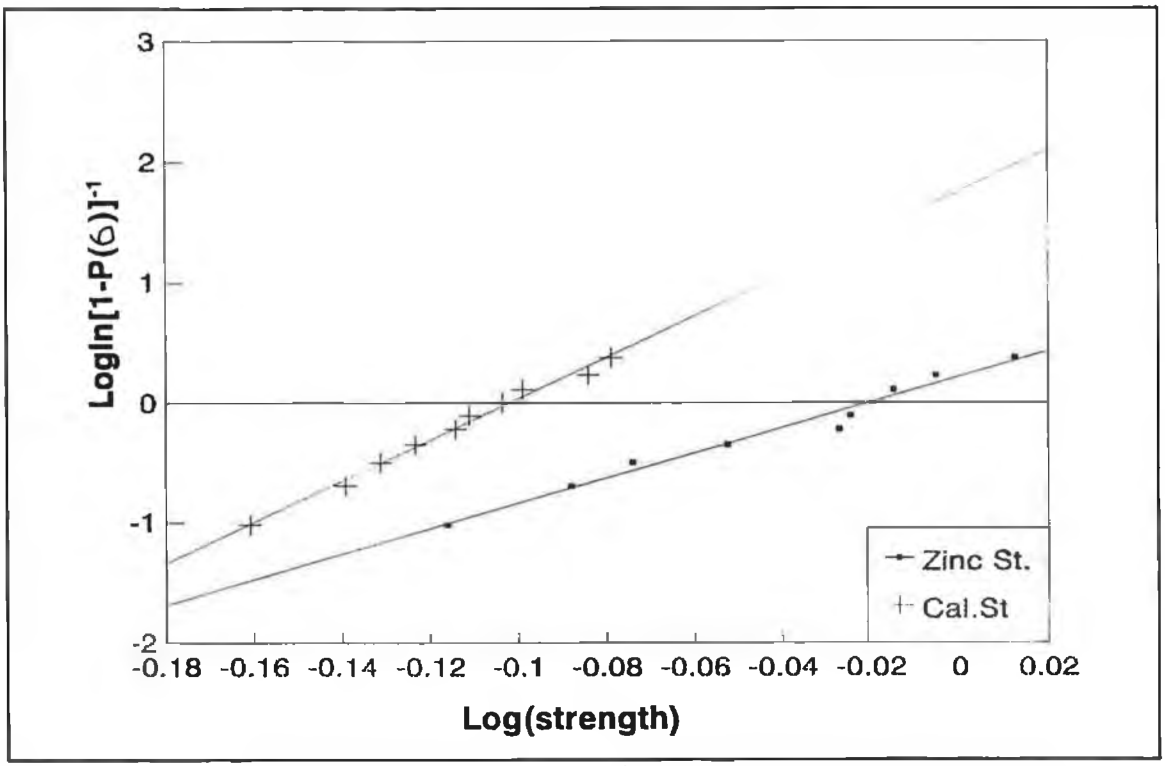

Figure 3.18 Probability of failure for green compacts of Al/Al_2O_3 composite of 10% alumina for 1% zinc and calcium stearate.

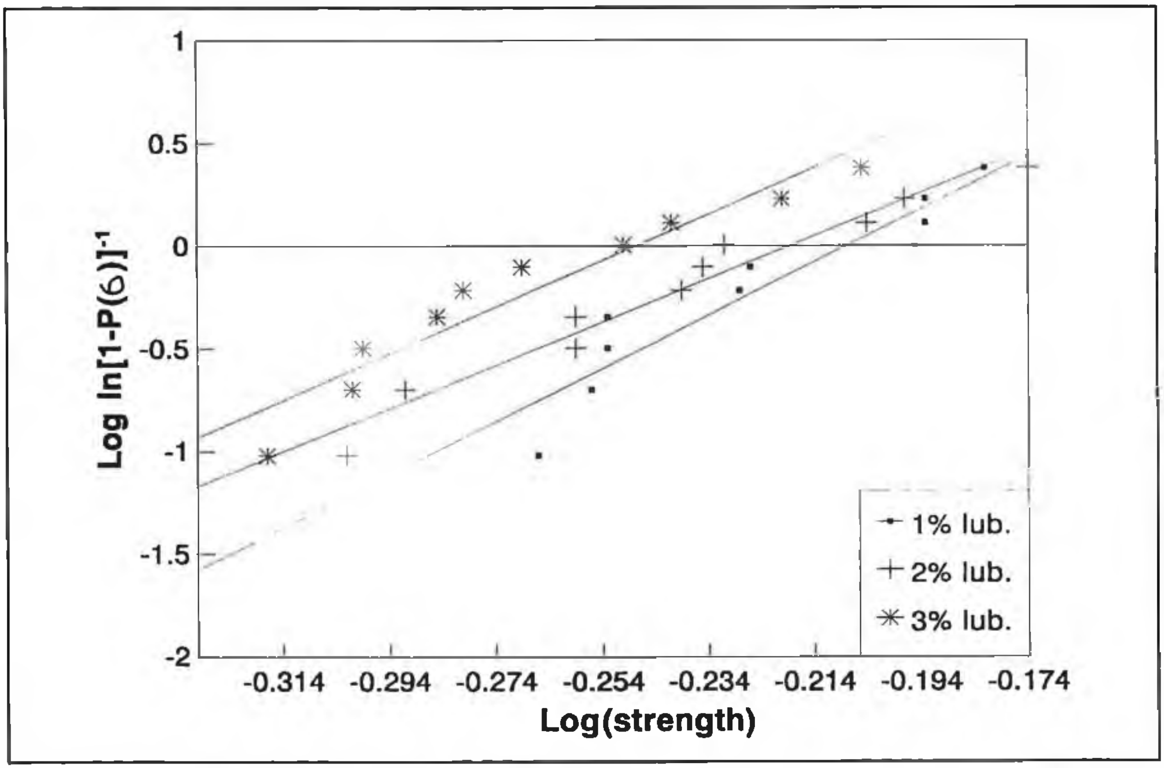

Figure 3.19 Probability of failure for green compacts of Al/Al_2O_3 composite with varying lubricant for 20% alumina.

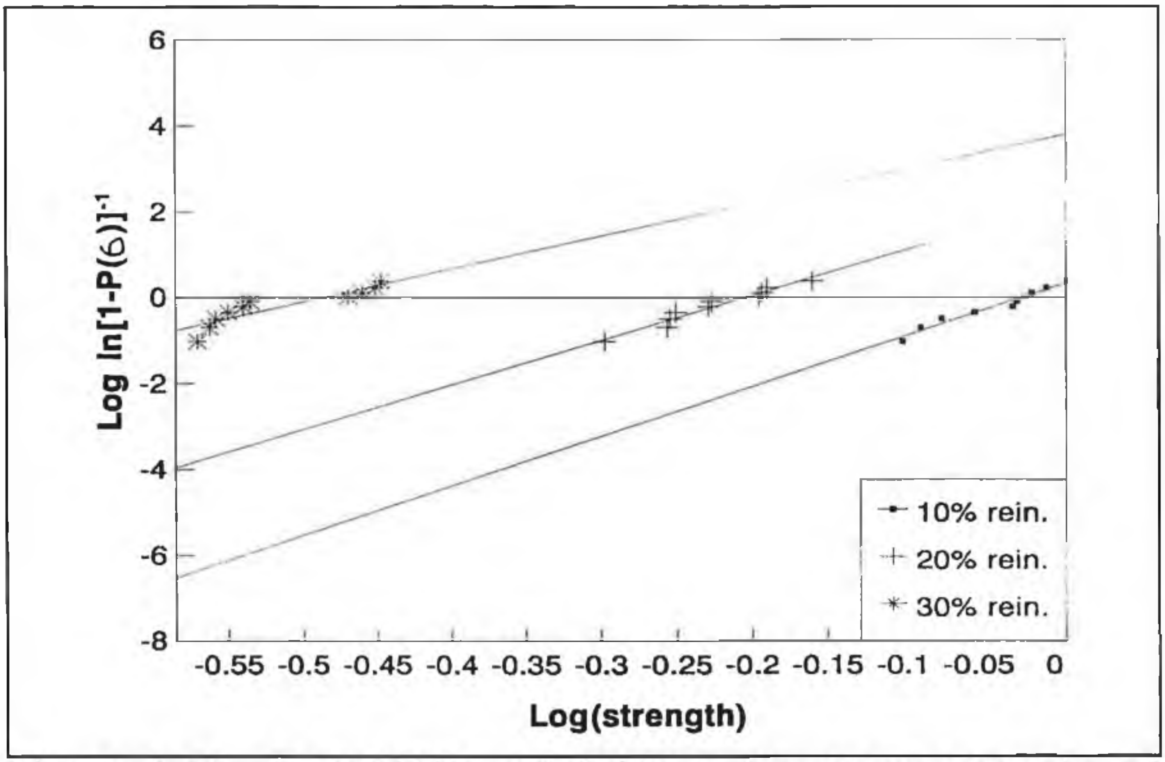

Figure 3.20 Probability of failure for green compacts of Al/Al_2O_3 composite with varying reinf. for 1% zinc stearte.

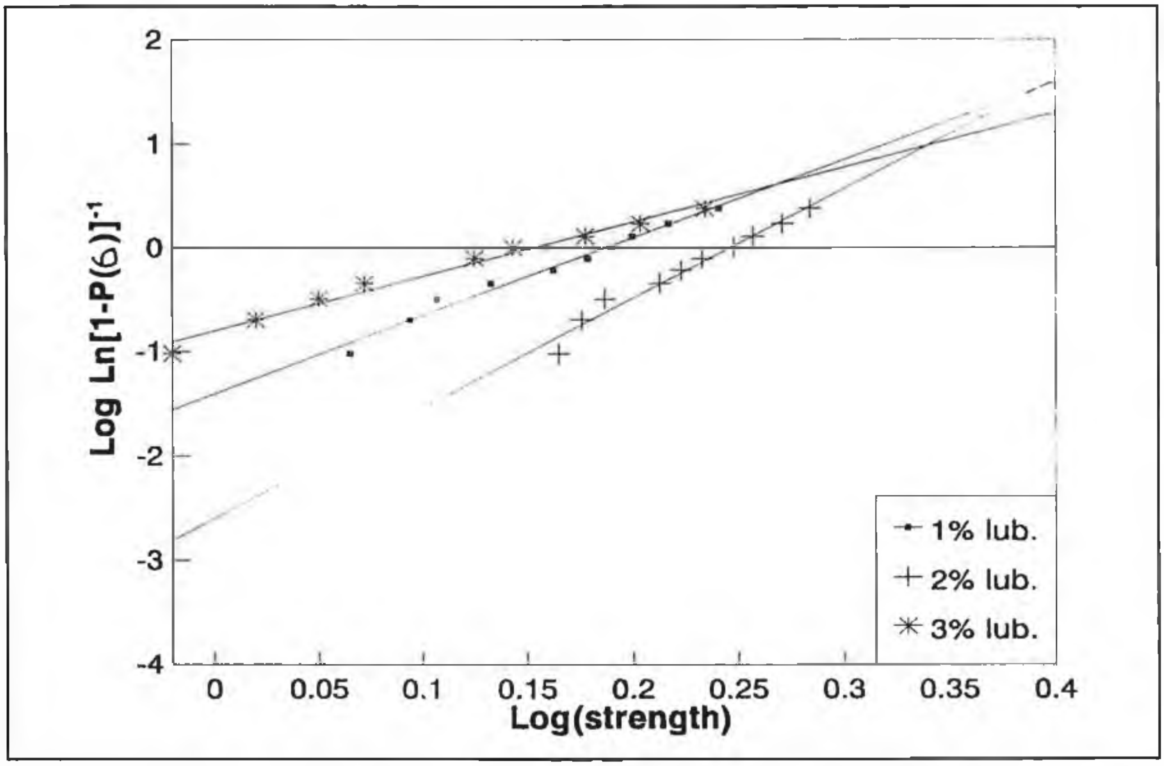

Figure 3.21 Probability of failure for fired compacts of Al_2O_3 composite with varying zinc ste. lub. for 20% alumina.

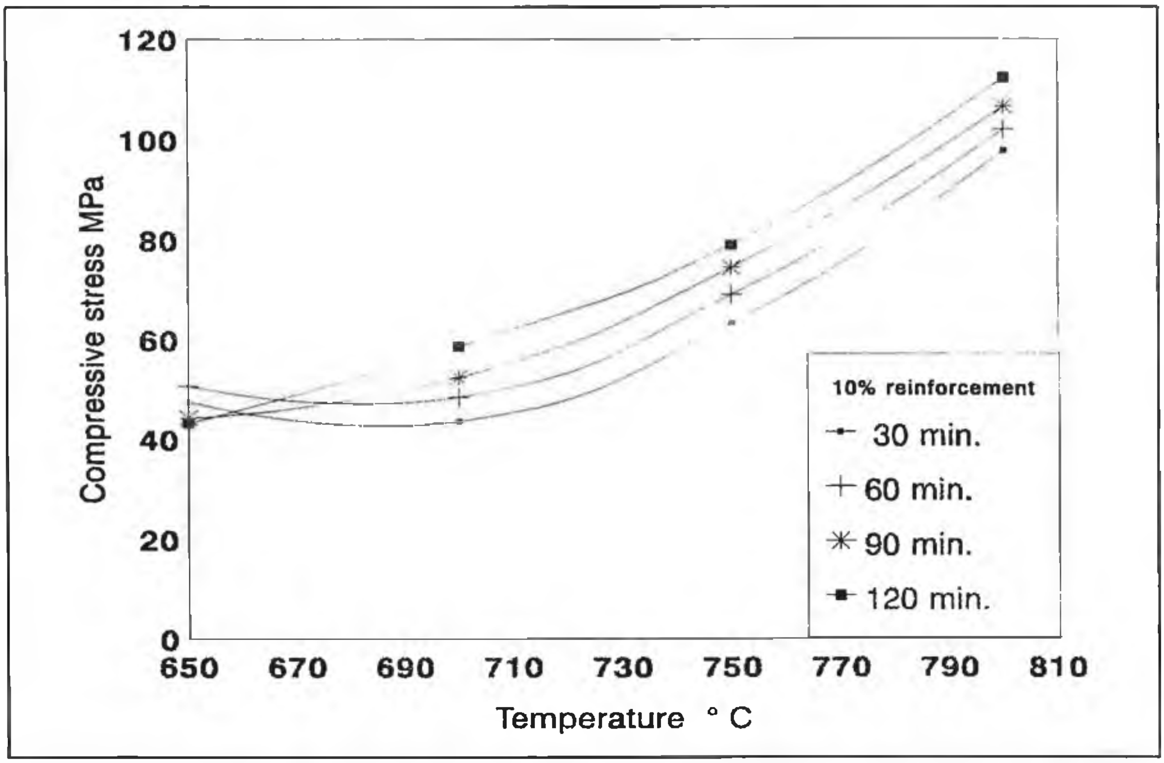

Figure 3.22 Effect of time on compressive stress of Al/Al_2O_3 composite for 10% reinforcement.

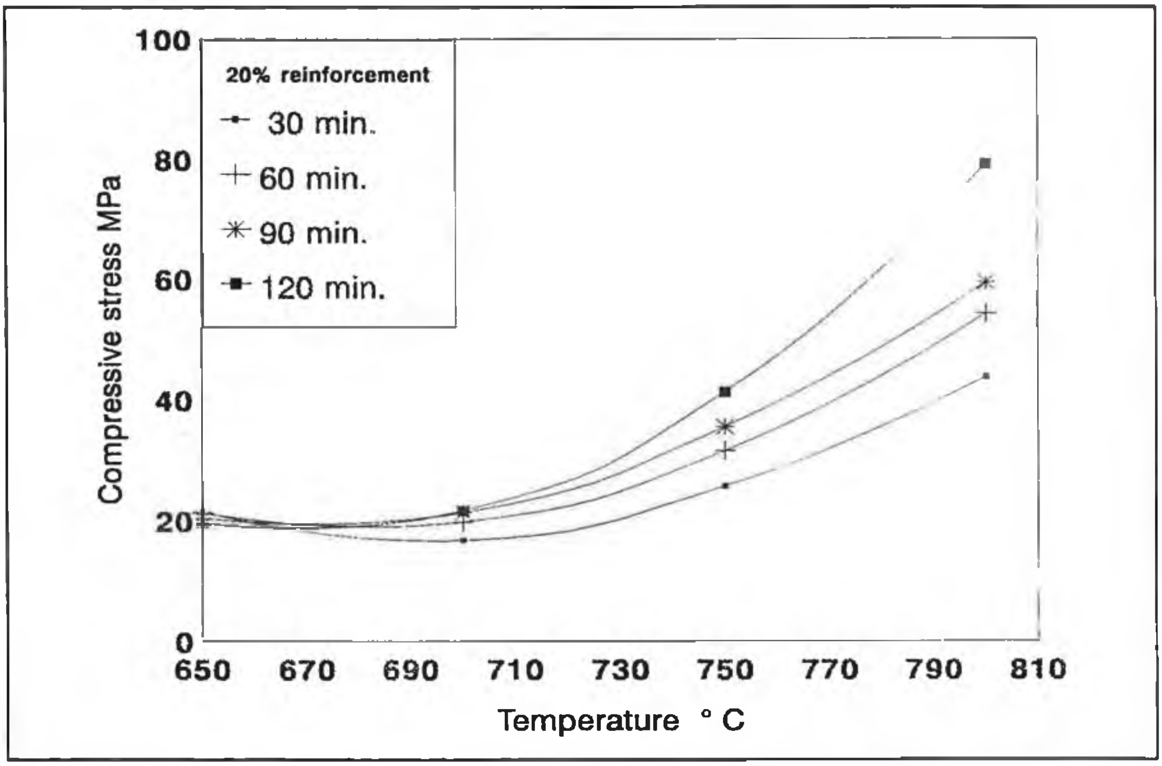

Figure 3.23 Effect of time on compressive stress of Al/Al_2O_3 composite for 20% reinforcement.

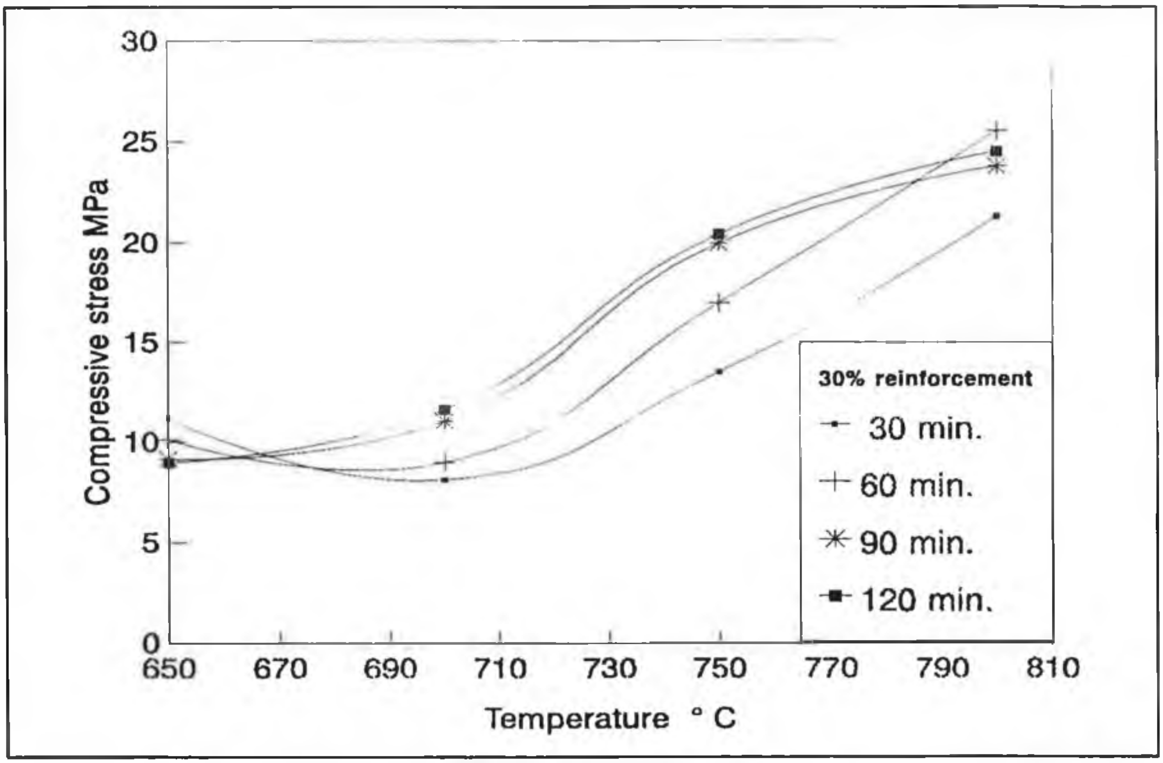

Figure 3.24 Effect of time on compressive stress of Al/Al_2O_3 composite for 30% reinforcement.

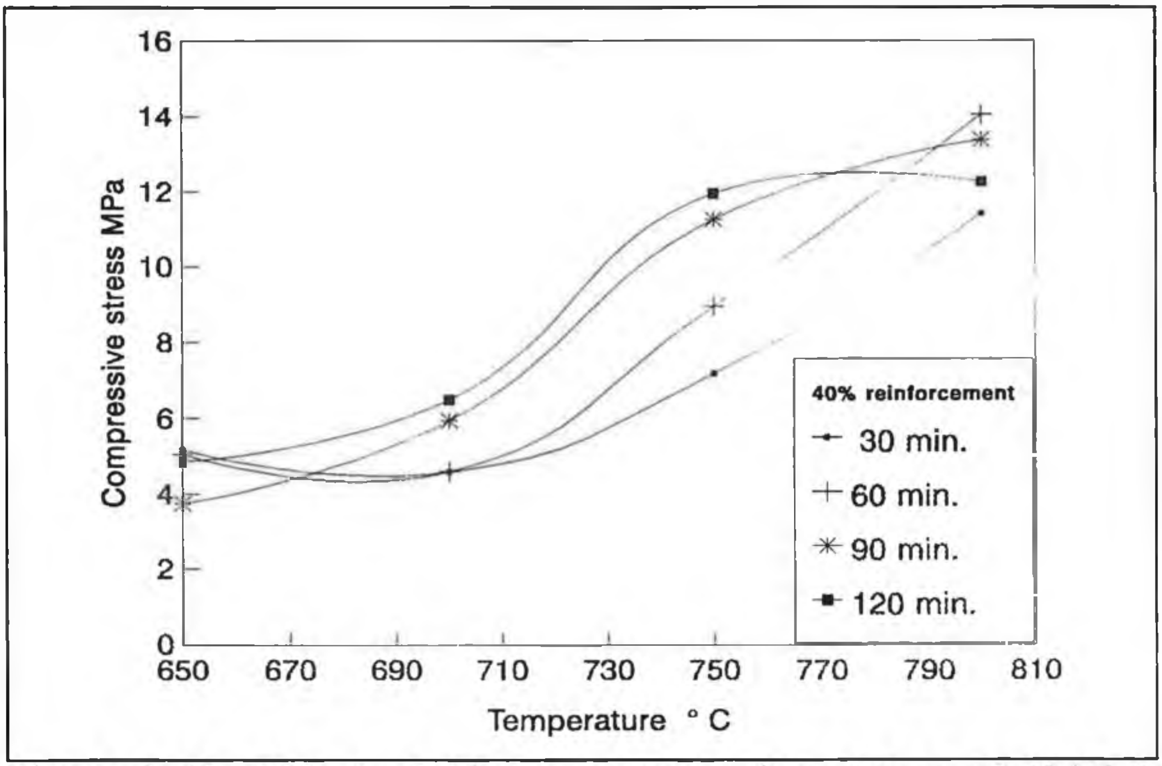

Figure 3.25 Effect of time on compressive stress of Al/Al_2O_3 composite for 40% reinforcement.

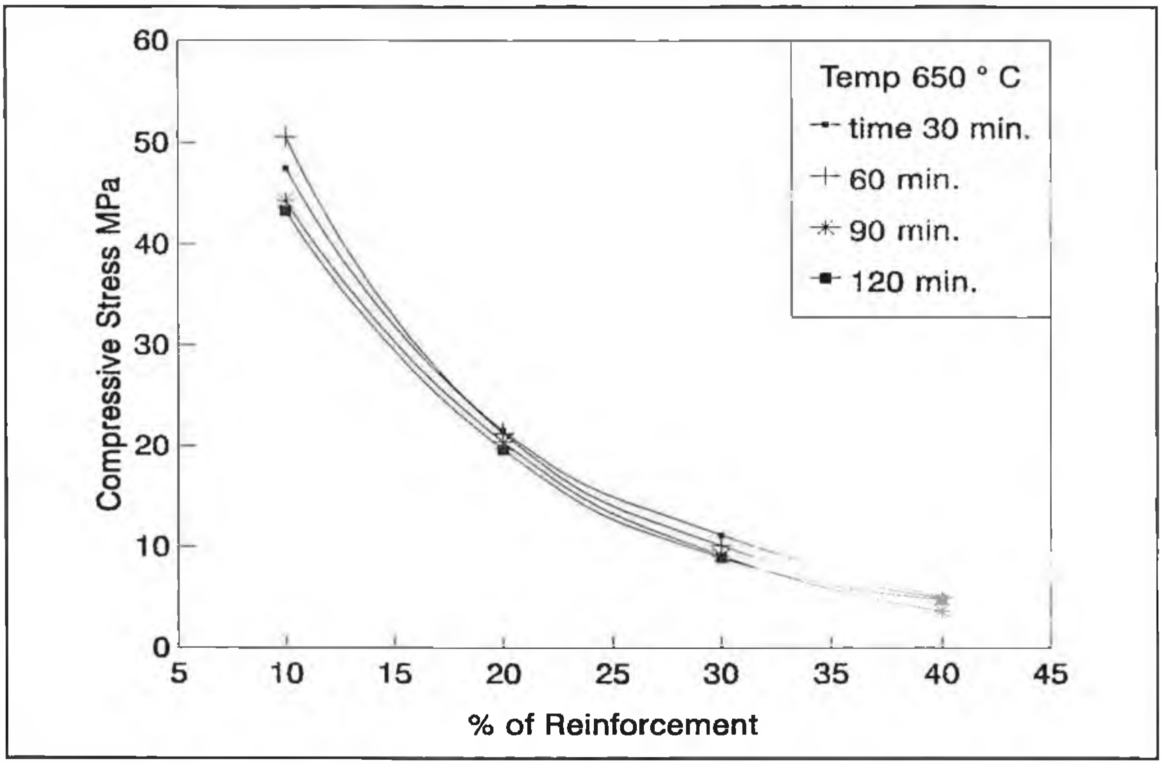

Figure 3.26 Effect of time on compressive stress of Al/Al_2O_3 composite for temperature 650 °C.

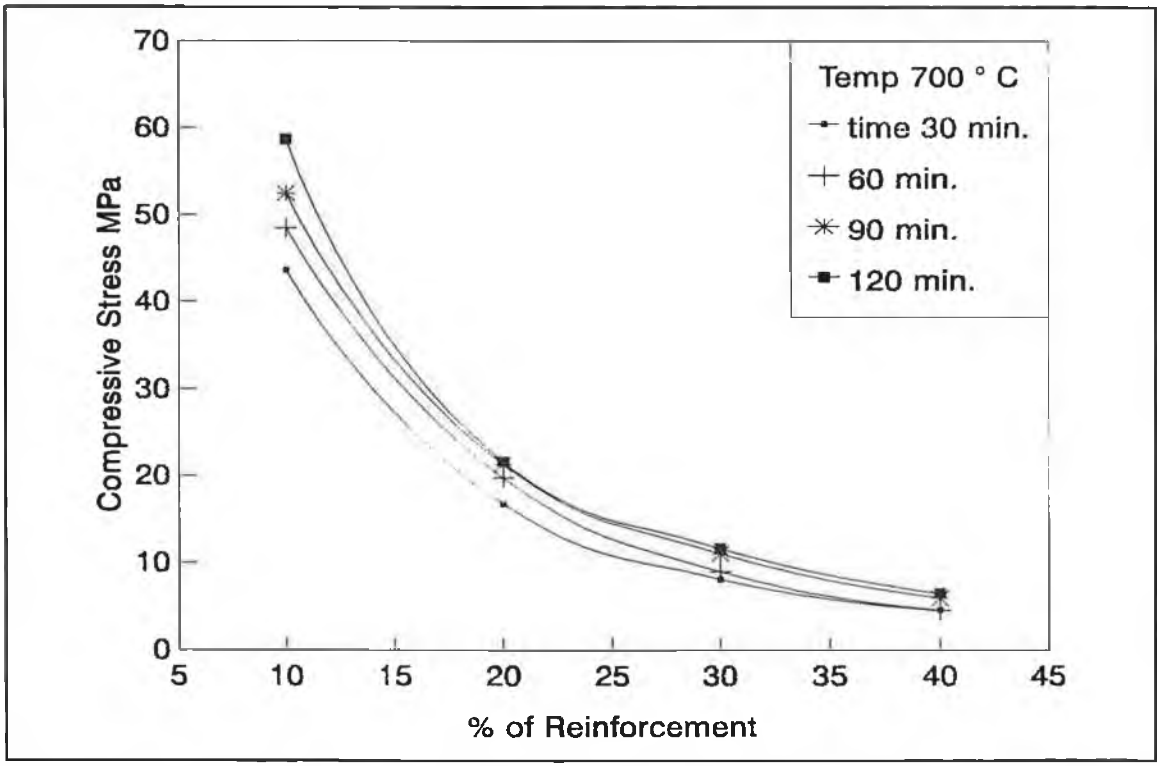

Figure 3.27 Effect of time on compressive stress of Al/Al_2O_3 composite for temperature 700 °C.

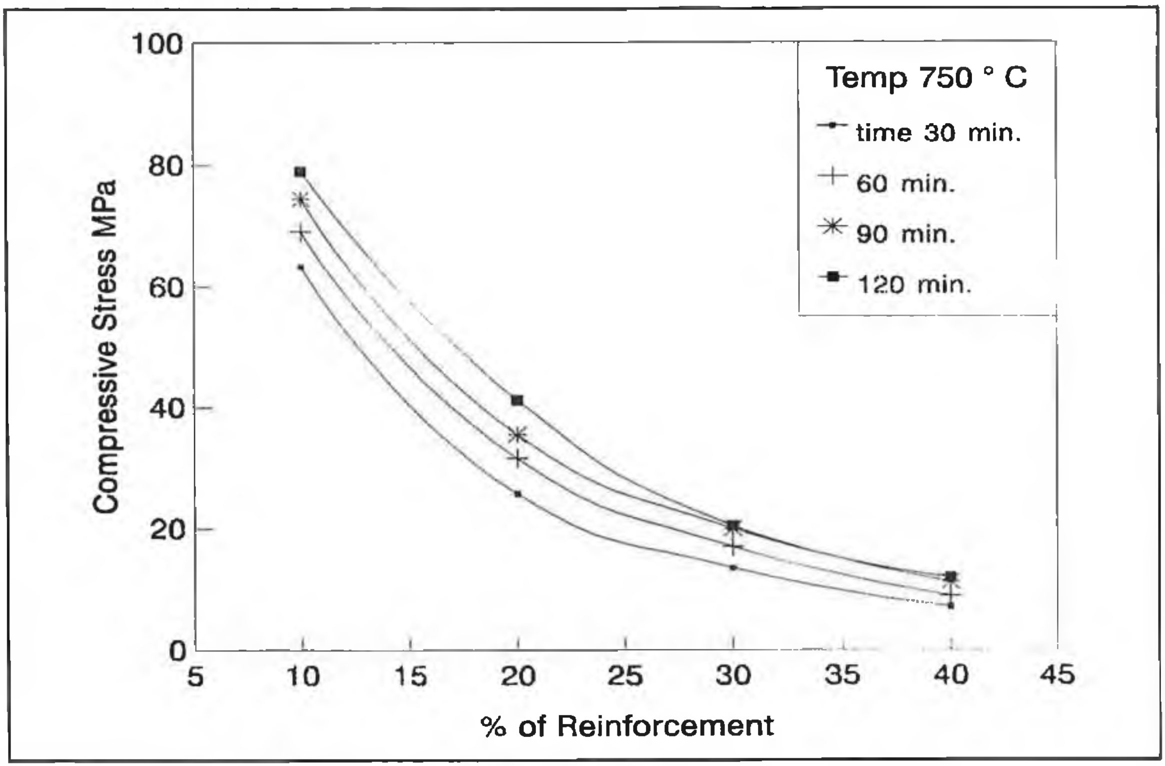

Figure 3.28 Effect of time on compressive stress of Al/Al_2O_3 composite for temperature 750 °C.

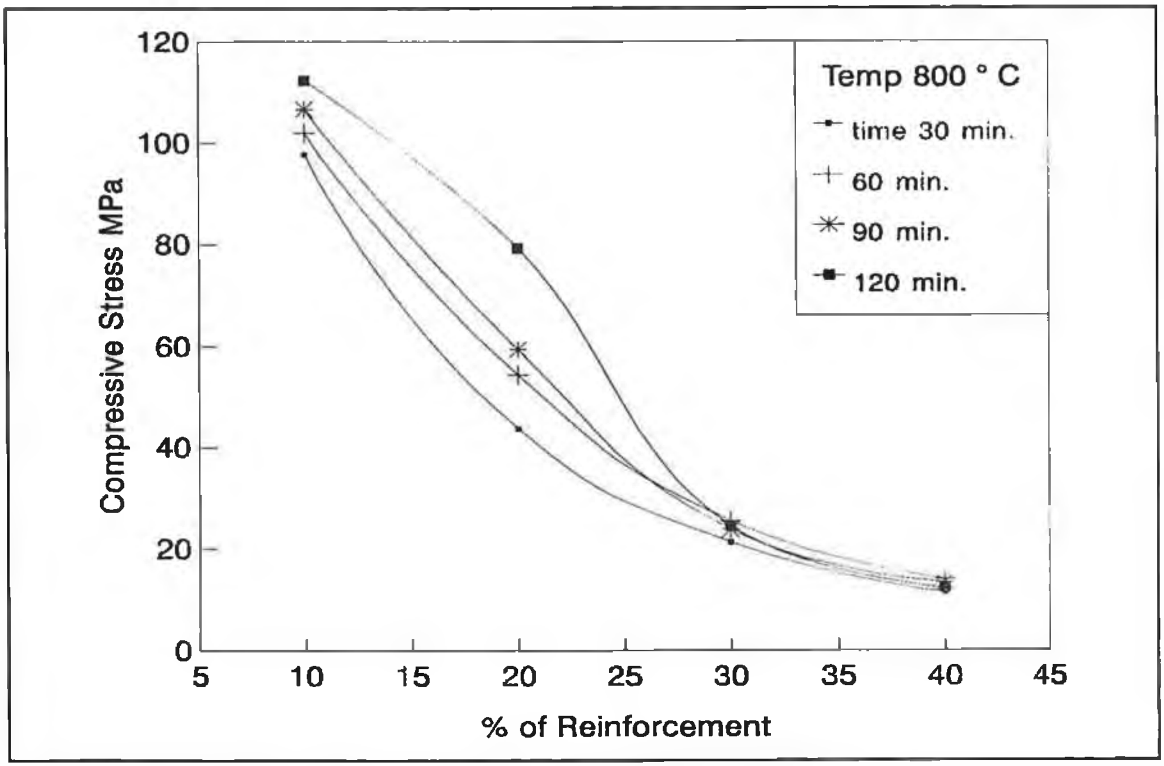

Figure 3.29 Effect of time on compressive stress of Al/Al_2O_3 composite for temperature 800 °C.

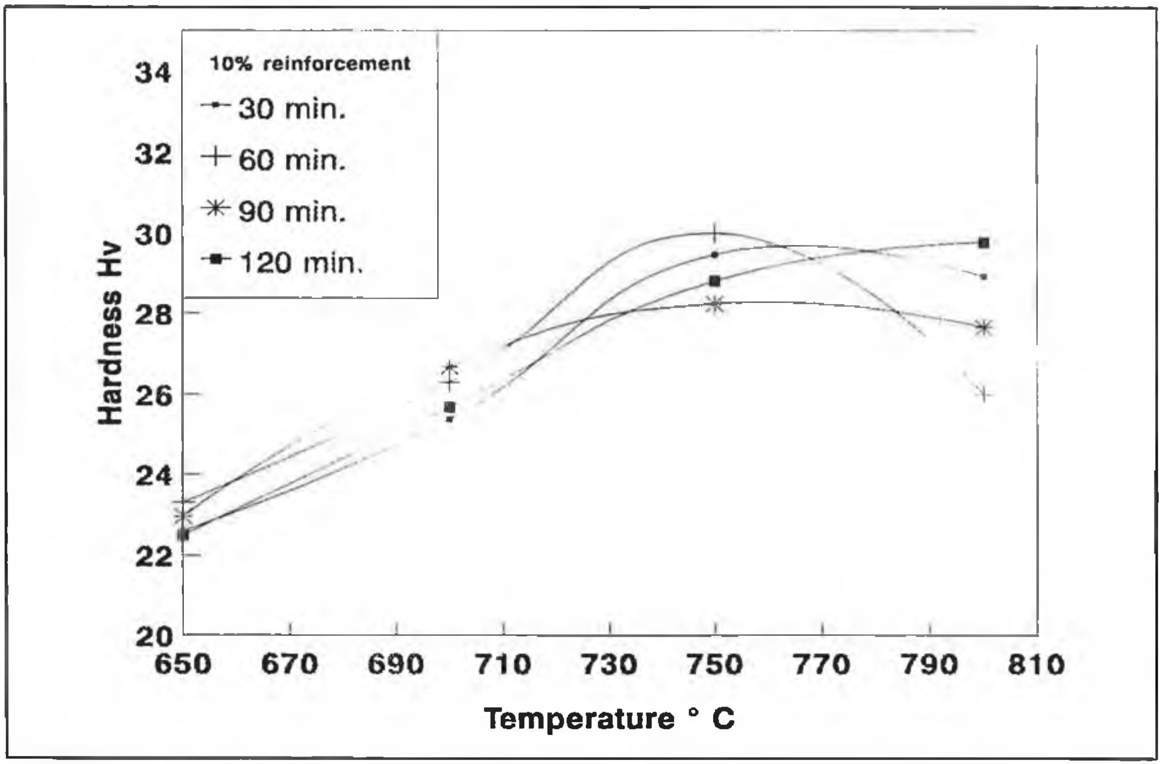

Figure 3.30 Effect of time on hardness of Al/Al_2O_3 composite for 10% reinforcement.

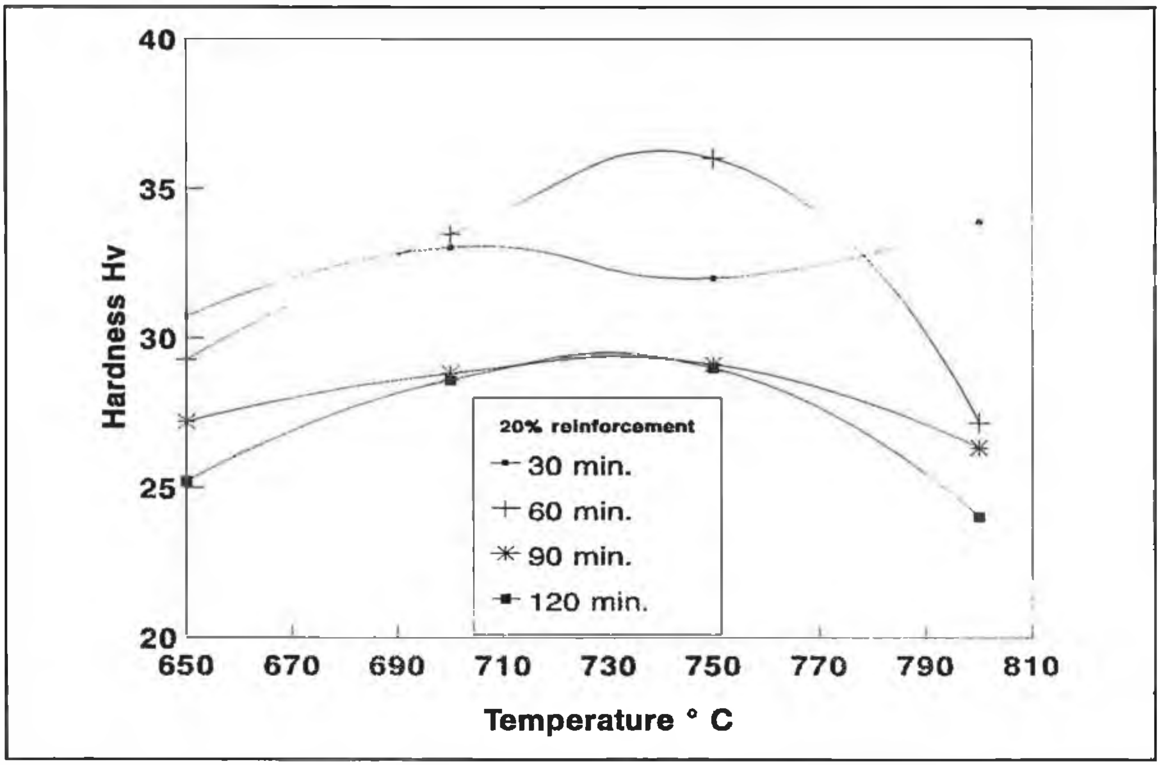

Figure 3.31 Effect of time on hardness of Al/Al_2O_3 composite for 20% reinforcement.

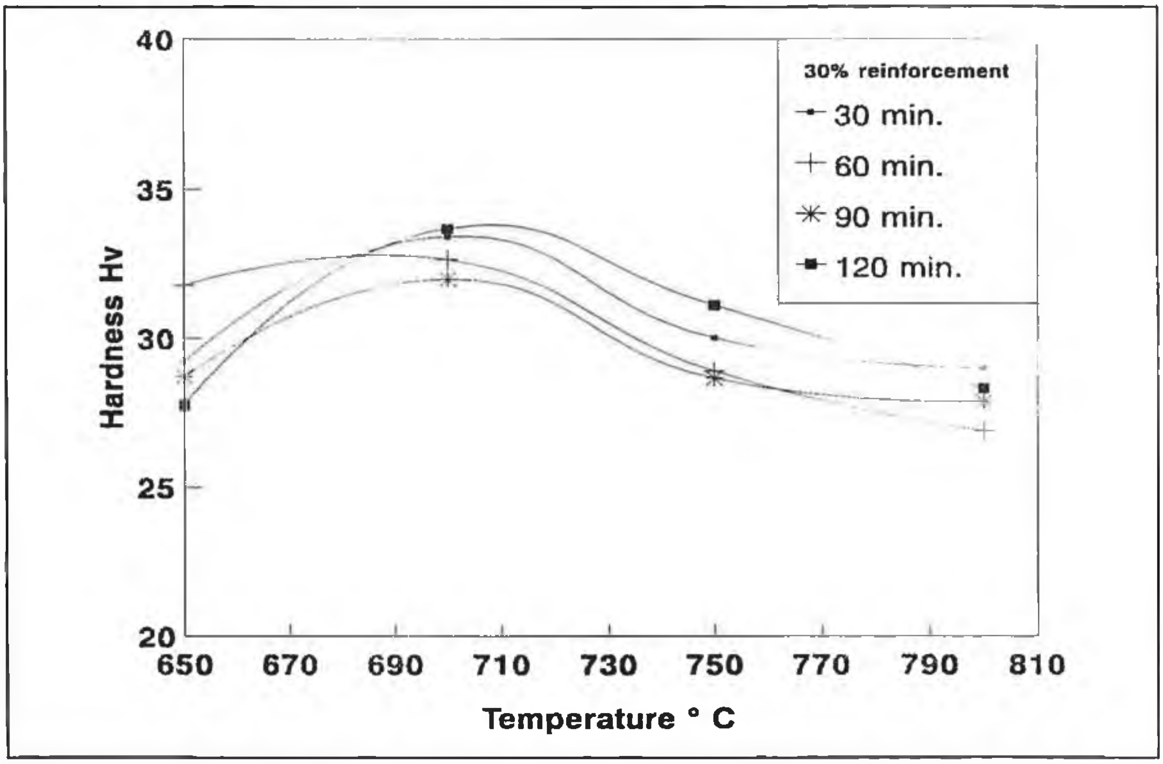

Figure 3.32 Effect of time on hardness of Al/Al_2O_3 composite for 30% reinforcement.

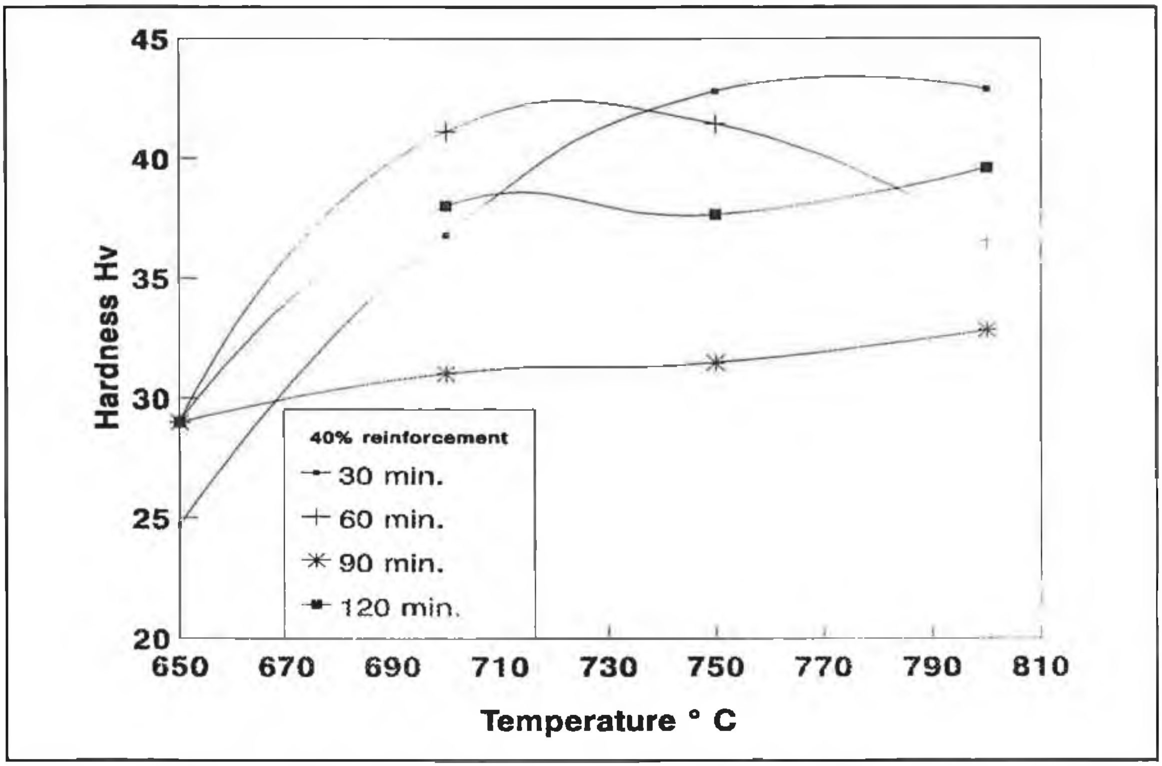

Figure 3.33 Effect of time on hardness of Al/Al_2O_3 composite for 40% reinforcement.

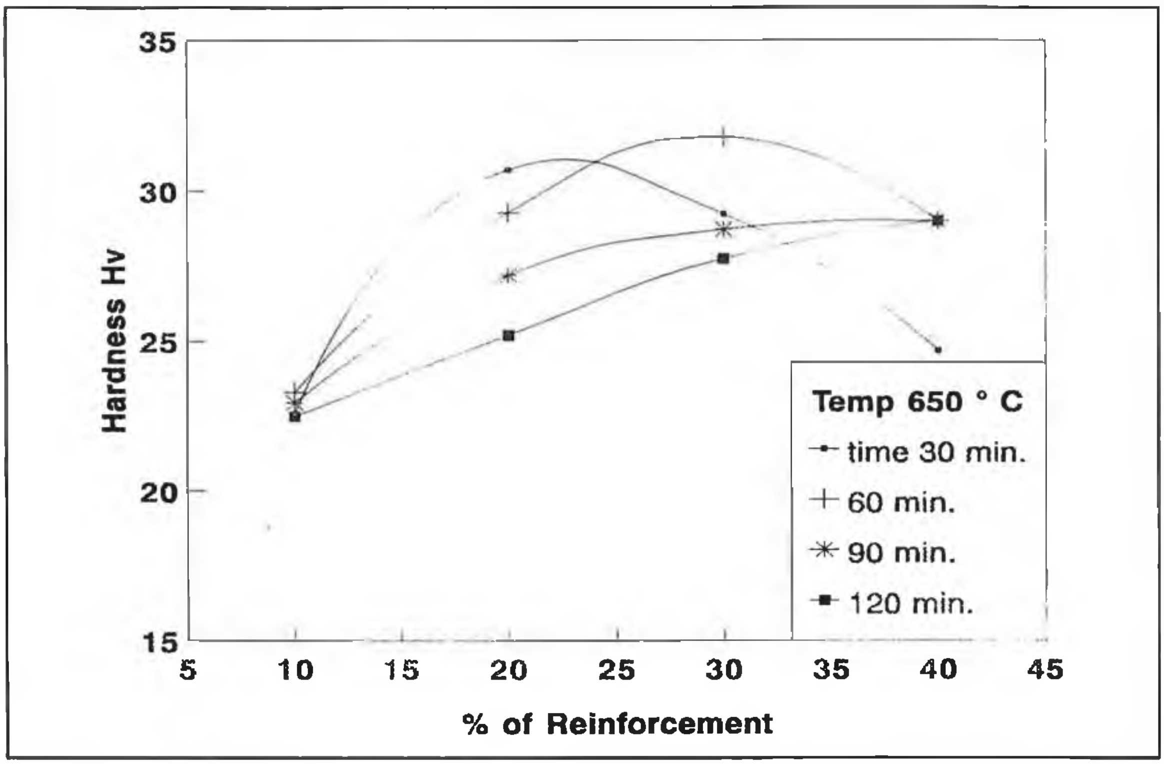

Figure 3.34 Effect of time on hardness of Al/Al_2O_3 composite for temperature 650 °C.

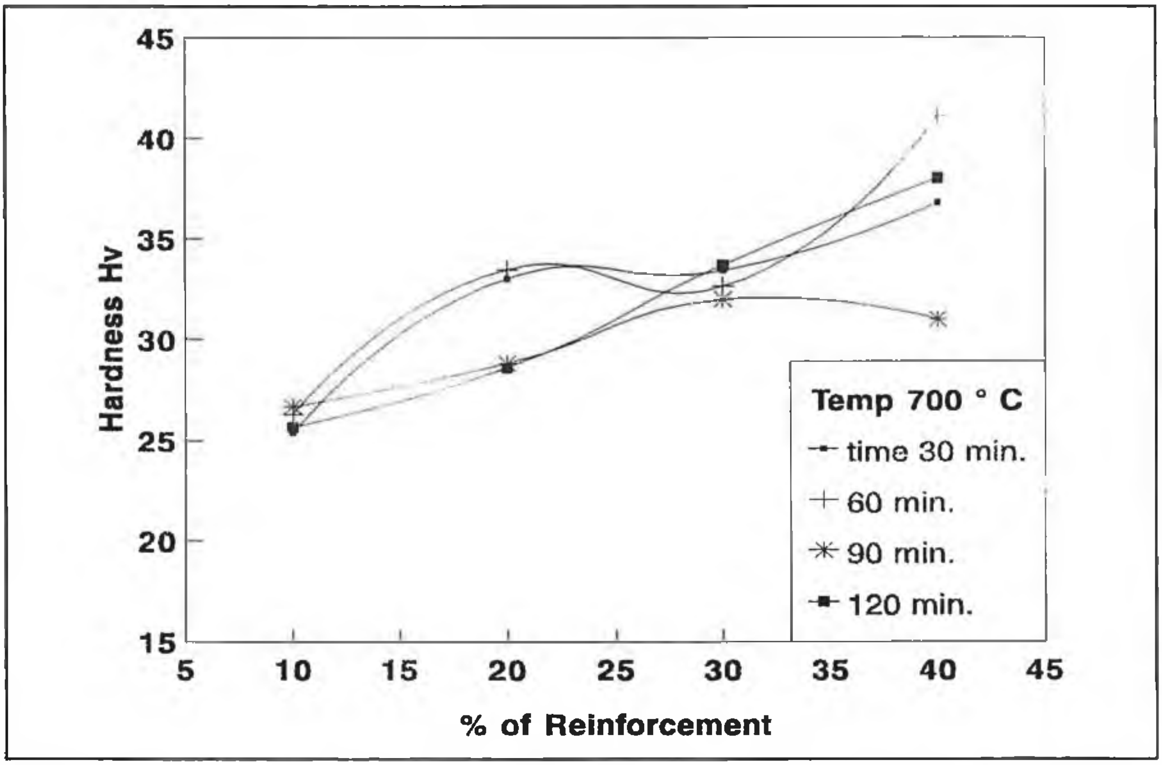

Figure 3.35 Effect of time on hardness of Al/Al_2O_3 composite for temperature 700 °C.

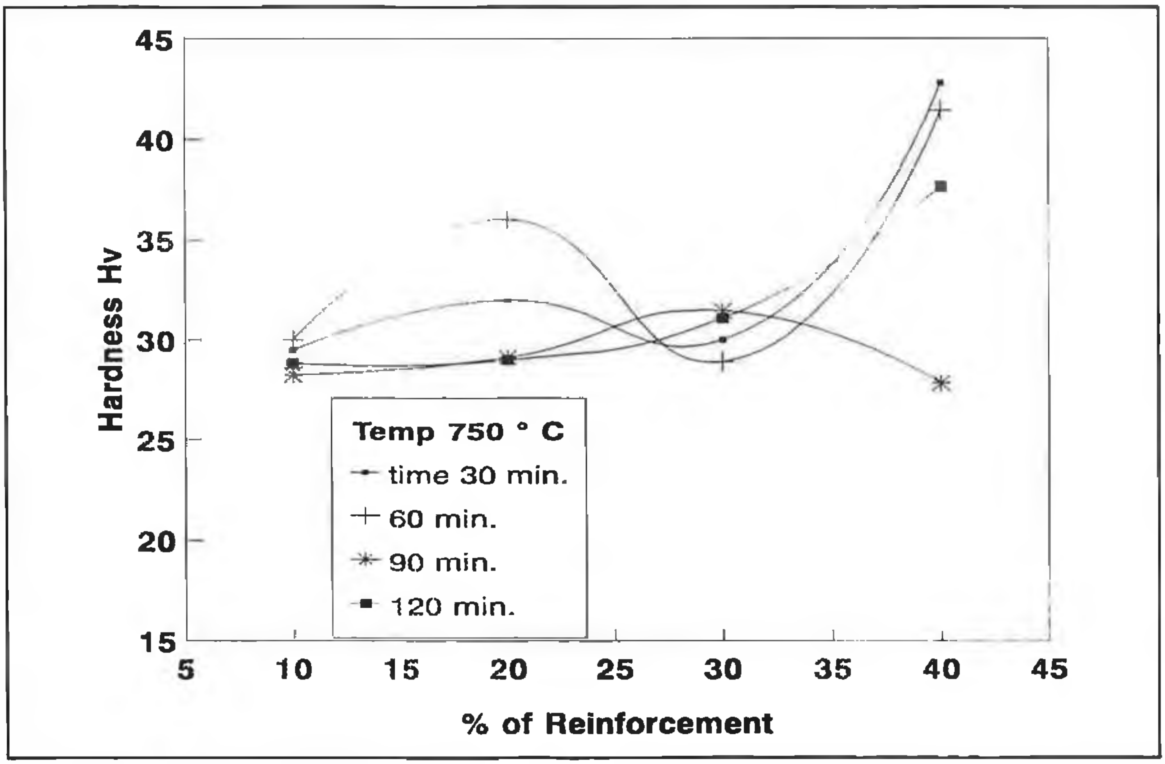

Figure 3.36 Effect of time on hardness of Al/Al_2O_3 composite for temperature 750 °C.

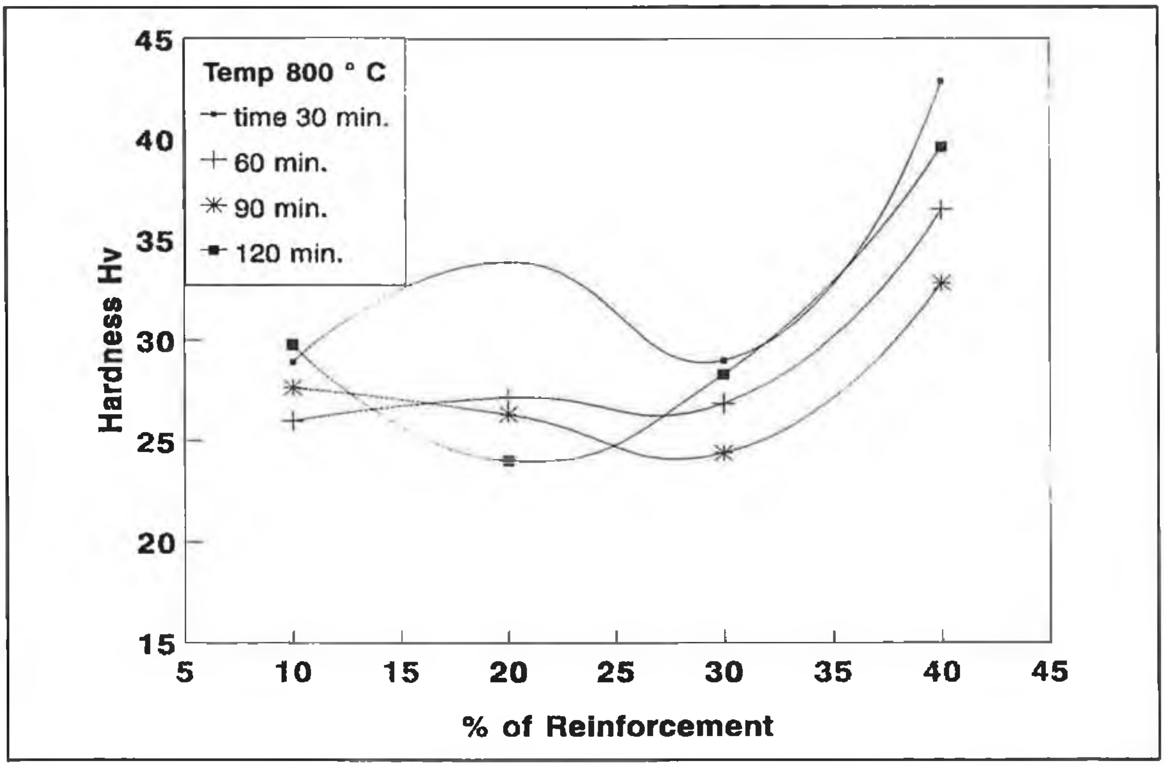

Figure 3.37 Effect of time on hardness of Al/Al_2O_3 composite for temperature 800 °C.

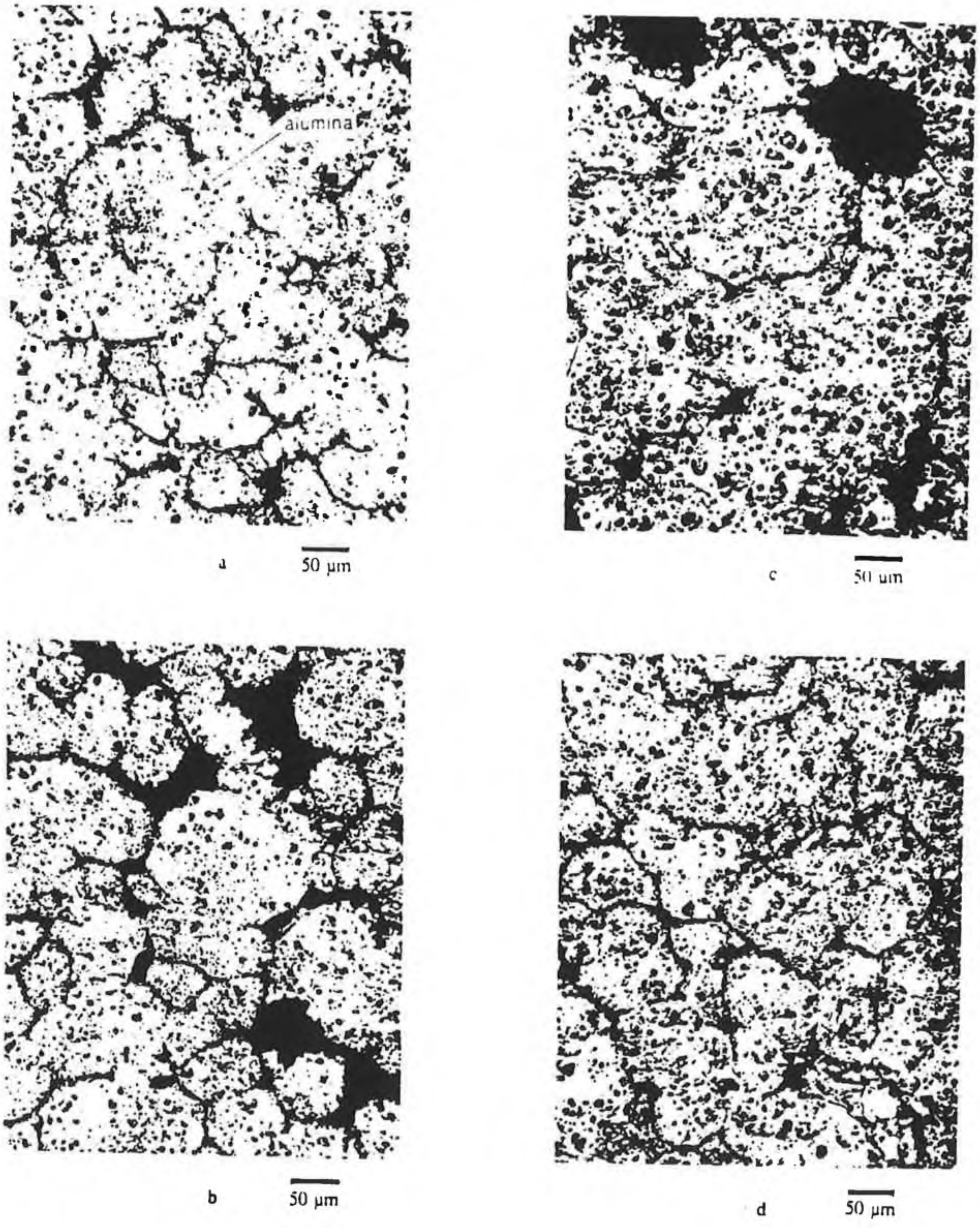

Figure 3.38 Microstructure of samples (10% reinf.) for different sintering time and temperature; (a) 60 min., 750 °C; (b) 60 min., 800 °C; (c) 120 min., 750 °C and (d) 120 min., and 800 °C.

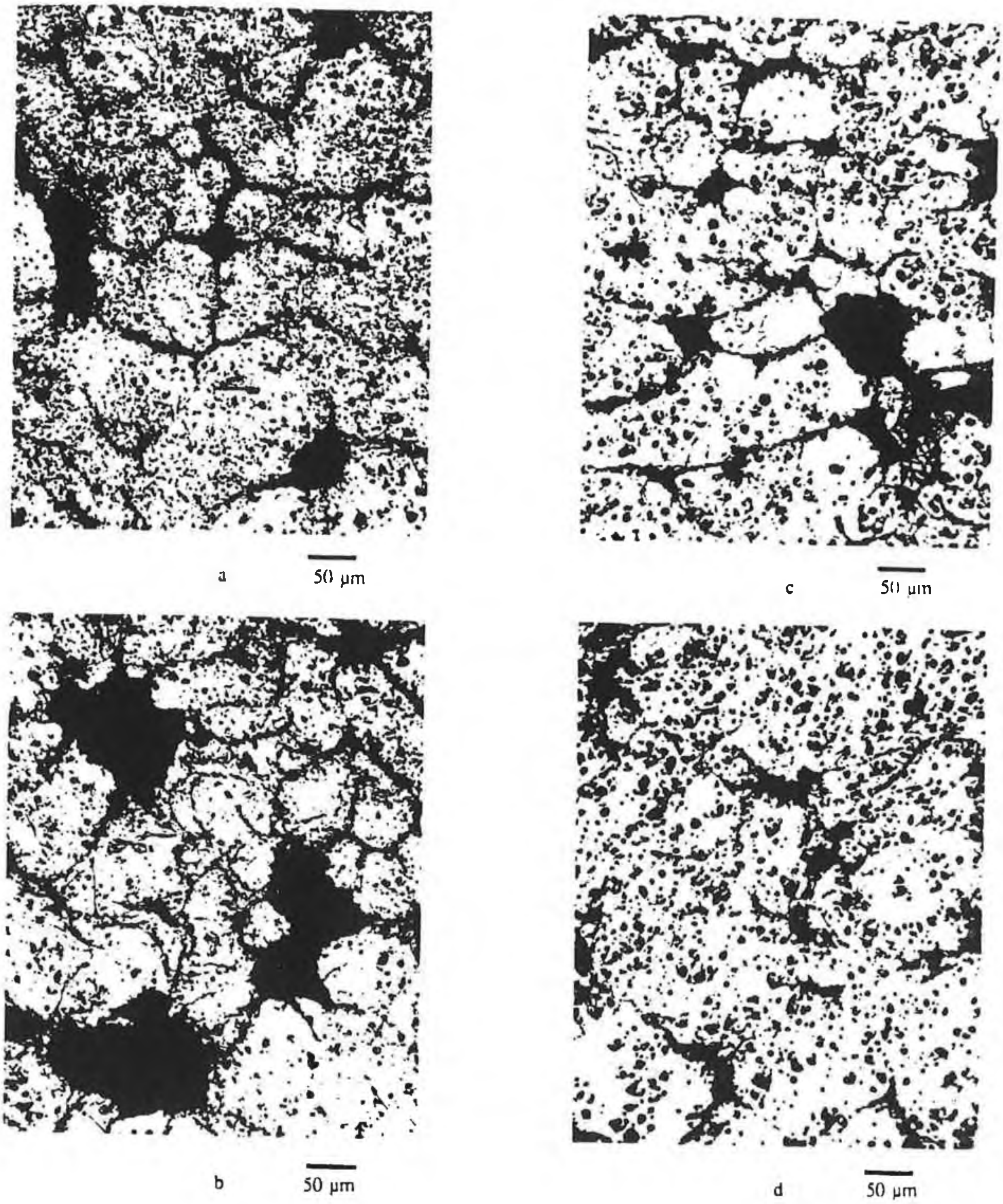

Figure 3.39 Microstructure of samples (20% reinf.) for different sintering time and temperature; (a) 60 min., 750 °C; (b) 60 min., 800 °C; (c) 30 min., 750 °C and (d) 30 min., and 800 °C.

CHAPTER FOUR

RATE CONTROLLED SINTERING OF ZINC OXIDE VARISTORS

4.1 INTRODUCTION

The computer controlled weight loss and shrinkage for sintering have been discussed in this chapter. Two software programmes have been specially developed for controlling the weight loss and shrinkage to obtain a linear weight loss and linear shrinkage. The relationship between the heating rate and the weight loss rate has been established to get the linear weight loss curve. The size effect of the discs on the firing profile for a specific binder burnout rate has been also studied.

4.2 COMPUTER CONTROLLED WEIGHT LOSS

The binder burnout stage is the initial stage of sintering. During this stage, the fugitive binders and other organic additives used in the compaction of ZnO varistors discs are eliminated at temperatures from 20 to 450 °C. Binders are added to the powder to give it necessary plasticity required for compaction and necessary strength required for subsequent handling. Figure (4.1) shows the binder burnout of the samples when they are fired by constant heating rate of 2.5 °C/min. It is seen from that figure that the initial burnout rate is too high and shows a maximum of 13 g/kg/h but at higher temperature it becomes small. This maximum weight loss rate will increase if the furnace heating rate is increased. This uneven binder burnout rate can create defects such as voids, cracks, bubbles inside the discs. An attempt has been made during the present research work to achieve linear weight loss by controlling the heating rate of the furnace through a computerized feedback loop. For operating the system, interfacing and instrumentation has to be properly integrated.

4.2.1 Design Interface and Instrumentation

The following instruments are used for the weight loss control set up:

- Balance (METTLER PM 6100) with interfacing facility and resolution 0.01 g
- Pot furnace (Surefire TS25, K+F Ltd.) equipped with WEST 2054 controller programmer.
- Personal computer (AMSTRAD 1512, 614 kB).
- SCIA-30 serial communication interface adapter.

The balance is connected with computer through COM1 serial port. The connection between the balance and the computer should be implemented according to table (4.1). The computer works as a data logging terminal and process control console. In this work, the balance is connected to the computer through a 25 pin connectors. The connection has been made according to the table (4.2).

The interface command for balance is as follows

```
OPEN "COM1:2400,E,7,1,CS,DS,LF" FOR RANDOM AS #1
```

where COM1: designated for the first RS 232C data interface

2400 - transmission rate for data transfer (called 2400 baud rate)

E - even parity

7 - number of data bits

1 - number of stop bits

CS - CTS (clear to send) do not process handshake signal

DS - DSR (data set ready) do not process handshake signal

Table 4.1 Pin/cable connection in multipin connectors for balance and computer.

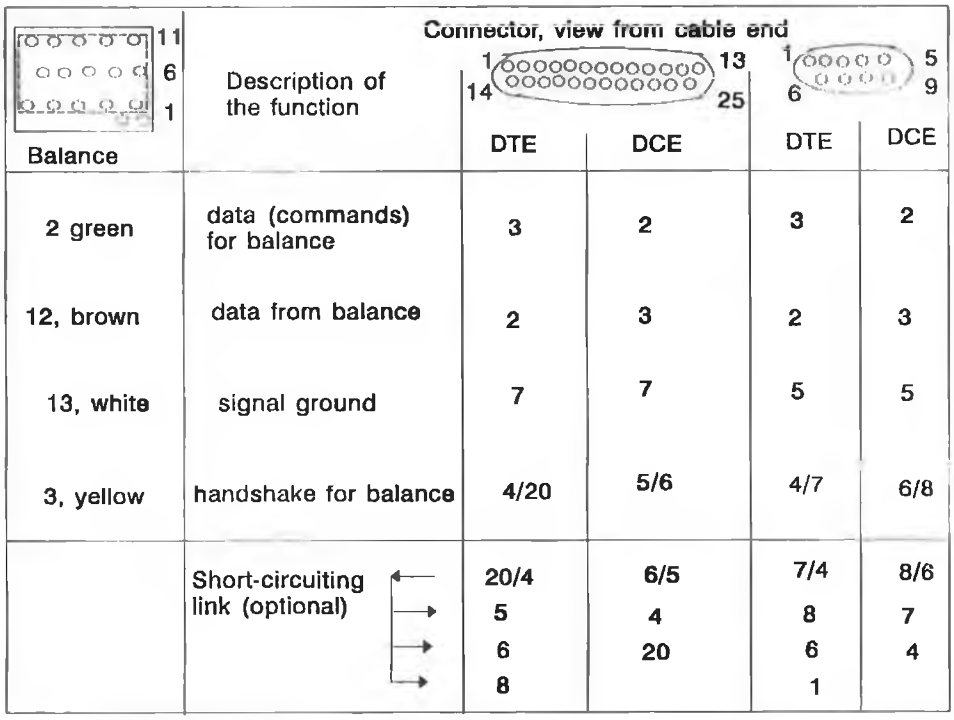

Balance	Description of the function	Connector, view from cable end			
		DTE	DCE	DTE	DCE
2 green	data (commands) for balance	3	2	3	2
12, brown	data from balance	2	3	2	3
13, white	signal ground	7	7	5	5
3, yellow	handshake for balance	4/20	5/6	4/7	6/8
	Short-circuiting link (optional)	20/4 5 6 8	6/5 4 20	7/4 8 6 1	8/6 7 4

Table 4.2 Connection used for balance and computer

Balance	Computer
PIN	PIN
2 green 12 brown 13 white	2 3 7

LF - data string automatically terminated with CR and LF (CR-carriage return and LF- line feed)

The test program for transferring the data from the balance to the computer is given in Appendix B.

The computer is connected to the furnace controller through a WEST SCIA-30 serial communication interface adapter. The computer is connected with SCIA-30 by RS 232C and SCIA-30 with controller by RS 422 interface. The layout for the interfacing is as follows:

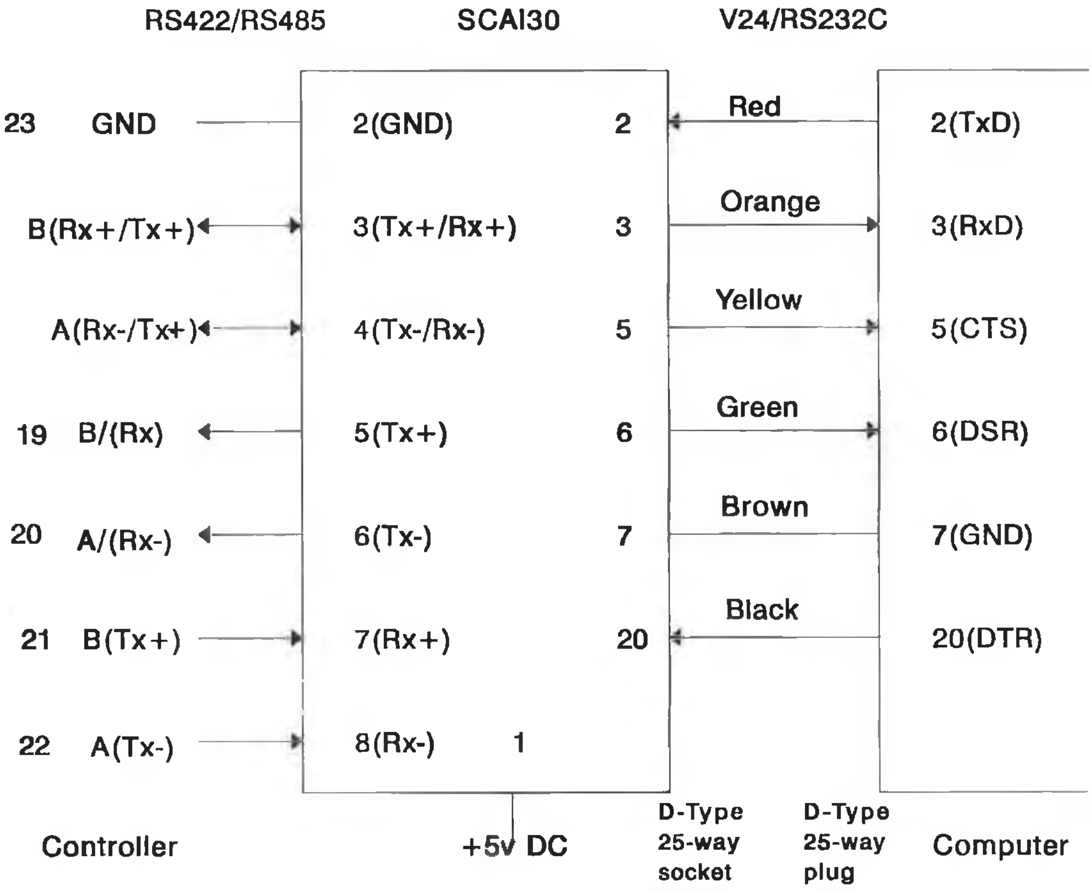

The interface command for controlling the controller through SCIA-30 by the computer is `OPEN "COM2:4800,E,7,1,RS,CS0,DS0,CD0,,PE" FOR RANDOM AS # 2` where this command opens communication channel 2 in random access mode at a speed of 4800 baud, even parity, 7 data bits and 1 stop bit and data will be save in file number 2.

The test program for checking the command transfer to the controller is given in Appendix B.

4.2.2 Experimental Setup

The set up for weight loss control is shown in figure (4.2).This setup is the feed back loop control system. The weight reading from the balance is monitored at regular interval by computer and according to the weight loss rate calculated, a command is given to the controller to change the heating rate and continues up to the completion of the binder burnout process. A small hole of 12 mm diameter was made at the middle of the bed of the furnace. The balance was placed underneath the furnace. A rod containing a bench for holding the disc passing through the furnace was placed on the stand. The stand placed on the balance. The balance was connected to the personal computer through a communication link to transfer the weight of the samples to the computer. The furnace controller was connected to the personal computer through a communication link to sustain the feed back loop. Plate (4.1) shows the photograph of the weight loss control set up while plate (4.2) shows the actual layout of the samples inside the furnace.

4.2.3 Results and Discussion

A computer software developed by Al-Tounsi A. [106] was modified to control the weight loss routine. The flow chart of the programme is given in figure (4.3). The computer programme operates as follows:

The weight reading is transferred from balance to computer at a predetermined time interval. Normally 6 minutes were taken as the time interval. The weight loss and weight loss rate are then calculated according to the following equations

$$W_l=\frac{W_i-W_0}{W_0} \qquad g/kg \qquad (4.1)$$

where: W_l is the weight loss in g/kg

W_i is the weight of the samples at time t_i and

W_0 is the initial weight of the samples before the firing starts.

The weight loss rate was calculated as follows:

$$\dot{W}_l=\frac{\dfrac{W_{i+1}-W_i}{W_0}}{t_{i+1}-t_i} \qquad g/kg/h \qquad (4.2)$$

where: $\dot{W}_l$ is the weight loss rate at time t_i

W_{i+1} is samples weight at time t_{i+1}

and $t_{i+1}-t_i$ is the time interval which is set in the software and equal to 6 minutes.

According to the current weight loss rate, the heating rate was calculated and the software gives commands to the furnace controller to change the previous heating rate of the furnace. Initially during running the programme, it was necessary to specify only the initial temperature which is normally taken as room temperature, then automatically this software will create the temperature profile for a certain weight loss rate limit. The source code of the software is shown in Appendix C. The previous researcher [106] used three different functions for the relation of heating rate with current weight loss rate. These functions were exponential the decay function, the elliptical function and the linear function. It was concluded that a linear relationship between the heating rate and weight loss rate was the best suitable to control the weight loss at a certain rate. But the relationship between the heating rate and the weight loss rate was not established. So a relationship between heating rate and weight loss rate has been established to get the linear weight loss as

$$\dot{H} = m\,\dot{W}_l + C \tag{4.3}$$

where: $\dot{H}$ is the heating rate

m is the ratio of maximum heating rate at weight loss rate zero and the maximum weight loss rate limit at heating rate zero. m is therefore the slope of the line.

$\dot{W}_l$ is the current weight loss rate

and C is the maximum allowable heating rate which corresponds to a weight loss rate of zero. C was set in the software to 2.5 °C/min.

The samples were fired for the weight loss rate limits 0.75, 1, 1.5, 2 and 3 g/kg/h. For all of the firings 6 discs of 49 mm diameter and 51 mm height were used. The initial total weight of the discs was about 2 kg. Figures (4.4), (4.5), (4.6), (4.7) and (4.8) show the weight loss, weight loss rate and temperature profile for weight loss rate limit 0.75, 1, 1.5, 2 and 3 g/kg/h respectively. From these figures, it is seen that for the lower weight loss rate limit, the linearity of the weight loss curve has improved and a perfectly straight line can be seen. So equation (4.3) is capable to generate a temperature profile that will produce a linear weight loss curve. It is seen from each figure that at the starting time for few minutes the weight is increased about 0.1 g though temperature increases, so weight loss rate becomes positive value. It seems at the initial time, the discs gain some weight by absorbing some volatile materials exist in the furnace. This creates the unstable weight loss rate with temperature. It can be minimised by either controlling the atmosphere or preheating the feeding zone at very low temperature 30 to 40 °C for 6-10 minutes. Appendix D shows the sample of the data file for the weight loss rate limit 0.75 g/kg/h. The firing time increases with decreasing the weight loss rate limit. Table (4.3) gives the weight loss rate set up, initial and final weight, total weight loss, duration for completing binder burnout and final temperature.

Figure (4.9) shows the resultant temperature profiles which were generated through the above 4 weight loss rate limit 0.75, 1, 1.5 and 2 g/kg/h. From each of these curves it is seen that the first and second ramps are high and after that it becomes low and again high after 300 °C. The first ramp corresponds to moisture evaporation. This ramp is high enough as the moisture percentage in the sample is very low. The second ramp is high because after moisture evaporation, there is less material to be eliminated. At about 175 °C , the organic binders start to burnout. To keep the weight loss rate constant, a large number of ramps and dwells are generated and these increase with lower binder burnout rates. So, the firing time increases with decreasing of weight loss rate limit.

Table 4.3 Wt. loss and temperature data for different wt. loss rate limit

Figures	Weight loss rate limit (g/kg/h)	Initial weight (g)	Final weight (g)	Total weight loss (g/kg)	Total time (h)	Final temp. (°C)
4.4	0.75	1931.78	1901.39	-15.74	22.7	416
4.5	1	1940.34	1908.53	-16.39	19.1	429
4.6	1.5	1932.12	1901.27	-15.97	12.8	417
4.7	2	1937.58	1906.27	-16.16	9.9	419
4.8	3	1933.49	1902.79	-15.88	7.6	439

To see the effect of the device size on the firing profile, three sizes of discs were studied. Their dimensions were:

	Green size	
	Diameter in mm	Height in mm
Size A	38	42
Size B	73	22
Size C	38	50

The temperature profile for weight loss and weight loss rate curve are drawn in figures

(4,10), (4.11) and (4.12) for the sizes of A, B and C respectively for the weight loss rate limit 1.5 g/kg/h. The total weight losses for the discs of size A, B and C are 12.67, 13.39 and 12.95 g/kg respectively. The discs of size A and C have the same binder percentage. This can be cleared from the figure (4.13) which shows the weight loss curves for the above discs. It is seen that though the binder percentage for the disc A and C is same, but the slope for the weight loss is different. This is because of the variation of the surface to volume ratio. The surface to volume ratio for the discs of A and C are 1.5288 and 1.452 $^{-}$cm respectively. The temperature profile is also different for the above two disc size. This is shown in figure (4.14). Since the surface to volume ratio is low for the case of C type disc, they have smaller area for the binder burnout and so the heating rate should be high as the weight loss rate is low. So the disc of lower surface to volume ratio have the lower firing time to complete the binder burnout. The surface to volume ratio for the discs of B is 1.457. So though the surface to volume ratio is same for the discs C and B, but the temperature profile is not same. It is because of the variation of the binder percentage.

Figure (4.15) shows the temperature profile, weight loss and weight loss rate curve for the weight loss rate limit 0.56 g/kg/h. Here the same dimensional discs were used as for 0.75 g/kg/h. Since the binder percentage is smaller for the case of 0.56 g/kg/h, as the total weight loss for 0.75 g/kg/h was 15.74 and for 0.56 g/kg/h was 12.22, so though the weight loss rate is smaller for 0.56 g/kg/h but the firing time is relatively smaller than that of 0.75 g/kg/h. So the temperature profile varies with the binder percentage. As the binder percentage increases, the firing time also increases. So an average temperature profile should be taken for the same weight loss rate curve.

4.3 COMPUTER CONTROLLED SHRINKAGE

Shrinkage starts at about 825 °C when bismuth oxide melts. The peak sintering temperature is about 1100 to 1200 °C. At the initial stage of shrinkage it starts rapidly and then slow down. Figure (4.16) shows the shrinkage and shrinkage rate curve for the heating rate of 5 °C/min.. It is seen that after 900 °C, the shrinkage is very high up to temperature 1000 °C. This uneven shrinkage can cause defects such as cracks, trapped pores etc. So a set-up has been done to get the linear shrinkage by controlling the heating rate of the furnace through a computer.

4.3.1 Design Interface and Instrumentation

The following instruments were used for the shrinkage control setup.

- PC (AMSTRAD 1512, 614 kB), the same one which was used for the weight loss equipment.
- Pot furnace (Surefire TS25, K+F Ltd.) equipped with WEST 2054 controller programmer the same one as used for the weight loss equipment.
- Displacement transducer with spring return armature (LVDT type ACT/500/A, RDP Group). The transducer can measure displacements of up to ± 12.5 mm.
- Digital transducer indicator and conditioner (model 400/LVDT, RDP Group). The indicator has a resolution of 1 μm.
- SCIA-30, the RS 232C/RS 422 signal converter, the same one as used for weight loss equipment.

As the signal conditioner was connected to the PC through the communication link via

COM1 port, it transferred the shrinkage data to the computer. The connection for the transducer conditioner is shown in table (4.4).

Table 4.4 Connection of transducer conditioner

RS 232 connect. wiring	
DPM	25 PIN
TXD 4	3 RXD
DSR 3	6 DSR
GND 2	7 GND
DTR 1	20 DTR

The interface command for the transducer signal conditioner is:

```
OPEN "COM1:4800,N,8,1,DS,ASC" FOR INPUT AS #1
```

where COM1: designates the first RS 232C data interface (communication port1- serial port)

4800 - transmission rate for data transfer 4800 baud (speed)
N - no parity (type of error checking)
8 - number of data bits : 8 (number of data bits per byte, one must specify eight data bits when transmitting or receiving numeric data)
1 - number of stops bits
DS - DSR (data set ready)
ASC - Ascii mode

This program fragment opens the communication channel 1 in input mode at a speed of 4800 baud, no parity bit, eight data bits and one stop bit. Input will be in the ASCII mode as file number 1. The test program is given in Appendix B. The interfacing of SCIA-30 was the same as for the weight loss equipment.

4.3.2 Experimental Setup

The schematic diagram for the shrinkage setup is shown in figure (4.17). Plate (4.3) shows the photograph of the set up, while plate (4.4) shows the actual set up inside the furnace. A green disc was placed on the platform inside the furnace. The transducer extended by a metallic rod was fitted with a ceramic rod and mounted on a stand with X-Y-Z movement facility. The transducer was lowered until the ceramic rod touched the plate which was placed on the top of the disc. If the ceramic rod directly placed on the samples, during shrinkage as bismuth melts, the rod penetrated the surface and the data transfer will be incorrect. Before putting the ceramic rod, the bed of the green disc must be levelled.

Some powders were distributed on both the top and bottom surfaces of the disc and one small plate placed on each of the top and bottom surface. If the powder was not used, the plate adhered to the surface during shrinkage and creates a crack. If the plate dimensions becomes large, it also accelerated the cracking as the contact surface area with the sample increased. Plate (4.5) shows the crack generated due to the use of large plates on top and bottom of the disc.

The operating temperature of the transducer is 50 °C. Care was taken so that the surface temperature of the transducer does not exceed the limit. In order to protect the transducer, some metal sheets were placed around the ceramic rod which pass through the furnace vent to radiate and dissipate the heat coming from the vent.

Before starting the experiments on shrinkage, the transducer has to be calibrated. The calibration was done according to the instruction manual (RDP 400/LVDT) and fixed 20 mm for shrinkage and 5 mm for expansion. So according to the calibration the transducer can measure up to 20 mm of contraction of the whole unit if it is fixed at the condition of zero reading of transducer conditioner. For getting the true shrinkage, at first the expansion of the whole unit at different temperature must be known. In order to do that, a fired ZnO disc was placed into the surface with placing extension rod of transducer on it and the furnace was run at a constant heating rate up to 1250 °C. The reading for the expansion of unit were taken at a certain interval. For getting the shrinkage reading instead of fired disc, green disc were placed and reading from the transducer were taken. This reading combined with expansion and contraction of the setup. Then if the expansion data is subtracted from this, the value of contraction can be obtained. The expansion of the unit is shown in figure (4.18) where the expansion and contraction can be seen in figure (4.19).

4.4 RESULTS AND DISCUSSION

The shrinkage and shrinkage rate were calculated as follows:

$$\delta = \frac{l_i - l_0}{l_i} \tag{4.4}$$

$$\dot{\delta} = \frac{\dfrac{l_{i+1} - l_i}{l_i}}{t_{i+1} - t_i} \tag{4.5}$$

where δ is the shrinkage

$\dot{\delta}$ is the shrinkage rate

l_0 is the initial height of the disc

l_i is the current height at time t_i

l_{i+1} is the current height at time t_{i+1}

and $t_{i+1}-t_i$ is the time interval, taken 8 minutes.

The software was modified to get the actual data from the transducer for getting the linear shrinkage curve. The relationship between heating rate and the current shrinkage rate which was developed by the previous researcher [106] was modified and put as

$$\dot{H} = m\,\dot{\delta} + C \tag{4.6}$$

where: C represents the maximum allowable heating rate which corresponds to a shrinkage rate of zero. C was set in the software 0.125 and 0.3125 °C/min corresponding up to 900 °C and after 900 °C respectively, m is the slope of the line, it is the ratio of maximum heating rate at shrinkage rate zero and the shrinkage rate limit.

Two slopes were necessary to maintain the shrinkage linear. Since at the initial stage shrinkage is very high, the heating rate should be low as C is taken 1.25, whereas to keep the slope of shrinkage constant, since shrinkage is low after 900 °C, the heating rate fixed high by taking C=3.125. The flow chart of this software works according to the figure (4.20). To run the program, first a constant ramp of 2.5 °C/min. up to 1200 °C was set in the programmable controller. When the program was run, the temperature of the furnace was only monitored up to temperature 620 °C, after that the controls of the heating rate starts for the constant shrinkage and data were saved in a file. The data for shrinkage from transducer conditioner were collected after 8 min. in the computer and calculated the shrinkage and shrinkage rate according to equation (4.4) and (4.5) respectively. When calculating shrinkage, the shrinkage data was corrected considering the expansion of the unit. After calculating the shrinkage rate, the heating rate was calculated according to the equation (4.6) and the command was sent to the controller to change the heating rate and works up to 1200 °C. The source code of the software is shown in Appendix E. Appendix F shows the sample of the data file for the shrinkage rate limit 10 μm/mm/h. According to equation (4.6), for the shrinkage rate limits 10, 20, 30, 40, 53 μm/mm/h, the temperature profiles were generated. Figures (4.21), (4.22), (4.23), (4.24) and (4.25) were obtained for the shrinkage rate limits 10, 20, 30, 40 and 53 μm/mm/h respectively. It is seen that the equation (4.6) is capable to control the sintering process to get linear shrinkage. According to the above figures it is seen that as there is very little shrinkage up to temperature 800 °C, so the heating rate up to this temperature is very high. Then according to the shrinkage rate limit, the number of ramps and dwells varies and these increase with decreasing shrinkage rate limits. So the firing time increases with decreasing the shrinkage rate limit. This can be seen from the temperature profiles which are shown in figure (4.26) for the shrinkage rate limits 10, 20 and 40 μm/mm/h. The ramp are high at the initial stage to keep the shrinkage rate constant and then low enough and then high again to keep the trend.

Plate 4.1 Photagraph of the weight loss control equipment.

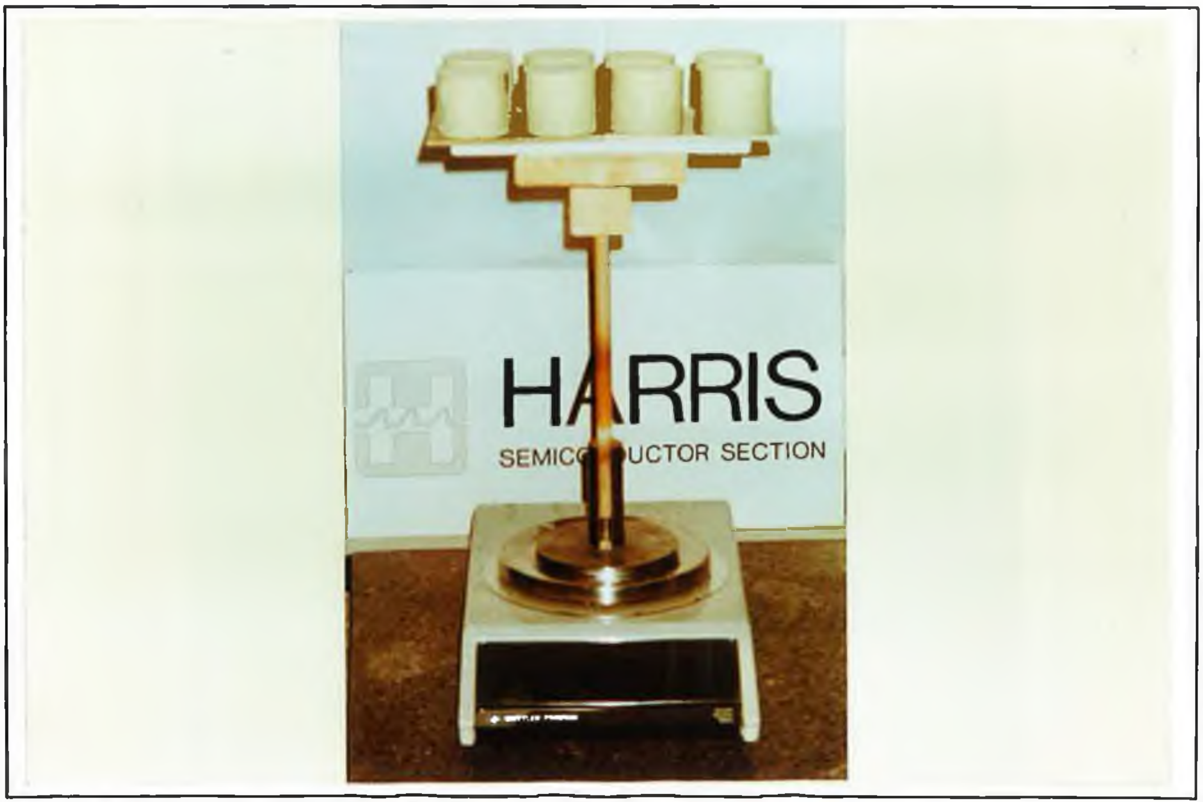

Plate 4.2 The layout of the samples inside the furnace for the weight loss control experiment.

Plate 4.3 Photograph of the shrinkage control setup.

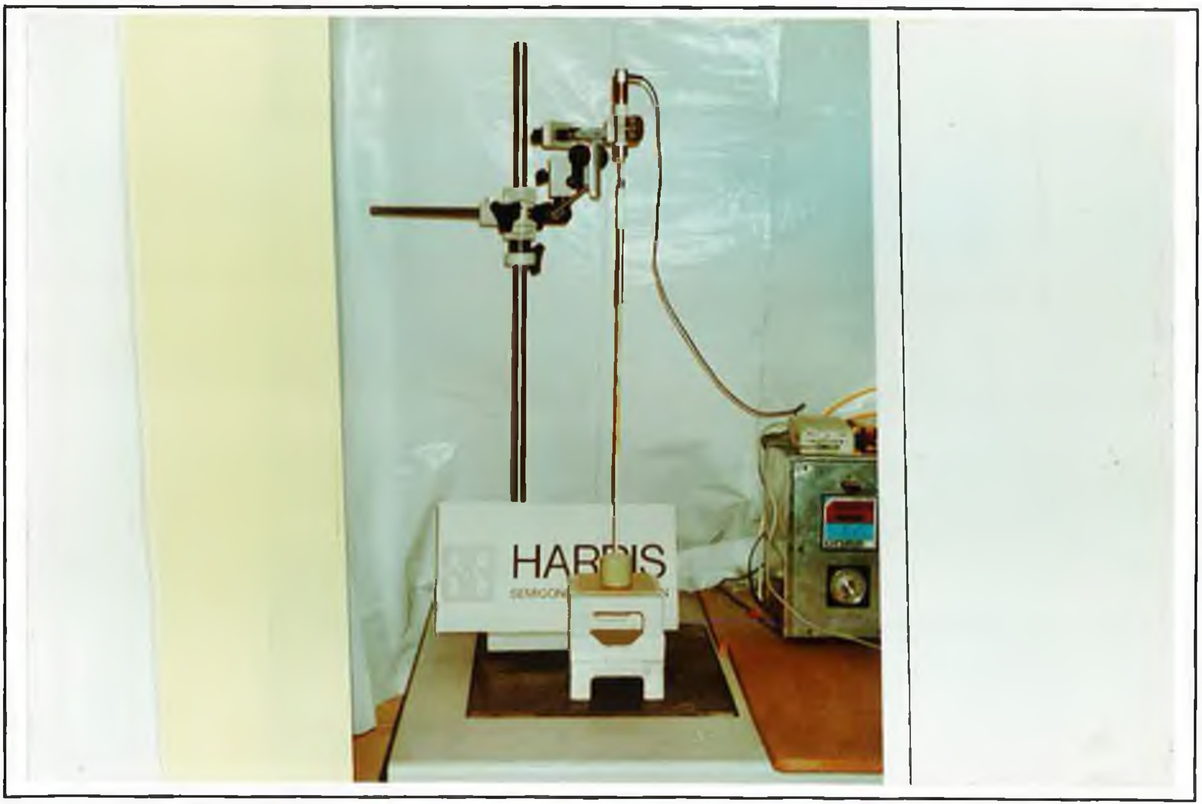

Plate 4.4 The layout of the transducer and the sample inside the furnace for shrinkage measurements.

Plate 4.5 Photograph of the cracked disc due to the use of large plates on top and botton surfaces of the disc during sintering.

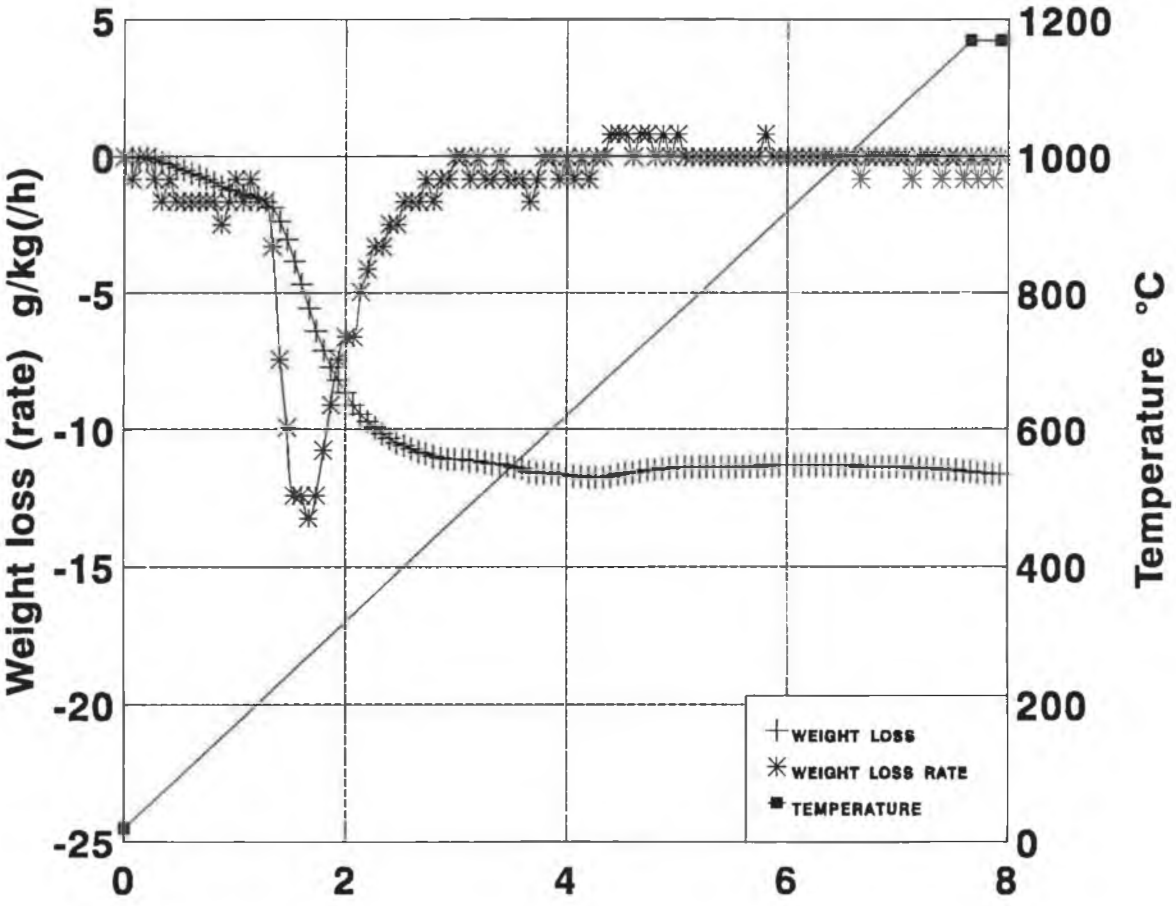

Figure 4.1 Weight loss, weight loss rate and temperature vs. firing time for heating rate of 2.5 °C/min.

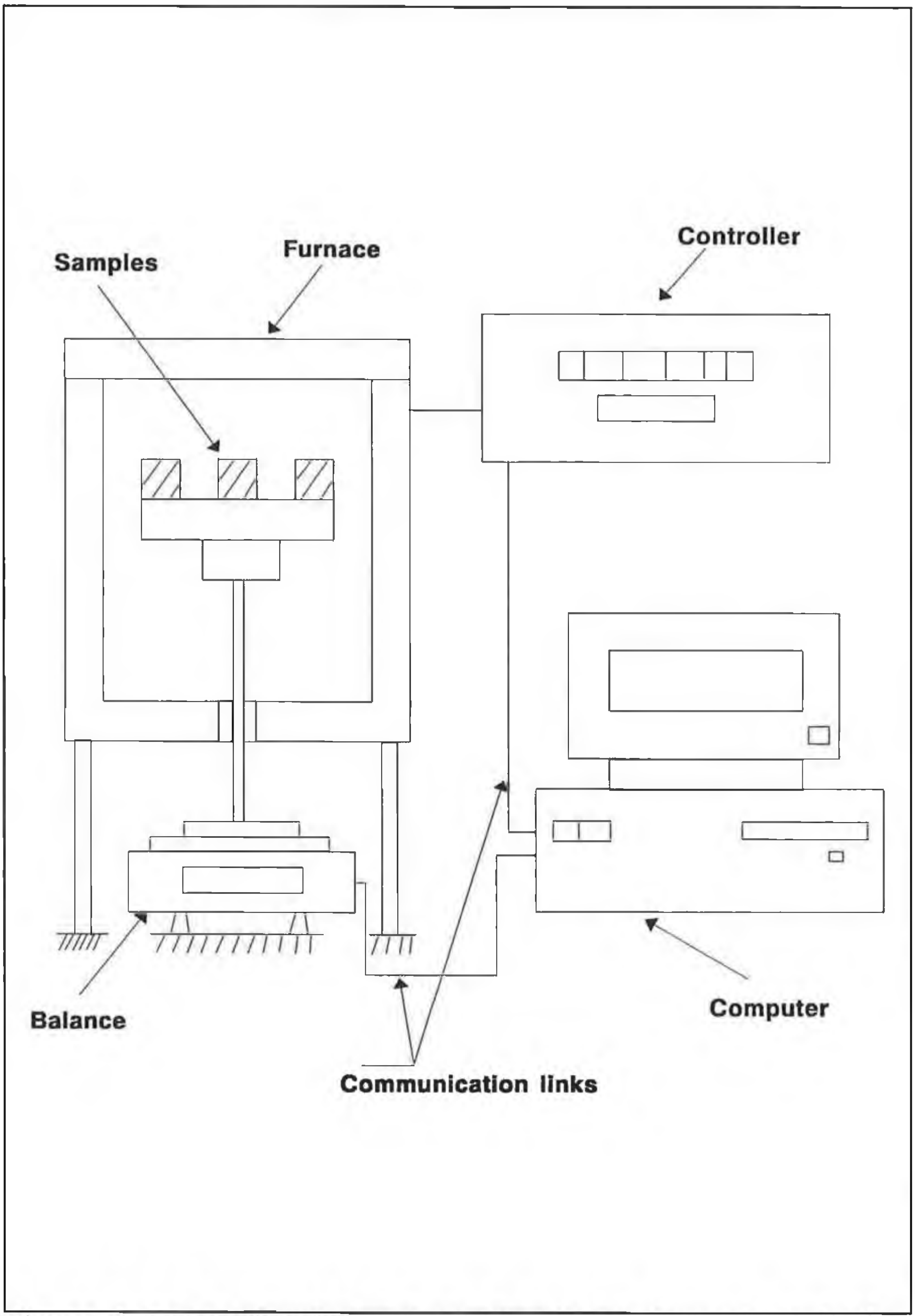

Figure 4.2 Experimental set up for binder burnout control

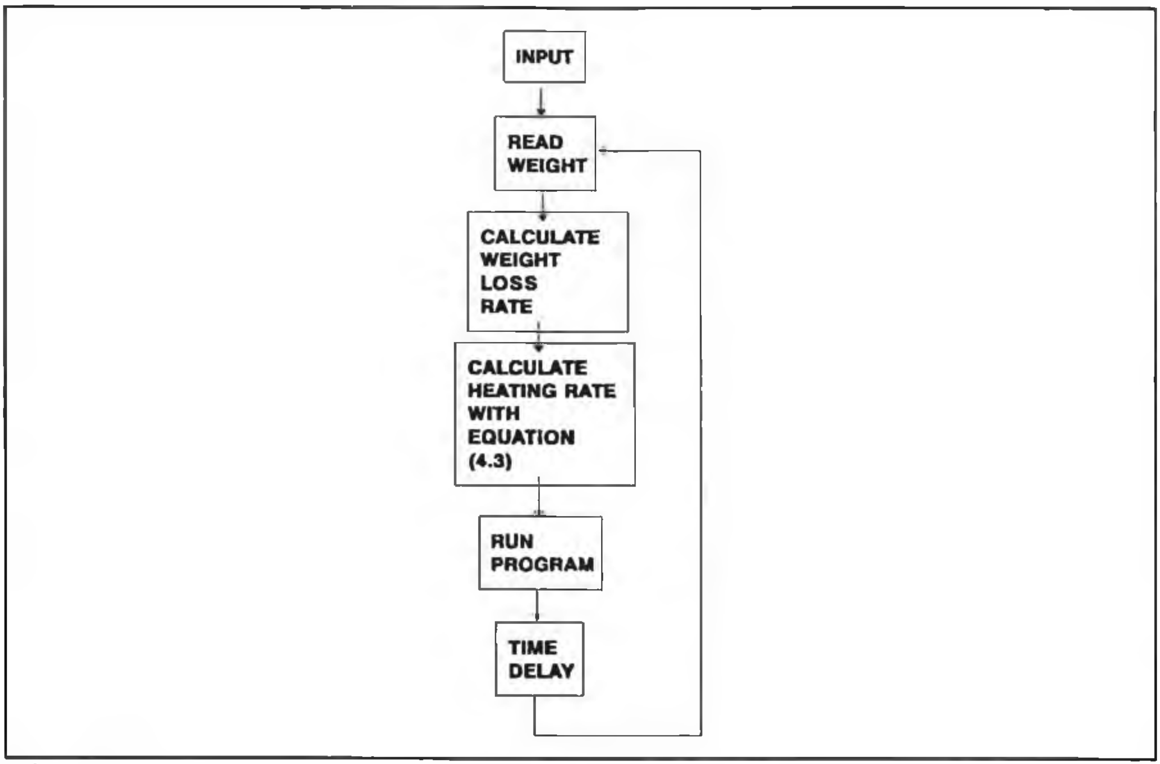

Figure 4.3 Flow chart of the software for controlling the disc's shrinkage

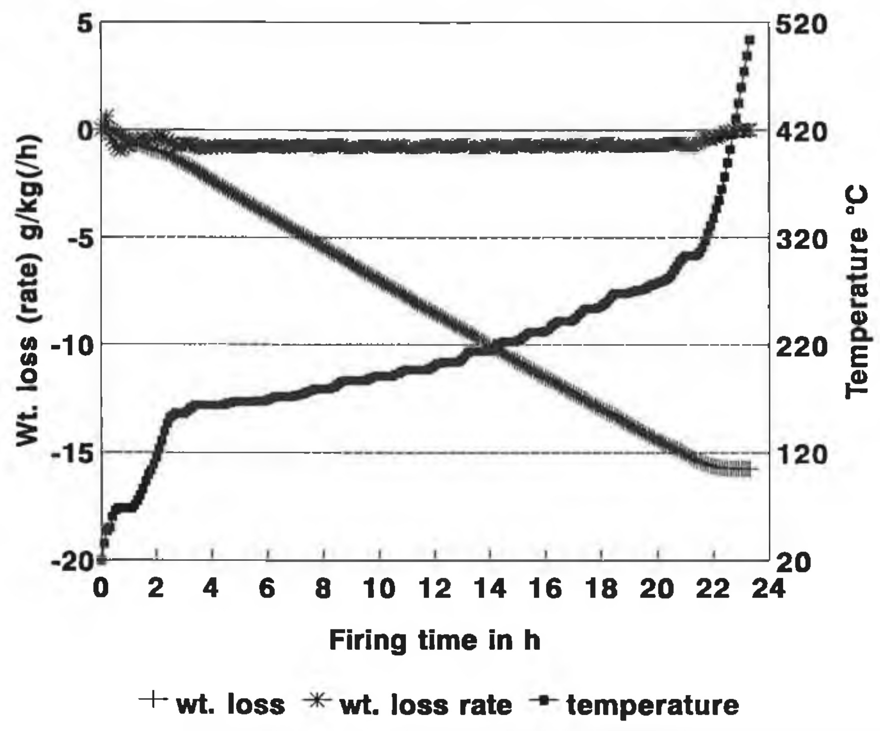

Figure 4.4 Weight loss, weight loss rate and teemperature vs firing time for weight loss rate limit 0.75 g/kg/h.

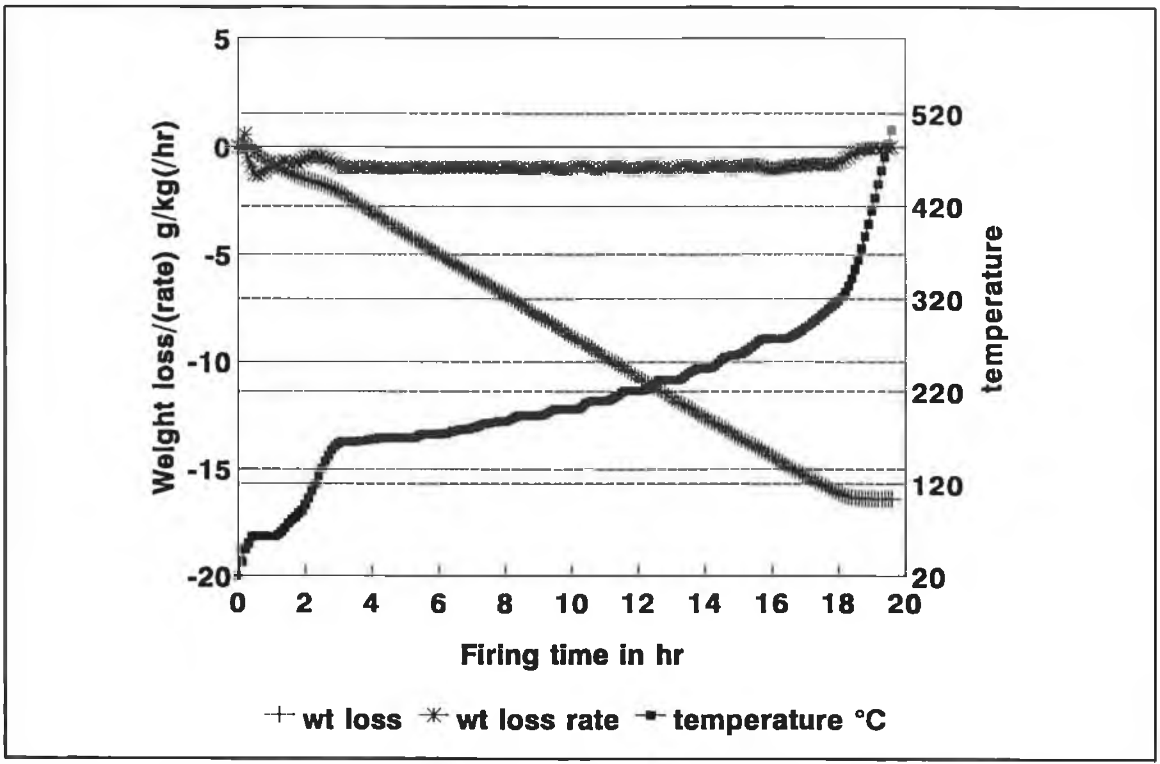

Figure 4.5 Weight loss, weight loss rate and temperature curves vs. firing time for weight loss rate limit 1 g/kg/h

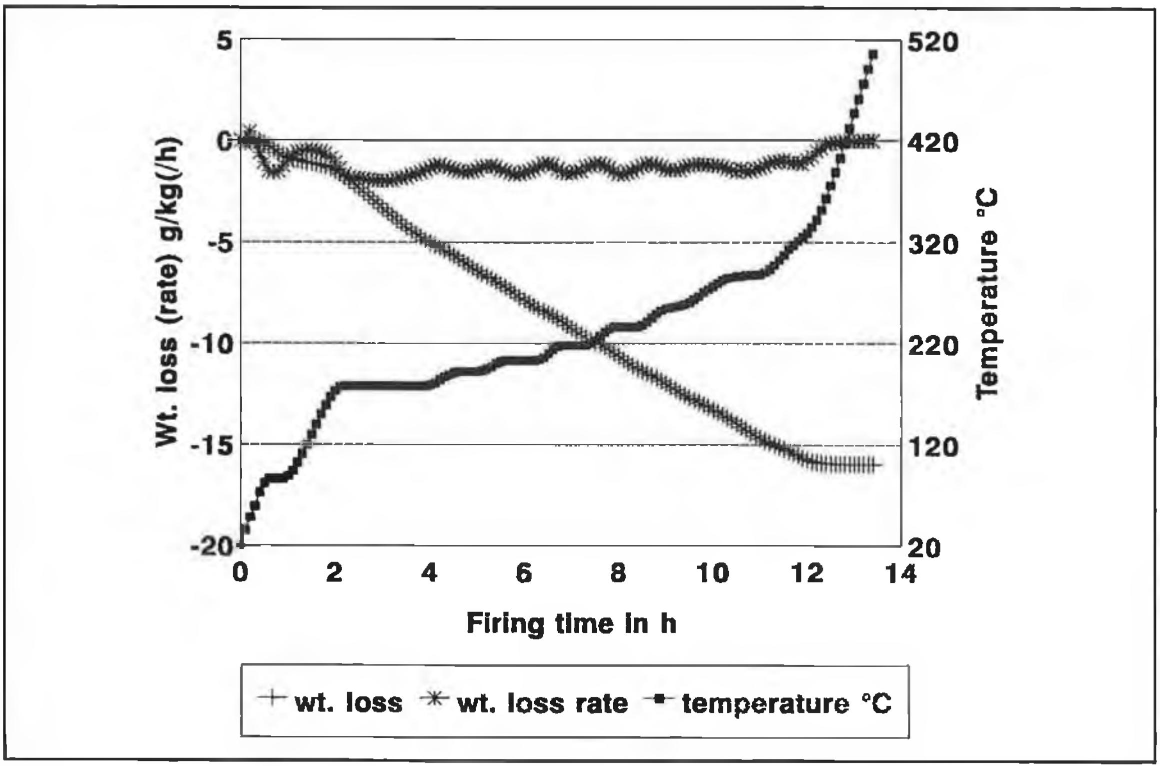

Figure 4.6 Weight loss, weight loss rate and temperature curves for weight loss rate limit 1.5 g/kg/h.

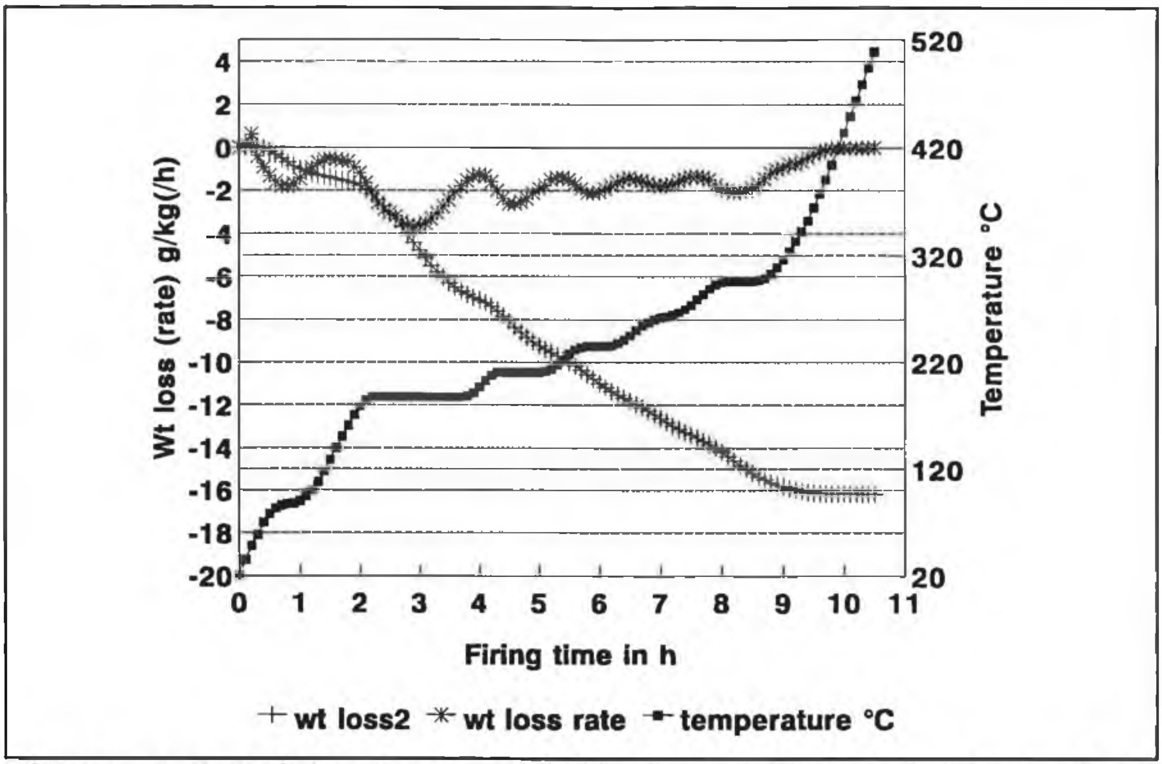

Figure 4.7 Weight loss, weight loss rate and temperature curves for weight loss rate limit 2 g/kg/h.

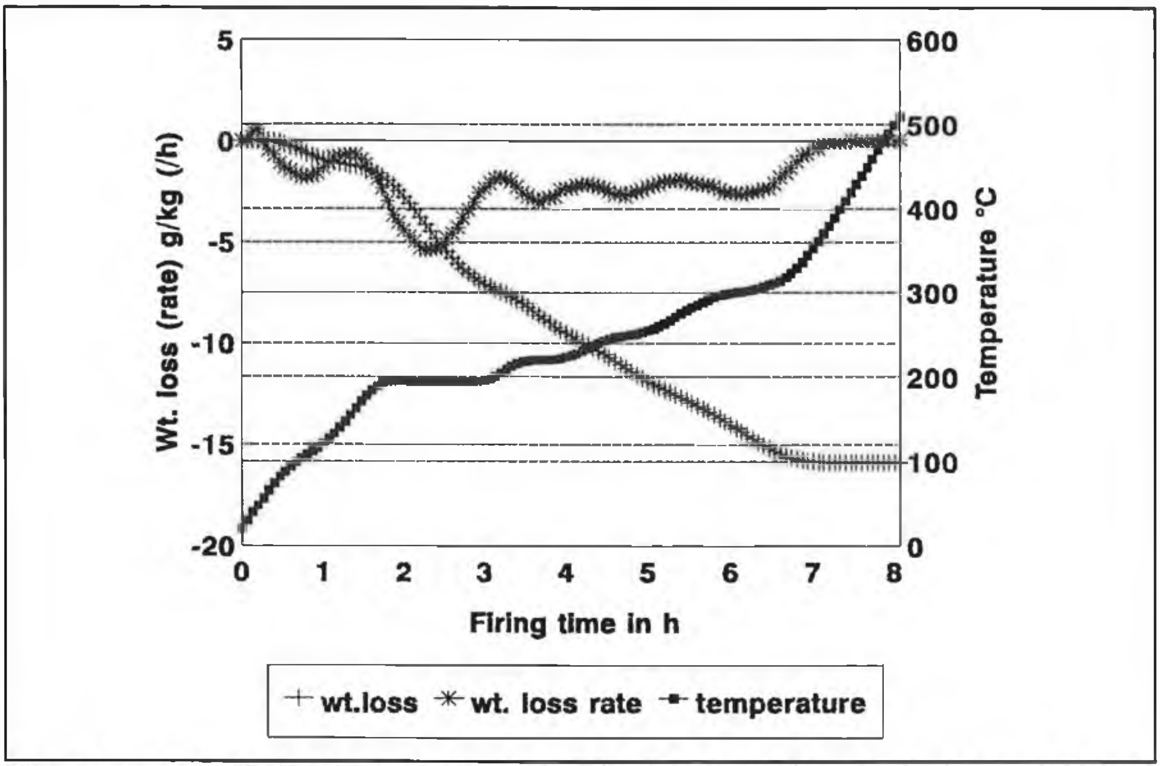

Figure 4.8 Weight loss, weight loss rate and temperature curves for weight loss rate limit 3 g/kg/h.

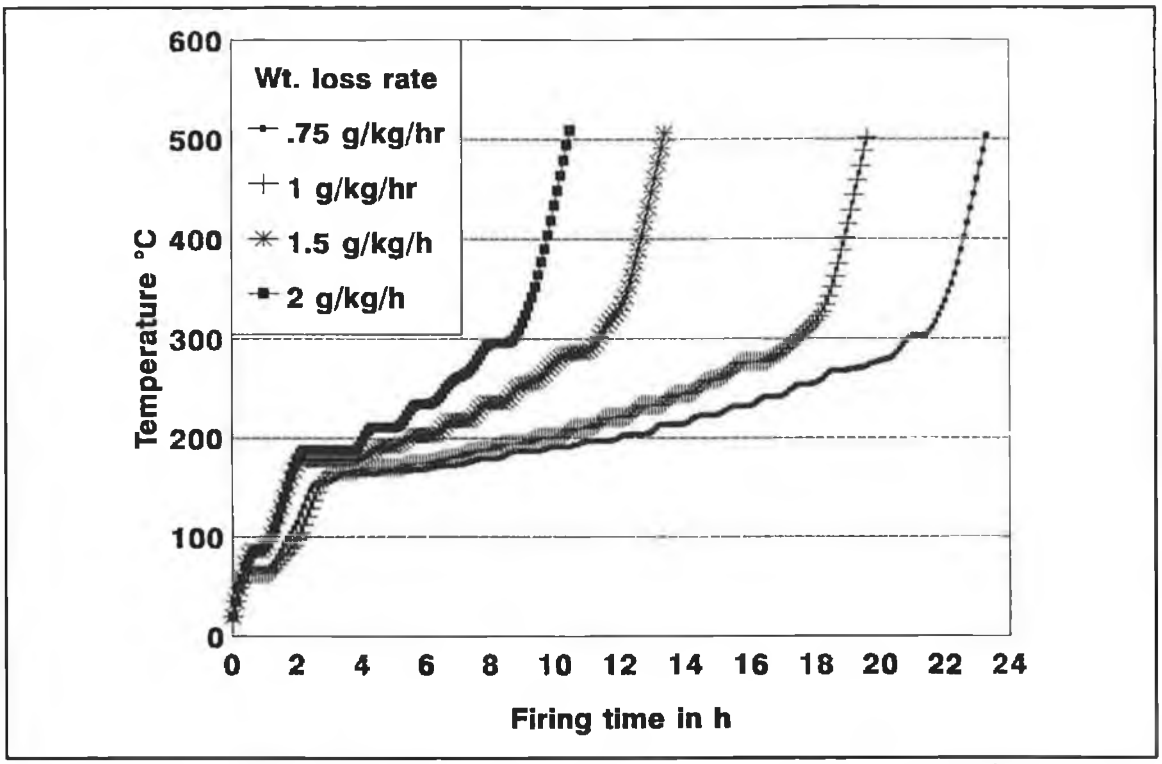

Figure 4.9 Comparison of the temperature profiles for different weight loss rate limit

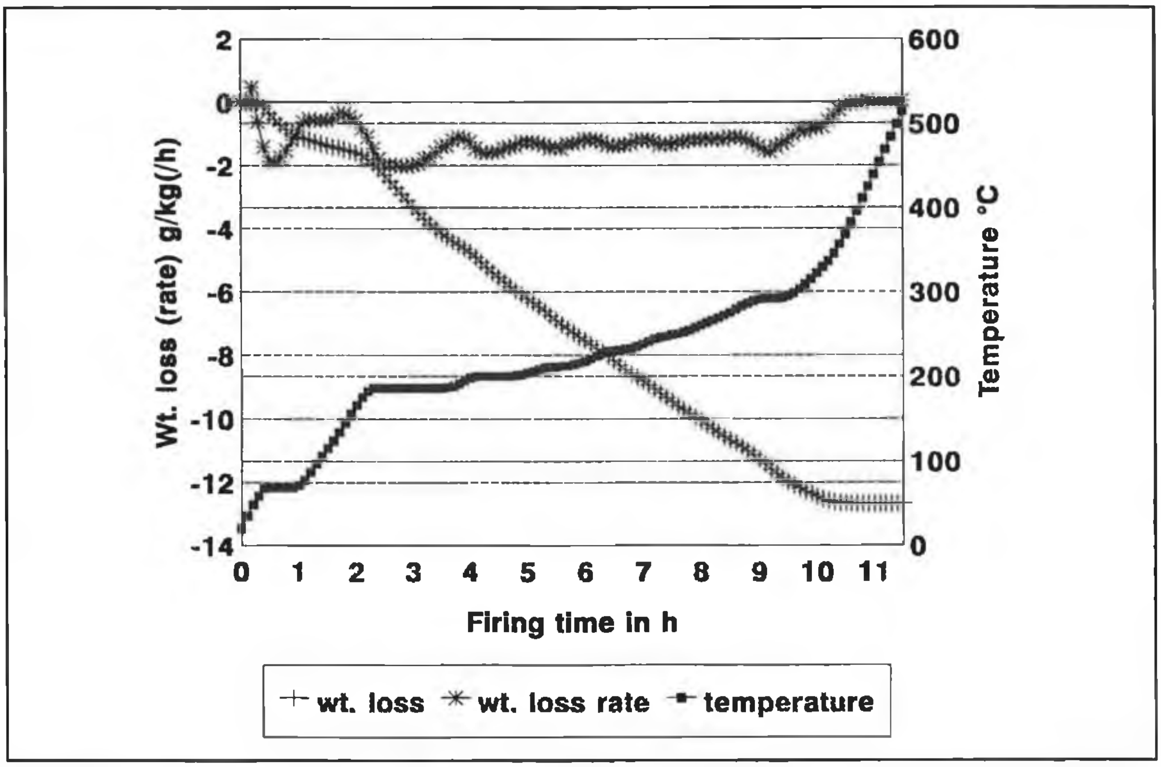

Figure 4.10 Weight loss, weight loss rate and temp. curves for the disc of l/d ratio=42/38 using 1.5 g/kg/h.

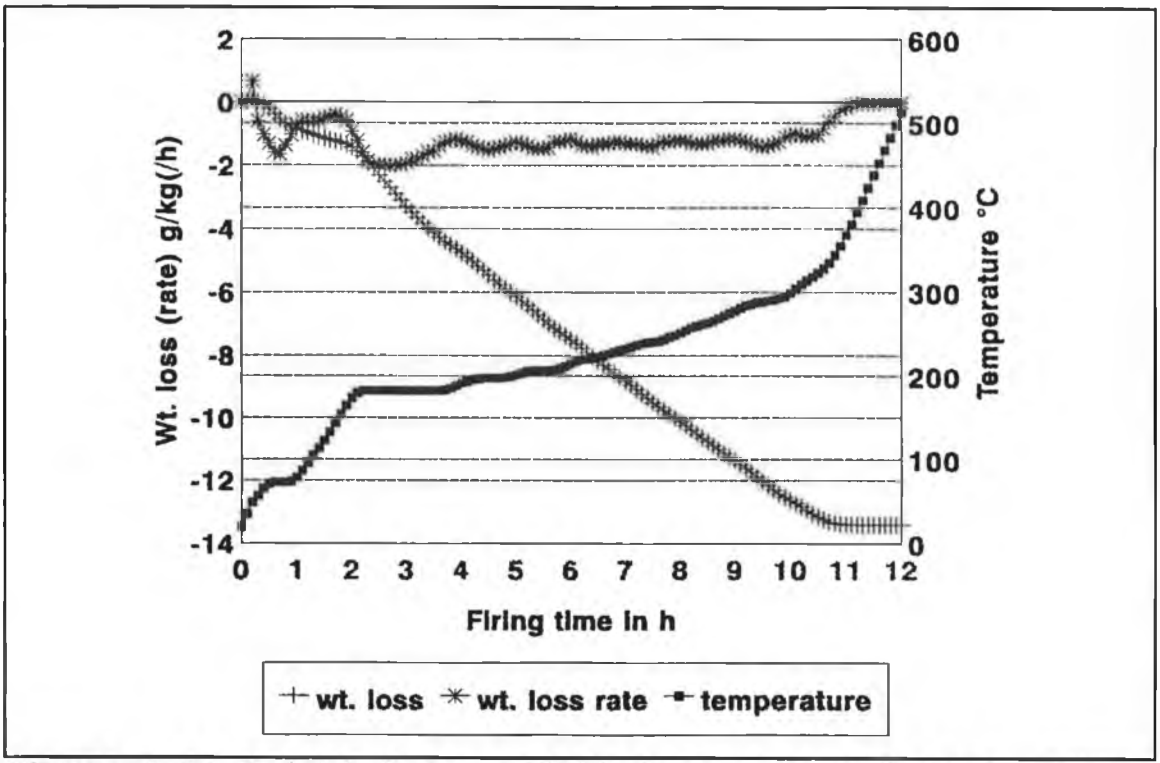

Figure 4.11 Weight loss, weight loss rate and temp. curves for the discs of l/d ratio=22/73 using 1.5 g/kg/h.

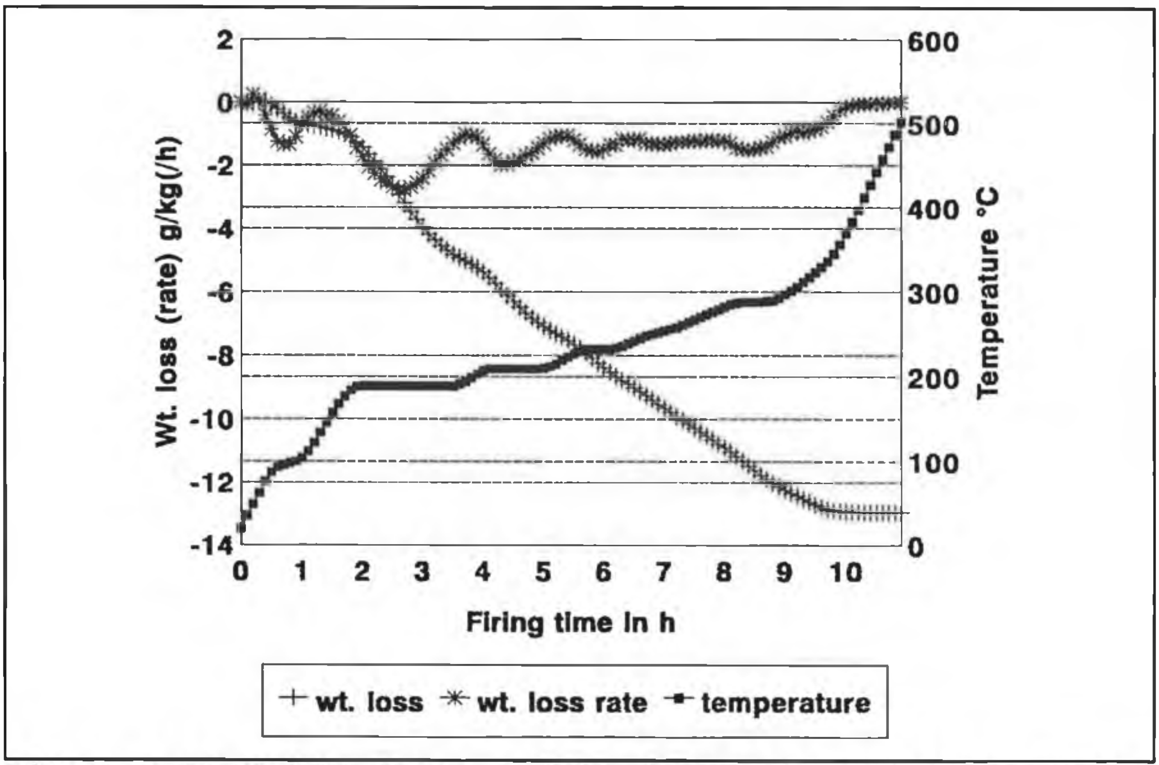

Figure 4.12 Weight loss, weight loss rate and temp. curves for the discs of l/d=50/38 using 1.5 g/kg/h

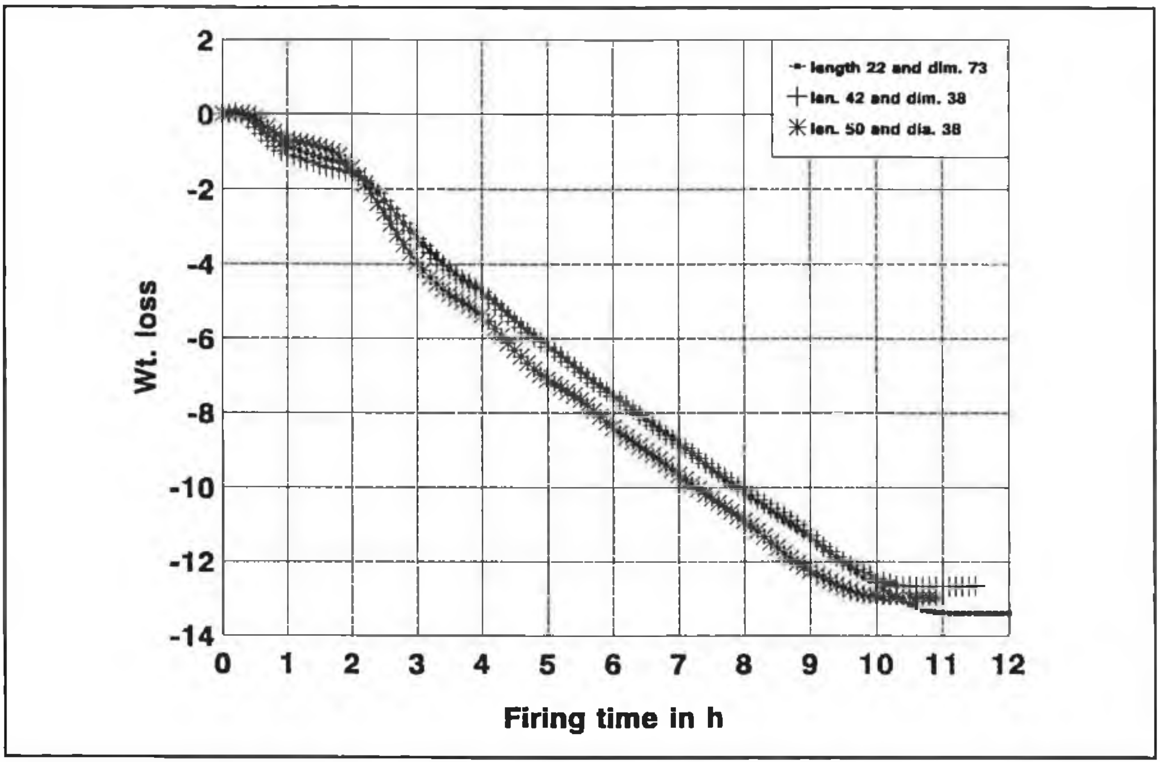

Figure 4.13 Comparison of the weight loss curve for the different sizes of discs with wt. loss rate limit 1.5 g/kg/h.

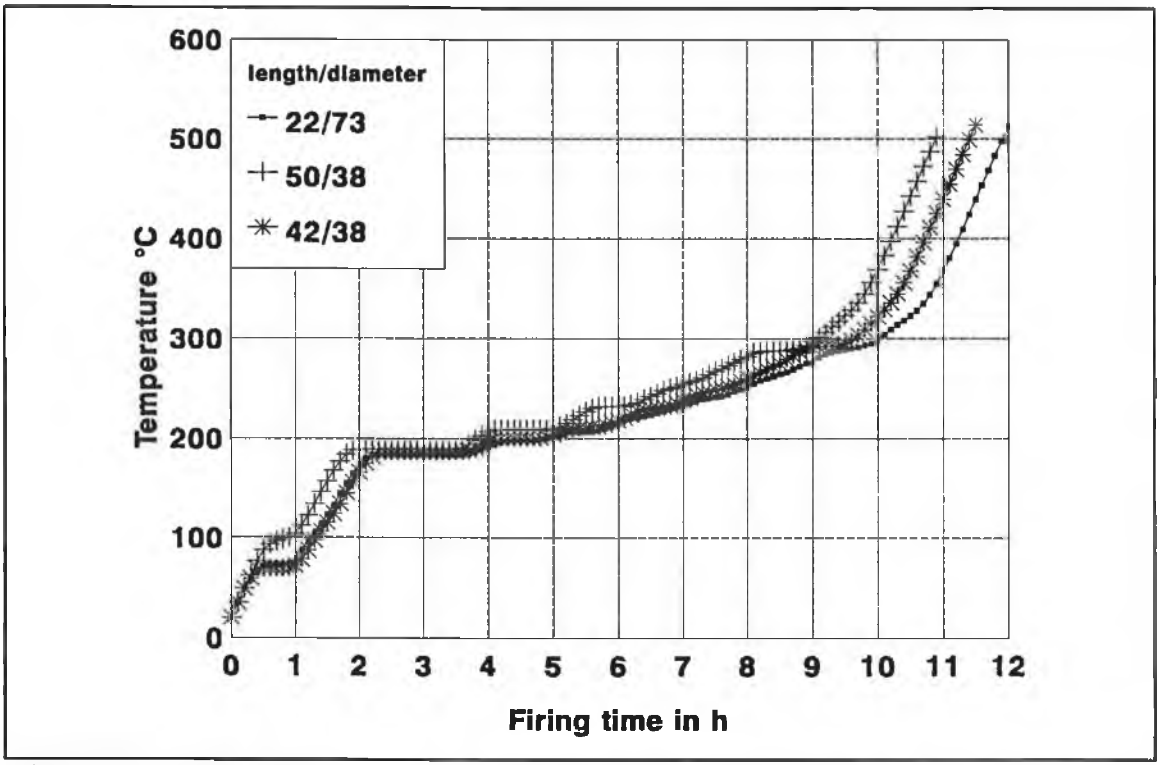

Figure 4.14 Comparison of temperature profiles for the different sizes of discs with wt. loss rate limit 1.5 g/kg/h.

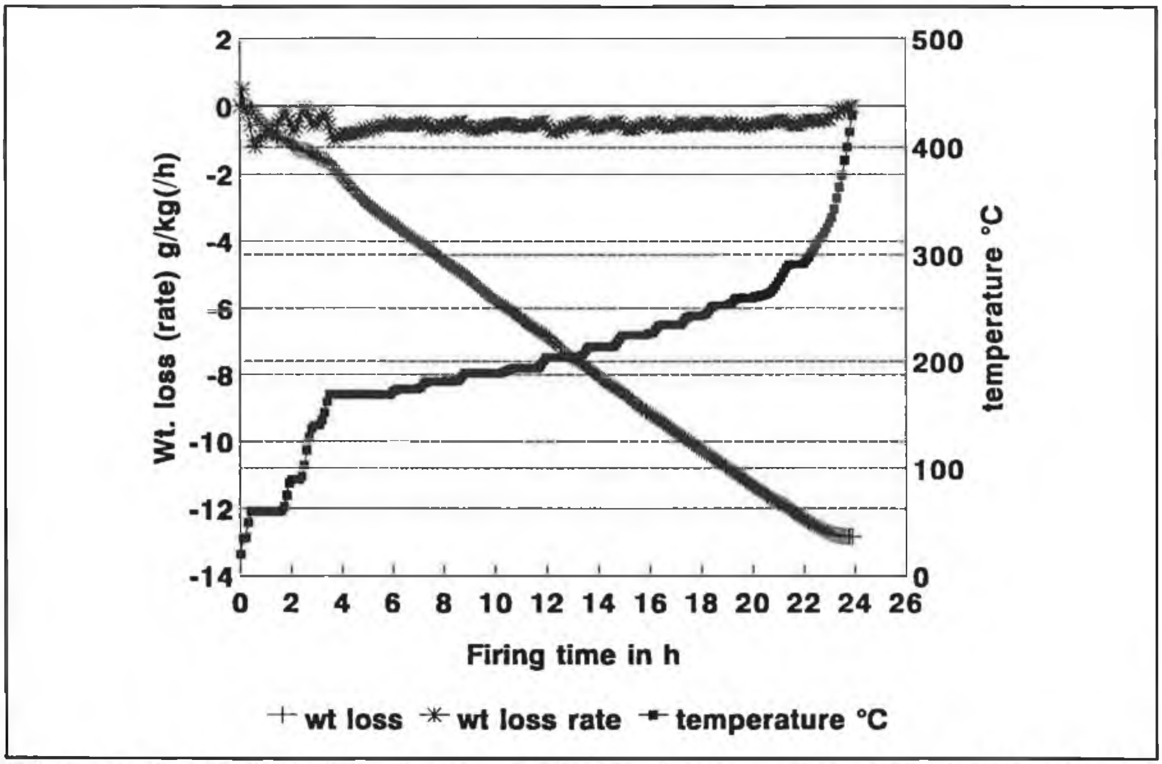

Figure 4.15 Weight loss, weight loss rate and temperature curves for wt. loss rate limit 0.56 g/kg/h

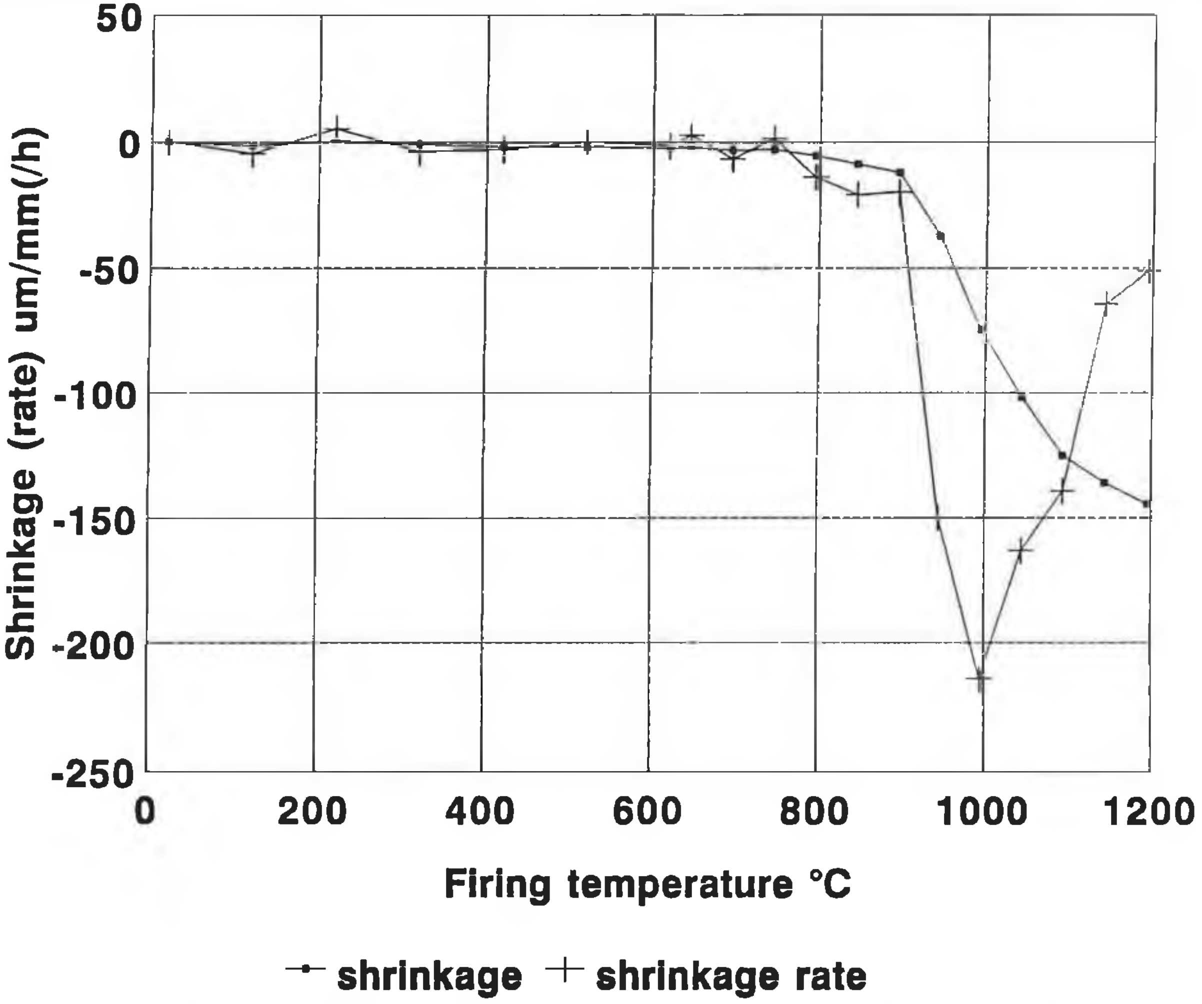

Figure 4.16 Shrinkage and shrinkage rate curves vs. firing temperature for the heating rate of 5 °C/min.

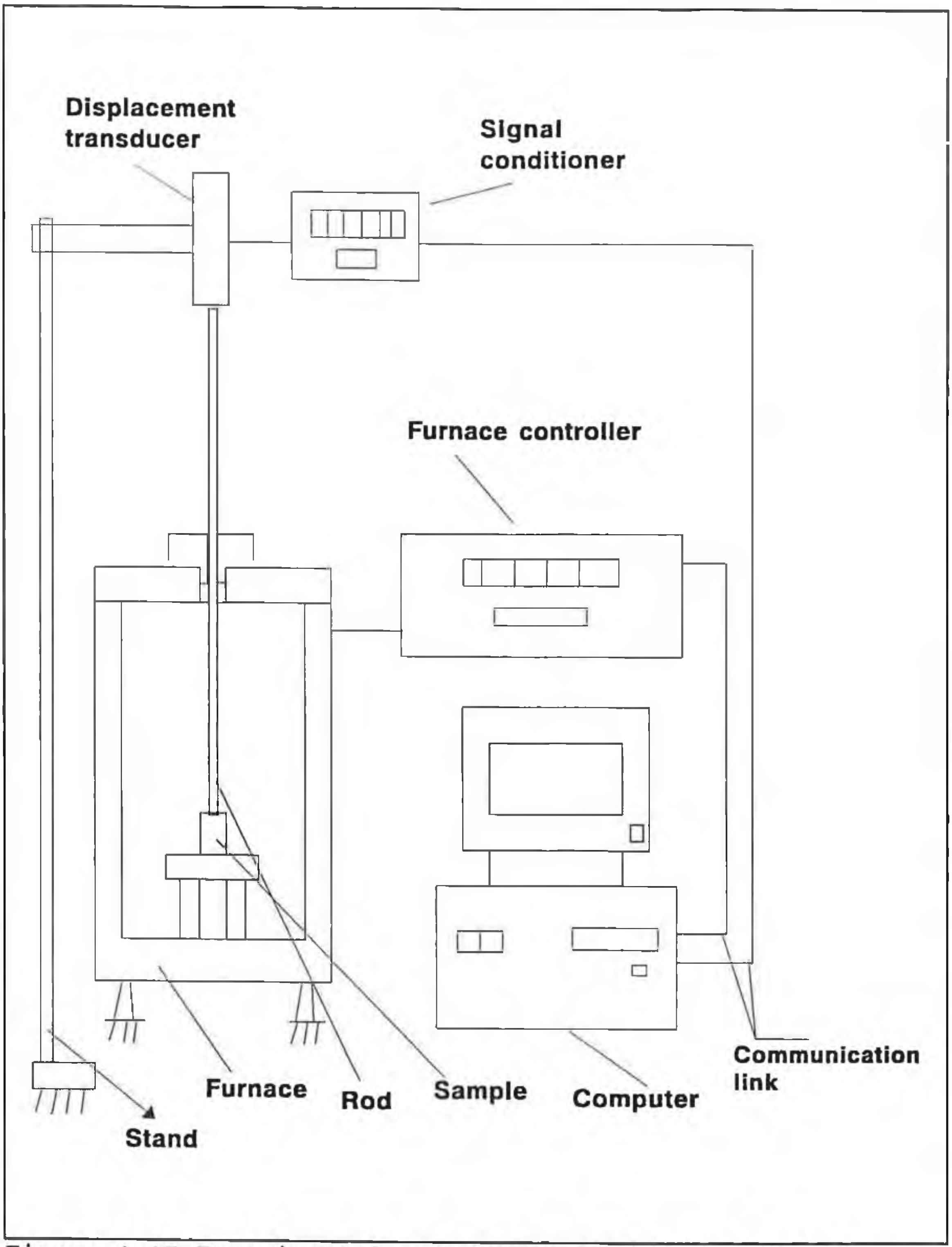

Figure 4.17 Experimental set up for shrinkage control

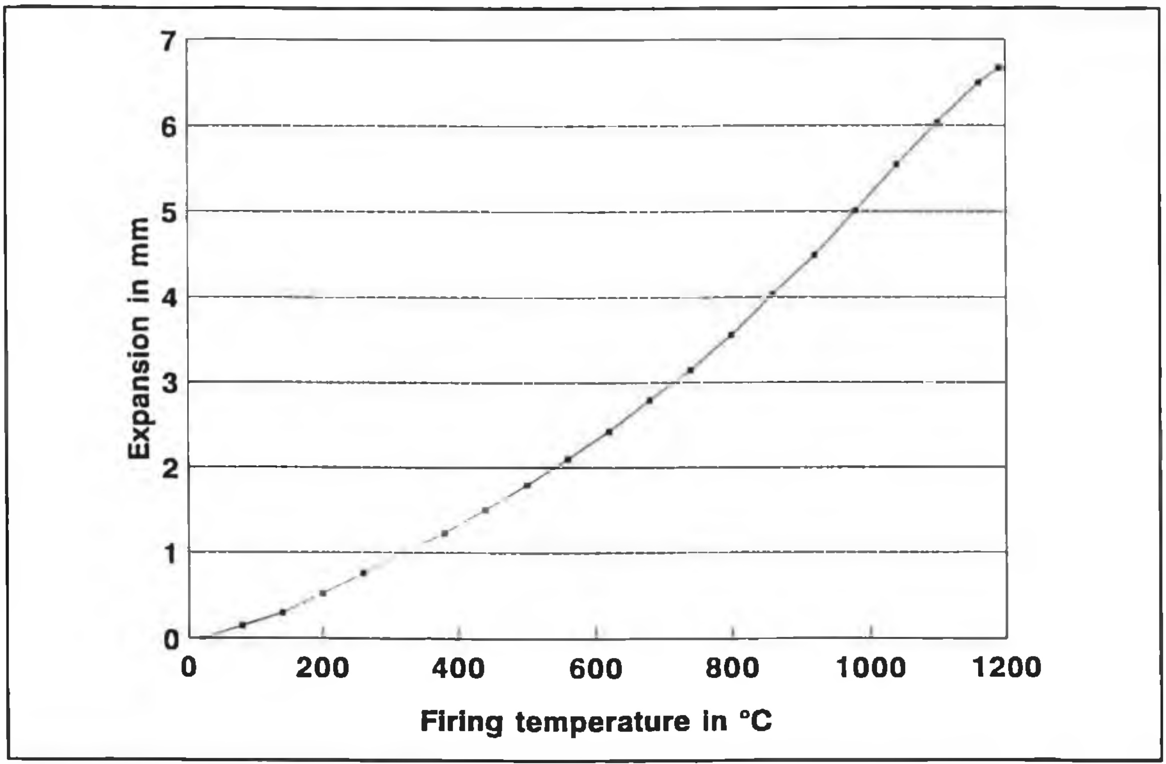

Figure 4.18 Expansion of the unit for callibration

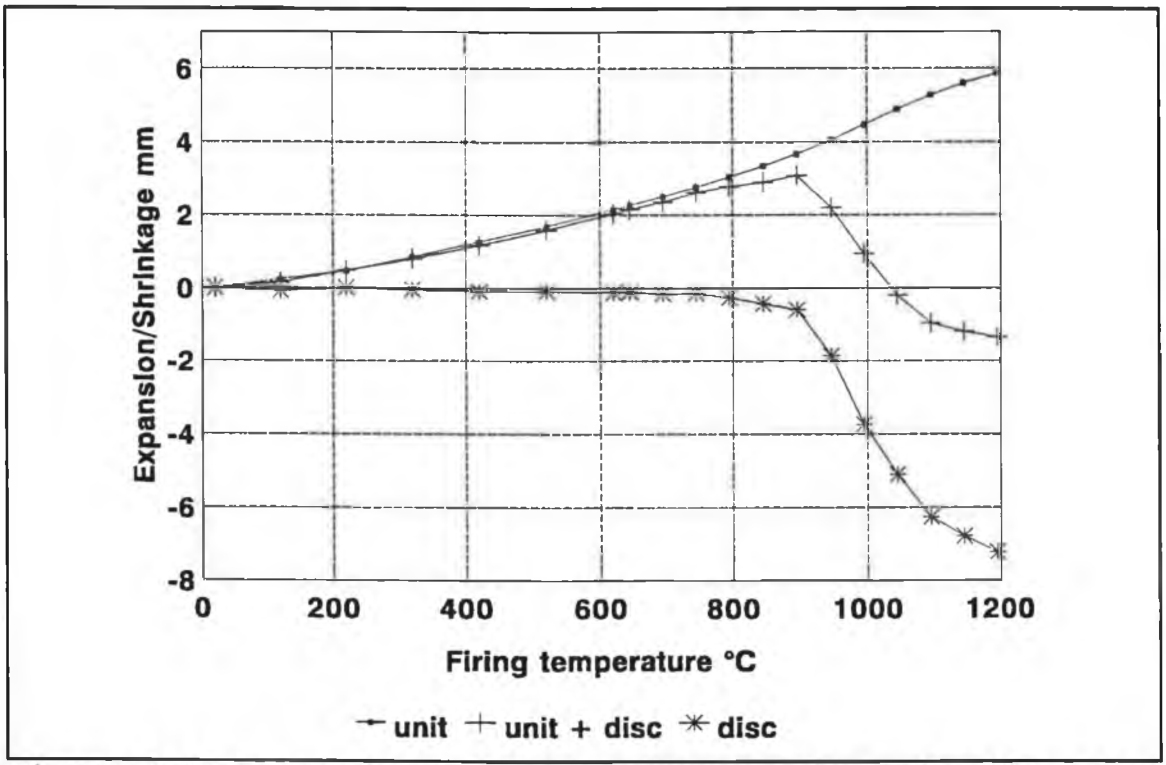

Figure 4.19 Expansion and contraction of the unit with green disc

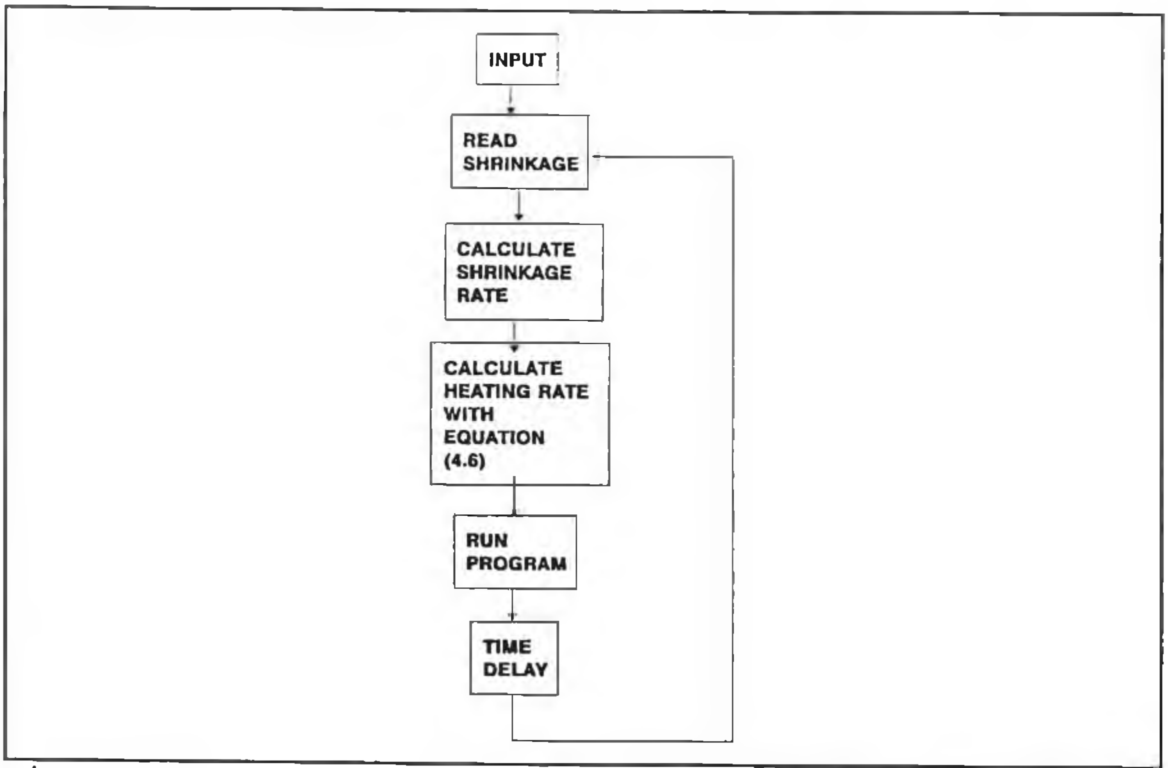

Figure 4.20 Flow chart of the software for controlling the shrinkage of the disc.

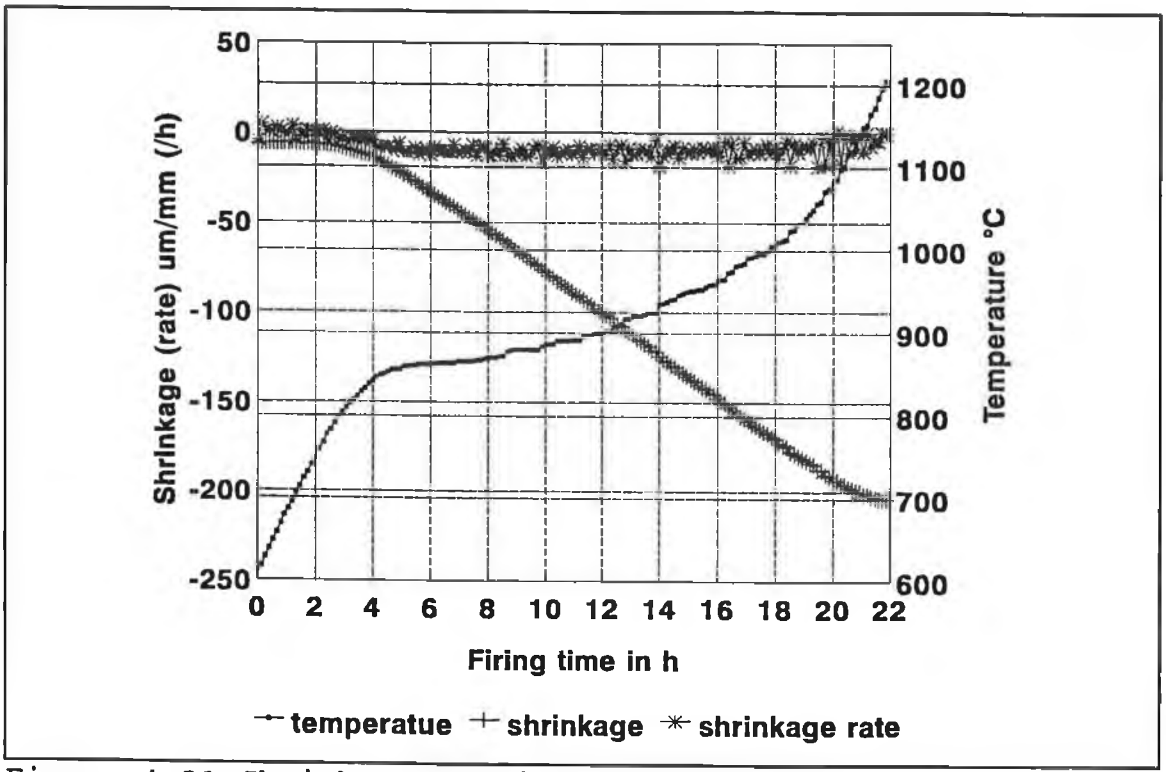

Figure 4.21 Shrinkage, shrinkage rate and temperatue curves shrinkage rate limit 10 $\mu m/mm/h$.

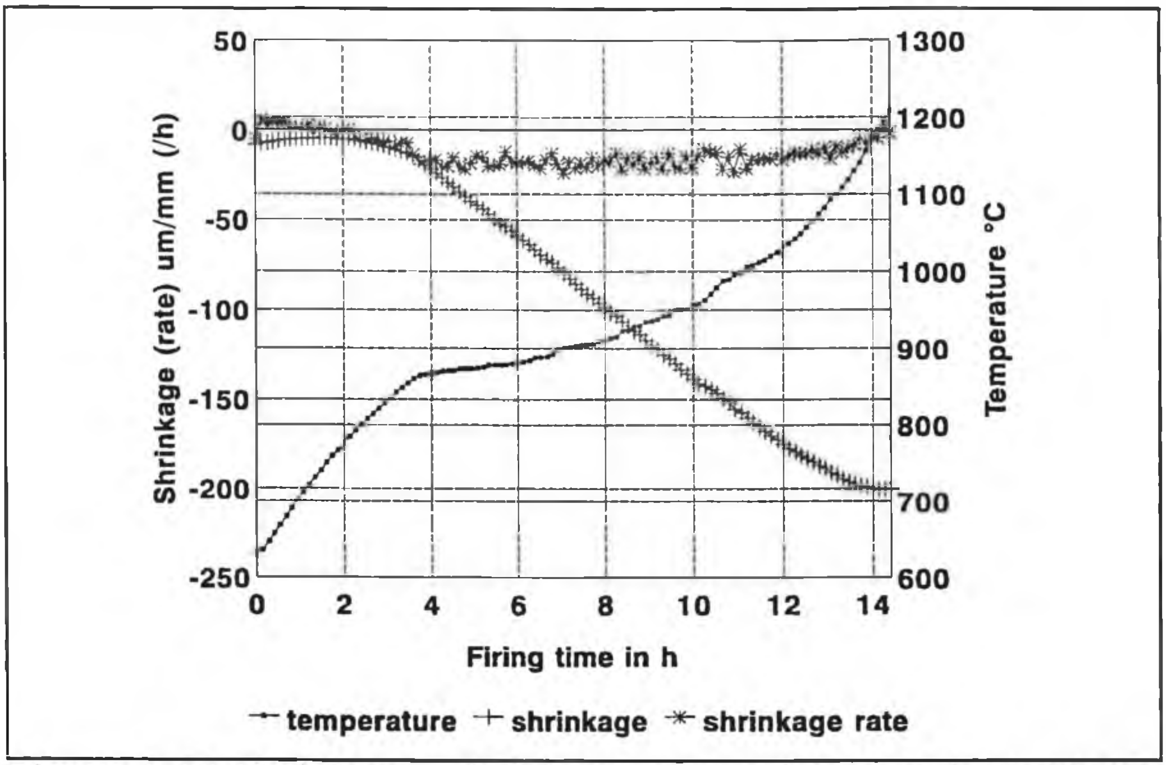

Figure 4.22 Shrinkage, shrinkage rate and temperature curves for shrinkage rate limit 20 μm/mm/h.

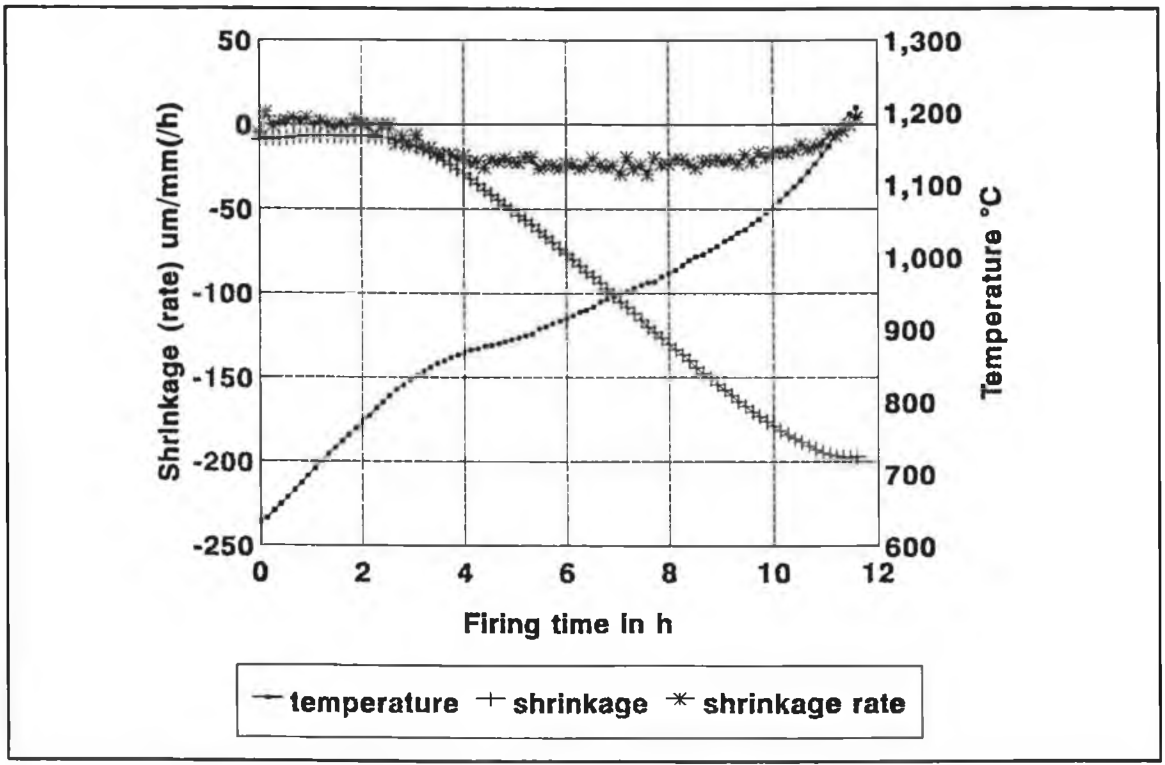

Figure 4.23 Shrinkage , shrinkage rate and temperature curves for shrinkage rate limit 30 μm/mm/h.

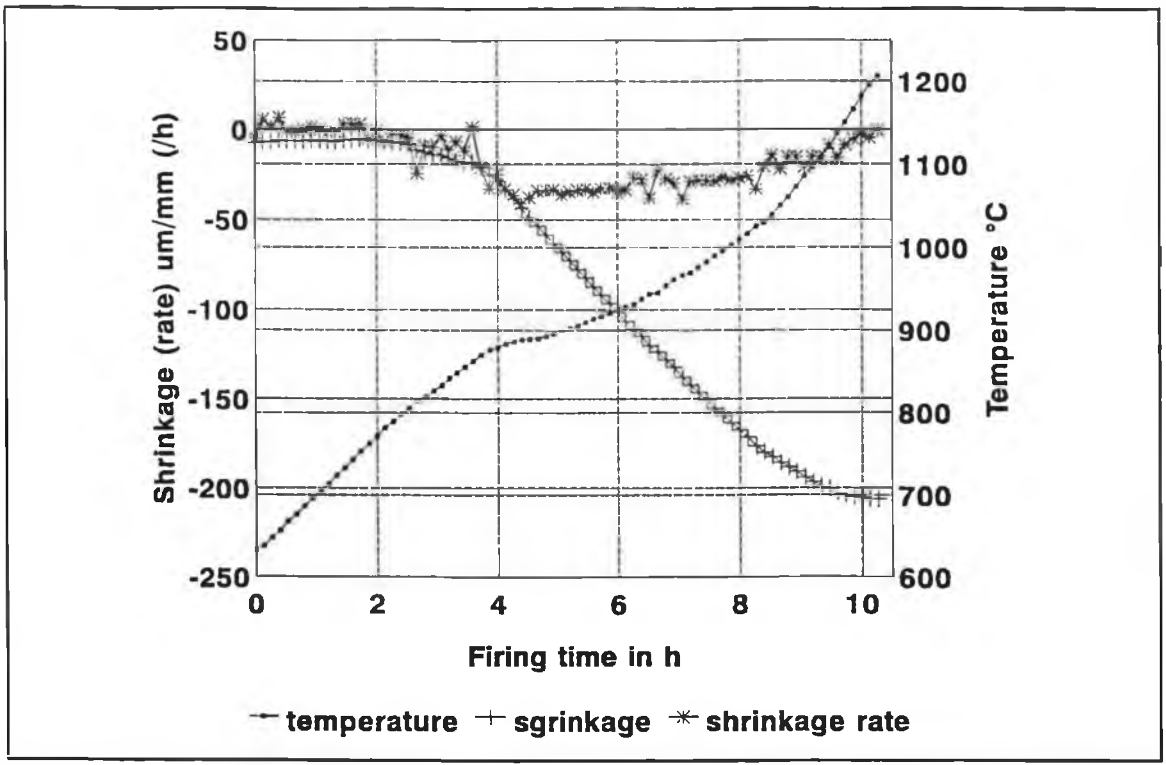

Figure 4.24 Shrinkage, shrinkage rate and temperature curves for shrinkage rate limit 40 μm/mm/h.

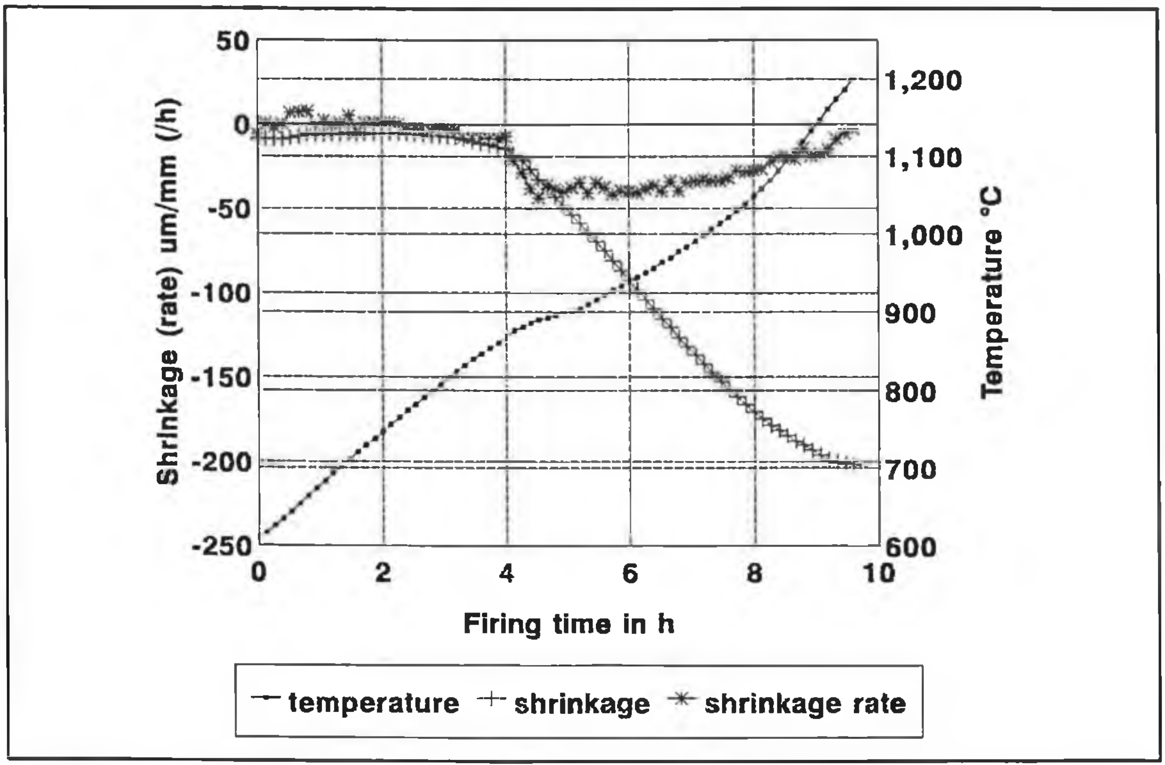

Figure 4.25 Shrinkage, shrinakge rate and temperture curves for shrinkage rate limit 53 μm/mm/h.

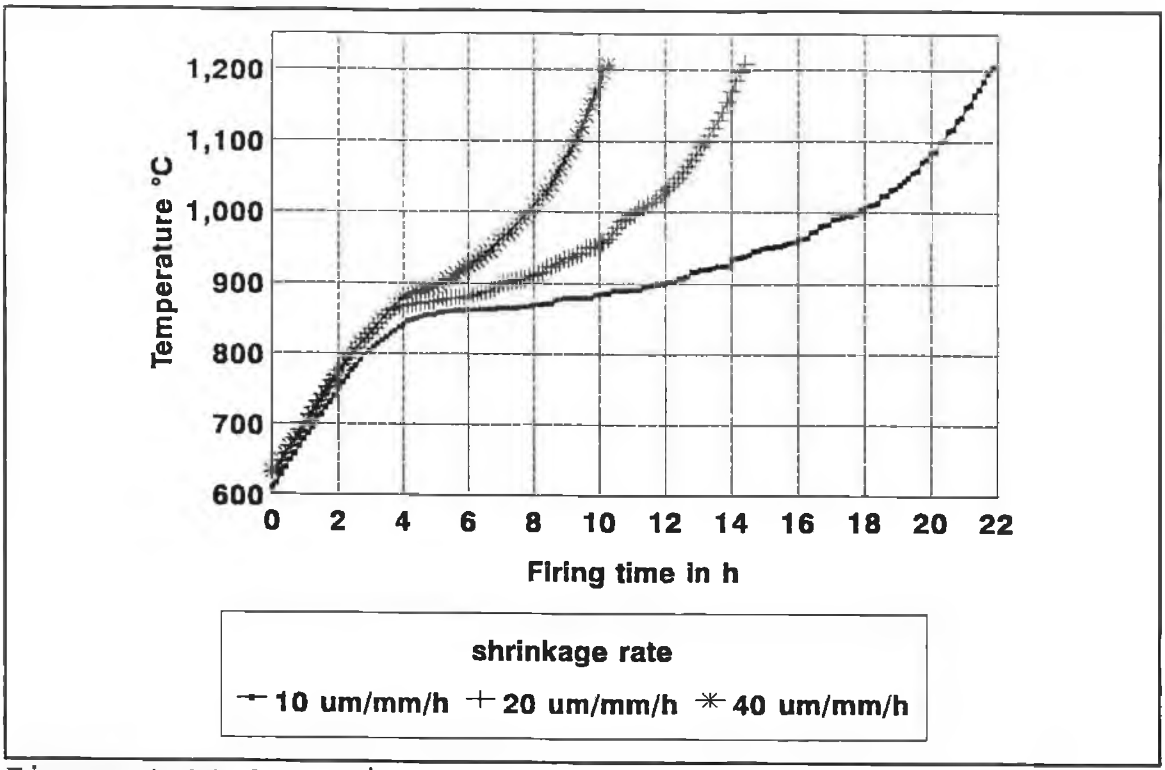

Figure 4.26 Comparison of the temperature profiles for the different shrinkage rate limit.

CHAPTER FIVE

CHARACTERISTICS OF VARISTORS AND PERFORMANCE EVALUATION

5.1 INTRODUCTION

Varistors are essentially evaluated by their electrical properties. Their main electrical properties are V_{nom}, I_R value, clamp ratio, nature of V-I curve and energy absorption capability. The electrical properties depend on the ceramic microstructure of the varistors. Further details on the properties of zinc oxide varistors and their electrical characterization can be found in reference [94]. The electrical properties and microstructure of the samples which were obtained through rate controlled sintering has been analyzed for discs of 42 mm diameter with V_{nom}=5 kV.

5.2 ELECTRICAL CHARACTERISTICS

To study the effect of rate controlled sintering on the varistor electrical characteristics, the samples were sintered using different rate controlled sintering profile and tested electrically to know the improvement of the process. The electrical property has been improved using firing profile through rate controlled sintering.

5.2.1 Samples Preparation

Figure (5.1) shows the different steps for manufacturing the varistors. For doing the experiment, Green discs were collected from the production line. Six different temperature profile were used for sintering, five profiles from rate controlled sintering and the conventional profile as control. The rate controlled sintering profiles were chosen to see the combined effect of binder burnout rate and shrinkage rate. Table (5.1) shows the profile number, weight loss rate, shrinkage rate and total firing cycle time of the above six firing profiles.

Table 5.1 Firing profile numbers with weight loss rate and shrinkage rate and total firing time

Profile number	Weight loss rate [g/kg.hr]	Shrinkage rate [μm/mm.hr]	Total firing cycle time [hrs.min]
1	0.75	10	64.27
2	3	10	49.11
3	0.75	40	53.29
4	3	40	38.13
5	1.5	20	47.42
6 (conventional profile)	-	-	69.15

The complete sintering profile for the rate controlled sintering and conventional profile were shown in figures (5.2), (5.3), (5.4), (5.5), (5.6) and (5.7) as denoted by profiles numbers 1, 2, 3, 4, 5 and 6 respectively. Every time 40 discs were sintered in a pot kiln at the Development Facility of Harris Ireland using each one of the above sintering cycles.

Grinding: After sintering, the black discs were ground the top and bottom surfaces as they were not smoothed. The grinding was done by the diamond cutter with the accuracy of 0.0001 inch deviation of the cutting plane.

Ultrasonic Wash: After grinding, the samples were passed through an ultrasonic cleaner. The cleaning was carried out by cold water. The samples were placed on the rack of the rotating belt. First the samples were washed and then dried with a hot air jet. During washing, the samples were vibrated minutely and thus cleaned properly with water. At the end of cleaner, the samples were 100% inspected. Normally, there are two types of problem that can be seen here. One is bad edges and other is chips. Since the black discs are brittle, the edge of the samples sometimes showed rough, and broken down. The samples containing bad edges or chips were reground if the height of the chips or bad edges were not so high as after regrinding the length of the samples were within the standard limits. The standard height for this sample is 42 ± .75 mm.

Electroding: The next operation is electroding (coating with aluminium). The electroding was carried out by spraying aluminium particles on top and bottom faces of the discs by an automatic machine. Electroding is the crucial step for preparing the samples.

Buffing: The surfaces become rough after electroding. For proper working of the product, these surfaces should be cleaned. So after aluminium spraying, all the samples were cleaned by a grinding wheel which contains wool on the grinding surface by holding the sample against the wheel manually. This operation is called buffing.

Rewash: As during buffing the surfaces becomes full of dust, these are again washed by the ultrasonic bath and checked again whether the surfaces are properly electroded and cleaned. Normally all samples pass after rewash if electroding was done properly. **Glassing:** The last stage for preparing the samples for electrical test is glassing. The side surface of the varistor block must be passivated to avoid flashover, i.e. the dielectric breakdown of the block surface-air interface. Passivation is achieved by coating the blocks with a glass coating. First the samples were preheated in a furnace and passes through the spray booth. As the sample crosses the spray booth, automatically glass were sprayed by the spray gun. After this, the samples were passed to the main oven to fire the glasses. Plate (5.1) shows chips, bad edge quality, bad electroding and non uniform diameter of the varistors.

5.2.2 Electrical Test and Results

Electrical test: The samples were classified into two groups. 24 samples were taken for the strength testing and 8 samples were used further electrical characterization. The strength test was carried out using a HAEFELY generator. During this test, the energy absorption capability of the disc was measured by passing a determined electrical energy through the samples. The product which absorbs more energy without failure, represents the better product. A current pulse of square wave form was passed through the samples for 2 mili seconds three times (three shots test). The electrical energy was increased with increasing the charging voltage. The initial charging voltage was selected in such a way that at first shot there should be no failure. It was found that 22 kV was a suitable initial charging voltage. For each consecutive test, the charging voltage was increased by 1.2 kV. During each shot, the sample temperature increased significantly due to the electrical energy being absorbed. Before the subsequent shots, the samples were cooled down using an electric fan and this process continued up to the complete failure of the lot. Normally the initial energy was exhibited 108 j/cc and with each consecutive shots, it was increased by 14-15 j/cc. Figure (5.8) shows the testing procedure of the strength testing. This test is a time consuming process. If the equipment was available, then in a day only a maximum of 4 shots could be done and to complete this test for one type of sample, 4 to 5 days were needed. The energy was calculated by

$$E=K.\ V.\ I.\ t \tag{5.1}$$

where E is expressed as joules, K is a constant, it's value is 1.14 for square wave, V is the voltage in volts, I is the current in amperes and t is the time in secs. The energy absorption capability E_c was calculated by

$$E_c=\frac{E}{V} \tag{5.2}$$

where E_c is expressed as joules/cc and v is the volume of the disc.

Results: The percentage of cumulative failures of all types of samples can be seen in figure (5.9). It is seen that the samples which fired with number 1 profile i.e. profile for binder burnout rate 0.75 g/kg/h and shrinkage rate 10 μm/mm/h show the highest electrical energy absorption capability. The first failure occurs at 267 j/cc. Normally in the present situation the absorption energy of the disc is considered 100 j/cc. Research is going on to improve this absorption energy capability. The starting failure for number 6 (conventional profile) curve is 122 j/cc whereas curves for No. 2, 3, 4 and 5 show the improvement of the absorption capability of the products. So the rate controlled sintering improve the energy capability of the product. The initial failure of no. 2 curve is 149 but the initial failure for no. 3 and 4 are 232 and 200 j/cc. It indicates that by increasing the binder burnout rate, the absorption capability of the product is negatively affected. It is better to use a profile generated by very low weight loss rate.

One thing can be noticed, especially for no. 2, 3 and 4 is that, when samples starts to fail, the slope of the curve is very steep. Since the condition of the samples deteriorates with each shot, the increase of charging voltage for the consecutive shots is taken the same for all types of samples. A replication was done for no. 1 and no. 6 profile by taking samples of different powder lots. The results can be seen in figure (5.10). Here we can see also, the failure starts for no. 1 at 248 j/cc. So a product can be made with 200 j/cc by this no. 1 profile. The curve for replication of no. 6 is shifted right side showing improvement of the product. This could be a kiln effect. Because the samples for the replication of no. 6 were sintered in a different kiln (the same one, used for no. 1, 2, 3, 4 and 5) than the original no. 6. The types of failure is also recorded. This will be discussed later.

Electrical characteristics test: The varistors were characterized at low, medium and high current. The low current characteristics (mA's) of a varistor block are associated with the leakage currents. The medium currents are in the working range of the blocks, usually from a few hundred amperes up to 5 k or 10 kA depending on the block type. The high current properties of the block will give a measure of their power withstand capability. The leakage currents were measured using the watt loss tester. The

HAEFELY strength tester was used to measure the energy capability of the blocks when subjected to long duration square impulses. The high current region was characterized using the high amplitude short duration tester (HA-SD test). For the 42 mm blocks, the peak current amplitude was 100 kA. This region represents the power limiting condition for protection from high-current spikes as those generated by lightning strikes.

In the watt loss tester, one sample was placed each time in the measuring chamber and electrical pulses with peak currents of 100 μA, 500 μA, 1 mA and 5 mA were given to the sample at room temperature and the corresponding peak voltage was recorded from the display. The watt loss was also measured at a peak voltage for currents 100 and 500 μA and 80% of peak voltage at 5 mA.

For the 100 A and the 10 kA tests, the samples were placed in a fixture at the base of the classifier. The charging voltage was maintained at 29.9 kV and the charging time at 5 sec. The set up was different for the 100 A and 10 kA test. The results for 100 A were recorded from the display and voltage for 10 kA was marked automatically on the sample after correcting this voltage for an exact current of 10 kA. The 100 kA test is very critical, because at this test an electrical charge with very high frequency is passed through the disc for very short period as to simulate the test with an actual lightning strike which have very high frequency components and its duration is of the order of 4 μs. Two shots were given simultaneously with 8/20 μs pulse to the samples where 8 μs is needed for the peak and 20 μs is the decay time for 50% of the peak pulse. The shape of the test waves varies with the nature of application. For power apparatus 1.2/50 μs and 8/20 μs waveshapes are used whereas for communications equipments 10/560 μs waveshape is used [94]. Normally the short duration pulse is more detrimental than the long one and cracks of the samples are observed both longitudinally and cross wise.

Results: Figure (5.11) shows the V-I characteristics of the samples which were prepared using sintering profiles no. 1, 2, 3, 4, 5 and 6. All the curves at the leakage region coincide. So leakage is not affected by rate controlled sintering. Nevertheless, a better leakage is observed for lower nominal voltages. The V-I curve for profile no. 1 shows a better leakage than the others. In the varistor operating region, it is seen that the curves for profile no. 3, 4 and 5 coincide and no. 1 and 2 coincide but with higher voltage value. The V-I curve for profile no. 6 shows the highest voltage value. It is important to know the clamp value to see the improvement of the varistor. The clamp ratio is defined as the ratio of voltage at 10 kA and 5 mA. It is seen from the following table (5.2) that although the voltage at the varistor operating region for profile no. 1

Table 5.2 Voltage in kV at different currents and clamp ratio for each profile

Profile number	100 μA	500 μA	1 mA	5 mA	100 A	10 kA	100 kA	clamp ratio
1	1.26	6.39	8.80	9.30	11.59	16.48	28.07	1.77
2	1.41	6.62	7.89	8.72	11.19	15.93	27.55	1.82
3	1.50	6.94	8.15	8.90	11.44	16.2	27.87	1.81
4	1.43	6.92	8.61	9.28	11.72	16.55	28.43	1.78
5	1.29	6.29	8.07	8.80	11.16	16.05	27.46	1.82
6	1.36	6.62	9.09	9.60	11.95	17.18	29.2	1.78

and 6 are higher than that of profile no. 2, 3, 4 and 5, the clamp value shows the lower value. So for a better clamping, profiles no. 2 or 3 can be used.

The most desirable device should have a high value of nonlinear coefficient, a low value of leakage current, a long time stability life and a high energy absorption capability. Table (5.3) shows the values of nonlinear coefficient, nominal voltage, leakage current, life stability and energy absorption capability.

Table 5.3 Values of nonlinear coefficient, nominal voltage, leakage current, life stability and energy absorption capability for different firing profiles.

Profile Number	Nonlinear coefficient α	Nominal voltage C=V at 1 mA	Leakage current I_R	Life $P_G < P_D$	Energy Absorption j/cc
1	29.12	8.80	0.022	pass	267
2	16.09	7.89	0.0494	pass	149
3	18.28	8.15	0.0461	pass	232
4	21.47	8.61	0.031	pass	200
5	18.58	8.07	0.0274	pass	197
6	29.48	9.09	0.0271	pass	122

The nonlinear coefficient was calculated by equation (2.2) where I_2 and I_1 are 5 and 1 mA respectively and V_2 and V_1 are corresponding to I_2 and I_1.

No. 1 and no. 6 profiles show the higher value of nonlinear coefficient indicating a better device and a lower value of leakage current. It is needed to get a disc of higher energy capability and simultaneously withstand the high peak pulse for a μ sec. The discs sintered using profile No. 1 shows the higher energy capability, however its performance at HA-SD test does not show a significant improvement. This is because the failure mechanism is different as that observed with low amplitude- long duration pulses. The type of failure and failure percentage in HA-SD test is shown in table (5.4).

Table 5.4 Failure analysis in HA-SD test for the different firing profile

Profile number	No. of failure	% of failure	Failure pattern
1	2	22.22	mixed and long. crack
2	2	16.66	mixed split
3	0	0	no crack
4	2	18.18	mixed and long. crack
5	2	33.33	crack
6	1	25.00	crack

The above table (5.4) shows that the profile no. 3 is the best for making a sample of withstanding high amplitude-short duration pulses. So according to the application of the varistors both no. 1 and no. 3 sintering profile can be used. Plate (5.2) shows the failure pattern in HA-SD test.

The watt loss is presented in table (5.5). The lower value of watt loss is seen for profile no. 1. The low value is better showing less power loss. Normally the power loss data was taken at the 80% of the voltage at 5 mA before and after 100 kA test. Since after 100 kA test, there is a local charge redistribution, a higher watt loss value is desired. In the present data, the watt loss values were taken at three different currents but the watt loss value after 100 kA test was not measured.

Table 5.5 Watt loss (P_d) at 100, 500 μA and at 80% voltage of 5 mA

Profile number	P_d at 100 μA	P_d at 500 μA	P_d at 80% peak voltage at 5 mA
1	0.012	0.1408	1.7058
2	0.0119	0.3273	1.7179
3	0.0116	0.3206	1.7528
4	0.012	0.2146	1.7327
5	0.015	0.1726	1.71
6	0.0153	0.18	1.75

Table (5.6) shows the types of failure during strength (destruction) test. The good disc should not fail by flash over. But flash over may happen due to improper glassing, buffing and aluminium in chips during electroding. During flash over the electrical charge passes through the weak region of the product. A pin hole can be formed for various reasons. It may be a powder problem. If there are particulate contaminants in the powder, then pin hole occurs at the particulate position. If the spray

Table 5.6 Types of failure during strength test.

Profile number	Pin hole (PH)	Flash over (FO)	Puncture	FO+PH	FO+Punc.
1	1	1	1	8	9
2	3	1	1	14	3
3	9	0	0	12	9
4	7	0	0	13	4
5	5	3	0	5	11
6	9	2	3	7	3

dryer is not properly cleaned organic, particulates can contaminate the powder. It can also happen if the additives are not properly mixed during the milling operation. Plate (5.3) shows the failure of the disc for pin hole, flash over and puncture.

5.3 MICROSTRUCTURE ANALYSIS

The microstructure of the samples sintered with profiles no. 1, 2, 3, 4, 5 and 6 were analyzed by SEM. The secondary emission image (SEI) and backscattered electron image (BEI) of samples sintered with profiles no. 1, 2, 3, 4, 5 and 6 are shown in plates (5.4 a, b), (5.5 a, b), (5.6 a, b), (5.7 a, b), (5.8 a, b) and (5.9 a, b). In each plate the top photograph is taken by SEI and desinated as a and the bottom photograph is taken by BEI and designated as b. The BEI photograph is taken at the same place where SEI is taken. SEI photograph shows the topography of that place whereas the different phases of that place can be clearly seen by BEI photographs. The four basic compounds formed are ZnO, spinel, pyrochlore and several bismuth rich phases. The location of spinel and pyrochlore is the intergranular phase between the ZnO grains. Bi-rich phases exist mainly at the Triple point.

In plate (5.4 a, b), it can be seen that the grain size range is between 5 -20 μm (average 10 μm). Porosity is evenly distributed and is intergranular. The pore size is approximately 1-8 μm. Twinning is evident. Antimony spinel phase and glassy bismuth phase are visible with good distribution between the zinc oxide grains. The grain size range for plate (5.5 a, b) is between 3-20 μm (average 10 μm). The porosity content is low and intergranular. The pore size is approximately 1-4 μm. Twinning is evident in some grains. Antimony spinel phase and glassy bismuth phase are visible, however these phases are not evenly distributed between the zinc oxide grains, and can be seen that they are clumped together. In plate (5.6 a, b), it is seen that the grain size range between 3-20 μm (average 10 μm). Porosity content is low and primarily intergranular, pore size is approximately 1-4 μm. Twinning is evident in some grains. Antimony spinel phase and glassy bismuth phase are visible. However, in some areas these phases are not evenly distributed between the zinc oxide grains and can be seen that they are clumped together.

Grain size range in plate (5.7 a, b) is between 5-20 μm (average 12 μm). Porosity content is low and primarily intergranular, pore size is approximately 1-10 μm. Twinning is evident in some grains. Antimony spinel phase and glassy bismuth phase are visible. These phases are reasonably well distributed between the zinc oxide grains. Grain size range in plate (5.8 a, b) is between 5-15 μm (average 8 μm). Porosity is primarily intergranular with some intragranular. Pore size is approximately 1-5 μm. Twinning is evident in some grains. Antimony spinel phase and glassy bismuth phase are visible. These phases are reasonably well distributed between the zinc oxide grains. It is seen in plate (5.9 a, b) that the grain size range is between 5-25 μm (average 10 μm). It is very porous. Porosity is primarily intergranular with some intragranular. Pore size is approximately 1-20 μm. Twinning is evident in some grains. Antimony spinel phase and glassy bismuth phase are visible. These phases are reasonably well distributed between the zinc oxide grains.

In comparison the samples with firing no. 1 and no. 6 profiles, it is cleared why no. 1 gives the better energy capability than that of no. 6 which is very porous. Thus for improving the energy absorption capability of the product, the phases should be well distributed and porosity should be low and also distributed uniformly. The pore should be intergranular.

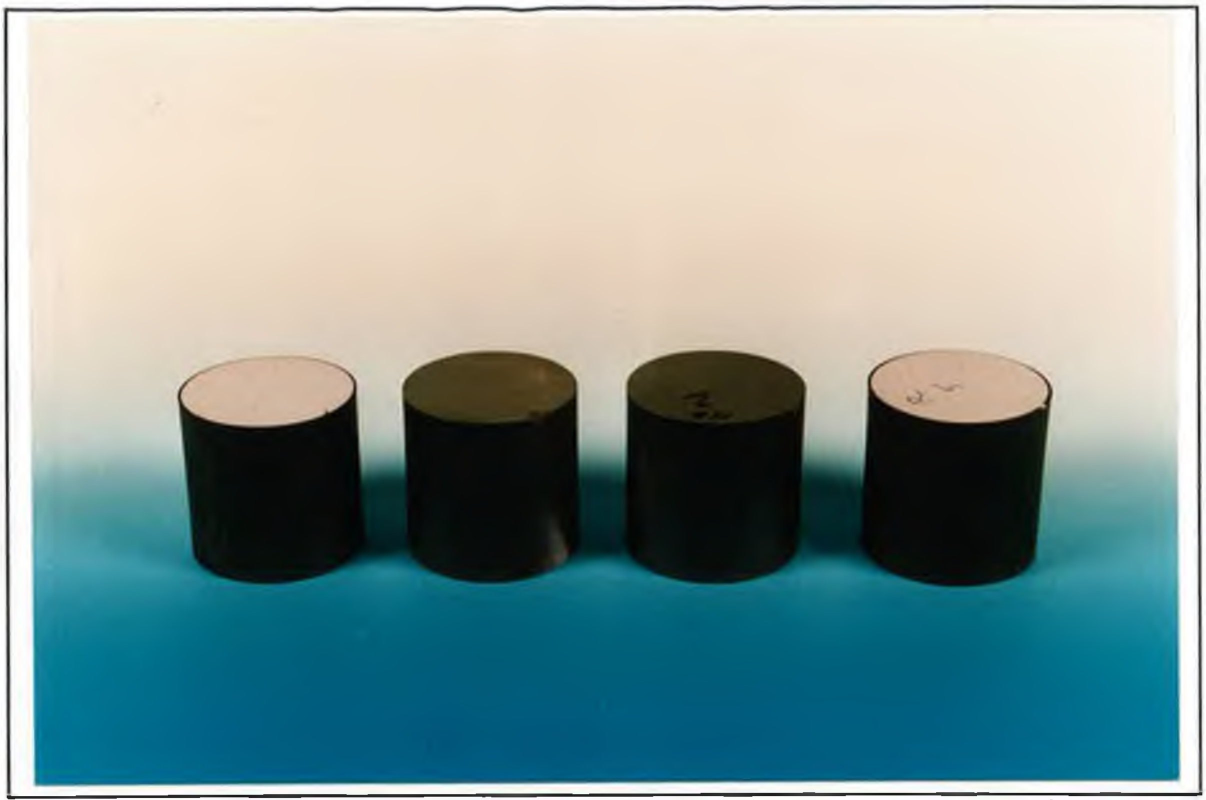

Plate 5.1 Photograph of rejected varistors due to chips, bad electroding and non uniformity.

Plate 5.2 Photograph of varistor's failure in HASD test.

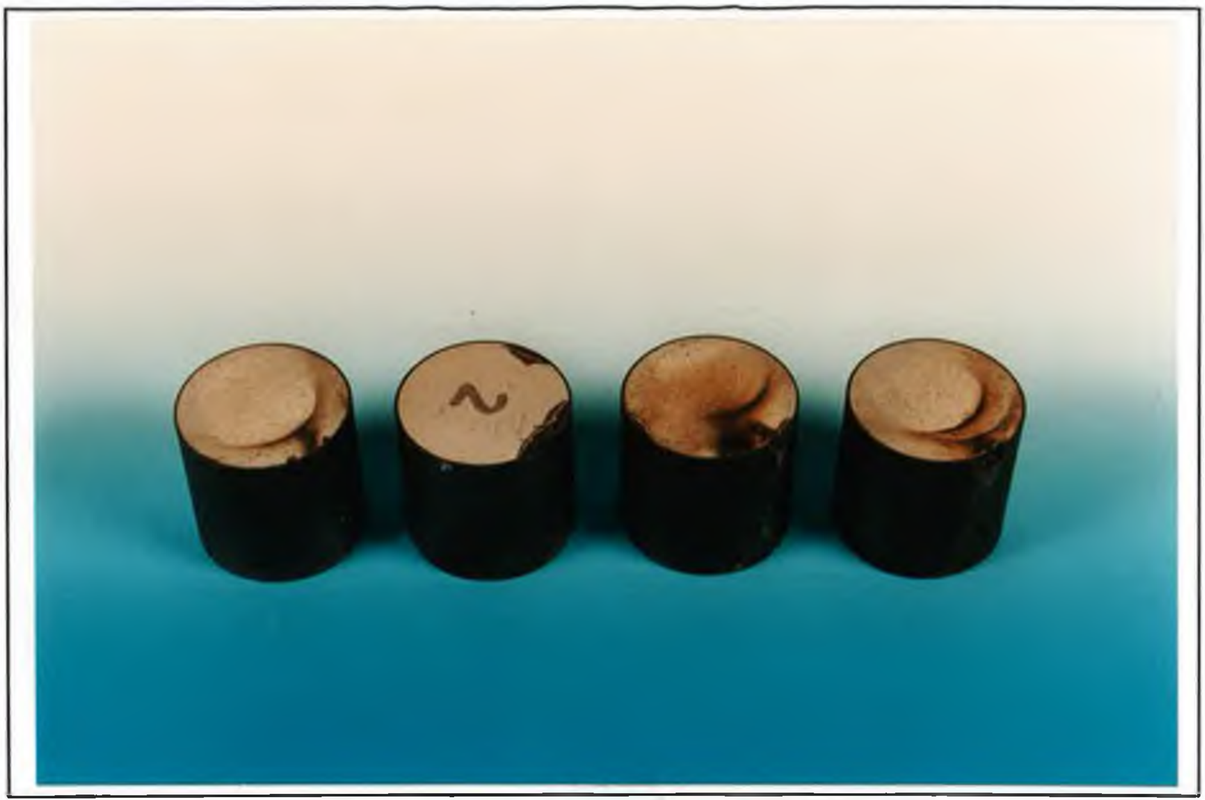

Plate 5.3 Photgraph of varistor failure due to pin hole, puncture and flash-over during strength test.

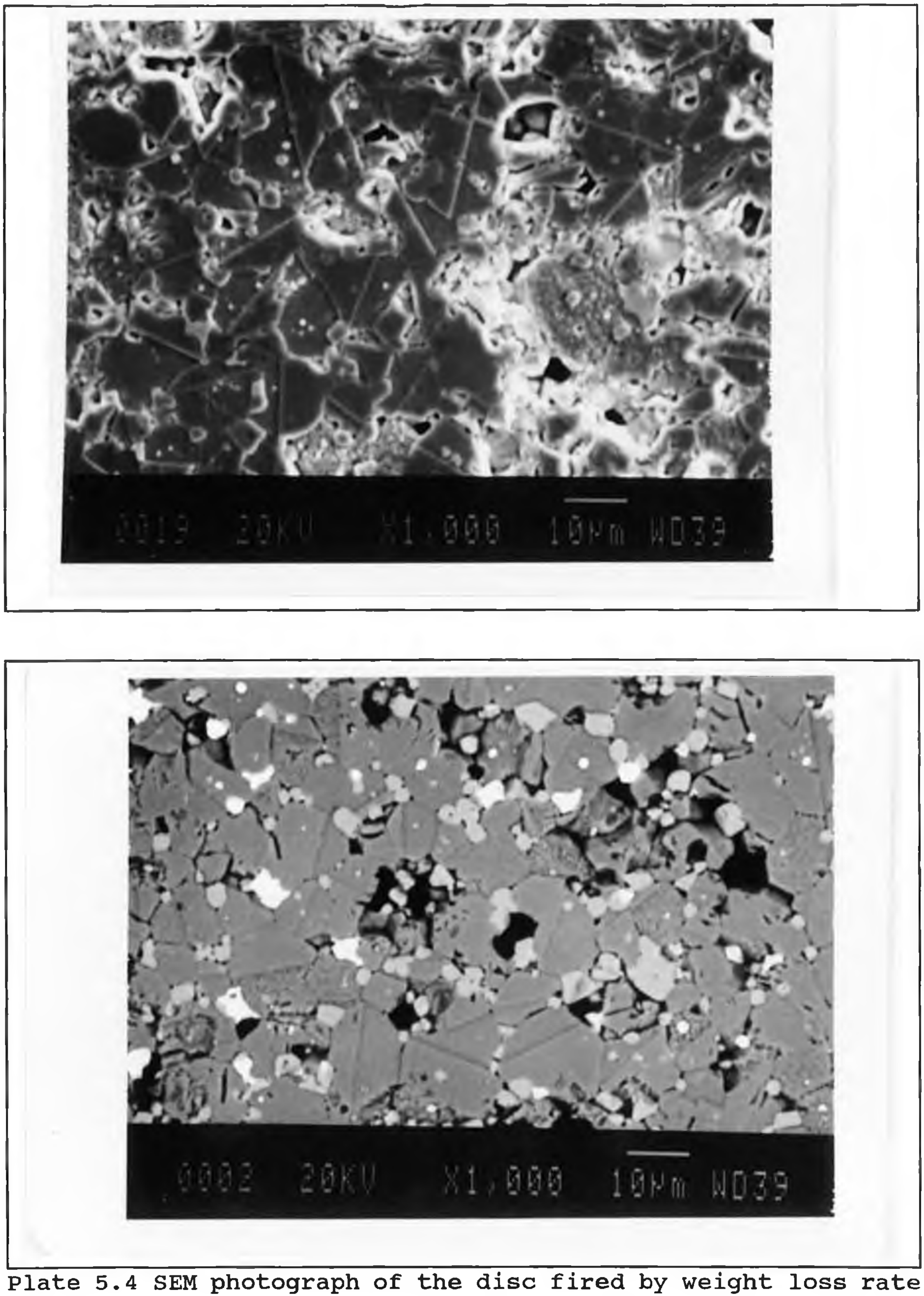

Plate 5.4 SEM photograph of the disc fired by weight loss rate and shrinkage rate limit 0.75 g/kg/h and 10 µm/mm/h.

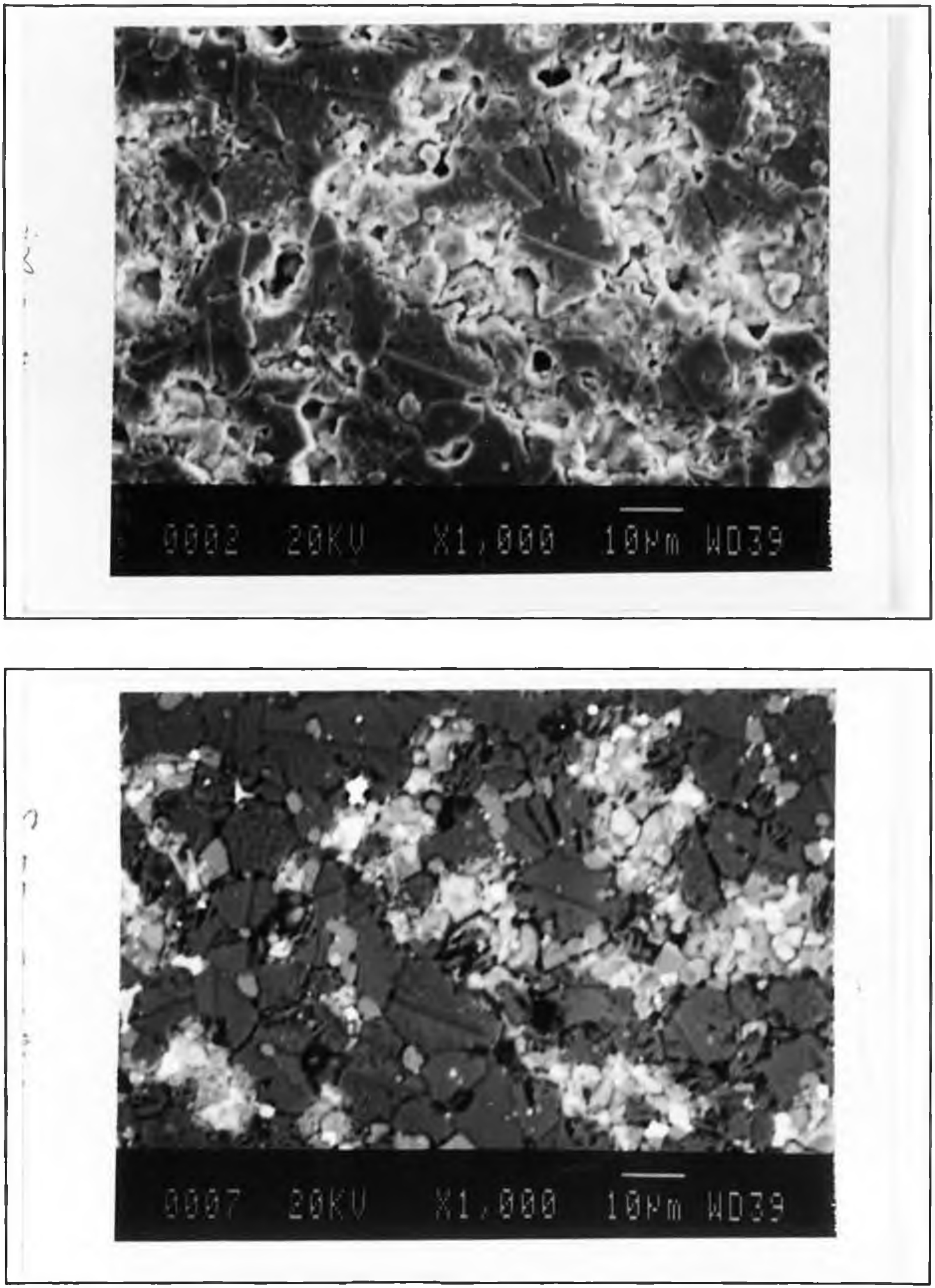

Plate 5.5 SEM photograph of the disc sintered by weight loss rate and shrinakge rate limit 3 g/kg/h and 10 µm/mm/h respe.

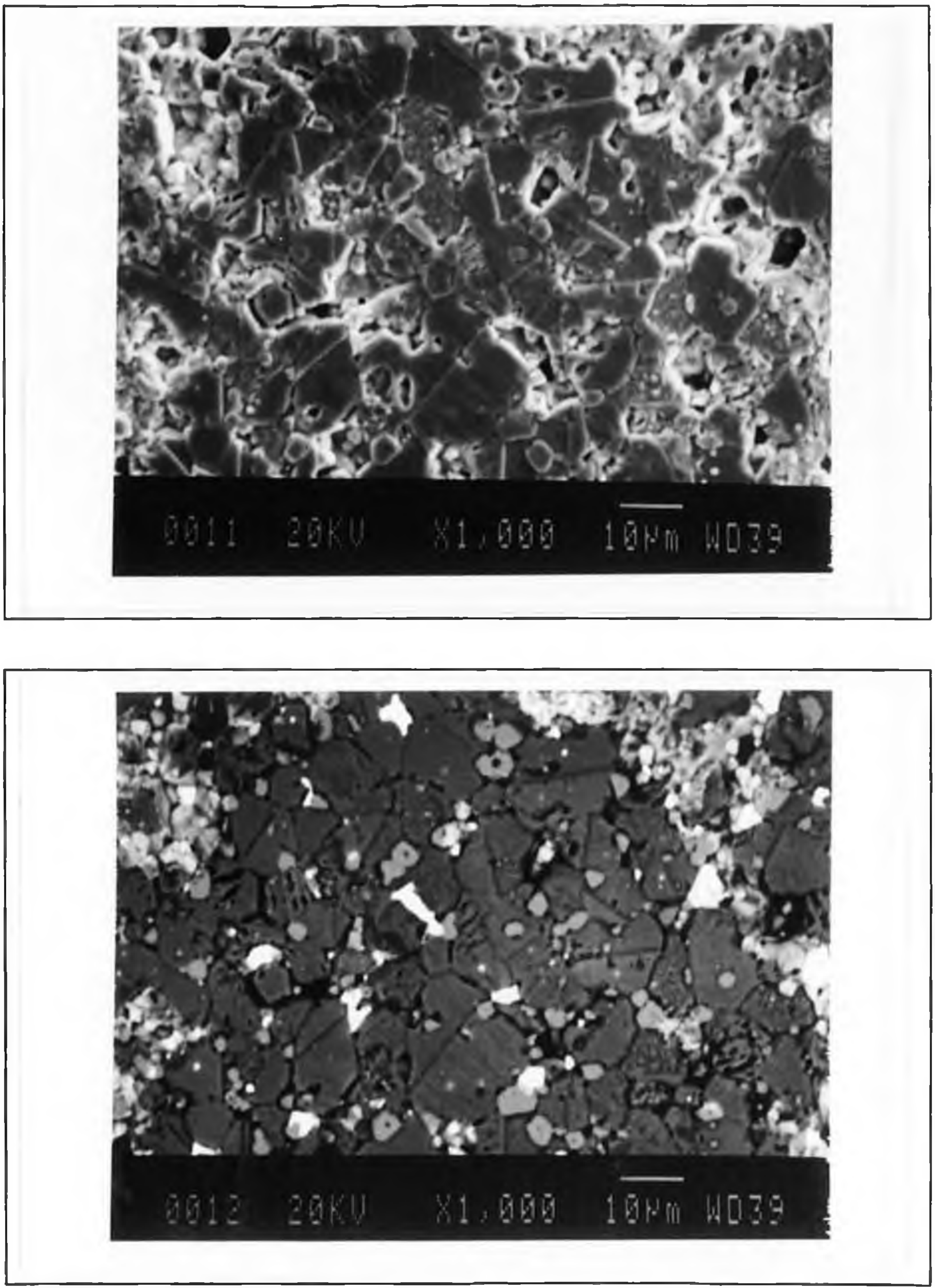

Plate 5.6 SEM photograpg of the disc fired by weight loss rate and shrinkage rate limit 0.75 g/kg/h and 40 µm/mm/h.

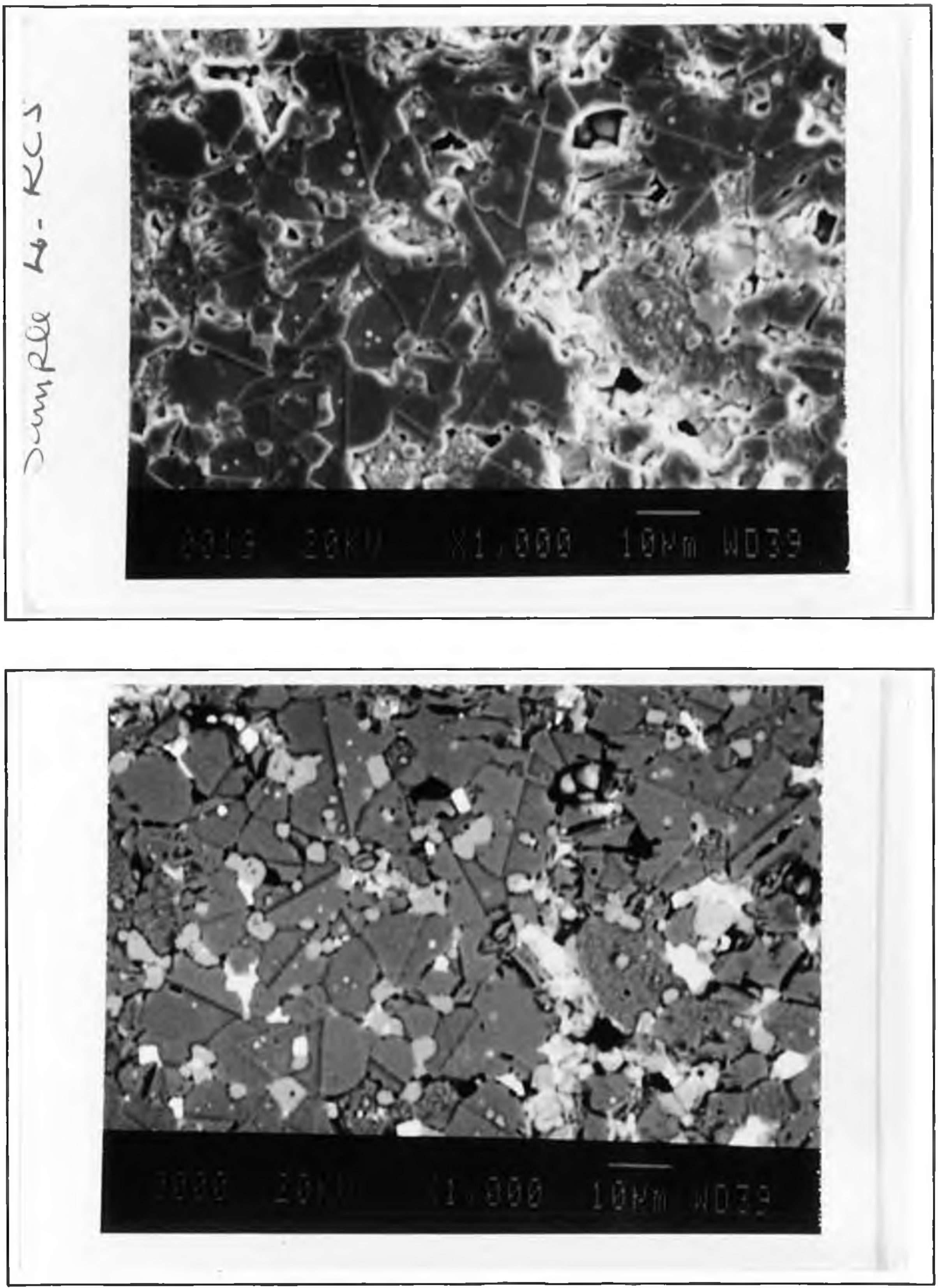

Plate 5.7 SEM photograph of the disc fired by weight loss rate and shrinkage rate limit 3 g/kg/h and 40 μm/mm/h.

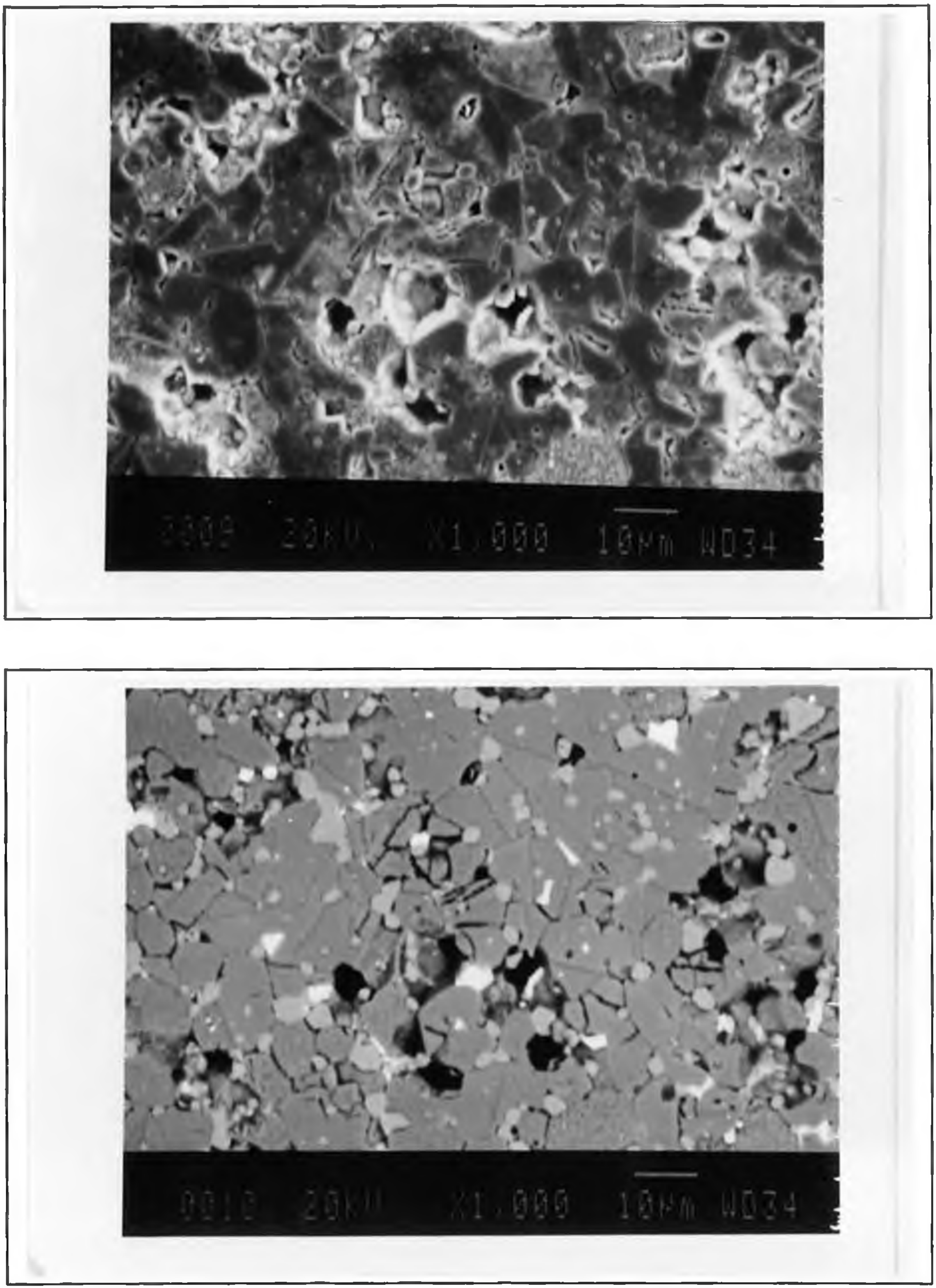

Plate 5.8 SEM photograph of the disc fired by weight loss and shrinkage rate limit 1.5 g/kg/h and 20 µm/mm/h.

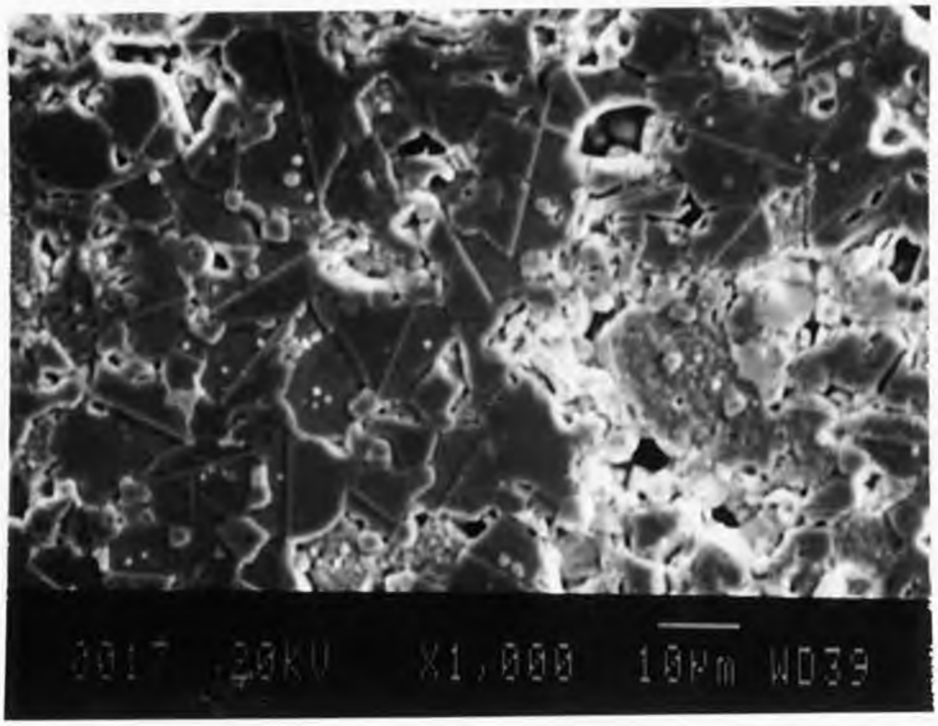

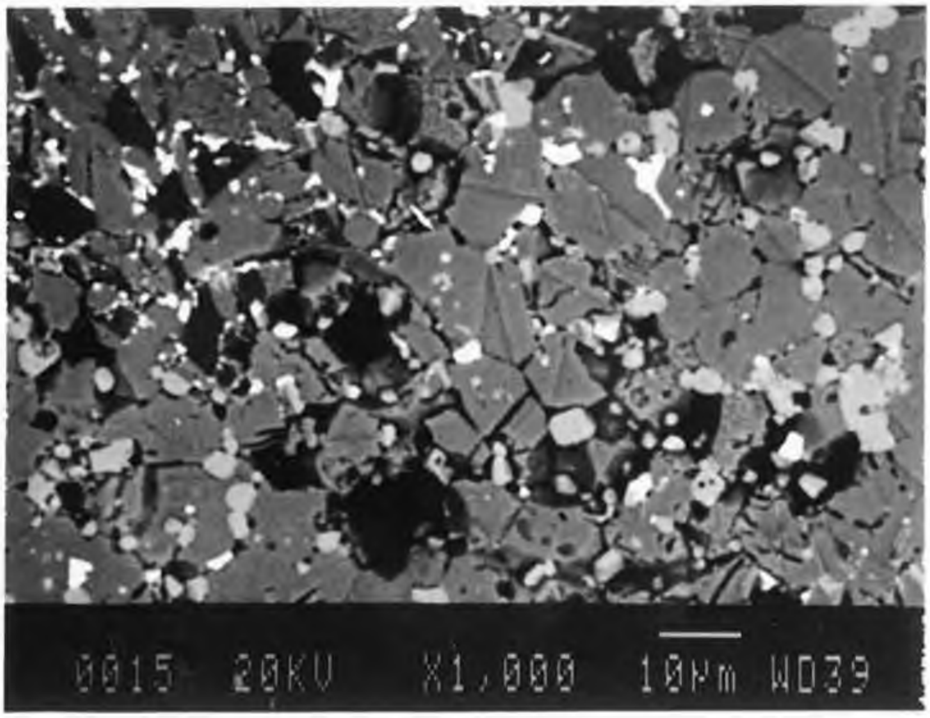

Plate 5.9 SEM photograph of the disc fired by conventional temperature profile.

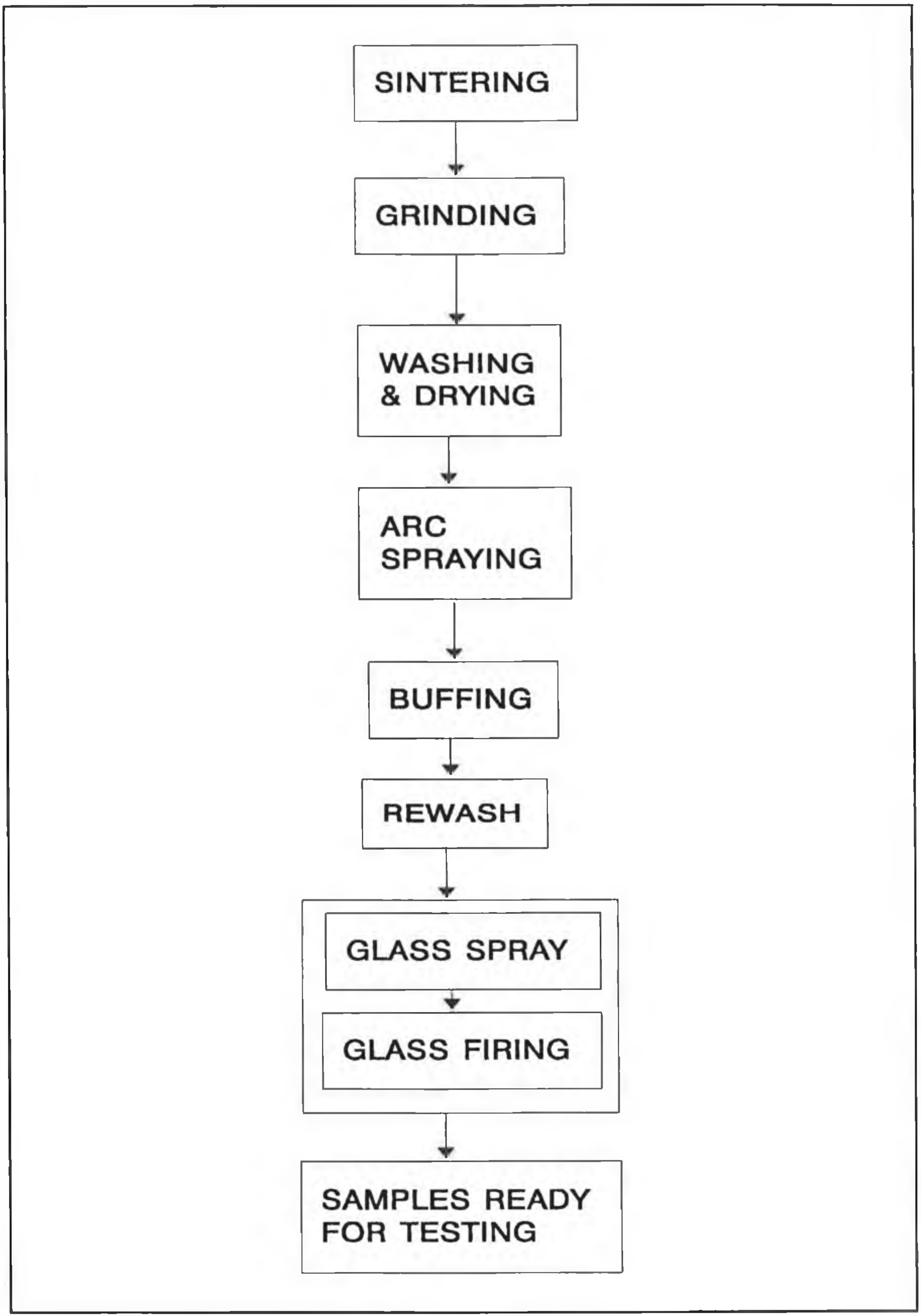

Figure 5.1 Flow chart of the different steps for preparing the samples.

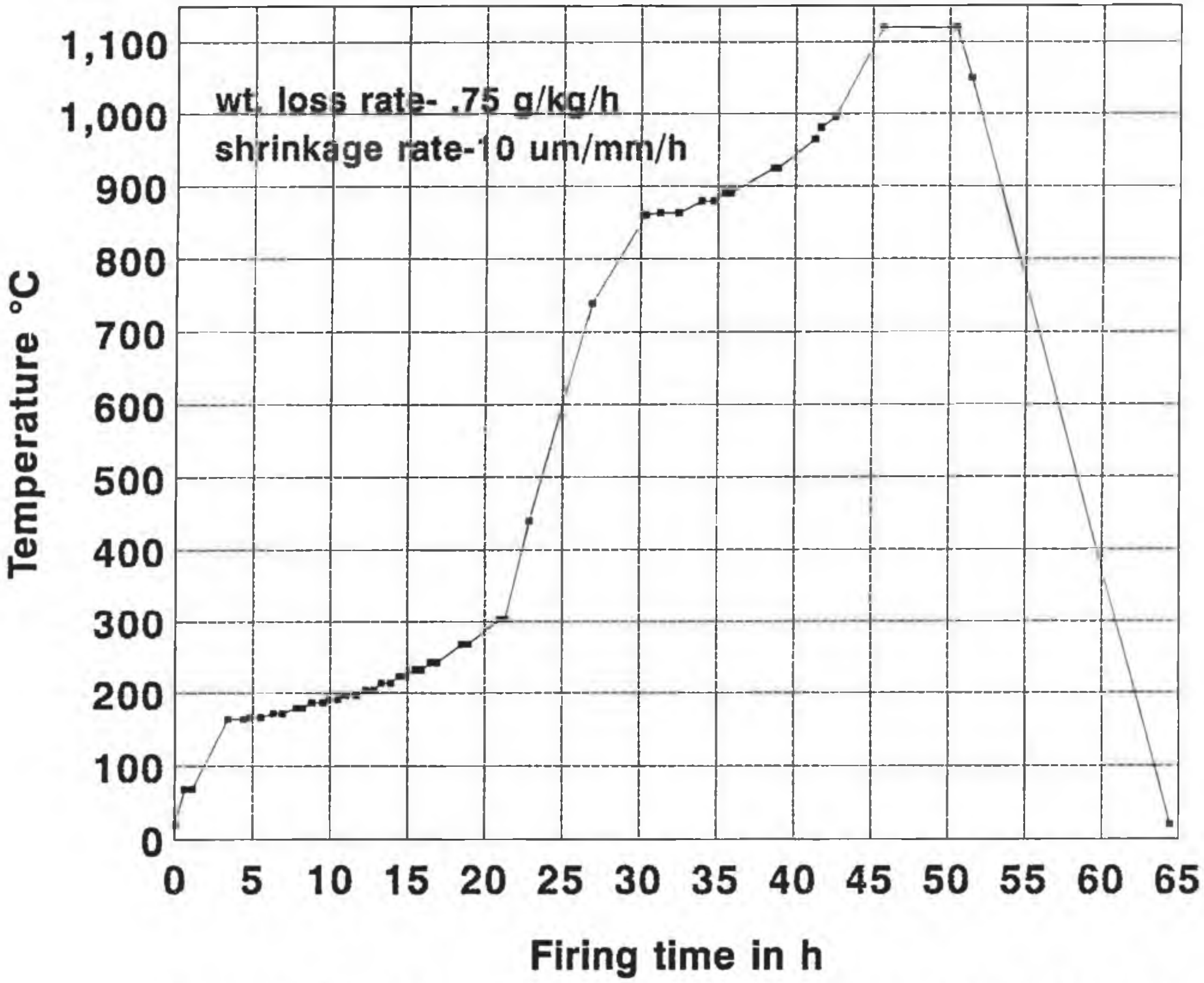

Figure 5.2 Complete firing profile with weight loss rate limit 0.75 g/kg/h and shrinkage rate limit 10 um/mm/h

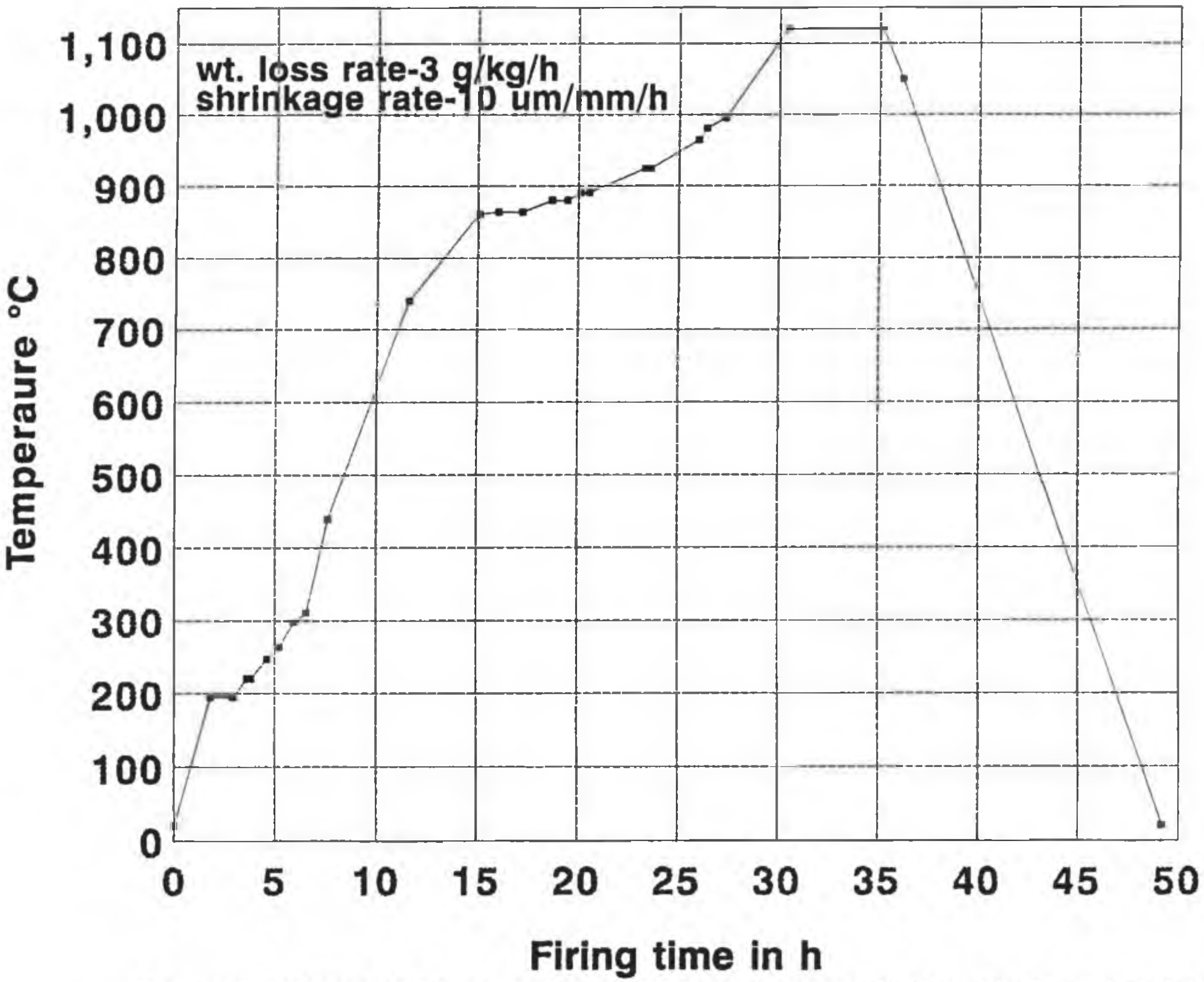

Figure 5.3 Complete firing profile with weight loss rate limit 3 g/kg/h and shrinkage rate limit 10 um/mm/h

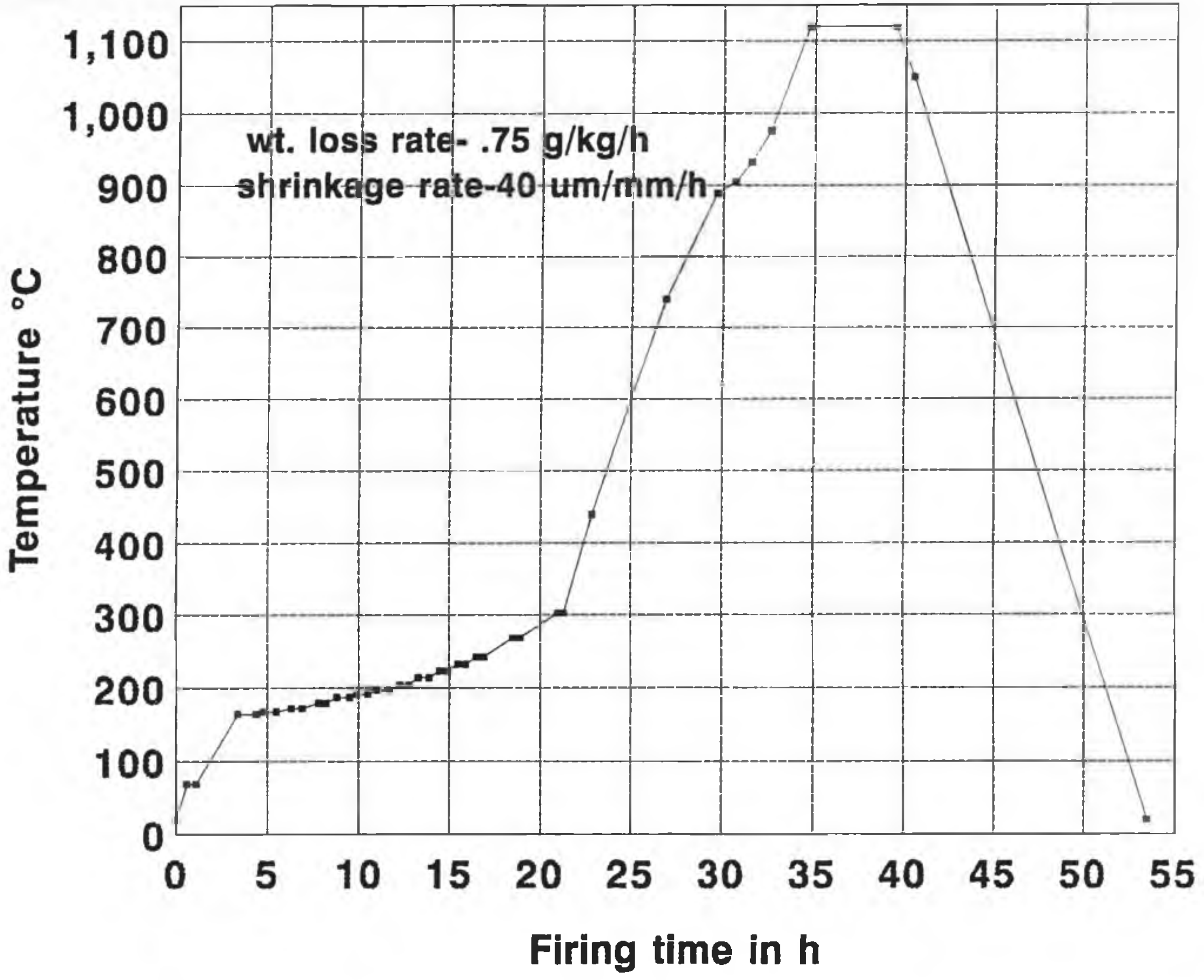

Figure 5.4 Complete firing profile for weight loss rate limit 0.75 g/kg/h and shrimkage rate limit 40 um/mm/h

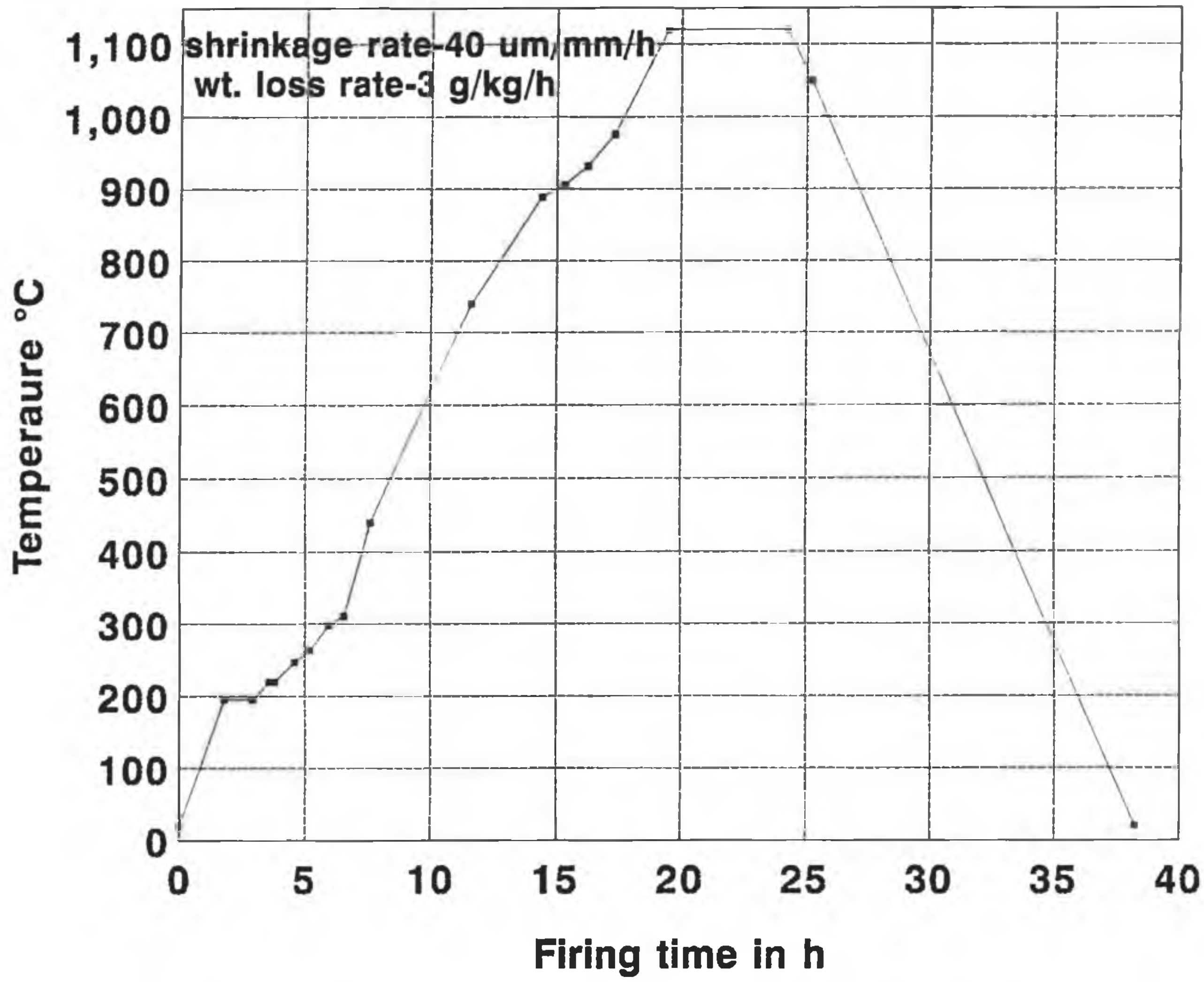

Figure 5.5 Complete firing profile for weight loss rate limit 3 g/kg/h and shrinkage rate limit 40 um/mm/h

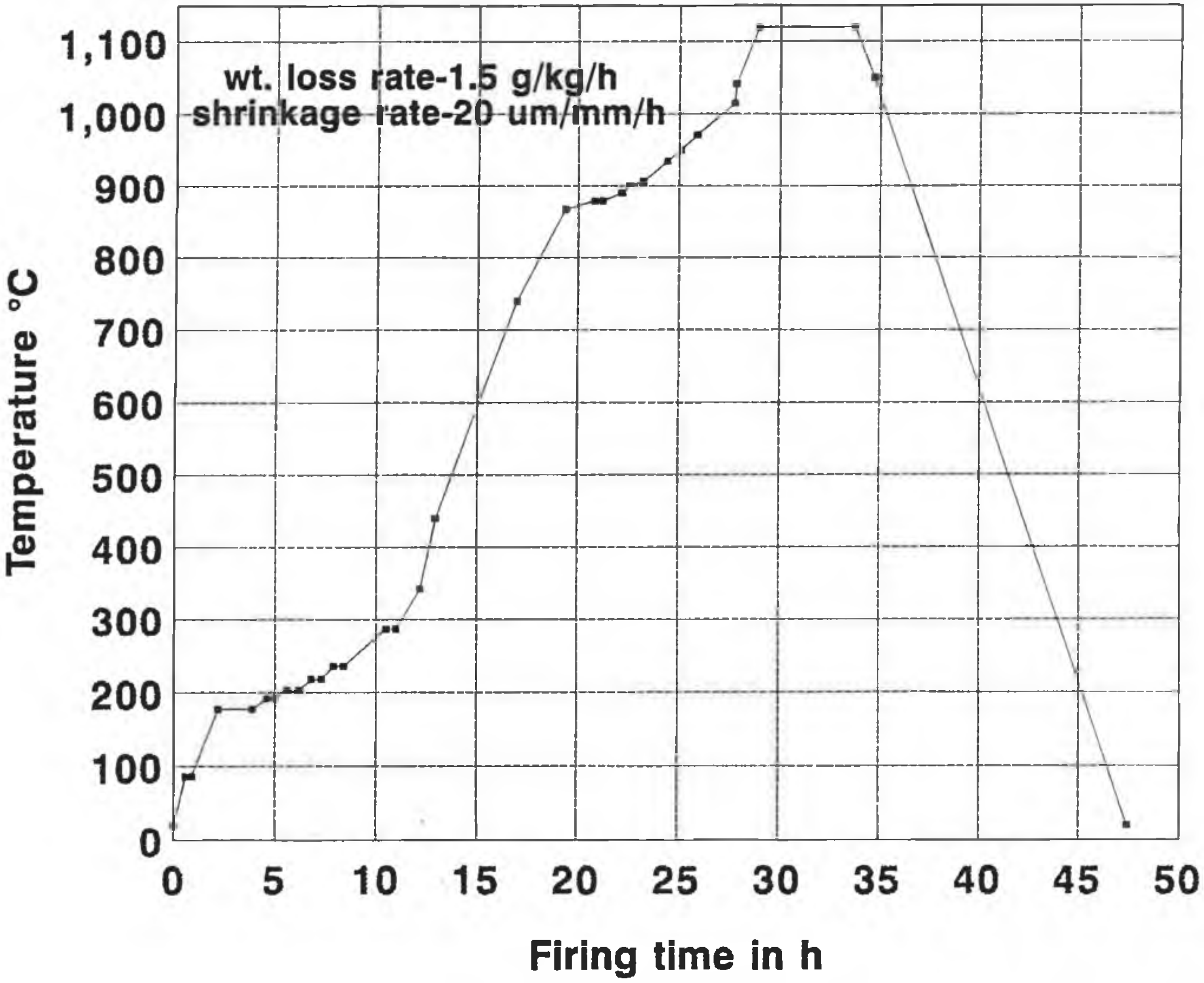

Figure 5.6 Complete firing profile for weight loss rate limit 1.5 g/kg/h and shrinkage rate limit 20 um/mm/h

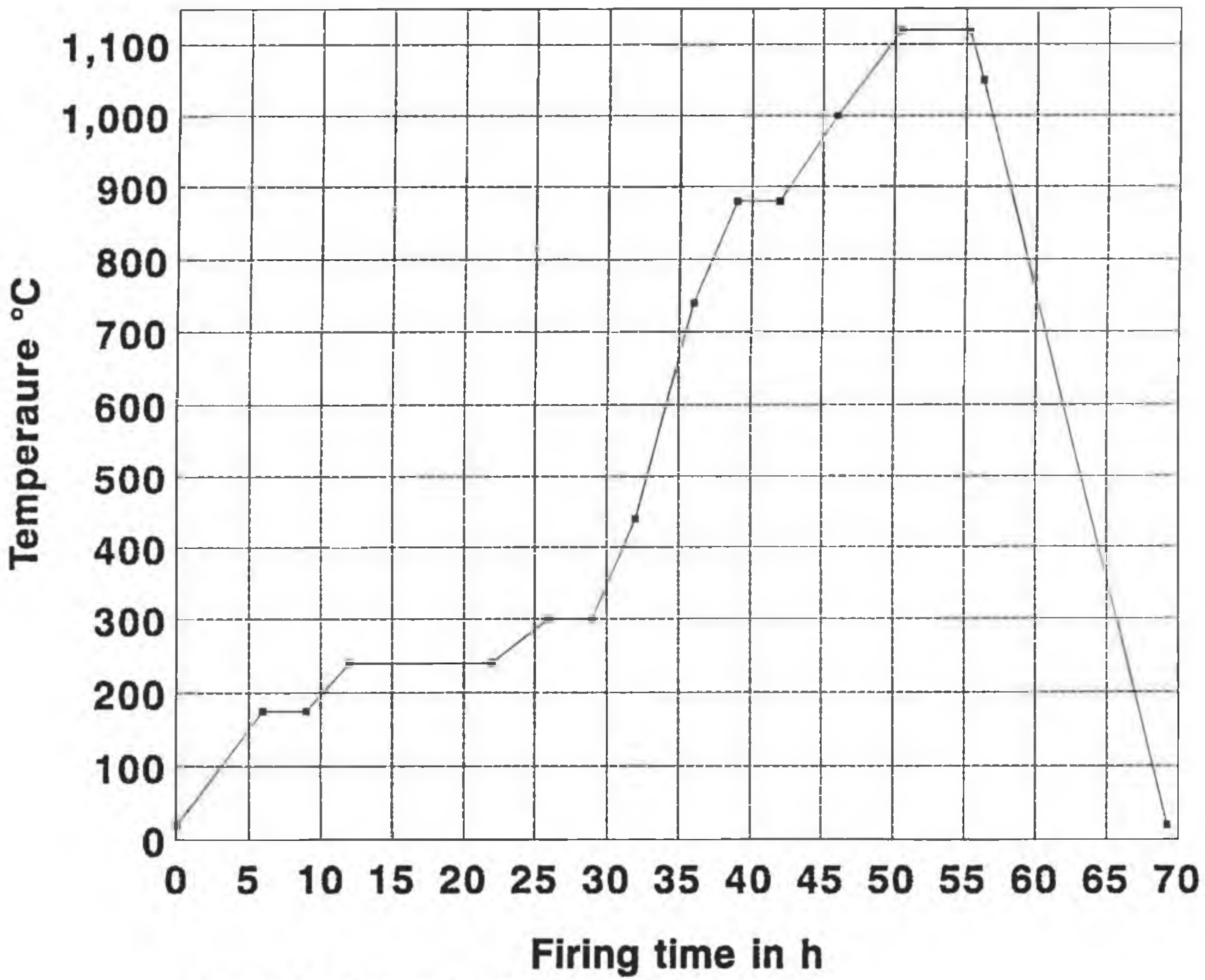

Figure 5.7 Conventional firing profile

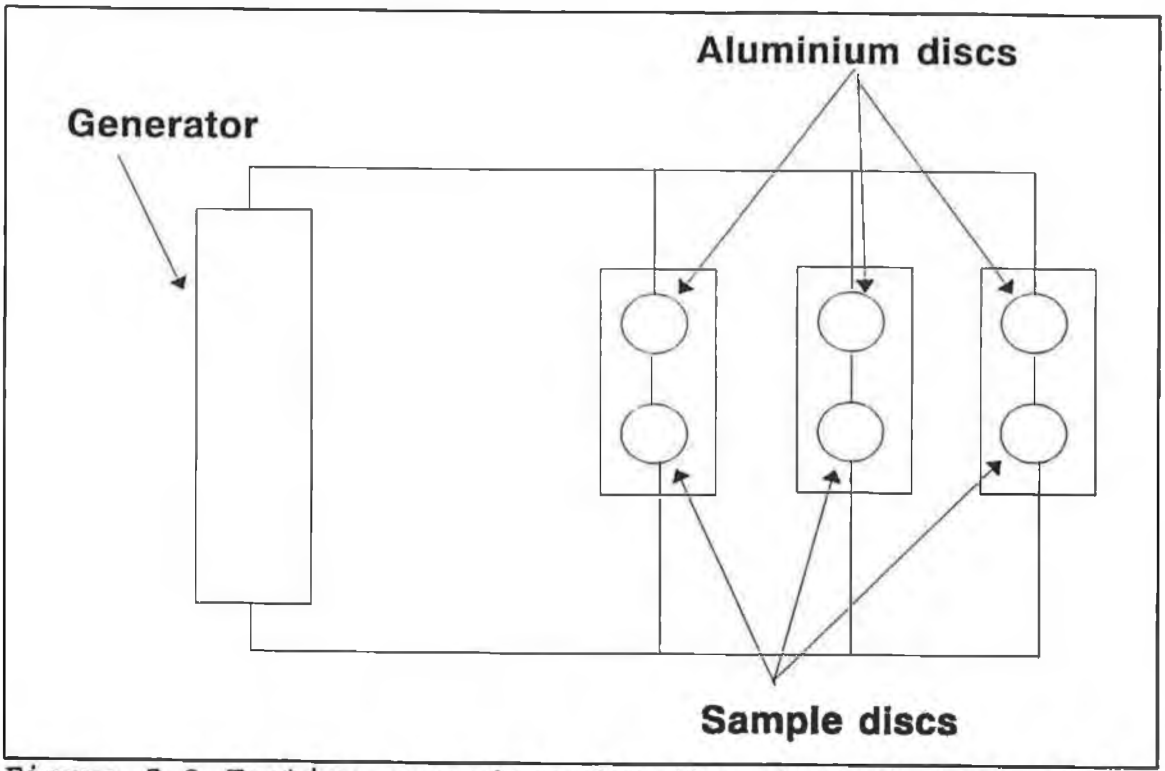

Figure 5.8 Testing procedure for the strength test of the discs

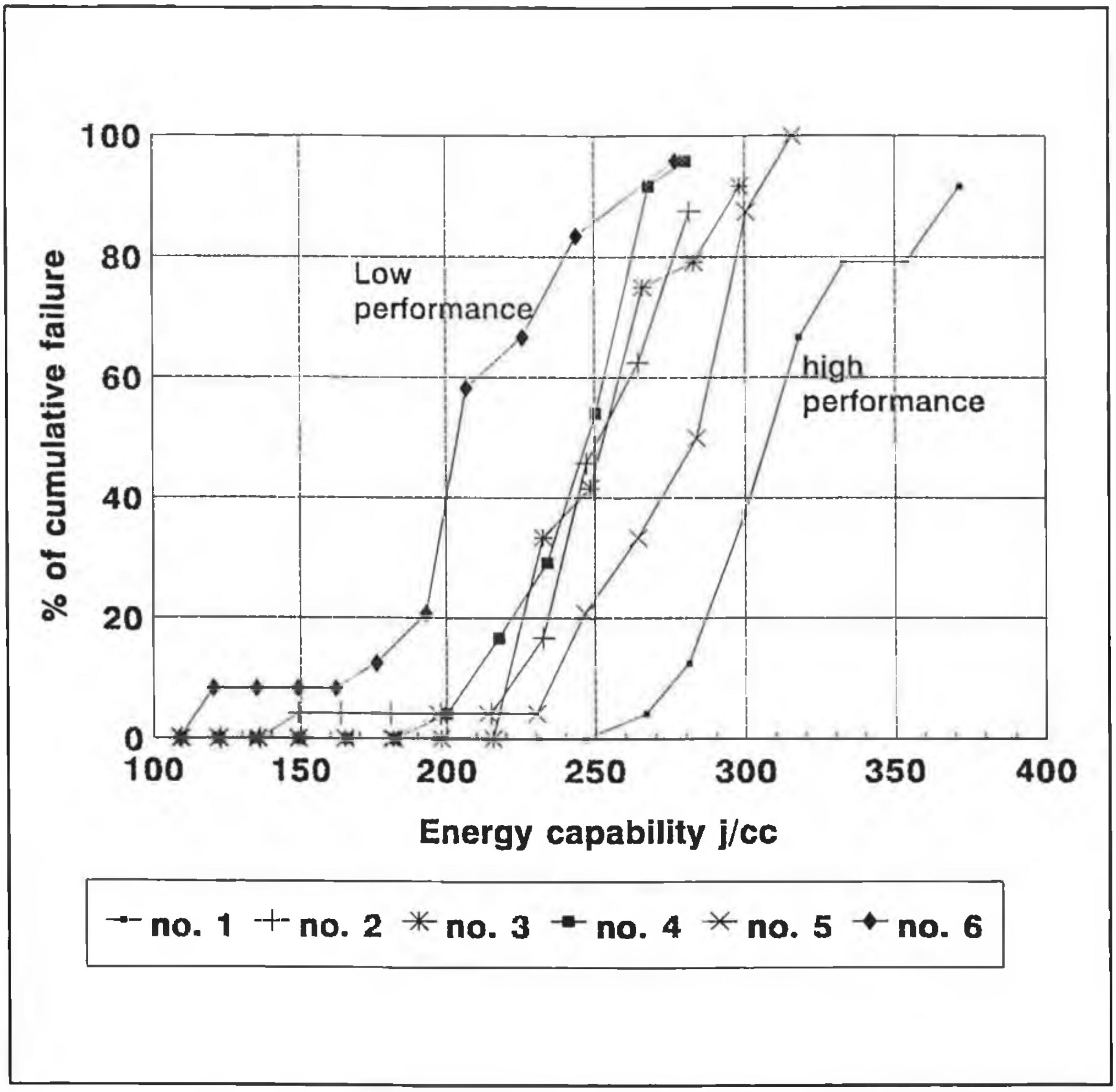

Figure 5.9 Percentage of cumulative failure vs. energy capability of the discs for different temperature profiles

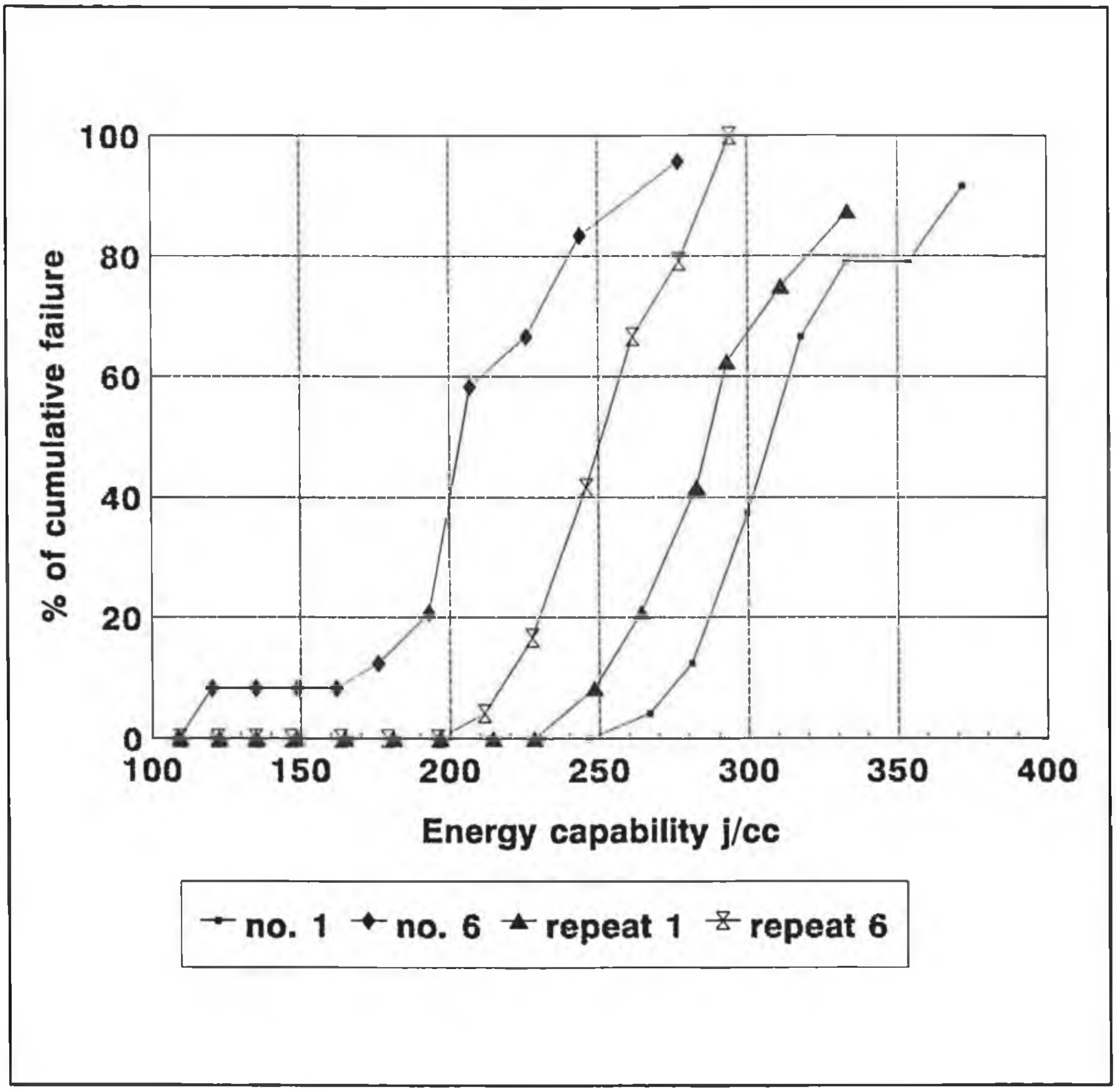

Figure 5.10 Replication of the strength test for the samples for the temperature profile no. 1 and no. 6.

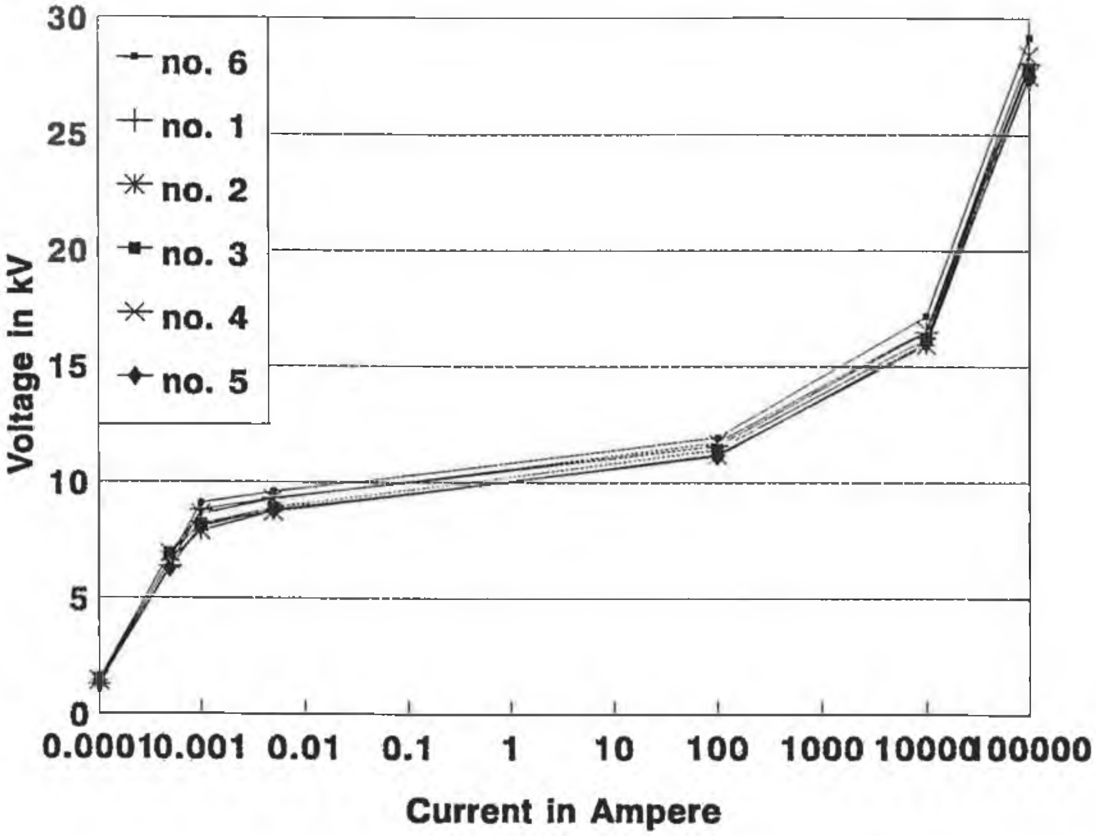

Figure 5.11 V-I curves of the discs using temperature profiles no 1, 2, 3, 4, 5 and 6.

CHAPTER SIX

DESIGN OF EXPERIMENTS AND RESPONSE SURFACE METHODOLOGY

6.1 INTRODUCTION

The design of experiments utilizing response surface methodology has been used to develop mathematical models for MMCs and zinc oxide varistors. The mathematical models have been developed for predicting and optimizing the hardness and compressive strength of MMCs and the electrical energy absorption capability of zinc oxide varistors. The aim of developing the mathematical model is to optimize the process which gives a better performance in relation to strength, time and cost. The work is divided as follows:

(1) Design of experiments

(2) Hardness modelling of Al/Al_2O_3 composites

(3) Compressive strength and hardness modelling of Al-6061/SiC composites

(4) Failure modelling for ZnO varistors

6.2 DESIGN OF EXPERIMENTS

Statistically designed experiments are needed to replace the traditional one-variable-at-a time approach which is evidently inadequate and time consuming. A well designed experiment can substantially reduce the number of experiments. Suppose that there are four factors (independent variables) which have to be investigated with three level each, then 81 (3*3*3*3) numbers of experiment should be needed to determine the effect of those factors. But with proper design, it can be done only by 24 experiments. Factorial designs are widely used in experiments involving several factors where it is necessary to study the joint effect of these factors on a response. The factorial designs are expressed as 2^k, 3^k etc where 2 and 3 are the no. of levels and k is the no. of factors. The design of experiment utilizing response surface methodology has been developed [107] in the study of optimization problems in chemical process engineering. Response surface methodology (RSM) has been used due to its successful application, in tool life [108], surface roughness analysis [109-110]. The general steps involving for the application of RSM was described in reference [111].

RSM is a collection of mathematical and statistical techniques useful for analyzing problems in which several independent variables (input) influence a dependent variable or response (output) and the goal is to optimize this response [112]. It is assumed that the independent variables are continuous and controllable with negligible error. The response is assumed to be a random variable.

6.3 HARDNESS MODELLING OF Al/Al_2O_3 COMPOSITES

6.3.1 Introduction

This work presents a study of the development of a Hardness model for aluminium matrix composite (Al/Al_2O_3) which was made by powder metallurgy route. The mathematical prediction models for Hardness were developed in terms of sintering temperature, sintering time and volume fraction of reinforcement. The effect of these manufacturing parameters on the Hardness had been investigated using design of experiments and response surface methodology.

6.3.2 Postulation of the Mathematical Model

The functional relationship between response (Hardness) after the sintering process and the investigated independent variables can be represented by the following form:

Hardness= f(sintering temperature, sintering time, volume fraction of reinf.)

and mathematically it can be written as

$$H=CT^{k}t^{l}v^{m} \tag{6.1}$$

where H is the Vicker's hardness (Hv), while T, t and v are the sintering temperature (°C), sintering time (min.) and volume fraction of reinforcement (%) respectively. C, k, l and m are the model parameters to be estimated from experimental data.

Equation (6.1) can be written as

$$\ln H=\ln C+k\ln T+l\ln t+m\ln v \tag{6.2}$$

which may represent the following linear mathematical model

$$\xi=\beta_0 x_0+\beta_1 x_1+\beta_2 x_2+\beta_3 x_3 \tag{6.3}$$

where ξ is the true response of Hardness on a logarithmic scale, $x_0 = 1$ (a dummy variable), x_1, x_2, and x_3 are the logarithmic transformations of the temperature, time and volume fraction of reinforcement, while β_0, β_1, β_2 and β_3 are the parameters to be estimated.

Equation (6.3) can also be written as

$$\hat{Y}=Y-\epsilon=b_0x_0+b_1x_1+b_2x_2+b_3x_3 \tag{6.4}$$

where $\hat{Y}$ is the estimated response and Y is the measured hardness on a logarithmic scale, ϵ is the experimental error, and b's are the estimates of the β parameters by the least square method. The basic formulae of b is given as

$$b=(X^TX)^{-1}X^TY \tag{6.5}$$

where b is the matrix parameter estimates, X is the calculation matrix, X^T is the transpose of X, X^TX is the variance matrix, $(X^TX)^{-1}$ is the covariance matrix which is the inverse of X^TX and Y is the matrix of measured response (output) on a logarithmic scale.

6.3.3 Experimental Design and Conditions

A design consisting of twelve experiments has been used to develop the first order model. Eight experiments represent a 2^3 factorial design, where the experimental points are located at the vertices of a cube as illustrated in figure (6.1).

Four experiments represent an added centre point to the cube, repeated four times to estimate the pure error. The complete design consists of twelve experiments in two blocks, each block containing six experiments. The first block of experiments includes numbers 1, 4, 6, 7, 9 and 10.

The four parameters in the postulated hardness equation can be estimated using these six experiments and the adequacy of the first order linear model can also be checked. The central experiments provide the estimate of the experimental error.

The second block of six experiments (numbers 2, 3, 5, 8, 11 and 12) has been added to provide a more precise estimate of the parameters. The design matrix is shown in table (6.1).

Table 6.1 Experimental Conditions and Results

Trial No	Block No	Temperature T (°C)	Time t (min.)	Volume fraction of rein. v (%)	Coding x_1	x_2	x_3	Hardness H (Hv)
1	1	700	30	10	-1	-1	-1	25.38
2	2	800	30	10	1	-1	-1	28.93
3	2	700	120	10	-1	1	-1	25.68
4	1	800	120	10	1	1	-1	29.78
5	2	700	30	40	-1	-1	1	36.80
6	1	800	30	40	1	-1	1	42.90
7	1	700	120	40	-1	1	1	38.02
8	2	800	120	40	1	1	1	39.02
9	1	750	60	20	0	0	0	36.02
10	1	750	60	20	0	0	0	37.30
11	2	750	60	20	0	0	0	35.30
12	2	750	60	20	0	0	0	36.80

The design provides three levels for each variable. These variables are coded for convenient identification and for easy calculation. The levels adopted are indicated in table (6.2).

Table 6.2 Levels of the Independent Variables and Coding Identification

	Low	Centre	High
Coding	-1	0	1
Temperature T (°C)	700	750	800
Time t (min.)	30	60	120
Volume fraction of rein. v (%)	10	20	40

The independent variables were coded as follows

$$x_1 = \frac{\ln T - \ln 750}{\ln 800 - \ln 750} \tag{6.6}$$

$$x_2 = \frac{\ln t - \ln 60}{\ln 120 - \ln 60} \tag{6.7}$$

$$x_3 = \frac{\ln v - \ln 20}{\ln 40 - \ln 20} \tag{6.8}$$

6.3.4 Experimental Procedure

Powder mixing was carried out using a double cone V shape mixture. Aluminium powder with reinforcement element Al_2O_3 in different volume fraction were loaded separately into the mixture and zinc stearate was added in the ratio of 1% by wt.. The blender was held in a lathe and rotated at 40 rpm for 90 minutes.

Compaction was carried out using the INSTRON universal testing machine and a 17 mm diameter die compaction set. The compacts for the hardness test had an average green density of 2.38 g/cc (relative density 84% for 10% reinf.). The green compacts were sintered in a box furnace for three different durations of 30, 60 and 120 minutes and at three different sintering temperatures. These temperature were 700, 750 and 800 °C. The compacts passed through a burn out stage at 540°C for 30 minutes to burn out the undesirable lubricant. After sintering the surface of the compacts was ground and polished for the hardness test. The die set and sintering unit are shown in figure (3.1) and (3.2) respectively in chapter three.

6.3.5 Analysis of Results

The first order model of the hardness was developed by utilizing the least square methods. Using the first block of 6 tests, the parameters in equation (6.5) were estimated, yielding the hardness predicting equation

$$\hat{Y}=3.5379+0.07115\, x_1+0.0098\, x_2+0.1923\, x_3 \qquad (6.9)$$

To increase the precision associated with the estimates of the parameters of the model, the second block of 6 tests was added. Combining the results of all 12 tests, the fitted Hardness predicting equation was found to be

$$\hat{Y}=3.5243+0.05921\ x_1-0.0007375\ x_2+0.180385\ x_3 \quad (6.10)$$

This predicting equation (6.10) can be represented graphically in a three dimensional space of temperature, time and the volume fraction as depicted in figure (6.2). Since the equation is a first order linear equation, the response surface (surface of constant hardness) are planes. Planes of constant hardness of 28, 30, 32, 34, 36, 38, 40 and 42 Hv are shown in figure 6.2 (a) and (b) respectively. These planes are obtained utilizing an Autocad Computer software Package.

Equation (6.10) can be transformed using equation (6.6), (6.7) and (6.8) to provide the hardness (Hv) as a function of the sintering temperature (°C), time (min.) and vol. fraction of reinf. (%) as follows

$$H=0.03612T^{0.91798}t^{-0.002564}V^{0.26025} \quad (6.11)$$

This equation is valid for calculating hardness of AMC where pure aluminium powder is the matrix using powder metallurgy route and

$$700 \leq T \leq 800 \quad °C$$

$$30 \leq t \leq 120 \quad \text{min.}$$

$$10 \leq v \leq 40 \quad \%$$

Equation (6.11) indicates that an increase either in temperature or the volume fraction increases the hardness while an increase in the time decreases the hardness. However it should be noted that the volume fraction of reinforcement has the major effect on hardness.

6.3.6 Utilization of the First Order Hardness Model

Equation (6.10) has been plotted in figure (6.3) as contours (sections) for each of the response surface at three selected levels of time. These selected level were chosen as low (t=30 min.), centre (t=60 min.) and high (t= 120 min.).
Fig. (6.3) shows the contours of Hardness H at the selected levels of sintering time (30, 60 and 120 min.) in planes containing the sintering temperature (°C) and the volume fraction (v). These contours were obtained utilizing the MATLAB Computer Package. It can be seen from figure (6.3) that Hardness increases with an increase in sintering temperature and volume fraction of reinforcement. It is also seen that there is very small effect of time on Hardness. Hence, a better hardness is obtained at combination of high temperature and high volume fraction of reinforcement. However, in order to make the object under PM route, the temperature must not be so high.

6.3.7 Adequacy of the predicted model

The analysis of variance technique was used to check the adequacy of the postulated models. As per this technique for the first order model the calculated ratio (F_0) of the mean square of lack of fit to the mean square of pure error is 24.14, while the tabulated F ratio for 95% confidence at 1 (lack of fit) and 1 (pure error) degree of freedom is 161. Hence the model is adequate. The results of analysis of variance is shown in the following table (6.3).

Table 6.3 Analysis of variance for the first order model

Source of variation	Sum of squares (SS)	Degrees of freedom (DF)	Mean squares (MS)	F_{cal}	F_{tab}	Remarks
Zero-order terms	75.10	1	75.1			
First order terms	0.1679	3	0.0559			
Lack of fit	0.014	1	0.014	24.14	161	Adequate
Pure error	.00061	1	0.000609			
Residuals	0.01531					
Total	75.2818	6				

Conclusion

- A reliable Hardness model has been developed and utilized to enhance the production system of metal matrix composite when using pure Al as the matrix element.
- The first order hardness prediction equation is valid within the temperature range of 700-800 °C.
- The effect of temperature and the volume fraction of reinforcement is very dominant while time effect is not so significant

- An increase in either the temperature or the volume fraction of reinforcement increases the hardness while sintering time has the little effect on hardness.
- Contours of the Hardness outputs were constructed in planes containing two of the independent variables.

6.4 COMPRESSIVE STRENGTH AND HARDNESS MODELLING FOR Al-6061/SiC MMCs

6.4.1 Introduction

Compressive strength and hardness of metal matrix composite fabricated by powder metallurgy route is dependent on various parameters such as density of the green compact, volume fraction of reinforcement, size of the particles, sintering temperature and time. This work presents the development of a compressive strength and hardness models for aluminium matrix composite (Al-6061/SiC) which are made by powder metallurgy. The mathematical prediction models for compressive strength and hardness have been developed in terms of sintering temperature, sintering time and volume fraction of reinforcement.

6.4.2 Postulation of Mathematical Models

The functional relationship between response (compressive strength and hardness) after the manufacturing process and the investigated independent variables can be represented by the following equation:

$$S=C_1T^{k_1}t^{l_1}v^{m_1} \tag{6.12}$$

$$H_{(Al/SiC)}=C_3T^{k_3}t^{l_3}v^{m_3} \tag{6.13}$$

where S and $H_{(Al/SiC)}$ are the compressive strength (MPa) and hardness (Hv) respectively, and T, t and v are the sintering temperature (°C), sintering time (hr) and volume fraction of reinforcement (%) respectively. C_1, k_1, l_1 and m_1 are the model parameters for the compressive strength model and C_3, k_3, l_3 and m_3 are the model parameters for hardness model to be estimated from experimental data.

Equation (6.12) and (6.13) may be written as

$$\ln S=\ln C_1+k_1 \ln T+l_1 \ln t+m_1 \ln v \tag{6.14}$$

$$\ln H_{(Al/SiC)}=\ln C_3+k_3 \ln T+l_3 \ln l+m_3 \ln v \tag{6.15}$$

which may represent the following linear mathematical model:

$$\eta=\beta_0x_0+\beta_1x_1+\beta_2x_2+\beta_3x_3 \tag{6.16}$$

where η is the response of compressive strength on a logarithmic scale, $x_0=1$ (a dummy variable), x_1, x_2 and x_3 are logarithmic transformations of the temperature, time and volume fraction of reinforcement, while β_0, β_1, β_2 and β_3 are the parameters to be estimated.

Equation (6.16) can also be written as

$$\hat{Y}=Y-\epsilon=b_0x_0+b_1x_1+b_2x_2+b_3x_3 \tag{6.17}$$

where $\hat{Y}$ is the estimated response and Y is the measured compressive strength and hardness on a logarithmic scale, ϵ is the experimental error and b_0, b_1, b_2 and b_3 values are estimates of the β parameters. This is the proposed first order model.

The second order model can be extended from the first order model's equation as

$$\begin{gathered}Y-\epsilon=b_0+b_1x_1+b_2x_2+b_3x_3+b_{11}x_1^2+b_{22}x_2^2+b_{33}x_3^3\\+b_{12}x_1x_2+b_{13}x_1x_3+b_{23}x_2x_3\end{gathered} \tag{6.18}$$

where b_0, b_1, b_2,. . ., etc. are to be estimated by the method of least squares, and the basic formula is

$$b=(X^TX)^{-1}X^TY \tag{6.19}$$

where b is the matrix of parameter estimates, X is the calculation matrix, X^T is the transpose of X, X^TX is the variance matrix, $(X^TX)^{-1}$ is the covariance matrix which is the inverse of X^TX and Y is the matrix of measured response (output) on a logarithmic scale. Hence upon determining the b values by using equation (6.19), the proposed second order model is rewritten as:

$$\begin{gathered}\hat{Y}=Y-\epsilon=b_0x_0+b_1x_1+b_2x_2+b_3x_3+b_{11}x_1^2+b_{22}x_2^2+b_{33}x_3^3\\+b_{12}x_1x_2+b_{13}x_1x_3+b_{23}x_2x_3\end{gathered} \tag{6.20}$$

where $\hat{Y}$ is the estimated response on a logarithmic scale.

6.4.3 Experimental Design and Conditions

A design consisting of twelve experiments has been used to develop the first order model. The 12 tests consisted of a 2^3 factorial design and four centre points as shown in figure (6.4). These twelve tests were divided into two blocks (blocks 1 and 2) of 6 tests each.

As the first-order model is only applicable over a narrow range of the variables, the experiments were extended to obtain a second order model. Six augment points were added at the face of the cube, where each was chosen at a selected augment length of $\sqrt{2}$. The implications of selecting the distance from the centre of the design of these augments have been discussed in references [112, 113]. These six experiments were repeated twice for increasing the model accuracy as shown in figure (6.4).

Table (6.4) shows the manufacturing conditions and the compressive strength and hardness results. The resulting 24 experiments form a central composite design [107]. All these 24 experiments were performed in four blocks. The first block consisted of experiments 1,4,6,7,9 and 10, while the second block consisted of experiments 2,3,5,8,11 and 12. These two blocks were used to develop the first-order model. The third block consisted of experiments 13,14,15,16,17 and 18, while experiments 19,20,21,22,23 and 24 formed the fourth block as shown in figure (6.4).

The central composite design with 24 experiments provided five levels for each independent variable, as shown in table (6.5); and were used to develop the second-order model.

Table 6.4 Experimental conditions and results

Trial	Block	Temperature	Time	Volume fraction	Coding			Compr. Streng.	Hardn.
No.	No.	T(°C)	t(hr)	of rein., v(%)	X_1	X_2	X_3	S (MPa)	Hv
1	1	600	3	10	-1	-1	-1	200	33
2	2	760	3	10	1	-1	-1	243	29
3	2	600	8.33	10	-1	1	-1	206	48
4	1	760	8.33	10	1	1	-1	251	59
5	2	600	3	23	-1	-1	1	267	73
6	1	760	3	23	1	-1	1	324	88
7	1	600	8.33	23	-1	1	1	386	105
8	2	760	8.33	23	1	1	1	396	158
9	1	675	5	15	0	0	0	285	44
10	1	675	5	15	0	0	0	275	54
11	2	675	5	15	0	0	0	290	38
12	2	675	5	15	0	0	0	272	28
13	3	570	5	15	$-\sqrt{2}$	0	0	260	29
14	3	800	5	15	$\sqrt{2}$	0	0	320	36
15	3	675	2.43	15	0	$-\sqrt{2}$	0	275	39
16	3	675	10.3	15	0	$\sqrt{2}$	0	295	39
17	3	675	5	8	0	0	$-\sqrt{2}$	250	32
18	3	675	5	28	0	0	$\sqrt{2}$	400	143
19	4	570	5	15	$-\sqrt{2}$	0	0	250	27
20	4	800	5	15	$\sqrt{2}$	0	0	322	47
21	4	675	2.43	15	0	$-\sqrt{2}$	0	271	35
22	4	675	10.3	15	0	$\sqrt{2}$	0	301	37
23	4	675	5	8	0	0	$-\sqrt{2}$	245	27
24	4	675	5	28	0	0	$\sqrt{2}$	410	148

Table 6.5 Levels of the independent variable and coding identification

	Lowest	Low	Centre	High	Highest
Coding	$-\sqrt{2}$	-1	0	1	$\sqrt{2}$
Temperature T(°C)	570	600	675	760	800
Time t(hr)	2.43	3	5	8.33	10.3
Vol. Frac. Rein., v(%)	8	10	15	23	28

The independent variables were coded as follows:

$$X_1=\frac{\ln T-\ln 675}{\ln 760-\ln 675} \tag{6.21}$$

$$X_2=\frac{\ln t-\ln 5}{\ln 8.33-\ln 5} \tag{6.22}$$

$$X_3=\frac{\ln v-\ln 15}{\ln 23-\ln 15} \tag{6.23}$$

6.4.4 Experimental Procedure

Powder mixing was carried out using a double cone mixer. Aluminium alloy powder and SiC reinforcement in particulate form with different volume fractions were loaded separately into the mixture and the solid lubricant (zinc stearate) was added in the ratio of 1% by weight. The blender was held in a lathe and rotated at 40 rpm for 60 minutes for the homogeneous and uniform distribution and mixing of the powders. Compaction was carried out using a 50 kN INSTRON-4204 universal testing machine and a 17 mm diameter die compaction set. The compacts for the strength test had an average relative density of 78%. The green compacts were sintered in a box furnace using five different time durations of 2.43, 3, 5, 8.33 and 10.3 hours and at five different sintering temperatures 570, 600, 675, 760 and 800 °C. The volume fractions of reinforcement are taken as 8, 10, 15, 23 and 28%. The compacts passed through a burn out stage at 520 °C for 30 minutes to burn out the fugitive lubricant.

For compression test of the compacts, a thin sheet of teflon (0.125 mm) smothered with a film of petroleum jelly was used as the lubricant. The test was carried out using a 100 kN AVERY DENISON universal testing machine at a load of 25 kN/min.. The test method ASTM D 3410 [114] was used for the evaluation of the compressive properties of unidirectional or cross-ply fibre-resin composites. This test method is an indirect compressive test method best for fibre matrix composites. These specimens were made by particulate reinforcements making the samples isotropic and the test was carried out according to IS/EN 10,002. With the increase of reinforcement, ductility of the samples decreases and the samples were broken down suddenly without preliminary cracks for higher reinforcements. The load at breaking point of the specimen for higher volume fraction of reinforcement was taken to calculate the compressive strength. At lower volume fraction of reinforcement, the cracks were generated at the edge of the samples and the load was taken at the point of cracks for calculating the compressive strength. Plate (6.1) shows the sintered disc with and without the adherance of the low temperature material. Plate (6.2) shows the two parts of the disc after cutting while plate (6.3) shows the fracture in compression test. The die set and sintering unit used for this experiments are shown in figures (3.1) and (3.2) respectively of chapter three.

For the hardness testing, the samples were cut off 1 mm from the top and then ground by DAP-V (STRUERS). The readings were taken throughout the surface by Micro-hardness tester (LEITZ MINI LOAD) and the average value was taken as the hardness of that sample.

6.4.5 Analysis of Results

The first order model of the compressive strength was developed by utilizing the least square method. Using the first block of 6 tests, the parameters in equation (6.19) were estimated, yielding the compressive strength prediction equation

$$\hat{Y}_{(comp.stren.)} = 5.6377 + 0.013X_1 + 0.1005X_2 + 0.228X_3 \qquad (6.24)$$

To increase the precision associated with the estimates of the parameters of the model, the second block of 6 tests was added. Combining the results of all 12 tests, the fitted compressive strength predicting equation was found to be

$$\hat{Y}_{(comp.stren.)} = 5.6241 + 0.0764X_1 + 0.0789X_2 + 0.2074X_3 \qquad (6.25)$$

and the hardness predicting equation as:

$$\hat{Y}_{hardness} = 4.0028 + 0.0841X_1 + 0.2541X_2 + 0.4589X_3 \qquad (6.26)$$

Equation (6.25) has been plotted in figure (6.5) as contours (sections) for each of the response surfaces at three selected levels of sintering time. These selected levels were chosen as low (t=3 hr), centre (t=5 hr) and high (t=8.33 hr).
Figure (6.5) shows the contours of compressive strength, S at the selected levels of sintering time (3, 5 and 8.33 hr) in planes containing the sintering temperature (°C) and the volume fraction (v). These contours were obtained utilizing the MATLAB software package. It can be seen from figure (6.5) that the compressive strength increases with an increase in sintering temperature and volume fraction of reinforcement. It is also seen that there is considerable effect of sintering time on the compressive strength and it increases with the increase of time. Hence, a better compressive strength can be obtained at combination of high temperature and high volume fraction of reinforcement.

The predicting equation (6.26) for hardness can be plotted in figure (6.6) as contours for each of the response surfaces at three selected levels of sintering time chosen as low (t=3 hr), centre (t=5 hr) and high (t= 8.33 hr). These contours were obtained by a computer package "GT". It can be seen from this figure (6.6) that hardness increases with increase of sintering temperature, sintering time and volume fraction of reinforcement but volume fraction of reinforcement has more effect on it. This figure also shows that a varieties of combination of sintering temperature and vol. fraction of reinforcement can be chosen for getting the same hardness value.

Equations (6.25) and (6.26) can be transformed using equations (6.21), (6.22) and (6.23) to provide the compressive strength S (MPa) and hardness H (Hv) as a function of the sintering Temp (°C), time (hr) and volume fraction of reinforcement (%) as follows

$$S=.8741\ T^{0.6441}t^{0.1545}V^{0.485} \tag{6.27}$$

and

$$H_{Al/Sic}=0.0132\ T^{0.7090}t^{0.4977}V^{1.0735} \tag{6.28}$$

These equations are valid for calculating compressive strength and hardness of AMC where aluminium alloy Al-6061 is the matrix and SiC_p as the reinforcement, produced by powder metallurgy method and

$$600 \leq T \leq 760\ °C$$
$$3 \leq t \leq 8.33\ hr$$
$$10 \leq v \leq 23\ \%$$

Equation (6.27) indicates that an increase in either the temperature or the volume fraction of reinforcement increases the compressive strength; an increase in time also increases the compressive strength. However, it should be noted that sintering temperature and the volume fraction of reinforcement have a major effect on the compressive strength.

Equation (6.28) indicates that an increase in either the temperature or the volume fraction of reinforcement increases the hardness; an increase in time also increases the hardness.

6.4.6 Developments of the Second Order Model

The second order model was developed to extend the variable range to describe adequately the relationship between the sintering operation output (compressive strength and hardness) and the investigated independent variables. The model was developed utilizing the composite design as shown in figure (6.4) and table (6.4).

The second-order model for the compressive strength, including only the significant terms in its transformed state is given by:

$$\begin{aligned}\hat{Y}_{comp.\,stren.} &= 5.6678+0.0789X_1+0.0549X_2+0.1908X_3 \\ &\quad -0.0221X_1^2-0.0236X_2^2+0.0286X_3^2\end{aligned} \tag{6.29}$$

and the second order model for hardness is

$$\begin{aligned}\hat{Y}_{hardness} &= 3.5716+0.1102X_1+0.1320X_2+0.5122X_3 \\ &\quad +0.0329X_1^2+0.0825X_2^2+0.3609X_3^2 \\ &\quad +.0696X_1X_2+.0649X_1X_3-0.0171X_2X_3\end{aligned} \tag{6.30}$$

6.4.7 Utilization of the 2nd Order Models

As can be inferred from figure (6.7) for second order model of compressive strength a better compressive strength is obtained at combination of high temperature and high volume fraction of reinforcement. However, in order to make a component using PM route and solid phase sintering, the temperature must be below the melting temperature of the material of lower melting point. From the contours shown in figure (6.7), it is possible to select a combination of volume fraction and sintering temperature that reduces the processing time and the cost without decreasing the compressive strength, since there is a large number of combinations of volume fraction and sintering temperature which produces the same compressive strength. These contours are straight lines so that the 2nd order model is not necessary.

The equation (6.30) has been plotted for hardness in figure (6.8) as contours (sections) for each of the response surface at a selected level of sintering time of 3, 5 and 8.33 hours. These contours were constructed by GT graphics package for determining the optimum operating condition of sintering process for a required hardness. From the contours shown in figure (6.8), it is possible to select a combination of sintering temperature and volume fraction of reinforcement that reduces the operating cost without reducing the hardness. The contours are all curves, so adequacy of the model is checked in respect of second order model.

6.4.8 Adequacy of the Model

The first order model was tested for compressive strength model by analysis of variance. The calculated ratio (F_{cal}) of the mean square lack of fit to the mean square of pure error is 6.44, while the tabulated F_{tab} ratio for 95% confidence at 5 and 2 degrees of freedom is 19.30. Hence the model is valid. The result of analysis of variance is shown in the following table (6.6).

Table 6.6 Analysis of variance for the first order model for compressive strength

Source	SS	DF	MS	F_{cal}	F_{tab}	Remarks
Zero order terms	379.56	1	379.56			
First order terms	0.44	3	0.146			
Lack of fit	0.01364	5	0.0087	6.444	19.30	Adequate
Pure error	0.0027	2	0.00135			
Blocks	0.03	1	0.03			
Residuals	0.04634	8				
Totals	380.046	12				

The second order model for hardness was tested by analysis of variance and showed the model was valid for 99% confidence interval. The result of analysis of variance for hardness model is shown in the following table (6.7).

Table 6.7 Analysis of variance for the second-order hardness model

Source	SS	DF	MS	F_{cal}	F_{tab}	Remarks
Zero order terms	363.01	1	363.01			
First order terms	4.6705	3	1.5568			
2nd order terms	1.6057	3	0.5352			
Interaction terms	0.593	3	0.1976			
Blocks	0.384	3	0.128			
Lack of fit	.898	3	.299	4.957	7.59*	Adequate
Pure error	0.4681	8	0.0585			
Residual	1.75	14				
Total	371.629	24				

* 99% confidence probability for $F_{rat\ 3,8}$

Conclusions

(1) Reliable compressive strength and hardness models have been developed and utilized to enhance the production system of MMC materials when using sinter forming route.

(2) The first-order compressive strength prediction equation is valid within the temperature range of 600-760 °C and can be extended up to the range of 570 -800 °C.

(3) Although the model has been developed and tested from very few experimental results, it can be used to predict the compressive strength for any conditions within the boundaries of this research.

(4) It is evident that a second order equation would not be appropriate for compressive strength model.

(5) The first-order hardness prediction equation is valid within the temperature range of 600-760 °C.

(6) By utilizing the second- order model for hardness, it is possible to extend the

variable range. The predicting equation is valid within the temperature range of 570-800 °C, the volume fraction range of 8-28 % and sintering time range of 2.43-10.3 hour.

(7) An increase of temperature and volume fraction of reinforcement and time increases the hardness.

(5) Response surface methodology provides a large amount of information with a small amount of experimentation.

6.5 FAILURE MODELLING FOR ZnO VARISTORS

6.5.1 Introduction

In this work, the electrical energy capability of the varistor disc with a $V_{nom}=5$ kV and a diameter of 42 mm during strength testing by giving various electrical charging shots had been analyzed in respect of different binder burnout rate and shrinkage rate. A mathematical model had been developed for the electrical energy during the initial failure and 50% failure of the samples to get the optimum temperature profile for sintering operation.

6.5.2 Postulation of the Mathematical Model

The energy capability of the varistors deteriorates if the binder burnout and shrinkage of the discs are not properly controlled. So, in this postulation of the mathematical model, the energy capability is assumed to be a function of wt. loss rate ($\dot{w}$ (g/kg/h)) and shrinkage rate, ($\dot{\delta}$ (μm/mm/h)) and can be written as

Energy capability= $f(\dot{w},\dot{\delta})$

The above form can be expressed mathematically as

$$E= C\,\dot{w}^{l}\,\dot{\delta}^{m} \tag{6.31}$$

Where E is the electrical energy capability (joules/cc) of the varistors, $\dot{w}$ is the binder burnout rate of the samples and $\dot{\delta}$ is the shrinkage rate of the samples during sintering operation and C, l and m are the model parameters to be estimated using experimental data.

Equation (6.31) can be written as

$$\ln E = \ln C + l \ln \dot{w} + m \ln \dot{\delta} \tag{6.32}$$

Equation (6.32) can be written as linear equation

$$\hat{y}_{varistor} = b_0 x_0 + b_1 x_1 + b_2 x_2 \tag{6.33}$$

where $\hat{y}_{varistor}$ is the proposed predictive response of energy on natural logarithmic scale, while $x_0=1$ and x_1, x_2 the coded values of $\dot{w}$ and $\dot{\delta}$ with logarithmic transformations respectively and b's are the model parameters. The basic formula of b is given as

$$b = (X^T X)^{-1} X^T Y \tag{6.34}$$

where $b=b_0$, b_1 and b_2 is the matrix parameter estimates, X is the calculation matrix, X^T is the transpose of X, X^TX is the variance matrix, $(X^TX)^{-1}$ is the covariance matrix which is the inverse of X^TX and Y is the matrix of measured response (output) on a logarithmic scale.

6.5.3 Experimental Design and Conditions

In order to estimate the model parameters of the equation, a first-order orthogonal design was used. This design consists of nine experiments which have been used to develop the first - order model. Four experiments represent a 2^2 factorial design, where the experimental points are located at the corner of a square as shown in figure (6.9). Five experiments represent added centre points to the square, repeated five times to estimate the pure error.

The variables are selected according to the experience in this field which can cover the whole range for binder burn out rate and shrinkage rate. The coded values of the variables used for this analysis shown in table (6.8). The independent variables were coded as

$$x_1 = \frac{\ln \dot{w} - \ln 1.5}{\ln 3 - \ln 1.5} \qquad (6.35)$$

$$x_2 = \frac{\ln \dot{\delta} - \ln 20}{\ln 40 - \ln 20} \qquad (6.36)$$

6.5.4 Experimental Procedure

First, the temperature profiles for different binder burnout rates and different shrinkage rates were generated. Then 40 samples were sintered using the above temperature profile in a pot kiln at the Development Facility of Harris Ireland. After sintering, the black discs were ground, electroded and glassed. The procedure of preparing the samples for electrical testing had been discussed before in section 5.2 of chapter five. The failure test was carried out by the strength tester (HAEFELY). The square wave form was given each time for 2 mili seconds. Initial charging voltage is the crucial one. It was selected in such a way that at first shot there should be no failure. A voltage of 22 kV had been chosen as the initial value. Each time the charging voltage was increased by 1.2 kV. During the shots, the sample temperature increased significantly due to the electrical energy absorbed by the ceramic. Thus the samples were cooled down by fan before testing at the next higher energy level. This work continued up to the failure of all samples. Normally the initial energy value was exhibited 108 j/cc and with each consecutive shots, it increased by 14-15 j/cc. A set of 24 samples were used for this test from each trial. The initial failure energy is important to look at due to its relevance for the arrester field performance. Normally if there are 5 discs fail on the sample lots of 350-400 discs, the lots are rejected or tested again. So the energy capability at the initial failure was considered as an output. The energy at 50% failure of the samples has been also analyzed to see the actual effect of binder burn out rate and shrinkage rate. The results and conditions are shown in table (6.9).

Table 6.8: Levels of the independent variable and coding identification for electrical energy capability at the initial failure and at the 50% failure of the samples

Independent variables	Levels in Coded form		
	-1 (low)	0 (centre)	+1 (high)
Binder burnout rate $\dot{w}$, g/kg/h	0.75	1.5	3
Shrinkage rate $\dot{\delta}$, μm/mm/h	10	20	40

6.5.5 Analysis of Results

The first order model of the electrical strength capability failure was developed by utilizing the least squares method. The parameters of the model were calculated with the help of equation (6.34). The mathematical model for the electrical energy capability at the initial failure can be developed by substituting the model parameters as:

$$\hat{y}_{(initial\ failure)} = 5.2259 - 0.1830\ x_1 + 0.0385\ x_2 \qquad (6.37)$$

Similarly by substituting the model parameters, the mathematical model for electrical energy capability at 50% failure can be expressed as:

$$\hat{y}_{(at\ 50\%\ failure)} = 5.5767 - 0.0385\ x_1 - 0.0730\ x_2 \qquad (6.38)$$

The predicting equations (6.37) and (6.38) are plotted in figures (6.10) and (6.11) respectively. These contours were constructed by computer utilizing the "GT" package. Figure (6.10) shows that the failure energy decreases with the decrease of wt. loss rate and slightly increases with the increase of shrinkage rate during the initial failure. But in figure (6.11) shows that the failure energy decreases with increase of wt. loss rate and shrinkage rate. So the lower values for shrinkage rate simultaneously wt. loss rate are desirable for increasing the performance of the discs.

Equation (6.37) and equation (6.38) can be transformed using equations (6.35) and (6.36) as:

$$E_{(initial\ failure)} = 175.308\ \dot{w}^{-.264}\ \dot{\delta}^{0.0555} \qquad (6.39)$$

and

$$E_{(50\%\ failure)} = 370.42\ \dot{w}^{-0.0555} \dot{\delta}^{-0.1053} \qquad (6.40)$$

Equation (6.39) indicates that the energy at initial failure of the disc decreases with the increase of binder burnout rate but increases with the increase of shrinkage rate. It is shown that there is considerable effect of binder burnout rate on the initial failure. But equation (6.40) shows that energy at 50% failure, decreases with the increase of binder

Table 6.9: Results and testing conditions for electrical energy capability during initial and 50% failure.

Trial No.	Wt. loss rate $\dot{w}$ g/kg/h	Shrinkage rate $\dot{\delta}$ μm/mm/h	Coding		Energy capability at initial failure $E_{ini.fail.}$ j/cc	Energy capability at 50% failure $E_{50\%\ fail.}$ j/cc
			x_1	x_2		
1	.75	10	-1	-1	267	310
2	3	10	1	-1	149	270
3	.75	40	-1	1	232	252
4	3	40	1	1	200	248
5	1.5	20	0	0	138	258
6	1.5	20	0	0	197	284
7	1.5	20	0	0	150	250
8	1.5	20	0	0	213	286
9	1.5	20	0	0	167	230

burn out rate and shrinkage rate. So for increasing the performance of the disc, the binder burnout rate and shrinkage rate should be as low as possible. These equations are valid for disc of V_{nom} =5 kV and of diameter 42 mm. and

$$.75 \leq \dot{w} \leq 3 \ \text{g/kg/h}$$

$$10 \leq \dot{\delta} \leq 40 \ \mu\text{m/mm/h}$$

6.5.6 Adequacy of the Predictive Model

The first order model was tested by analysis of variance. The calculated F value for the lack of fit and pure error is 1.983 whereas the tabulated value is 6.94. So the model is adequate. The result of analysis of variance is shown in the following table (6.10).

Table 6.10 Analysis of variance for the initial failure energy model for varistors

Source	SS	DF	MS	F_{cal}	F_{tab}	Remarks
Zero order terms	245.82	1	245.82			
1st order terms	0.1398	2	0.0699			
Lack of fit	0.13086	2	0.0654	1.983	6.94 *	Adequate
Pure error	0.13195	4	0.0329			
Residual	0.26281	6				
Total	246.22	9				

* 95% confidence limit for $F_{2,4}$

Conclusions

(1) Reliable predictive electrical energy capability models for predicting the energy at initial failure and 50% failure have been developed for varistors with a V_{nom}=5 kV and a diameter of 42 mm.

(2) Although the energy capability model has been developed and tested from

few experimental results, it can be used to predict the mean resultant energy capability for any condition within the boundaries of research.

(c) Energy capability at initial failure decreases with increase of binder burnout rate but slightly increases with increase of shrinkage rate.

(d) But energy capability at 50% failure decreases with increases of binder burnout rate and shrinkage rate.

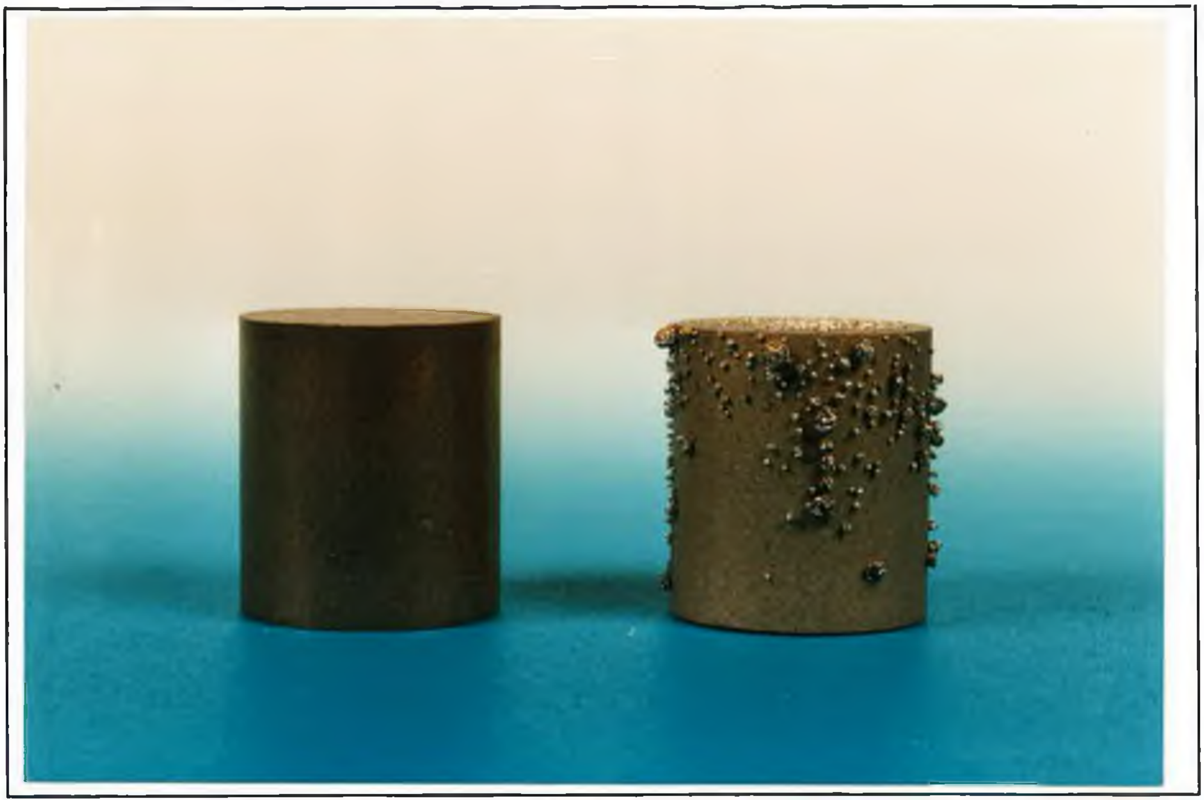

Plate 6.1 Sintered Al-6061/SiC composites disc with and without the adherance of the low temp. materials.

Plate 6.2 Photograph of two parts of Al-6061/SiC composite after cutting crosswise.

Plate 6.3 Photograph of fracture of Al-6061/SiC composites during compression test.

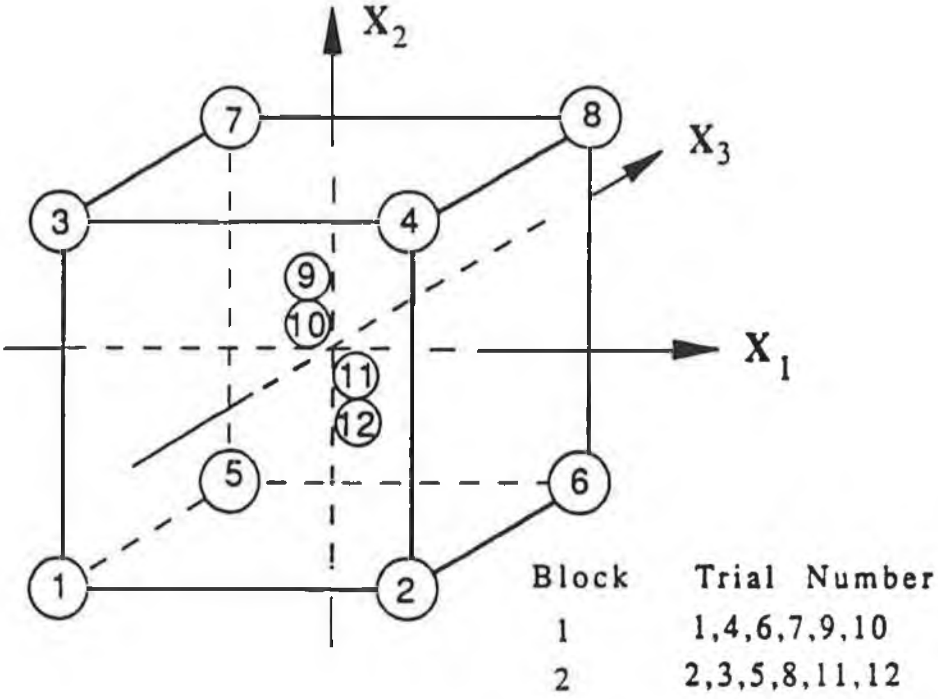

Block	Trial Number
1	1,4,6,7,9,10
2	2,3,5,8,11,12

Figure 6.1 First-order orthogonal design for 3 factors (K=3)

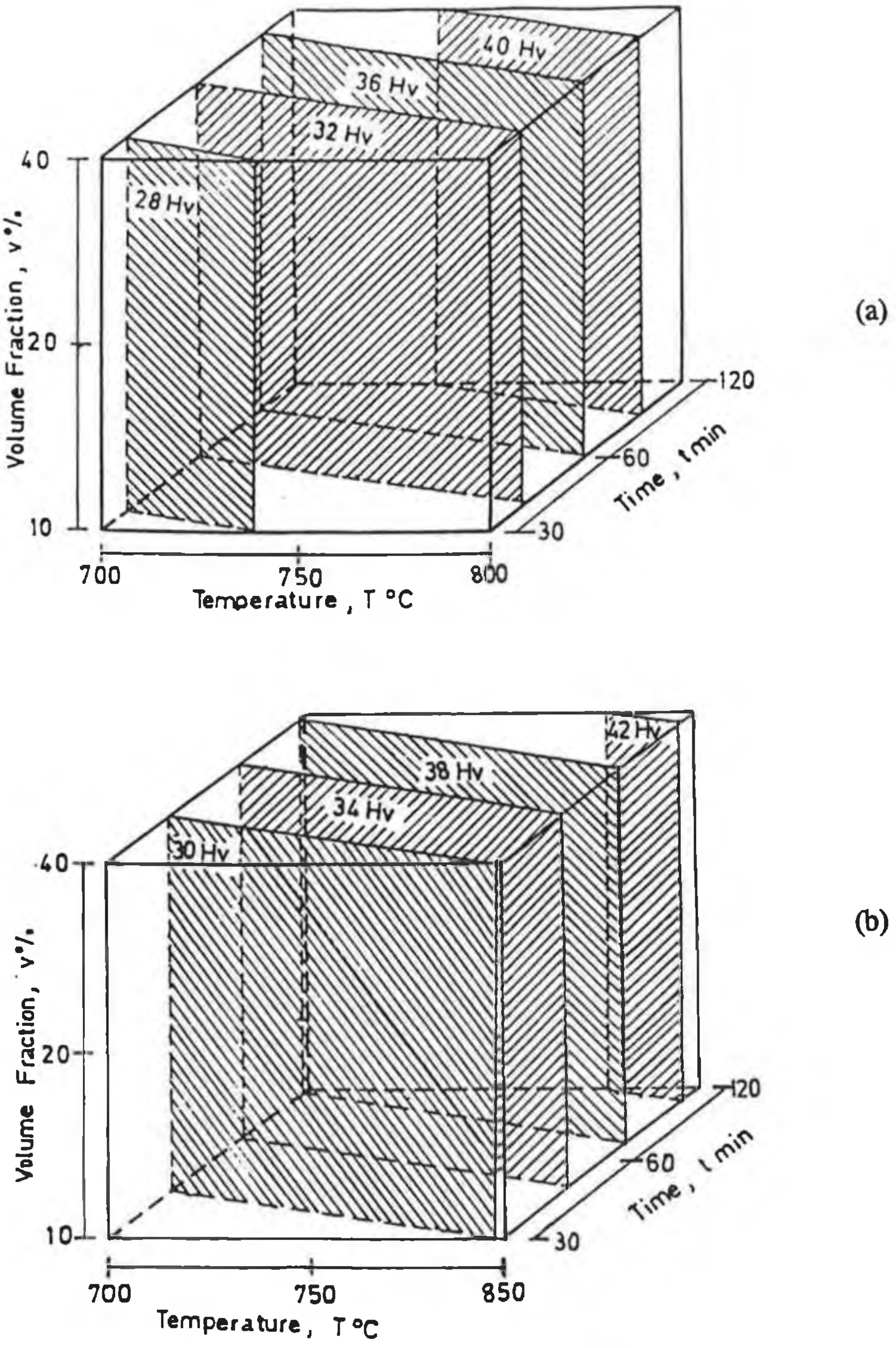

Figure 6.2 Hardness response planes, (a) H=28, 32, 36 and 40 Hv planes (b) H= 30, 34, 38 and 42 Hv planes

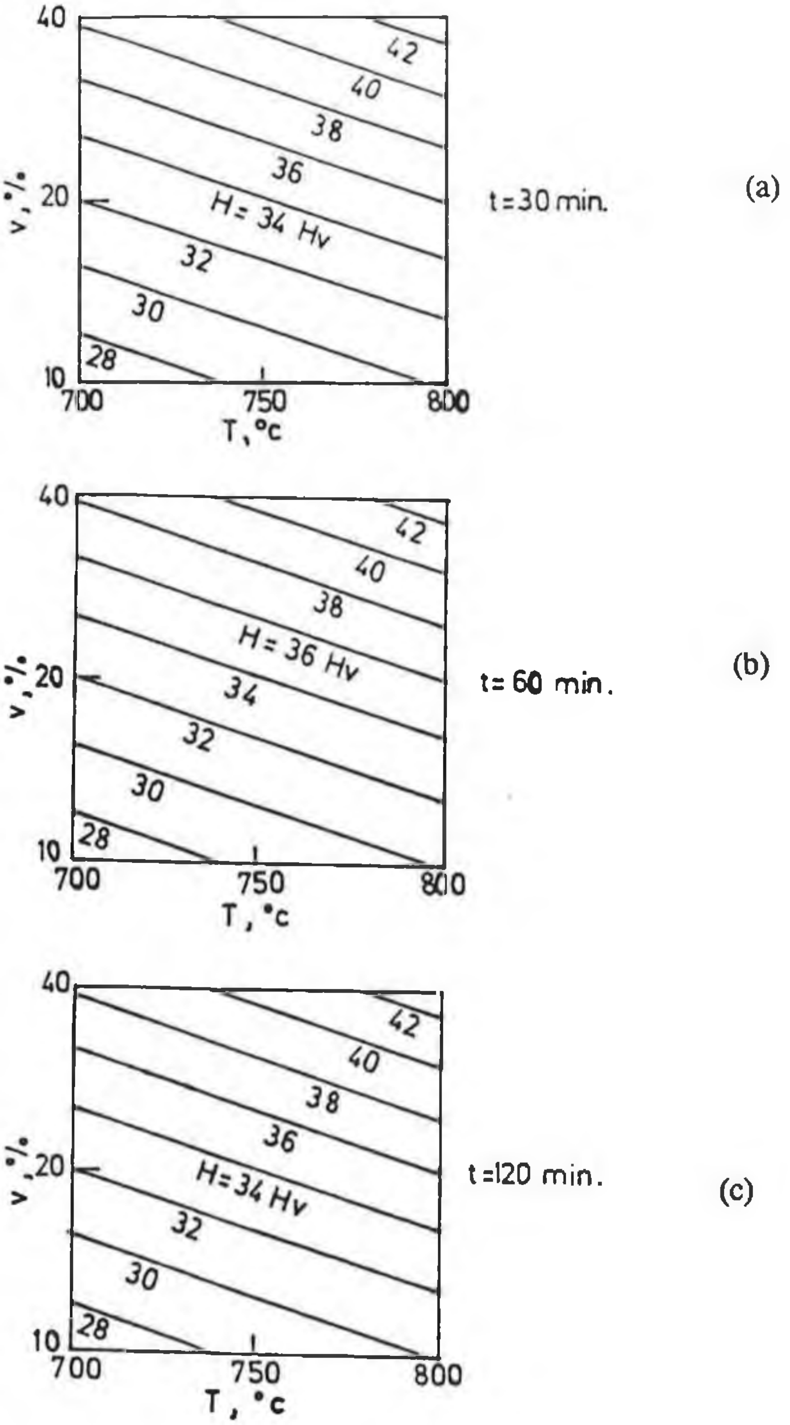

Figure 6.3 Hardness contours in Sintering temperature-Volume fraction of reinforcement at the selected levels of sintering time
(a) t=30 min. (b) t=60 min. and (c) t=120 min.

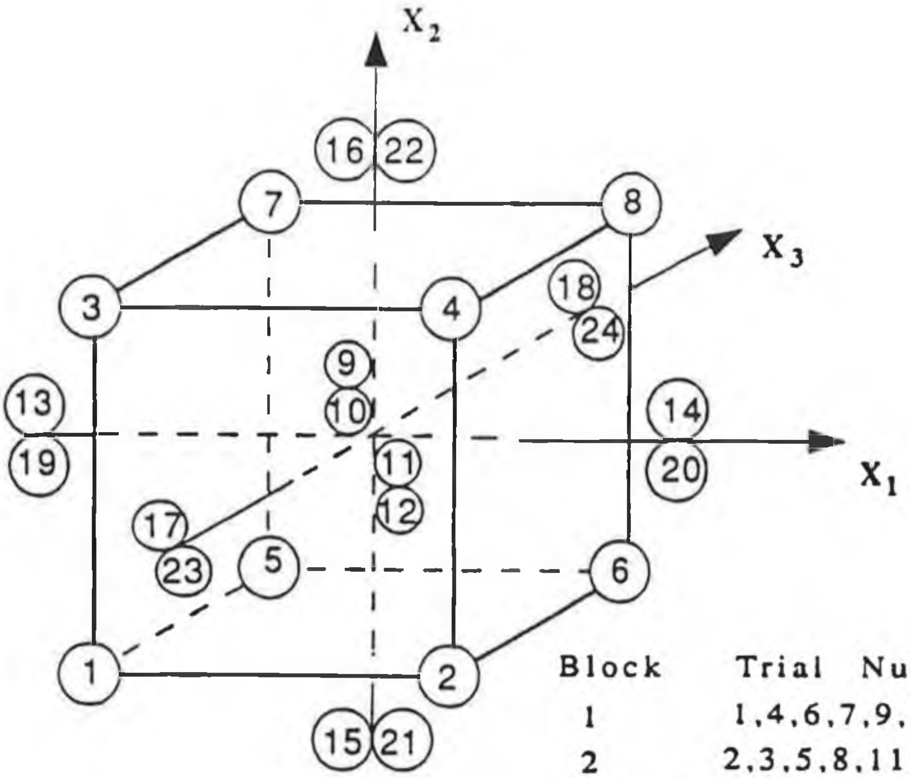

Block	Trial Number
1	1,4,6,7,9,10
2	2,3,5,8,11,12
3	13,14,15,16,17,18
4	19,20.21.22.23.24

Figure 6.4 Central composite design for 3 factors (K=3)

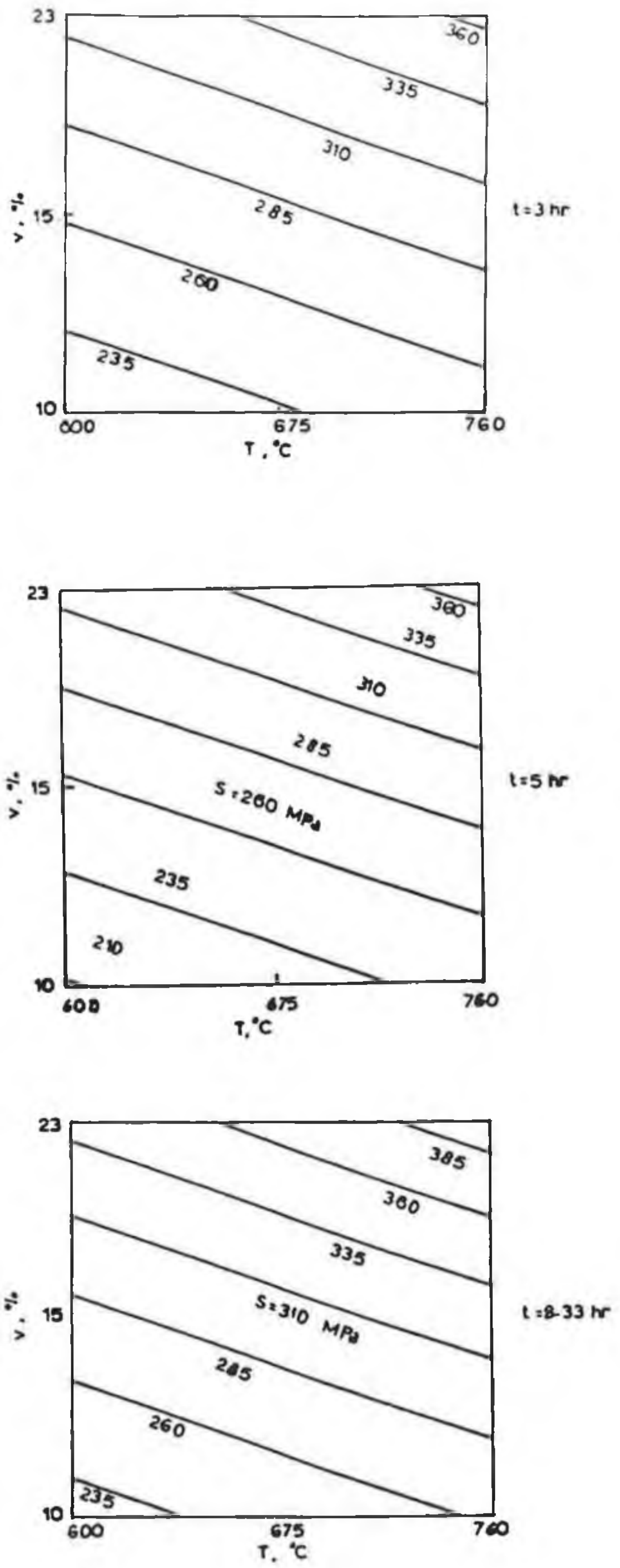

Figure 6. 5 Compressive strength contours (First order model) in sintering temperature-volume fraction planes at the selected levels of sintering time

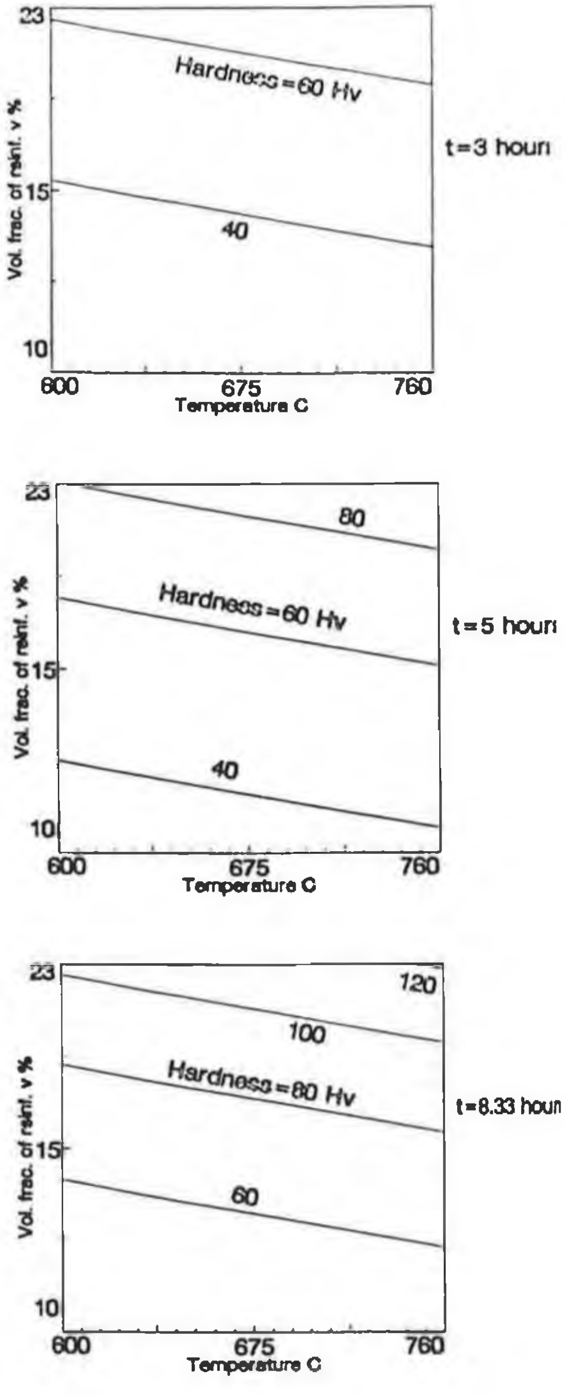

Figure 6.6 Hardness contours (1st order model) for Al-6061/SiC composites in temperature-vol. frac. of reinf. planes at selected levels of sintering time

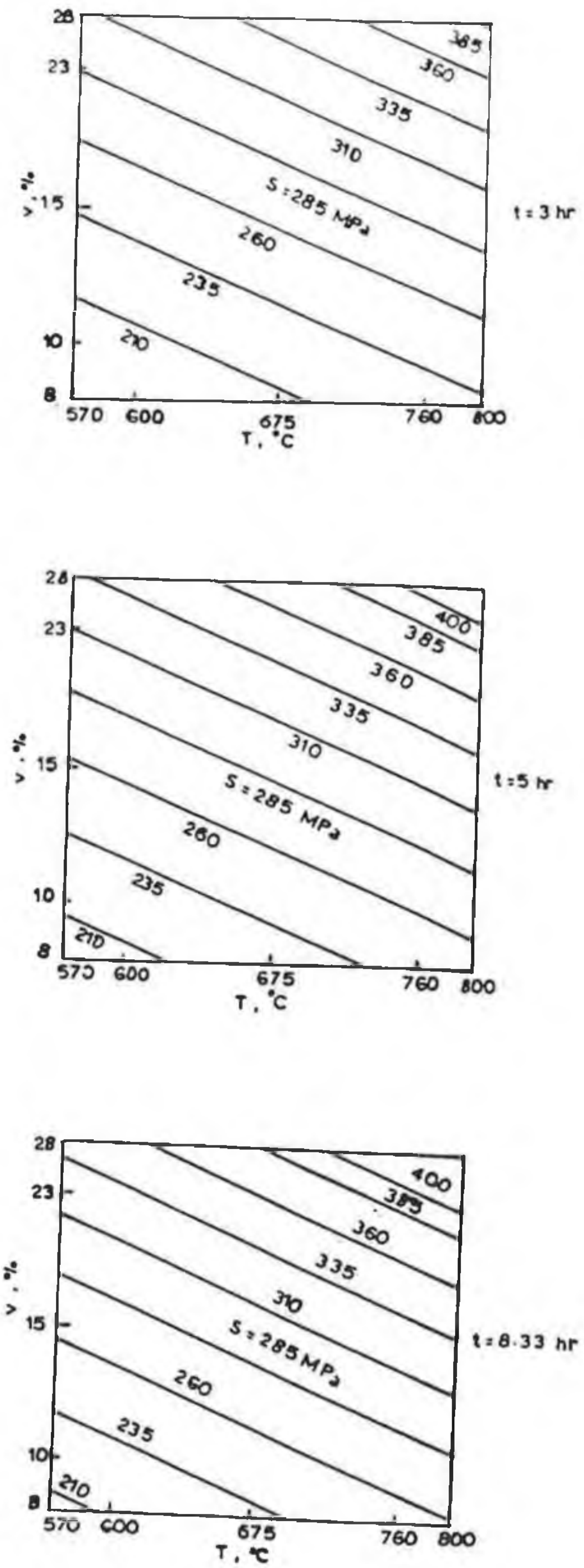

Figure 6.7 Compressive strength contours (2nd order model) in sintering temperature-volume fraction planes at the selected levels of sintering time

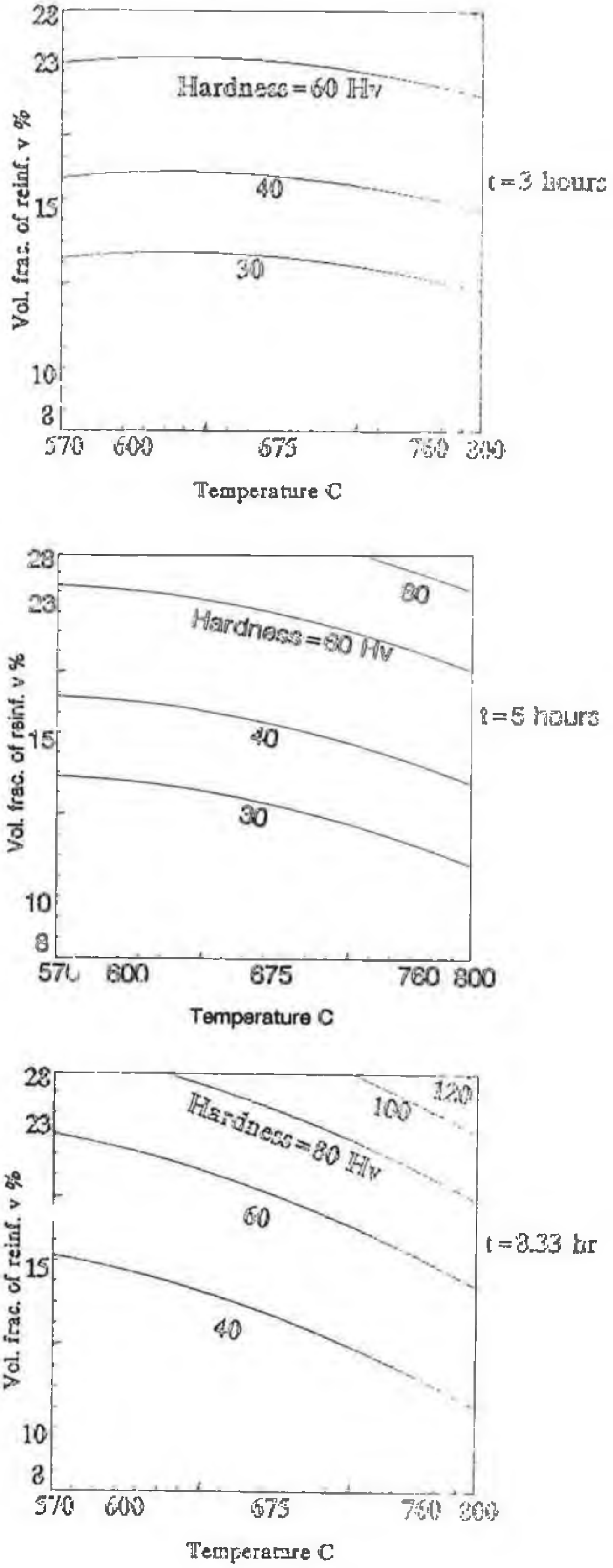

Figure 6.8 Hardness contours for second order model for Al-6061/SiC composites in temperature-vol. frac. of reinf. planes at selected levels of sintering time.

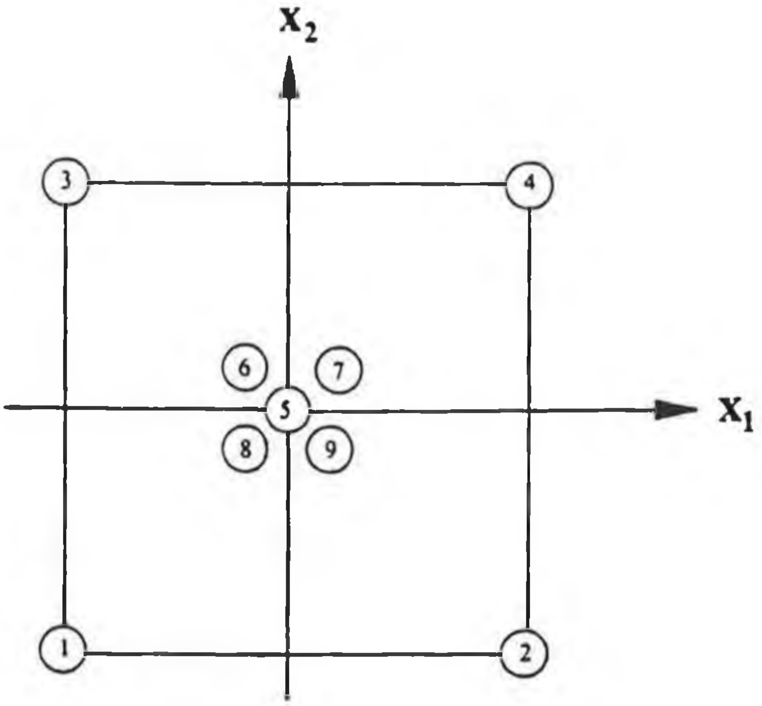

Figure 6.9 First-order orthogonal design for 2 factors (K=2)

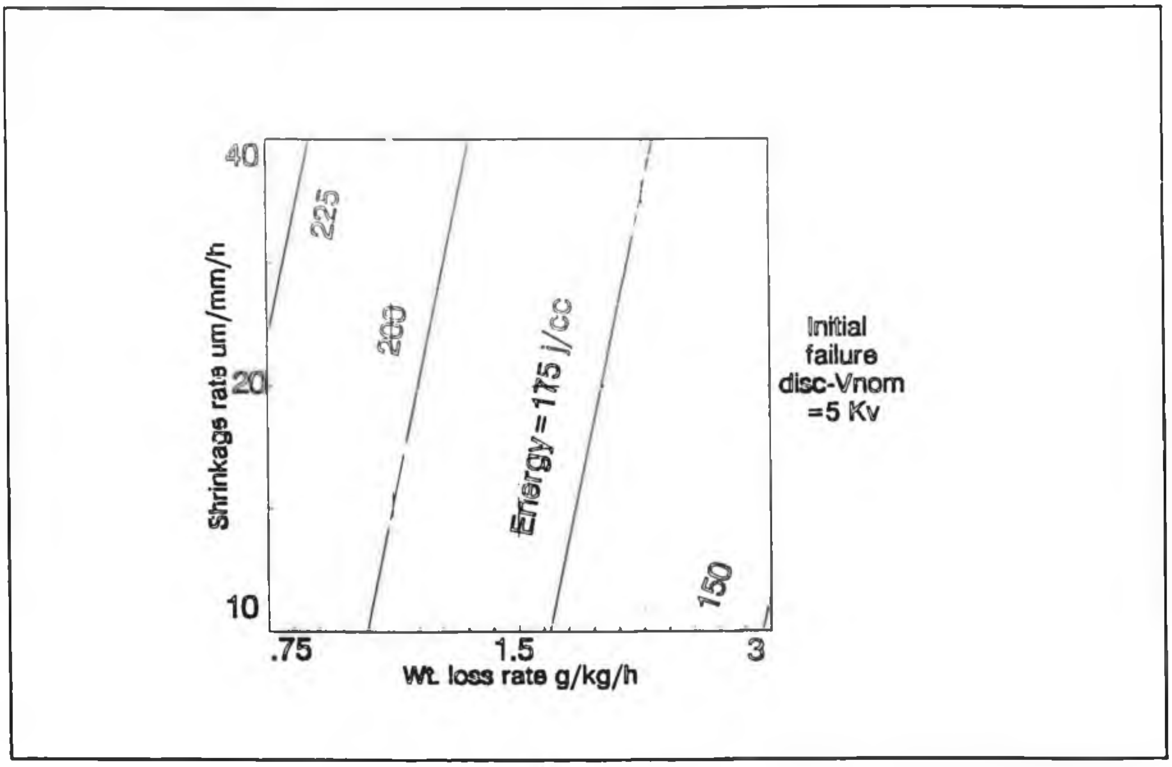

Figure 6.10 Energy capability contour at the initial failure (1st order model) for X1699 varistors in wt. loss rate-shrinkage rate planes.

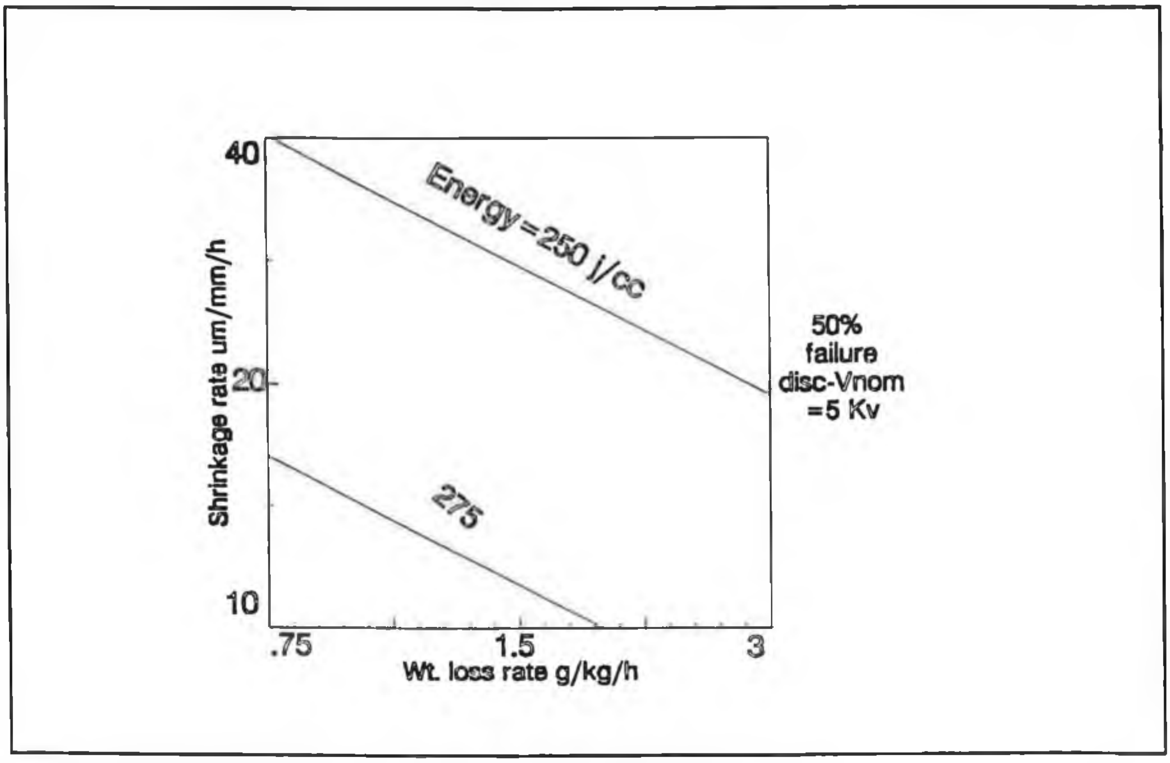

Figure 6.11 Energy capability contour at the 50% failure (1st order model) for X1699 varistors in wt. loss rate-shrinkage rate planes.

CHAPTER SEVEN

THEORETICAL MODELLING FOR THE FLOW STRESS BEHAVIOUR OF MMCs

7.1 INTRODUCTION

The stress of MMCs varies with the volume fraction of reinforcement, alignment of the fibres, size and shape of the particles and with the mismatch of the coefficient of thermal expansion. In this chapter the stress equation has been developed considering the effect of volume fraction of reinforcement, size and shape of the particles. The theoretical data are compared with the experimental results. There is good agreement between the experimental and theoretical data when considered the effect of volume fraction only. But theoretical value increases when the effect of the size and shape of the particles are considered.

7.2 DEVELOPMENT OF THE MATHEMATICAL MODEL

Consider an inclusion or inhomogeneity of ellipsoidal shape which is embedded in an elastic body (matrix). The elastic body has a domain Ω which has a non elastic strain or eigenstrain due to the inhomogeneity. If the total domain is D, the domain for the matrix is D-Ω. The elastic modulus tensor C_{ijkl} induces a stress field within and outside the inclusion. The Eshelby's model is shown in figure (7.1). According to

Eshelby [55], the average stress and strain of the inclusion becomes

$$\sigma = C\ (\epsilon - \epsilon^*) \tag{7.1}$$

where ϵ is the total strain and ϵ^* is the eigen strain and C is the elastic moduli tensor. The eigenstrain is determined by the Eshelby's tensor S by the relationship:

$$\epsilon = S\ \epsilon^* \tag{7.2}$$

Therefore

$$\sigma = C\ (S\ \epsilon^* - \epsilon^*) \tag{7.3}$$

In the above case, the elastic modulus tensor is considered the same for the inclusions and the matrix. But in an actual case, such as in composites, the stiffness tensor of the inclusion and the matrix are different. Suppose C_f and C_m are the stiffness tensors for fibre and matrix respectively.

Let an stress $\bar{\sigma}$ be applied to the body, a perturbed stress and strain are developed due to the mismatch of the elastic tensors of inclusions and matrix. So the stress in an inclusion becomes

$$\sigma_f = \bar{\sigma} + \sigma^{pt} = C_f\ (\epsilon_m + \epsilon^{pt}) \tag{7.4}$$

where $\bar{\sigma} = C_m\ \epsilon_m$, σ_f is the stress in the particle, ϵ_m is the strain of the matrix and σ^{pt} and ϵ^{pt} are the perturbed stress and strain respectively.

The eigen strain ϵ^* is only for inclusions, so its value will be zero in the matrix region.

If this inhomogeneity problem is reduced to the equivalent inclusion problem, then it can be written as

$$C_f\ (\epsilon_m + \epsilon^{pt}) = C_m(\epsilon_m + \epsilon^{pt} - \epsilon^*) \qquad (7.5)$$

So

$$\sigma_f = \overline{\sigma} + \sigma^{pt} = C_f(\epsilon_m + \epsilon^{pt}) = C_m(\epsilon_m + \epsilon^{pt} - \epsilon^*) \qquad (7.6)$$

The actual problem and the inclusion equivalent problem are shown in figure (7.2). In the above case, only the single inclusion inhomogeneity is considered where there is no interaction between the inhomogeneities. But in actual composites, there will be numerous inclusions and interaction between inhomogeneities will be important then. So we have to consider the effect of volume fraction in the actual case.

At finite concentration of particles, say with a volume fraction V_f ($0 < V_f < 1$), the average stress and strain in the matrix will be higher than that of only considering single inclusion and some additional value $\sigma^{\sim}$ and $\epsilon^{\sim}$, should be considered [56].

So the average stress and strain in the matrix will be $\sigma + \sigma^{\sim}$ and $\epsilon_m + \epsilon^{\sim}$ respectively. Therefore equation (7.6) can be modified as

$$\sigma_f = \overline{\sigma} + \sigma^{\sim} + \sigma^{pt} = C_f(\epsilon_m + \epsilon^{\sim} + \epsilon^{pt}) = C_m(\epsilon_m + \epsilon^{\sim} + \epsilon^{pt} - \epsilon^*) \qquad (7.7)$$

With the further constraint, equating the strength of composite to the strength of matrix and reinforcements

$$\bar{\sigma}=V_f\ \sigma_f+(1-V_f)\ (\bar{\sigma}+\sigma^{\sim})$$

$$\textit{Thus} \tag{7.8}$$

$$\sigma^{\sim}=-V_f\ \sigma^{pt}$$

Based on the above equations, using the elastic moduli of particle and a matrix and the Eshelby's tensor, the stress-strain relation of both phases can be determined. But in an actual case, there is same plastic deformation of the matrix which should be taken into account. So the above equations are not sufficient to calculate the deformation behaviour of the composites.

To facilitate the analysis for the elastic-plastic deformation of the composite let us introduce an identically shaped comparison material, with the property of the matrix as shown in figure (7.3).

Let the composite and the comparison material be both subjected to the same stress $\bar{\sigma}$. The strain in the comparison material $\epsilon_{(m)}$ is given by

$$\bar{\sigma}=C_{(m)}{}^{s}\ \epsilon_{(m)} \tag{7.9}$$

where $C_{(m)}{}^{s}$ is the secant moduli tensor of the comparison material at the applied stress state. The subscript, s and a parenthesis in a subscript represent a secant modulus and a comparison material respectively. Because of the inclusions of the particles, the average stress and strain in the matrix σ_m and ϵ_m are given by

$$\sigma_m=\bar{\sigma}+\sigma^{\sim}=C_m{}^{s}\ (\epsilon_{(m)}+\epsilon^{\sim}) \tag{7.10}$$

and

$$\epsilon_m=\epsilon_{(m)}+\epsilon^{\sim} \qquad (7.11)$$

For elastically deforming particles, the average stress and strain, σ_f and ϵ_f are given by

$$\begin{aligned}\sigma_f=\overline{\sigma}+\sigma^{\sim}+\sigma^{pt}&=C_f\ (\epsilon_{(m)}+\epsilon^{\sim}+\epsilon^{pt})\\ &=C_m^{\ s}\ (\epsilon_{(m)}+\epsilon^{\sim}+\epsilon^{pt}-\epsilon^*)\end{aligned} \qquad (4.12)$$

and

$$\epsilon_f=\epsilon_m+\epsilon^{pt} \qquad (7.13)$$

and again using Eshelby's tensor S_m corresponding to C_m, according to equation (7.2) can be written as

$$\begin{aligned}\sigma^{\sim}&=-V_f\ \sigma^{pt}\\ \epsilon^{pt}&=S_m^{\ s}\ \epsilon^*\end{aligned} \qquad (7.14)$$

Now from equations (7.9) and (7.10)

$$\sigma^{\sim}=(C_m^{\ s}-C_{(m)}^{\ s})\,\epsilon_{(m)}+C_m^{\ s}\epsilon^{\sim} \qquad (7.15)$$

and from equation (7.10) and (7.12)

$$\sigma^{pt}=C_m\ (\epsilon^{pt}-\epsilon^*)=C_m^{\ s}\ (S_m^{\ s}-I)\ \epsilon^* \qquad (7.16)$$

If $\sigma^{\sim}$ and σ^{pt} are substituted to equation (7.14), then

$$\begin{aligned} \epsilon^{\sim} &= -V_f\ (S_m{}^s - I)\ \epsilon^* - (I - C_m{}^{s-1}\ C_{(m)}{}^s)\ \epsilon_{(m)} \\ &= -V_f\ \epsilon^{pt} + V_f\ \epsilon^* - \epsilon_{(m)} + C_m{}^{s-1}\ C_{(m)}{}^s\ \epsilon_{(m)} \end{aligned} \tag{7.17}$$

where C^{S-1} is the inverse of C^S.

So from equations (7.12), (7.14) and (7.17)

$$\epsilon^* = -(C_m{}^{s-1}\ C^s_{(m)})\ \frac{\epsilon_{(m)}}{V_f\ I + (1-V_f)\ S_m{}^s + C_m{}^s} \tag{7.18}$$

when ϵ^* is known, the total strain of the composite is given by the weighted average of those of its constituents: this leads to

$$\begin{aligned} \overline{\epsilon} &= \epsilon_{(m)} + \epsilon^{\sim} + V_f\ \epsilon^{pt} \\ &= C_m{}^{s-1}\ C^s_{(m)}\ \epsilon_{(m)} + V_f\ \epsilon^* \end{aligned} \tag{7.19}$$

Based on the above mentioned model, the stress-strain behaviour of the particle reinforced composite can be calculated using the elastic moduli and the Eshelby's tensor of the particle and the stress-strain curve of the matrix.

The strain-stress curve for the matrix is generally represented by the following equation:

$$\sigma_m = h\ (\epsilon_m)^n \tag{7.20}$$

where h is the strength hardening constant and n is the strain hardening index. The value of h and n can be estimated from the experiment. When the stress strain curve of matrix material has been determined, then simultaneously the corresponding stress-strain curve of composite can be drawn from equation (7.18) and (7.19).

The Eshelby's tensor S_m deals with the geometry of the particles, and Mori-Tanaka's [56] concept for average stress considers the effect of volume fraction of reinforcement. In reality, there is an effect of particle size on the strength of the composite. So the equation (7.20) should be modified taking into account the effect of particle size.

During plastic flow in the matrix, the moving of dislocations may be restricted by the particles or secondary dislocations may be generated around the particles. The accommodating plastic flow shall give rise to a substantially increased dislocation density and hence to hardening of the matrix. Ashby [58] proposed a secondary slip model for explaining such a effect of a non-deforming particle in a plastic matrix. According to Ashby, the increase in the flow stress $\Delta\sigma_m$ of the matrix for a composite containing equiaxed particle is given by

$$\Delta\sigma_m = K_c G \left(V_f \frac{b}{d} \epsilon_m\right)^{\frac{1}{2}} \tag{7.21}$$

where d is the diameter of the particle, b is a Berger's vector and K_c is a constant, the value of which can be taken as 0.75 for the aluminium matrix composites and G is the matrix shear modulus.

So the general equation for the stress- strain relation of the matrix in the composite is represented as

$$\sigma_m = h\,(\epsilon_m)^n + K_c G \left(V_f \frac{b}{d} \epsilon_m\right)^{\frac{1}{2}} \tag{7.22}$$

Equation (7.22) in many cases can also be written as

$$\sigma_m=\sigma_y+h\ (\epsilon^p)^n \qquad (7.23)$$

where σ_m is the flow stress at the plastic strain ϵ^p and σ_y, h and n are the initial yield stress, the strength coefficient and the work-hardening exponent.

In a composite system, the stress and strain state of the matrix is usually triaxial. Equation (7.23) can be generalised to such a state by means of Von Mise's effective stress σ^* and strain ϵ^{p*} as

$$\sigma_m^*=\sigma_y+h\ (\epsilon^{p*})^n \qquad (7.24)$$

but

$$\sigma_m^*=b_0\ \overline{\sigma} \qquad (7.25)$$

where b_o is the stress concentration factor which is a function of Eshelby's constant, volume fraction of reinforcement and shear modulus of the material [54].

So for under uniaxed compression, the constitutive equation (7.24) can be rewritten as to provide the flow stress of the composite as

$$\overline{\sigma}=\frac{1}{b_0}[\sigma_y+\ h\ (\epsilon^{p*})^n] \qquad (7.26)$$

The details of the equations and calculations can be seen in Appendix G.

7.3. NUMERICAL RESULTS AND COMPARISON WITH EXPERIMENTS

A composite of Al-6061 reinforced with SiC particles has been considered for the comparison. The composites are manufactured by the sinter-forming route. Green disc of composites were produced by cold pressing at volume fractions 0, 10, 15, 23 and 28 % of SiC of particle size 75 μm. The green discs were fired in a pot kiln at 700 °C for 1 hour keeping sintering atmosphere air. After firing, the compression test of these discs was carried out by INSTRON machine. True stress and strain were calculated from the compression test. Figure (7.4) shows the effect of volume fraction of SiC particles which is drawn from the experimental data. Here the work hardening rate and strain hardening index are calculated from the experimental data of the matrix and the values are 124 and 0.23 respectively. The value of h is low, since the sintered sample's density has not been achieved as theoretical density. Figure (7.5) shows also the effect of volume fraction of reinforcement where the data taken from theoretical calculation. The theoretical calculation has been done with the help of equations (7.20) and (7.25) where secondary dislocation has not been considered. Figure (7.6) shows the comparison between the experimental and the theoretical results. Here the theoretical value always gives the lower value than that of experiment. It is because in theoretical calculation the effect of particle size is not considered. Figure (7.7) shows the effect of volume fraction considering the dislocation model. Equation (7.22) is used for the calculation. In this case the stresses are higher than those which are calculated without dislocation model. The value of the stresses are also higher than those of the experimental values. The effect of the ratio of the length and diameter of the cylindrical particle is shown in figure (7.8). The calculation is based on Ashby's [58] secondary slip model. The stresses for the 23% volume fraction are higher than those of the stresses for the 10% volume fraction for the same l/d. The strain-stress characteristics of composites mainly depends on the strain-stress relationship of the matrix material. Since the strain-stress characteristics of matrix material varies with the sintering parameter, the deformation nature of the composites will be also changed simultaneously. In this present case, the calculation is valid only for the sintering time 1 hr and sintering temperature 700 °C with air as a sintering atmosphere. This model can be generalised for the sintering process by using the mechanical properties of matrix and reinforcement materials for different sintering condition.

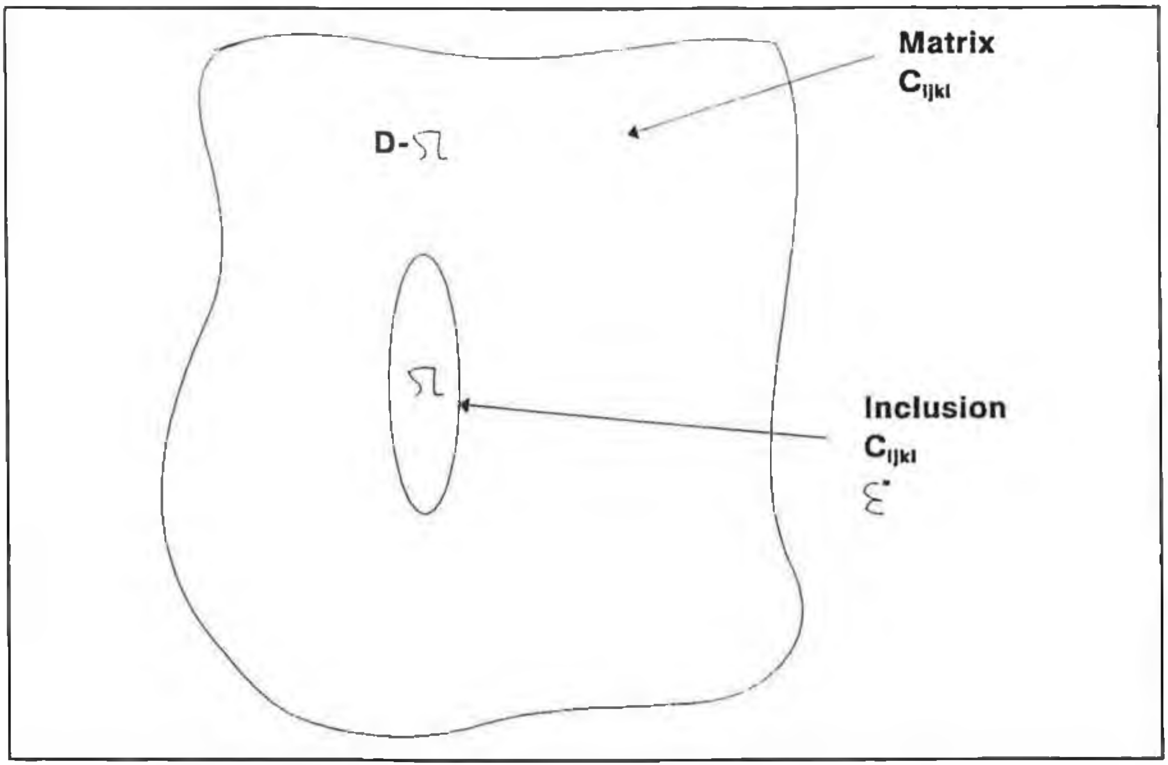

Figure 7.1 Eshelby's model.

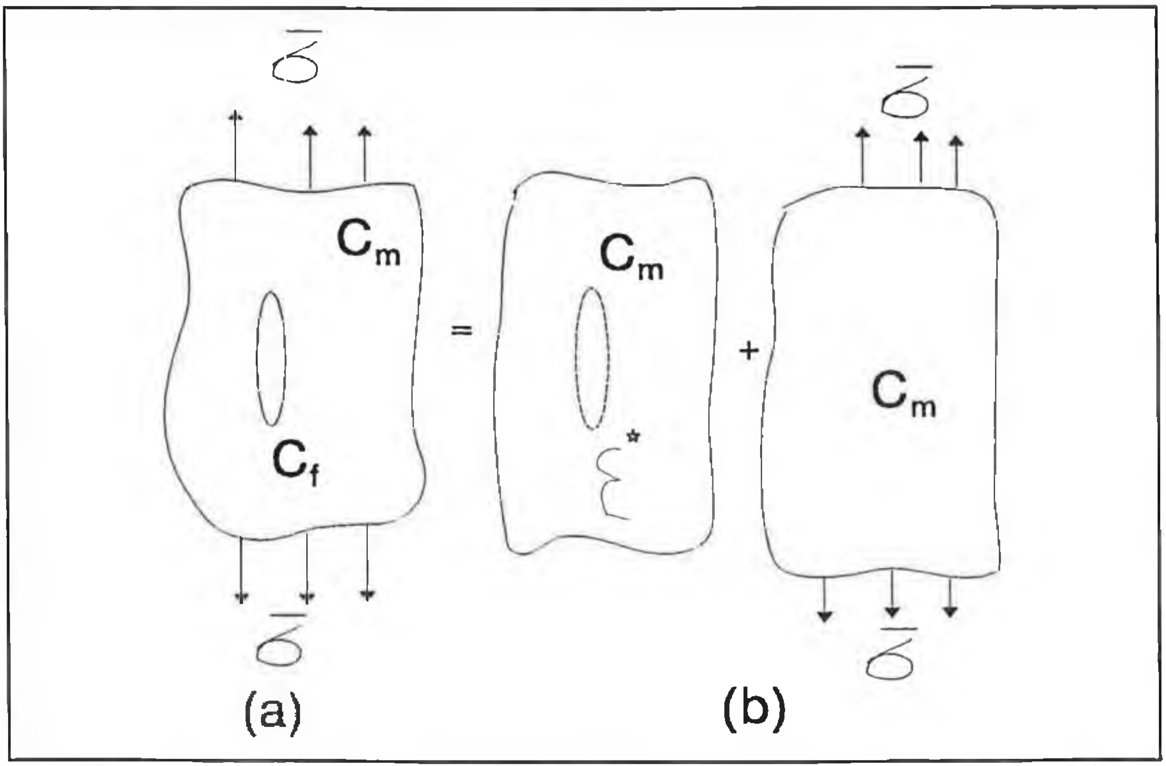

Figure 7.2 Infinite matrix with inhomogeneous particle subjected to applied stress (a) actual problem (b) equivalent inclusion problem.

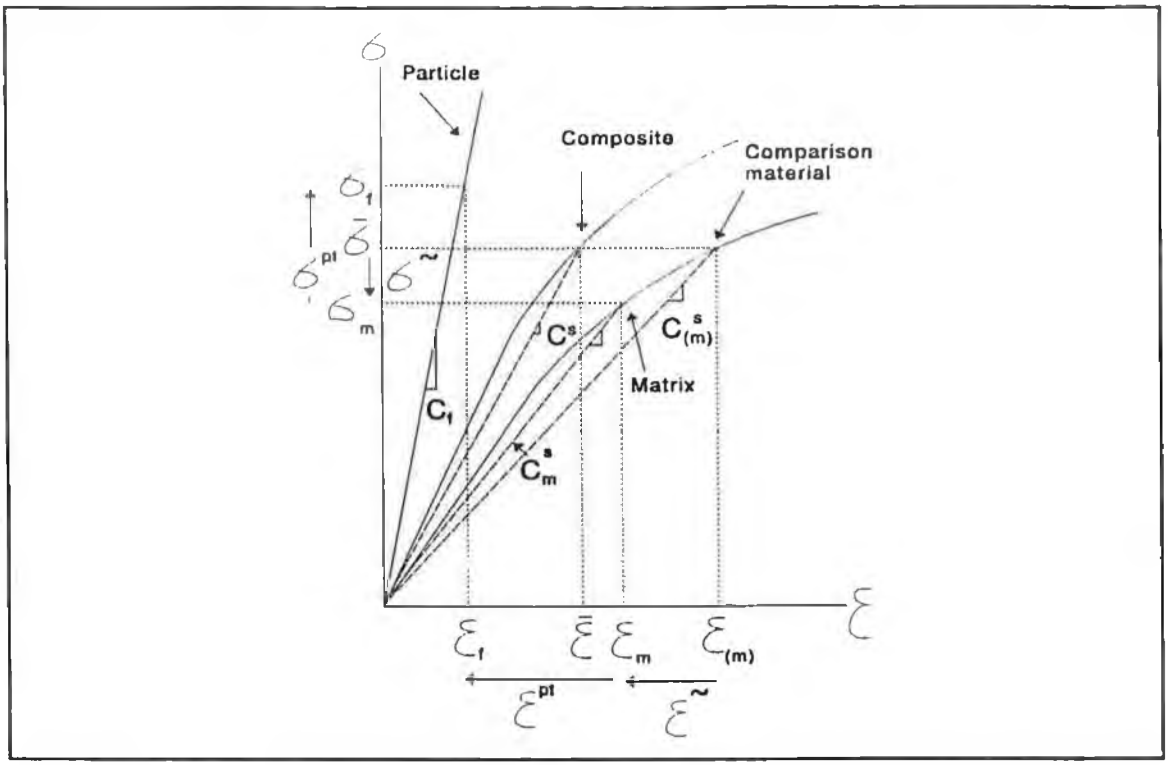

Figure 7.3 Schematic representation of the avearge stress and strain state of the constituents.

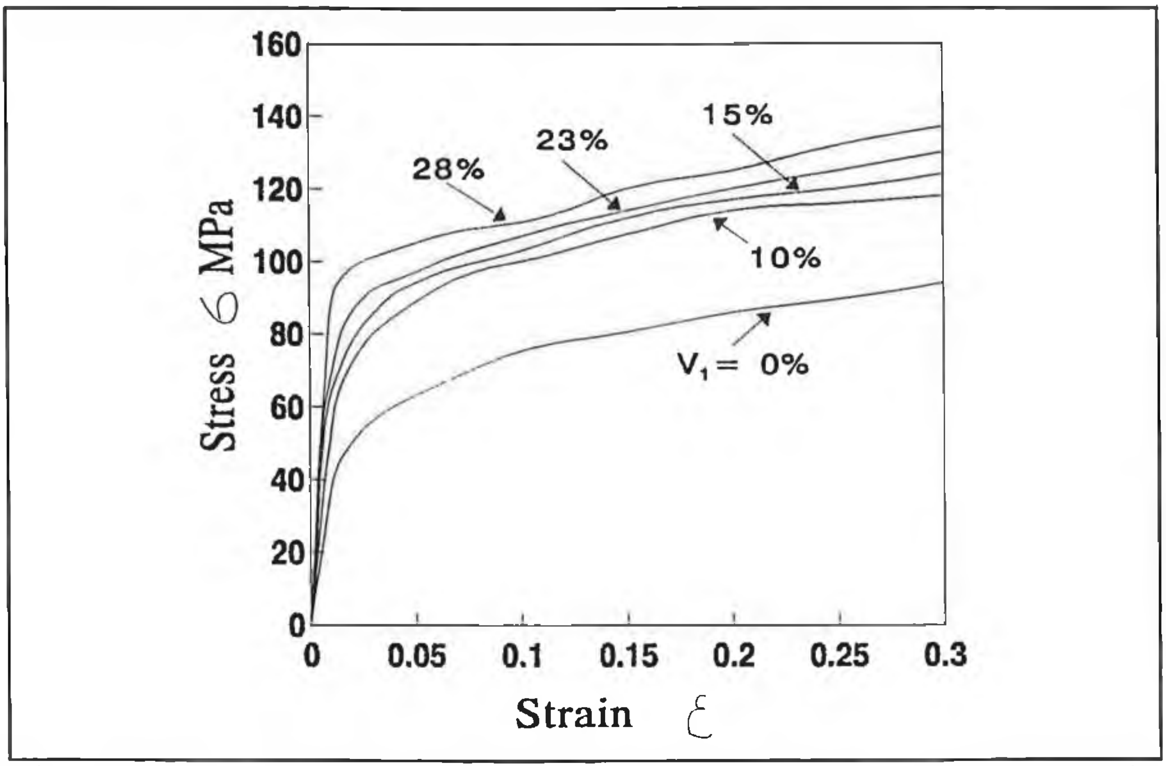

Figure 7.4 Stress-strain curves of the Al-6061/SiC composites under uniaxial compression (exp. data).

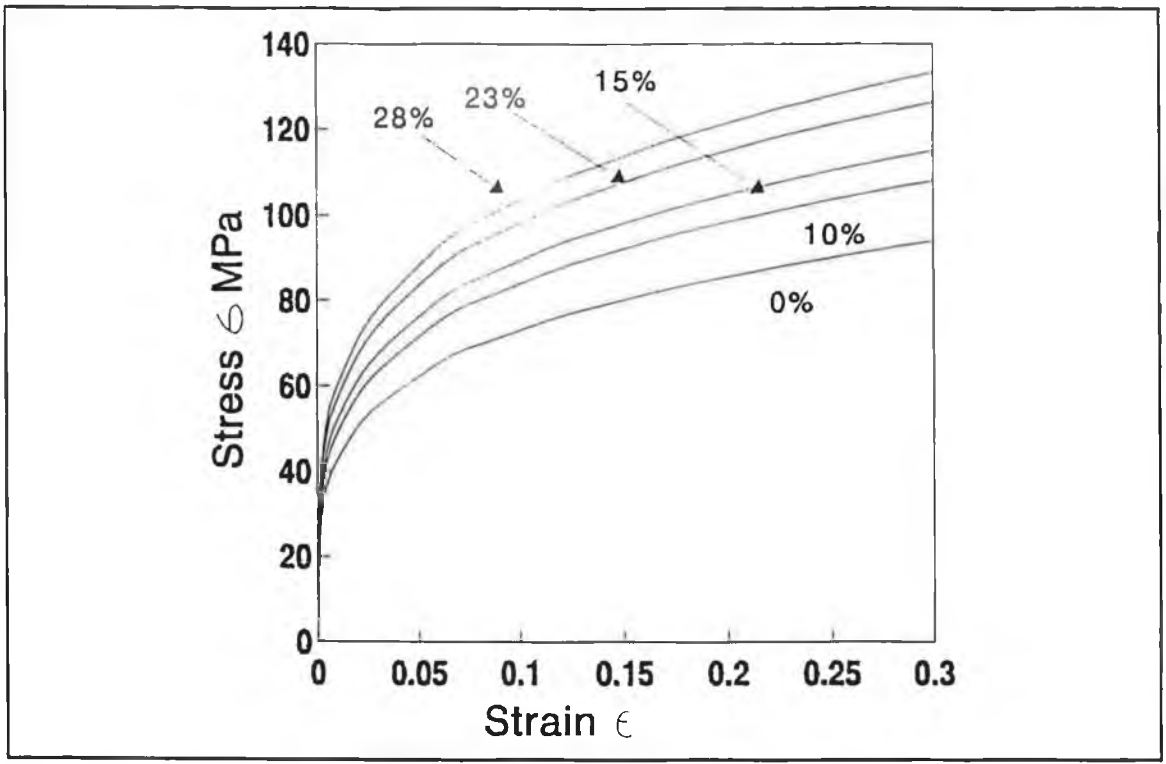

Figure 7.5 Stress-strain curve (theoretical data)

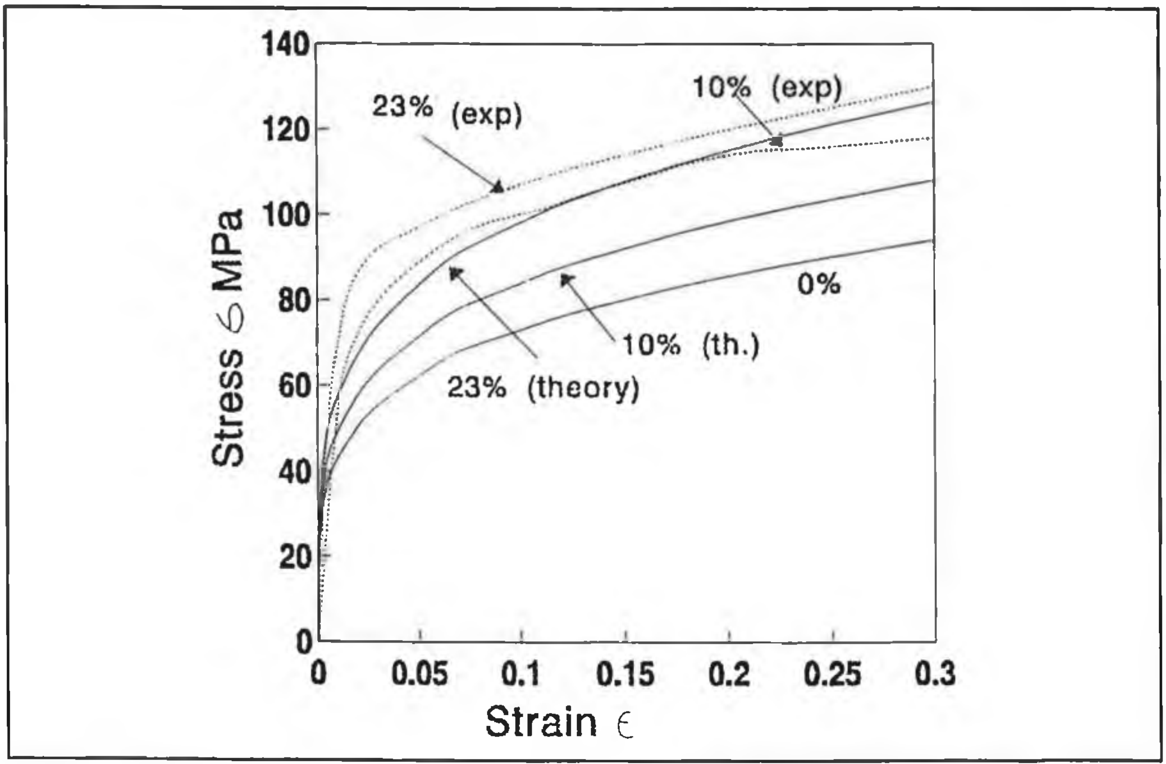

Figure 7.6 Comparison of the theoretical predictions with experimental data.

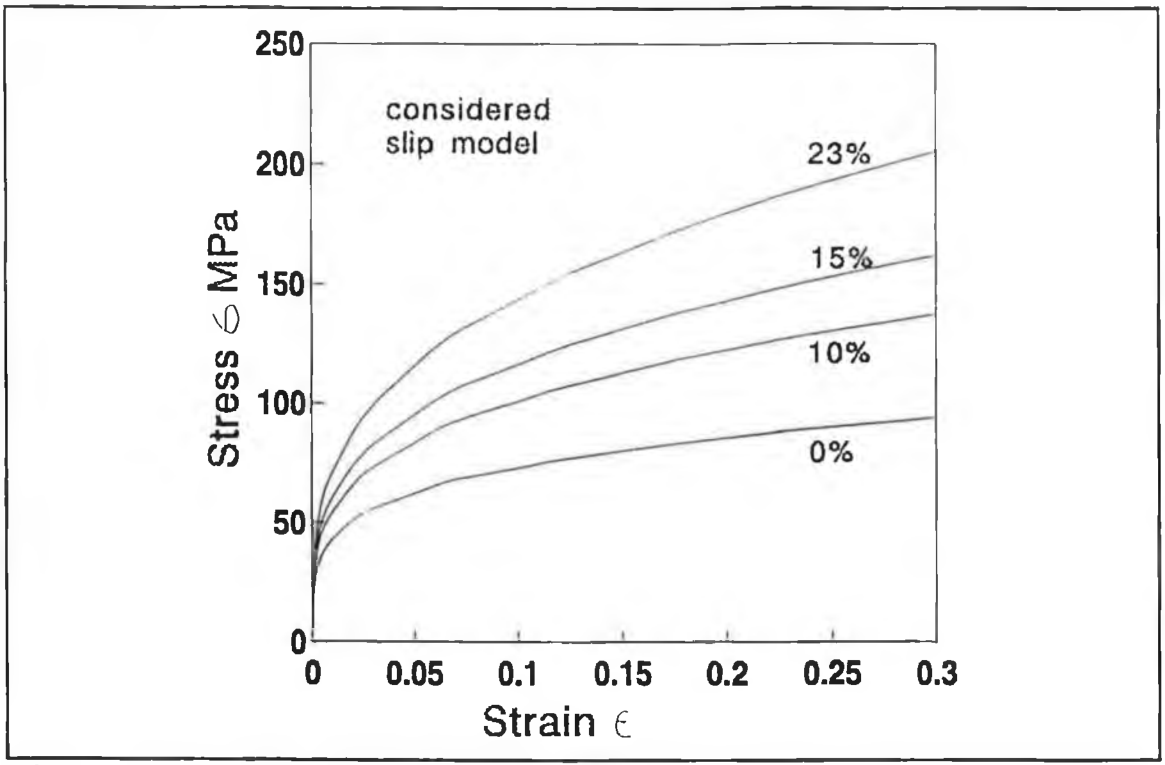

Figure 7.7 Stress-strain curve with considered slip model.

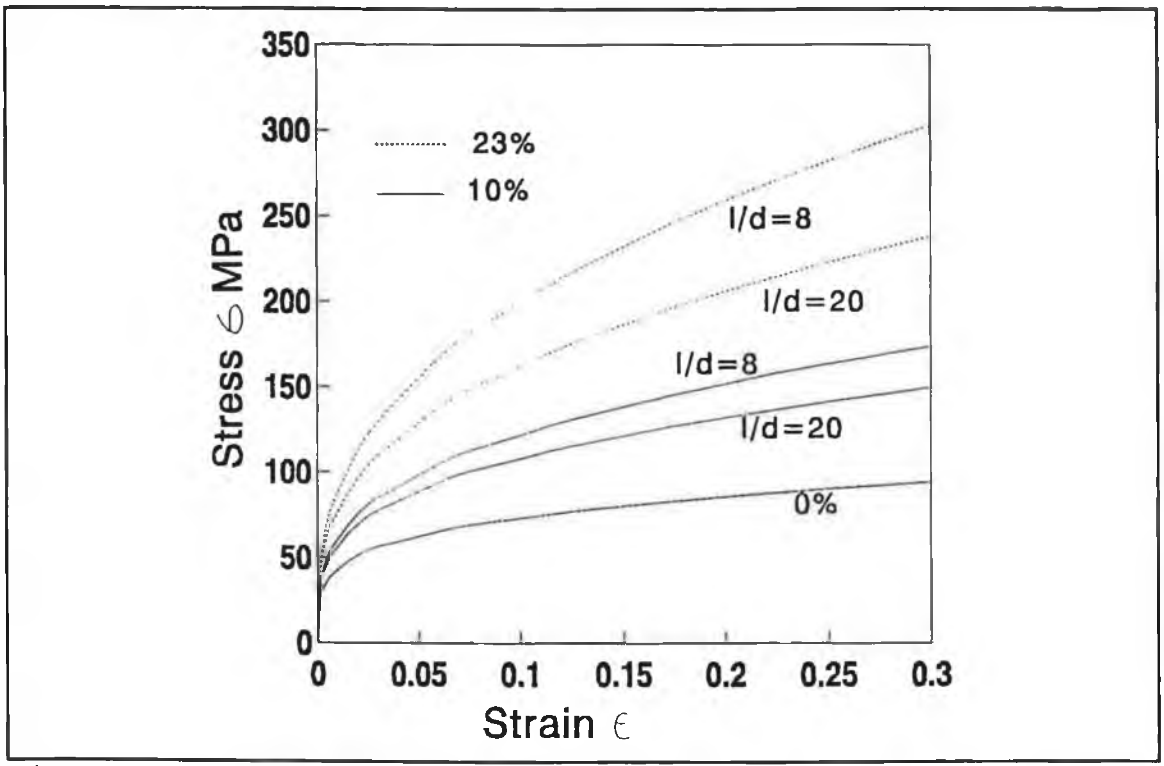

Figure 7.8 Stress-strain curve considering the size effect.

CHAPTER EIGHT

CONCLUSIONS AND RECOMMENDATIONS

8.1 CONCLUSIONS

8.1.1 Metal Matrix Composites

In MMCs, matrix powders of pure aluminium and aluminium alloy were used with particle size 400 and 45 μm respectively. As reinforcement, Al_2O_3 and SiC powders were used with average particle sizes 45 and 75 μm. The compressibility and strength of the Al/Al_2O_3 and Al-6061/SiC composites were determined in respect of lubrication amount, lubrication type, amount of reinforcement and sintering time and temperature.

- The compressibility does not vary with the lubrication amount and type but decreases with increase of reinforcement. With probability of failure, it shows that the 1% amount of lubrication gives the higher reliability. Though calcium stearate lubrication shows some increase in reliability of the green product, it gives a lower strength value than that obtained with zinc stearate.
- The compressive strength of Al/Al_2O_3 composites decreases with increasing amount of reinforcement. Because an expansion of the disc takes place as a big particle size of matrix powder was used which retards the sintering operation. But higher sintering temperature and longer sintering time accelerates the sintering process.

- The hardness value of Al/Al_2O_3 increases with an increase of sintering temperature and volume fraction of reinforcement but slightly decreases with an increase of sintering time.
- Al-6061/SiC composites give better performance over Al/Al_2O_3 composites mostlikely due to the use of smaller particle of matrix.
- The theoretical model for the flow stress behaviour of MMCs has been established taking into account the particle size, particle shape and volume fraction of reinforcement. A good agreement between theoretical data and experimental data has been obtained.

8.1.2 Zinc Oxide Varistors

- Two computer programmes have been developed, one for controlling the binder burnout and the other for controlling the shrinkage which are fully capable of generating a temperature profile automatically that produces a linear wt. loss and a linear shrinkage of the discs at predetermined rates.
- The temperature profile generated by the wt. loss rate limit 0.75 g/kg/h and the shrinkage rate limit 10 μm/mm/h gives the optimum firing profile as regarding the energy capability of the product. Normally some of the discs will fail before 150 j/cc when sintered using the conventional firing profile. No disc will be failed before 200 j/cc when using this optimized rate controlled temperature profile. This optimized firing profile also improves the leakage current characteristics.
- This firing profile simultaneously reduces the sintering time which can eventually reduce the production cost and increase the productivity.

- The rate controlled sintering also produces smaller grain size with more uniform distribution and reduces the porosity. These improvements in materials characteristics can translate in enhanced electrical properties.
- The optimized firing profile does not improve the failure characteristics at high amplitude-short duration pulses (4/10 current waves). But the firing profile with wt. loss rate limit 0.75 g/kg/h and shrinkage rate limit 40 μm/mm/h shows a better result as compared with those obtained with the other profiles.
- The model for energy capability failure was developed with respect to wt. loss rate limit and shrinkage rate limit. This model shows that at the initial failure, the energy capability increases with the decrease of wt. loss rate but slightly increases with increase of shrinkage rate. For 50 % failure, the model shows that the energy capability of the product decreases with increase of wt. loss rate and shrinkage rate. So lower value of wt. loss rate and shrinkage rate should be chosen for the best performance of the firing profile.

8.2 RECOMMENDATIONS

8.2.1 Metal Matrix Composites

The work of composite was carried out to see the sintering parameters on the mechanical strength of composite mainly hardness and compressive strength. It is recommended to work on the following areas :

- In this project, large particle sizes of the matrix and reinforcement were used. A further work can be carried out using small particle size in the range of 15 to 20 μm.

- Aluminium alloy with different grades such as 8xxx and magnesium alloy can be used as matrix materials for the further works.
- TiB_2 and Si_3N_4 can be used as the reinforcement materials for further investigations.
- A further study can be carried on compaction to see the effect of other compaction parameters such as holding time, load releasing time, binders.
- Other mechanical properties, such as tensile strength, fatigue can be investigated to see the effect of the compaction parameters as well as sintering parameters.
- A study can be done to increase the density and strength of the fired disc using hot and cold extrusion after sintering.
- Further study can be done using CIP and HIP for the manufacturing of composites.

8.2.2 Zinc Oxide Varistors

The study of rate controlled sintering was carried out for the varistors of $V_{nom}=5$ kV and diameter of 42 mm. So it is recommended to use and for further works on the following areas:

- The rate controlled sintering technology can be used for other varistors powders such as MEO (multi- elemental oxides).
- This rate controlled sintering technology can be expanded for other ceramic products such as multilayer devices.
- Since the firing profile varies with the size of the product and the binder percentage, the optimized firing profile will be also varied. It is better to use an average

firing profile can be used for the sintering operation. To find out this temperature profile a series of experiments can be carried out by varying binder percentage and using different sizes of discs.

- Shrinkage plays a dominant part for the high amplitude short duration pulses. So a further study can carried out to find out a new temperature profile combining the firing profile for different wt. loss rate and shrinkage rate which gives no failure in 100 kA test.
- The two computer programmes developed during this present work can be updated for a "Windows" platform by using Visual Basic.
- To monitor and control the evolved gas composition during sintering, chemical sensors can be incorporated which can be coupled with the computer for further control and optimization of the profile. These programmes then can be modified to control the atmosphere conditions in the furnace.

REFERENCES

[1] Chou, T.W, Kelly, A. and Okura, A.,"Fibre reinforced metal matrix composites" Composites, 16(1985) 187.

[2] Vinson, J.R. and Chou, T.W., Composite Materials and their use in structures, appled Science Publishers, London, 1975.

[3] Prewo, K.M. and Kreider, K.J., Metall. Trans, 3(1972) 2201.

[4] Metacalfe, A.G., in: Broutman, L.J. and Krack, R.H. (Eds.), Composite Materials, Vol 4, Academic Press, Newyork, 1974.

[5] Smith, P.R., Froes, F.H., and Cammett, J.T.,"Mechanical Behavior of Metal-Matrix Composites" in: Hack, J.E. and Amateau, M.F., TMS of AIME, Warrendale, PA 1983, p. 143.

[6] Champion, A.R., Krueger, W.H., Hartman, H.S. and Dhingra, A.K., "Fibre FP reinforced metal matrix composites", Proc. Int. Conf. on Composite Materials, AIME, Warrendale, PA 1978, p. 1883.

[7] Bhagat, R.B., "High pressure squeeze casting of stainless steel wire reinforced aluminium matrix composite", Composites, 19(1988) 393.

[8] Fukunaga, H. and Goda, K., "Composite structure of silicon carbide fibre reinforced metals by squeeze casting", Bull of JSME, 28(1985) 1.

[9] Fukunaga, H., Adv. Mater. Manuf. Process., 3(1988) 669

[10] Singer, A.R.E and Ozbek, S., "Metal matrix composites produced by spray codeposition" Powder Metall. 28(1985) 72.

[11] White, J. and Willis, T.C., "The Production of Metal Matrix Composites by Spray Deposition" Mater. Des., 10(1989) 121.

[12] Hosking, F.M., Portillo, F.F., Wunderline, R. and Mehrabian, R., J. Mater. Sci., 17(1982) 477.

[13] Abis, S., "Characteristics of an Aluminium Alloy/Alumina Metal Matrix Composite" Compos. Sci. Technol., 35(1989) 1.

[14] Kohara, S. and Muto, N., "Fabrication of Silicon Carbide Fiber Reinforced Aluminum Composites" Recent advances in composites in the united states and

Japan, ASTP 864, 457.

[15] Milliere, C. and Surey, M., "Fabrication and properties of metal matrix composites based on SiC fibre reinforced aluminum alloys", Mater. Sci. Tech., 4(1988) 41.

[16] Majumder, B.S., Yegneswaran, A.H. and Rohatgi, P.K., Mater. Sci. Eng., 68(1984) 85.

[17] Neih, T.G. and Chellman, D.J., Scr. Metall., 18(1984) 925.

[18] Divecha, A.P., Fishman, S.G. and Karmarkar, S.D., J. Met. 9(9181) 12.

[19] Wu, M.Y. and Sherby, O.D., Scr. Metall., 18(1984) 773.

[20] Girot, F.A., Quenisset, J.M. and Naslain, R., "Discontinuously reinforced aluminum matrix composites", Compos. Sci. Technol, 30 (9187) 155.

[21] Taya, M. and Arsenault, R.J., Metal Matrix Composites- Thermomechnical Bhaviour, Pergamon Press, 1988.

[22] Rack, H.J., Baruch, T.R. and Cook, J.L. in: Hayashi, R., Kawata, K. and Umekawa, S. (Eds), Progress in Science and Engineering of Composites, (Proc. ICCM-4), Japan Society for Compos. Mater., Vol. 2, 1982, P. 1465.

[23] Erich, D.L., "Metal matrix composites; Problems, Applications and Potential in the PM industry", Met. Powder Rep., 43 (June, 1988) 418.

[24] Smith, P.R. and Froes, F.H., J. Met., 36(1984) 19.

[25] Huda, D., El-Baradie, M.A. and Hashmi, M.S.J., Metal matrix composites: Manufacturing aspects. Part I, J. of Mat. Proce. Tech., 37(1993) 513-528.

[26] Trumper, R.L., "Metal matrix composites-application and prospects", Met. Mater., 3(1987) 662.

[27] Feest, E.A., Ball, M.J., Begg, A.R. and Biggs, D., "Metal matrix composites developments in japan" Report on OSTEM visit to Japan, Otober, 1986.

[28] Kainer, K.U., "Influence of the production technique and type of reinforcement on the properties of magnesium matrix composite", PD-Vol-37, Compos. Mater. Technol., 37(1991) 191.

[29] Arsenault, R.J. and Flom, Y., "Role of interface in SiC/Al Compoistes", Proceedings of a Symposium on Structure and Deformation of Boundaries, Oct. 13-17, Toronto, ONT, Canada, p. 261-279.

[30] Haar, J.H., Materials Science and Engg., 1991, A135, 65.

[31] Kao, A. and Koczak, M.J., "Mixing and Compaction Behaviour of Ferrous Powders" The Int. Jour. of Pow. Mett. and Pow. Tech, 1980, 16(2) 105.

[32] Frey, R.G. and Halloran, J.W., "Compaction Behaviour of Spray -Dried Alumina" J. Am. Ceram. Soc. 1984, 67(3) 199.

[33] Dynys, F.W. and Halloran, J.W., "Compaction of Aggregated Alumina Powder", J. Am. Ceram. Soc., 1983, 66(9) 655.

[34] Al-Tounsi, A., Puyane, R. and Hashmi, M.S.J., "Compaction of agglomerated zinc oxide powder", Journal of Materials Processing Technology, 37(1993) 543-550.

[35] Lubaba, N.C., Rand, B. and Brett, N.H., "Compaction studies of MgO-flake graphite mixtures relevant to the fabrication of composite refractory materials" Brit. Ceram. Trans. and Journal, 87(5), 1988, 158.

[36] Kim, T.W., Yoon, K.J., Jun, E.J. and Lee, W.I., "Compaction behaviour of composite laminates during cure" Sampe Journal, 1988, 24(5) 33.

[37] Reily, j.j. and Kamel, I.L., "Characterization and cold compaction of polyether-etherketone powders", Polymer Engg. and Science, 1989, 29[20], 1456.

[38] Huda, D., El-Baradie, M.A. and Hashmi, M.S.J., "Compaction Behaviour of Metal Matrix Composite", Key Engineering Materials, Vol. 86-87 (1993), pp. 85-92.

[39] Lal, S. and Upadhyaya, G.S., "Sintering of stainless steel and their based composite", Rev. Powder Metall. and Physical Ceramics, 3(2) 1986, 165-203.

[40] Liu, Y.L., "Microstructure, Texture and Mechanical Properties of Al-SiC_w Composites Manufactured by Powder Blending", Proc. of the 1989 Powder Metallurgy Conference and Exhibition, San-Diego, U.S.A. Jun 11-14, 1989, vol 3, p 461-474.

[41] Kloucek, F and Singer, R.F., "Properties of short fibre reinforced aluminium alloys", Proc. of Advanced materials research and developments for transport composite 1985, Nov, 26-28, France 1985, 249-256.

[42] Bassani, J.L. and Taggart, D.G., "Mechanics of matrix sintering in composites", Presented at the winter annual meeting of the American Society of Mechanical Engineers, Boston, Massachusetts, Dec. 13-18, 1987.

[43] Kanetake, N., "Deformation behavior and upsettability of particle dispersed aluminium matrix composites", Advanced Technology of Plasticity, Vol. 1, 1990, 53.

[44] Maclean, M. and Dower, R., "Aluminium alloy short fibre MMC using the PM

route", Proceedings of the World conference on powder metallurgy, 2-6 July, 1990, London, Vol. 2, pp. 251-254.

[45] Jha, A.K., Prasad, S.V. and Upadhyaya, G.S., "Sintering behaviour of 6061 aluminium alloy composites containing soft and hard dispersoids" Proceedings of the World conference on powder metallurgy, 2-6 July, 1990, London, Vol. 3, pp. 204-205.

[46] Thellman, E.L., Sandman, B.E. and Harrigan, W.C., "Application of powdered base metal matrix composites to torpedoes", Materials Science and Engineering, 68 (1984) 85.

[47] Metals and Materials for Research and Industry, Goodfellow metals limited, Catalogue, Cambridge Science park, cambridge CB4 4DJ, England, 1992-1993, p. 458.

[48] Divecha, A.P., Fishman, S.G. and Foltz, J.V., "Properties of SiC whisker reinforced aluminium alloys", The Enigma of the Eighties: Environment, Economics, Energy, SAMPE, Series, 2(1979) 1433.

[49] Mura, T., Micromechanics of Defects in Solids, 2nd ed. Martinus nijhoff Publishers, 1987.

[50] Taya, M., "Strengthening Mechanisms of Metal Matrix Composites", Material Transactions, JIM, 32(1) 1991, 1.

[51] Kelly, A., Strong Solids, 2nd ed. Oxford University Press, 1973.

[52] Nardon, V.C. and Prewo, K., Scripta Metal., 20(1986) 43.

[53] Weng, G.J., "Some Elastic Properties of Reinforced Solids, With Special Reference to Isotropic Ones Containing Spherical Inclusions", Int. Jour. of Engg. Sci., 22(1984) 845.

[54] Tandon, G.P. and Weng, G.J., "A Theory of Particle-Reinforced Plasticity", Transactions of the ASME, 55(1988) 126.

[55] Eshelby, J.D., "The Determination of the Elastic Field of an Ellipsoidal Inclusion, and Related Problems", Proc. of Royal Soc., london, A241(1957) 376.

[56] Mori, T. and Tanaka, K., "Average Stress in the Matrix and Average Elastic Energy of Materials with Misfitting Inclusions", Acta Metall., 21(1973) 571.

[57] Kanetake, N. and Ohira, H., "Analytical study on deformation behaviour of metal matix composites", J. of Mat. Pro. Technology., 24(1990) 281.

[58] Ashby, M.F., Strengthening Methods of Crystals, Kelly, A. and

Nicholson, R.B. (eds.), Elsevier, London, 1971, 137.

[59] Lange, F. and Kellett, B., "Influence of particle arrangement on sintering",

[60] Yeh, T. and Sacks, M., "Effect of green microstructure on sintering of alumina", paper presented at the 90th Annual meeting and exposition, Cincinnati, Ohio, May 1-5, 1988.

[61] Sarma, B. and Rama Mohan, T.R., "Initial sintering of Zinc Oxide", Transactions of the PMAI, Vol. 2, 1975 pp 27-33.

[62] Tetsuya, S. and Richard, C. B., "Grain growth in sintered Zno and ZnO-Bi_2O_3 ceramics", J. Am. Ceram. Soc. 73(1), (1990), pp 106-14.

[63] Debashis, D. and Richard, C.B., "Grain growth of ZnO during Bi_2O_3 liquid phase sintering", J. Am. Cram. Soc. 75(9) 1992, pp 2529-34.

[64] Kim, J., Kimura, T. and Yamaguchi, T., "Effect of Bismuth Oxide content on the sintering of Zinc Oxide", J. Am. Ceram. Soc. 72980 1989, pp 1541-44.

[65] Trontelj, M. and Kojar, D., "Sintering and grain growth in doped Zno", Journal of materials science letters, 13(1978), 1832-1834.

[66] Tsurumi, T. and Bowen, H.K., Binder burnout, CPRL report, Q4 MIT Cambridge, 1985, 48.

[67] Chu, M., Rahman, M.N. and De Jonghe, L.C., "Effect of heating rate on sintering and coarsening", J. Am. Ceram. Soc., 74(6), 1991, 1217.

[68] Kaysser, W.A. and Lenhart, A., "Optimization of densification of ZnO during sintering", Powder Metallurgy International , 13(3), 1981, pp 126-128.

[69] Chun Dong, C. and H.Kent Bowen, H.K., "Hot-stage study of bubble formation during binder burnout", J. Am. Ceram. Soc. 72(6) 1989, pp 1082-87.

[70] Huckabee, M.L. and Palmour III, H., "Rate controlled sintering of fine - Grained Al_2O_3", American Ceramic Society Bulletin, 51(7), 1972 pp 574-576.

[71] Al-Tounsi, A., Puyane, P. and Hashmi, M.S.J., "Weight loss control during the firing process of enhanced ZnO varistor", Proceedings of the 1992 powder Injection Moulding symposium, Editors Booker, P.H., Gaspervich, J. and German, R.M., June 21-26, San Francisco, Marriot hotel, San Francisco, California, U.S.A.

[72] Al-Tounsi, A., Puyane, R. and Hashmi, M.S.J., "Control of weight loss using closed feed back loop during the firing process of ZnO varistor", Presented at the 8th International symposium on Ceramic, Italian ceramic centre, Rimini

(Italy), November 10-12, 1992.

[73] Strauss, J.T. and German, R.M., "Analytical furnace and closed-loop feedback controlled sintering", Physical Chemistry of Powder Metals, Production and Processing Ed. Murray Small, W., The Minerals Metals and Materials Society, 1989, pp 83-91.

[74] Lackey, W.J., Angelini, P., Caputo, A.J., Devore, C.E., Mclaughlin, J.C., Stinton, D.P. and Hutchens, R.E., "Rate-Controlled Technique for Calcining and Drying", Communications of the American Ceramic Society,1984 ,pp c-102 to 104.

[75] Palmour III, H., Huckabee, M.L. and Hare, T.M., "Microstructural Development During Optimized rate Controlled Sintering", Ceramic Microstructure '76, Eds, Fulrath, R.M. and Pask, J.A., pp-308-319.

[76] Verweij, H. and Bruggink, W.H.M., "Reaction-Controlled Binder Burnout of Ceramic Multilayer Capacitors", J.Am. Ceram. Soc. 73(2) 1990, 226-231.

[77] Al-Tounsi, A., Puyane, R. and Hashmi, M.S.J., "Rate controlled shrinkage of ZnO varistors", Proceedings of International Conference AMPT' 93, 24-28th August, 1993, Dublin City University, Dublin 9, Ireland, pp. 2049-2055.

[78] Winkler, S., Davies, P. and Janoschek, J., "High-teperature dilatometer with pyrometer measuring system and rate controlled sintering capability", Journal of Thermal Analysis, Vol. 40, no. 3, 1993, pp. 999-1008.

[79] Speyer, R.F., Echiverri, L. and Lee, C.K., "A shrinkage Rate-Controlled Sintering Dilatometer", Journal of Materials Science Letters, Vol. 11, Iss. 16, 1992, pp. 1089-1092.

[80] Schwartz, M.M., Composite Materials Handbook, McGraw-Hill Book Company, 1984.

[81] Gilliland, R.G., "MMC-their structure, design, processing and application", Symposium on future industrial Technology, Kobe, Japan, March 23, 1988.

[82] Pai, B.C. and Rohatgi, P.K., J. Mater. Sci., 13(1978) 329.

[83] Krishnan, B.P., Surappa, M.K. and Rohatgi, P.K., J. Mater. Sci. 16(1981) 1209.

[84] Gibson, P.R., Clegg, A.J. and Das, A.A., Foundr Trade J., 152(1982) 253.

[85] Kohara, S., "Fabrication of SiC_p-Al Composite Materials", Mater. Manufact. process., 5(1990) 51.

[86] Huda, D., El Baradie, M.A. and Hashmi, M.S.J., "Metal matrix composite-

materials aspects, part II", Journal of Materials Processing Technology, 37(1993) 529-541.

[87] Charles, D., "Metal Matrix Composite-ready for take off?", Met. Mater., 6(1990) 78.

[88] Lock, J., "From strength to strength", Prof. Eng., (April,1990) 21.

[89] Aerospace materials for the year 2000, Eng. Mater. Des., (July/August,1988)26.

[90] Dural MMC, Dural aluminium Composites Corporation, San-Diego, Technical Data, May 1987.

[91] Tolka-whisker, Tokai Carbon Co., 1988.

[92] Crawley, E.F. and Van Schoor, M.C., J. Compos. Mater., 21(1987) 553.

[93] Reed, J.S., Introduction to the Principle of Ceramic Processing, John Wiely and Sons, 1988.

[94] Transient voltage suppression devices, Publ. Harris Semiconductor, 1994.

[95] Gupta, T.K., "Application of zinc oxide varistors", J. Am. Ceram. Soc., 73(7), 1990, 1817.

[96] O Sullivan, F.A., "Green body process variables in uniaxially and isostatically pressed varistor bodies", M.Sc. Thesis, University of Limerick, Ireland, 1990.

[97] Levine, J.D., "Theory of varistor electronic properties", Critical Review of Solid State Science, 5(1975) 597.

[98] German, R.M., Powder Metallurgy Science, Metal Powder Industries Corporation, 1984.

[99] Kendall, K., McNalford and Birchall, J.D., "The Strength of Green Bodies", Brit. Ceram. Proc. 1986, 37, 255.

[100] Griffith, A.A., "Proceedings of the 1st International Congress for Applied Mechanics" Eds. Biezeno, C.B. & Burgers J.M., Waltman, University, Delft, The netherlands. 1924 pp. 56-63.

[101] Batdorf, S.B. and Heinisch, H.L., "Weakest Link Theory Reformulated for Arbitrary Fracture Criterion", J. AM. Ceram. Soc., 1978, 61[78], 355.

[102] Weibull, W., "The Phenomenon of Rupture in Solids", INGVETENSK. AKAD. HANDL., 153 Publ. Royal Inst. Techn., Stockholm.

[103] Rudnick, A., Hunter, A.R. and Holden, F.C., "An analysis of the Diametal-

Compression Test", Materials Research and Standards, Apr. 1963, pp. 283-289.

[104] Timoshenko, S. and Goodier, J.N., Theory of Elasticity, 2nd edi. N.Y. McGrawHill Book Co. Inc. 1951

[105] Dally, J.W. and Reley, W.F., Experimental Stress Analysis, 3rd edi., Mcgraw-Hill Inc.

[106] Al-Tounsi, A., "Effect of Sintering Parameters on the Mechanical and Physical Properties of Sinter Formed Material", Ph.D. Thesis, Dublin City University, Dublin 9, Ireland.

[107] Box, G.E.P. and Wilson K.B. "On the experimental attainment of optimum condition", J. Royal Statistical Society, Vol. 13, 1951, pp. 1-45.

[108] Wu, S.M. "Tool Life Testing by Response Surface Methodology, Parts I and II", Trans. ASME, 86(1964), pp. 105-116.

[109] El Baradie, M.A., "Computer Aided Analysis of a Surface Roughness Model for Turning", J. Mat. Proc. Tech., 26(1991), pp. 207-216.

[110] El Baradie, M.A., "Surface roughness model for turning grey cast iron (154 BHN), Proc. Instn. Mech. Engrs. vol 207, pp. 43-54.

[111] Alauddin, M., "End Milling Machinability of Steel, a Nickel-Base Alloy (Inconel 718) and a Metal Matrix Composite", Ph.D thesis, Dublin City University, Ireland, 1993.

[112] Montegomery, D.C. "Design and Analysis of Experiment", 2nd edition, John Wiley, New York, 1984.

[113] Drapper, N.R. and Smith, H., "Applied Regression Analysis", 2nd edition, John Wiley and Sons, New York, 1966.

[114] Bethoney, W.M., Nunes, J. and Kidd, J.A., " Compressive Testing of Metal Matrix Composites" Testing Technology of Metal Matrix Composite, Eds. Digiovanni, P.R. and Adsit, N.R., ASTM, STP 964, 1988.

APPENDIXES

APPENDIX A

Technical Data for the INSTRON Universal Testing Machine

SPECIFICATIONS	Model 4204
Capacity	50 kN, or 5,000 kg
Force rating: (Tension and Compression below moving crosshead)	25 kN up to 500 mm/min. 50 kN up to 100 mm/min.
Load Range: (Using interchangeable load cells)	0.1 N to 50 kN
Load Weighing System (Accuracy at digital readout accessory or analog output)	± 1% of reading to 1/50 of load cell capacity. ± 1 count of the display
Strain Measuring System (Accuracy at digital readout accessory or analog output)	± 0.6% of reading ± transducer linearity, ±1 count of the display
Position Measuring Accuracy (no load)	± 0.05 mm
Position Measurement Repeatability (no load)	± 0.05 mm
Crosshead Speed range	0.05 to 500 mm/min.
Crosshead Speed Accuracy	± 0.2% over 100 mm
Return Speed	500 mm/min.
Crosshead Alignment	± 0.20 mm over 25 mm travel ± 0.51 mm over total travel
Axial Stiffness	175 kN/mm
Testing (sample) Space Lateral: Front to back	 560 mm Unlimited
Power requirements Voltage: Frequency: Power:	 100/120/220/240 volts ± 10%, single phase 47 to 63 Hz 2000 VA max.

APPENDIX B

TEST PROGRAME FOR BALANCE

```
OPEN "COM1:2400,E,7,1,DS,CS,LF" FOR RANDOM AS #1
DO
 PRINT #1, "S"                     ' give transmit command to balance
 INPUT #1, S$                      ' receive weighing result to computer
 CLOSE #1                          ' close file

 WEIGHT2 = VAL(MID$(S$, 3, 11))        ' select data
 PRINT WEIGHT2                         ' display weighing result on screen
 SLEEP 60                         ' stop data file
 LOOP                            ' execution starts again
```

TEST PROGRAM FOR CONTROLLER

```
OPEN "COM2:4800,E,7,1,RS,CS0,DS0,CD0,,PE" FOR RANDOM AS #2
command1$ = "R" + "1" + "??*"                          'interrogation command
PRINT #2, command1$                                  ' print in file
reply1$ = INPUT$(5, #2)                             ' data receive from controller
IF reply1$ = "R1?A*" THEN PRINT "controller is on line"
```

TEST PROGRAM FOR TRANSDUCER CONDITIONER

```
OPEN "COM1:4800,N,*,1,DS,ASC" FOR INPUT AS #1                  ' interface
command
DO
      a$ = INPUT$(16, #1)                              ' input all data
   CLOSE #1                                          ' close file
   FOR j = 1 TO 16
     sign$ = MID$(a$, j, 1)
```

```
    IF sign$ = "+" OR sign$ = "-" THEN GOTO process
    NEXT j
    PRINT "error in data transmission from LVDT"

process:
  height$ = MID$(a$, j, 6)                       ' receive string value
  power$ = MID$(a$, j + 6, 1)                      ' receive string value
  power = 10 ^ (-VAL(power$))                      ' covert numeric value
  height = VAL(height$) * power                   ' actual numeric value
  PRINT height                                 ' the display in transducer
                                          ' conditioner will show in the monitor
SLEEP 60                                   ' stop acquiring data for 60 seconds
LOOP                                           ' execution starts again.
```

APPENDIX C

PROGRAM FOR CONTROLLING WEIGHT LOSS

```
DECLARE SUB currenttemp ()
DECLARE SUB Massage2 (massage$, reply$)
DECLARE SUB WeightRead ()
DECLARE SUB PrintOut ()
DECLARE SUB InputData ()
DECLARE SUB WeightLoss ()
DECLARE SUB WeightLimit ()
DECLARE SUB FinalRecipe ()
DECLARE SUB StartProgram ()
DECLARE SUB FinalRampTemp ()
DECLARE SUB ProgramSetting ()
DECLARE SUB Initialization ()
DECLARE SUB ControllerInit. ()
DECLARE SUB PointSet (temp%)
DECLARE SUB Commands (a$, p$, decimal$, num%)
DECLARE SUB RampTime (temp2%, time1%, time%)

'DIM SHARED a$, p$, decimal$, num%, reply3$, reply4$
COMMON SHARED weight0, weight1, weight2, wkg0
COMMON SHARED wloss, wlr1, wlr2, wlrlim
COMMON SHARED i%, dt%, delay, hour, weighttime, hrmax
COMMON SHARED dtmax%, setpoint%, setpoint0%, ramptemp%
COMMON SHARED deltatemp%, current.temp%
COMMON SHARED shrinktemp%, firingtemp%, firingtime%
COMMON SHARED outfile$

CALL InputData
OPEN outfile$ FOR OUTPUT AS #3
CLOSE #3
    CLS
    CALL ControllerInit.
    CALL WeightRead
    CALL Initialization
    CALL WeightLoss
    CALL PrintOut
    CALL WeightLimit

DO
    CALL FinalRampTemp
```

```
    CALL ProgramSetting
    CALL StartProgram
    SLEEP delay
    CALL WeightRead
    CALL WeightLoss
    CALL WeightLimit
    CALL PointSet(ramptemp%)
    CALL currenttemp
    CALL PrintOut
LOOP UNTIL ramptemp% >= shrinktemp%

CALL FinalRecipe
CALL PointSet(setpoint0%)
CALL StartProgram
END

SUB Commands (a$, p$, decimal$, num%)

'     Subroutine for communication with the furnace controller
'     Two commands are used for the communication
'     The first one gives the parameter and its new value
'     and the second command is  to make sure that the controller
'     implement the changes in the first command.
'     For more information about these commands refer to
'     the instruction manual of the controller. These
'     commands are: Command 3 and Command 4

   OPEN "COM2:4800,E,7,1,RS,CS0,DS0,CD0,,PE" FOR RANDOM AS #2
   num$ = RIGHT$("0000" + LTRIM$(STR$(num%)), 4)
'   OPEN "COM2:4800,E,7,1,RS,CS0,DS0,CD0" FOR RANDOM AS #2
   command3$ = a$ + "1" + p$ + "#" + num$ + decimal$ + "*"
   command4$ = a$ + "1" + p$ + "I*"
'  OPEN "COM1:4800,E,7,1,RS,CS0,DS0,CD0" FOR RANDOM AS #2
   c$ = "z"
   DO WHILE NOT c$ = "I"
      PRINT #2, command3$;
      reply3$ = INPUT$(10, #2)
      c$ = MID$(reply3$, 9, 1)
   LOOP
   FOR j = 1 TO 5: NEXT j
   PRINT #2, command4$;
   reply4$ = INPUT$(10, #2)
   CLOSE #2
END SUB

SUB ControllerInit.
   CLS
   PRINT
```

```
   PRINT
   PRINT
   FOR module% = 1 TO 4
      PRINT "     Initializing module   . . . "; module%
      a$ = "R"
      p$ = "S"
    '  num% = 1
      decimal$ = "0"
     CALL Commands(a$, p$, decimal$, module%)
      FOR stage% = 1 TO 4
         p$ = "A"
     '    num% = 1
         decimal$ = "0"
         CALL Commands(a$, p$, decimal$, stage%)
         p$ = "B"
         num% = 0
         CALL Commands(a$, p$, decimal$, num%)
         p$ = "C"
         decimal$ = "2"
         CALL Commands(a$, p$, decimal$, num%)
         p$ = "E"
         CALL Commands(a$, p$, decimal$, num%)
      NEXT stage%
   NEXT module%
END SUB

SUB currenttemp
a$ = "L"
p$ = "M"
massage$ = a$ + "1" + p$ + "?*"
CALL Massage2(massage$, reply$)
current.temp% = VAL(MID$(reply$, 4, 4))

END SUB


SUB FinalRampTemp

'      Subroutine to calculate the final ramp temperature
'      which will be given to the controller
'
       ramptemp% = ramptemp% + deltatemp%
END SUB


SUB FinalRecipe

'      Subroutine to make the necessary commands for the
```

```
'     Controller to make the temperature profile for firing
'     after the binder burnout has been completed.
'
'     Calling module No. 1
'
   a$ = "R"
   p$ = "S"
   decimal$ = "0"
'   num% = 1
   module% = 1
   CALL Commands(a$, p$, decimal$, module%)
'
'     Calling stage No. 1
'
   p$ = "A"
  '  num% = 1
   stage% = 1
   CALL Commands(a$, p$, decimal$, stage%)
'
'     Setting the ramp time to zero to make the programmer
'     starts from the previous ramp temperature.
'
   p$ = "C"
   decimal$ = "2"
   num% = 0
   CALL Commands(a$, p$, decimal$, num%)
'
'     Calling stage No. 2 for heating to sintering temperature.
   p$ = "A"
   decimal$ = "0"
  '  num% = 2
   stage% = 2
   CALL Commands(a$, p$, decimal$, stage%)
'
'     setting the ramp temperature
'
   p$ = "B"
   CALL Commands(a$, p$, decimal$, firingtemp%)
'
'     Calculating the ramp time from the end of the burn
'     off temperature to the firing temperature.
'
   CALL RampTime(firingtemp%, ramptemp%, total.ramptime%)
   p$ = "C"
   decimal$ = "2"
   CALL Commands(a$, p$, decimal$, total.ramptime%)
'
'     setting the dwell time for the firing
```

```
'
   p$ = "E"
   CALL Commands(a$, p$, decimal$, firingtime% * 100)
'
'     Calling stage 3 for cooling.
'
   p$ = "A"
   decimal$ = "0"
  ' num% = 3
   stage% = 3
   CALL Commands(a$, p$, decimal$, stage%)
'
'     Setting the ramp temperature for cooling.
'
   p$ = "B"
   CALL Commands(a$, p$, decimal$, setpoint0%)
'
'     setting the ramp time for cooling.

   CALL RampTime(firingtemp%, setpoint0%, total.ramptime%)
   p$ = "C"
   decimal$ = "2"
   CALL Commands(a$, p$, decimal$, total.ramptime%)
END SUB


SUB Initialization
   weight0 = weight2
   weight1 = weight2
   i% = 0
   delay = dt% * 60          ' Time interval in seconds.
   wkg0 = weight0 / 1000     ' Initial weight in Kg
   weighttime = 60 / dt% / wkg0
   deltatemp% = 0
   setpoint0% = setpoint%
   ramptemp% = setpoint%
END SUB


SUB InputData

   INPUT "INITIAL WEIGHT OF DISKS IN GRAMS     "; weight0
   INPUT "TIME INTERVAL IN MINUTES             "; dt%
   INPUT "MAXIMUM TEMPERATURE INCREASE IN C    "; dtmax%
   INPUT "WEIGHT LOSS RATE LIMIT IN g/kg/h     "; wlrlim
   INPUT "INITIAL SET POINT IN C               "; setpoint%
   INPUT "TEMP. WHEN WEGHT LOSS ENDS IN C      "; shrinktemp%
   INPUT " FIRING TEMPERATURE IN C             "; firingtemp%
```

```
   INPUT "SOAKING TIME IN HOURS              "; firingtime%
   INPUT "MAXIMUM HEATING RATES IN C/MIN     "; hrmax
   INPUT "OUTPUT DATA FILE                   "; outfile$
END SUB

SUB Massage2 (massage$, reply$)

OPEN "COM2:4800,E,7,1,RS,CS0,DS0,CD0,,PE" FOR RANDOM AS #2
DO UNTIL a$ = "A"
PRINT #2, massage$;
reply$ = INPUT$(10, #2)
a$ = MID$(reply$, 9, 1)
LOOP
CLOSE #2

END SUB


SUB PointSet (temp%)
'       Subroutine to make the required command for the
'       controller to change the setpoint.
'
   a$ = "L"
   p$ = "S"
 ' num% = ramptemp%
   decimal$ = "0"
 ' PRINT ramptemp%
   CALL Commands(a$, p$, decimal$, temp%)
END SUB

SUB PrintOut
   wlr1 = wlr2
   hour = i% * dt% / 60
   PRINT USING "####.##  "; i%; hour; weight2; wloss; wlr2; ramptemp%;
current.temp%
   OPEN outfile$ FOR APPEND AS #3
   PRINT #3, USING "####.##  "; hour; weight2; wloss; wlr2; ramptemp%;
current.temp%
   CLOSE #3
   i% = i% + 1
END SUB


SUB ProgramSetting
'       Subroutine to set the programmer parameters for
'       temperature profile
'
'       Calling module No. 1
```

```
'
   a$ = "R"
   p$ = "S"
'   num% = 1
   decimal$ = "0"
   module% = 1
   CALL Commands(a$, p$, decimal$, module%)
'
'     Calling stage No. 1
'
   p$ = "A"
   stage% = 1
   CALL Commands(a$, p$, decimal$, stage%)
'
'     setting the ramp temperature.
'
   p$ = "B"    ' Parameter nam. B for ramp temperature
   CALL Commands(a$, p$, decimal$, ramptemp%)
'
'     Setting the ramp time.
'
   p$ = "C"             ' Parameter name. C for ramp time.
   decimal$ = "2"
   CALL Commands(a$, p$, decimal$, dt%)
END SUB

SUB RampTime (temp2%, temp1%, time%)
   ramptime.in.minutes% = INT(ABS(temp2% - temp1%) / hrmax)
   hours.ramptime% = INT(ramptime.in.minutes% / 60)
   minutes.ramptime% = ramptime.in.minutes% MOD 60

   minutes.ramptime$ = "00" + LTRIM$(STR$(minutes.ramptime%))
   minutes.ramptime$ = RIGHT$(minutes.ramptime$, 2)
   total.ramptime$ = LTRIM$(STR$(hours.ramptime%)) + minutes.ramptime$
   time% = VAL(total.ramptime$)
END SUB

SUB StartProgram
'     subroutine to run the program in the controller
'
   a$ = "R"
   p$ = "K"
   decimal$ = "0"
   num% = 21
   CALL Commands(a$, p$, decimal$, num%)
END SUB

SUB WeightLimit
```

```
'       This subroutine is to calculate the temperature
'       increase due to the resultant weight loss rate.
'       The temperature is increased according to the
'       linear relationship of heating rate and current
'       wt. loss rate.
deltatemp% = CINT(dtmax% - dtmax% * (ABS(wlr2 / wlrlim)))
 IF deltatemp% > dtmax% THEN
deltatemp% = dtmax%
 END IF
IF deltatemp% < 0 THEN
 deltatemp% = 0
END IF

END SUB


SUB WeightLoss

'       Subroutine to calculate the weight loss and weight
'       loss rate
'
    wloss = (weight2 - weight0) / wkg0
    wlr2 = (weight2 - weight1) * weighttime
    weight1 = weight2
END SUB


SUB WeightRead

'       Subroutine to read the value of the
'       current weight of the fired samples.
'
        OPEN "COM1:2400,E,7,1,CS,DS,LF" FOR RANDOM AS #1

      PRINT #1, "S"
      INPUT #1, W$
      CLOSE #1
       weight2 = VAL(MID$(W$, 3, 11))
END SUB
```

APPENDIX D

DATA FILE FOR WEIGHT LOSS RATE LIMIT 0.75 g/kg/h

Time in h	Current wt. in g	Wt. loss in g/kg	Wt. loss rate in g/kg/h	Given temp by program in °C	Actual temp. in furnace in °C
0.00	1931.78	0.00	0.00	20.00	20.00
0.10	1931.81	0.02	0.16	35.00	22.00
0.20	1931.93	0.08	0.62	47.00	41.00
0.30	1931.88	0.05	-0.26	50.00	53.00
0.40	1931.79	0.01	-0.47	60.00	58.00
0.50	1931.66	-0.06	-0.67	66.00	66.00
0.60	1931.49	-0.15	-0.88	68.00	70.00
0.70	1931.30	-0.25	-0.98	68.00	70.00
0.80	1931.13	-0.34	-0.88	68.00	68.00
0.90	1930.98	-0.41	-0.78	68.00	68.00
1.00	1930.83	-0.49	-0.78	68.00	68.00
1.10	1930.71	-0.55	-0.62	68.00	68.00
1.20	1930.60	-0.61	-0.57	71.00	70.00
1.30	1930.50	-0.66	-0.52	75.00	74.00
1.40	1930.41	-0.71	-0.47	80.00	79.00
1.50	1930.33	-0.75	-0.41	86.00	85.00
. . . .	. . . .	. . . .	. . . .	. . . .	. . . .
. . . .	. . . .	. . . .	. . . .	. . . .	. . . .
21.60	1901.90	-15.47	-0.47	311.00	310.00
21.70	1901.82	-15.51	-0.41	317.00	315.00
21.80	1901.74	-15.55	-0.41	324.00	323.00
21.90	1901.66	-15.59	-0.41	331.00	330.00
22.00	1901.60	-15.62	-0.31	338.00	337.00
22.10	1901.53	-15.66	-0.36	347.00	346.00
22.20	1901.48	-15.69	-0.26	355.00	354.00
22.30	1901.44	-15.71	-0.21	365.00	363.00
22.40	1901.42	-15.72	-0.10	376.00	375.00
22.50	1901.40	-15.73	-0.10	389.00	387.00
22.60	1901.39	-15.73	-0.05	402.00	400.00
22.70	1901.39	-15.73	0.00	416.00	414.00
22.80	1901.38	-15.74	-0.05	431.00	429.00
22.90	1901.38	-15.74	0.00	445.00	444.00
23.00	1901.38	-15.74	0.00	460.00	459.00
23.10	1901.37	-15.74	-0.05	475.00	474.00
23.20	1901.37	-15.74	0.00	489.00	488.00
23.30	1901.37	-15.74	0.00	504.00	502.00

APPENDIX E

PROGRAM FOR CONTROLLING SHRINKAGE

```
DECLARE SUB PrintOut ()
DECLARE SUB abortion ()
DECLARE SUB Commands (a$, p$, decimal$, num&)
DECLARE SUB ControllerInit. ()
DECLARE SUB CurrentTemp ()
DECLARE SUB Delay (time&)
DECLARE SUB Expansion ()
DECLARE SUB extension ()
DECLARE SUB Initialization ()
DECLARE SUB InputData ()
DECLARE SUB Limit ()
DECLARE SUB Massage2 (massage$, reply$)
DECLARE SUB NewTemp ()
DECLARE SUB PointSet (temp&)
DECLARE SUB RampSetting ()
DECLARE SUB RunProgram ()
DECLARE SUB TimeSetting ()


COMMON SHARED dt&, dt.second&, current.temp&, setpoint&
COMMON SHARED setpoint0&, ramp.temp&, delta.temp&, i&
COMMON SHARED delta.temp.max&, tem1&, temp2&, rod.expansion1, rod.expansion2
COMMON SHARED height0, height, disc.height, unit.shrink
COMMON SHARED shrink.rate, total.shrink1, total.shrink2
COMMON SHARED shrink.rate.limit, dt.hours, current.expansion
COMMON SHARED outfile$, correct.file$, total.expansion

CALL InputData
'CALL extension

CALL Initialization
CALL RunProgram

DO UNTIL current.temp& > = 600
   CALL Delay(dt.second&)
   CALL CurrentTemp
   PRINT current.temp&
LOOP
```

```
PRINT "Program Aborted"
CALL abortion
setpoint& = current.temp&
shrink.rate = 0
CALL PointSet(setpoint&)
CALL ControllerInit.
CALL TimeSetting
CALL Limit

DO UNTIL current.temp& >= 1200
   CALL NewTemp
   CALL RampSetting
   CALL RunProgram
   CALL Delay(dt.second&)
   CALL extension
   CALL CurrentTemp


  CALL PointSet(current.temp&)

   CALL Expansion
   CALL PrintOut
   i& = i& + 1
   CALL Limit
LOOP
CALL PointSet(setpoint0&)


SUB abortion
   a$ = "R"
   p$ = "K"
   decimal$ = "0"
   num& = 5
   CALL Commands(a$, p$, decimal$, num&)
END SUB


SUB Commands (a$, p$, decimal$, num&)
'
'      Subroutine for communication with the furnace controller
'
'      Two commands are used for the communication. The first
'      one gives the parameter and its new value and the second
'      command is to make sure that the controller implement
'      the changes in the first command.
'
'      For more information about these commands refer to the
'      instruction manual of the controller. These commands are:
```

```
'       Command 3 and Command 4
'
    num$ = RIGHT$("0000" + LTRIM$(STR$(num&)), 4)
    command3$ = a$ + "1" + p$ + "#" + num$ + decimal$ + "*"
    command4$ = a$ + "1" + p$ + "I*"
    OPEN "COM2:4800,E,7,1,RS,CS0,DS0,CD0,,,PE" FOR RANDOM AS #2

    DO UNTIL a$ = "I"
        PRINT #2, command3$;
        reply3$ = INPUT$(10, #2)
        a$ = MID$(reply3$, 9, 1)
    LOOP
    FOR j = 1 TO 5: NEXT j
    PRINT #2, command4$;
    relpy4$ = INPUT$(10, #2)
    CLOSE #2
END SUB


SUB ControllerInit.
    module& = 1
    PRINT "         Initializing module  . . . "; module&
    a$ = "R"
    p$ = "S"
    decimal$ = "0"
    CALL Commands(a$, p$, decimal$, module&)
    FOR stage& = 1 TO 4
        PRINT "          Initialization of stage . . . "; stage&
        a$ = "R"
        p$ = "A"
        decimal$ = "0"
        CALL Commands(a$, p$, decimal$, stage&)
        a$ = "R"
        p$ = "B"
        num& = 0
        CALL Commands(a$, p$, decimal$, num&)
        a$ = "R"
        p$ = "C"
        decimal$ = "2"
        CALL Commands(a$, p$, decimal$, num&)
        a$ = "R"
        p$ = "E"
        CALL Commands(a$, p$, decimal$, num&)
    NEXT stage&
END SUB


SUB CurrentTemp
```

```
    a$ = "L"
    p$ = "M"
    massage$ = a$ + "1" + p$ + "?*"
    CALL Massage2(massage$, reply$)
    current.temp& = VAL(MID$(reply$, 4, 4))

END SUB


SUB Delay (time&)
    SLEEP time&
END SUB


SUB Expansion

    total.expansion = height0 - height
    OPEN correct.file$ FOR INPUT AS #1
    DO
        INPUT #1, temp2&, rod.expansion2
        IF temp2& >= current.temp& THEN GOTO process2
        temp1& = temp2&
        rod.expansion1 = rod.expansion2
    LOOP

process2:
    CLOSE #1
    IF temp2& = current.temp& THEN
        current.expansion = rod.expansion2
    ELSE
  current.expansion = rod.expansion1 + (((current.temp& - temp1&) / (temp2& -
temp1&)) * (rod.expansion2 - rod.expansion1))
    END IF

    total.shrink2 = total.expansion - current.expansion
    unit.shrink = total.shrink2 * 1000 / (51.46 + total.shrink1)
    shrink.rate = (total.shrink2 - total.shrink1) * 1000 / (51.46 + total.shrink1) /
dt.hours
    total.shrink1 = total.shrink2
END SUB


SUB extension
'
'       the subroutine for reading the current extension
'       from the signal conditioner.
'
        OPEN "COM1:4800,N,8,1,DS,ASC" FOR INPUT AS #1
```

```
            a$ = INPUT$(16, #1)
        CLOSE #1

        FOR j = 1 TO 16
            sign$ = MID$(a$, j, 1)
            IF sign$ = "+" OR sign$ = "-" THEN GOTO process1
        NEXT j
        PRINT
        PRINT "Error in data transmision from the LVDT"

process1:

        height$ = MID$(a$, j, 6)
        power$ = MID$(a$, j + 6, 1)
        power = 10 ^ (-VAL(power$))
        height = VAL(height$) * power

     END SUB


SUB Initialization
    height0 = 10.056
    i& = 0
    current.temp& = 0
    dt.second& = dt& * 60

    dt.hours = dt& / 60
    total.shrink1 = 0
    OPEN outfile$ FOR OUTPUT AS #1
    CLOSE #1
END SUB

SUB InputData
    INPUT "Time interval in minutes              "; dt&
    INPUT "Initial set point in C             "; setpoint0&
    INPUT "Shrinkage rate limit  (+/-)          "; shrink.rate.limit
    INPUT "Maximum temperature incerase in C  "; delta.temp.max&
    INPUT "Disc height  in mm                    "; disc.height
    INPUT "Correction file name                 "; correct.file$
    INPUT "Output file name                    "; outfile$
END SUB


SUB Limit
    X1 = ABS(total.shrink2)
    IF X1 < 2.799 THEN
    delta.temp& = CINT(.5 * delta.temp.max& * (1 - (shrink.rate / shrink.rate.limit)))
    ELSE
```

```
   delta.temp&   =   CINT(1.25   *   delta.temp.max&   *   (1   -   (shrink.rate   /
shrink.rate.limit)))
   END IF
   IF delta.temp& > delta.temp.max& THEN
      delta.temp& = delta.temp.max&
   END IF
   IF delta.temp& < 0 THEN
      delta.temp& = 0
   END IF
END SUB


SUB Massage2 (massage$, reply$)
   OPEN "COM2:4800,E,7,1,RS,CS0,DS0,CD0,,,PE" FOR RANDOM AS #2
   DO UNTIL a$ = "A"
      PRINT #2, massage$;
      reply$ = INPUT$(10, #2)
      a$ = MID$(reply$, 9, 1)
   LOOP
   CLOSE #2

END SUB


SUB NewTemp

      ramp.temp& = current.temp& + delta.temp&
END SUB


SUB PointSet (temp&)
'     subroutine to make the required command for the controller
'     to change the setpoint
'
   a$ = "L"
   p$ = "S"
   decimal$ = "0"
   CALL Commands(a$, p$, decimal$, temp&)

END SUB


SUB PrintOut
   time.in.hours = i& * dt& / 60
   PRINT USING "####.##  "; time.in.hours; current.temp&;
   PRINT USING "###.###  "; unit.shrink; shrink.rate;
   PRINT USING "###.###  "; total.expansion; height; ramp.temp&
   OPEN outfile$ FOR APPEND AS #1
```

```
    PRINT #1, USING "####.##  "; time.in.hours; current.temp&;
    PRINT #1, USING "####.###  "; unit.shrink; shrink.rate;
    PRINT #1, USING "####.###  "; total.expansion; height; ramp.temp&
    CLOSE #1
'    PRINT unit.shrink, shrink.rate
END SUB


SUB RampSetting
'
'        Subroutine to set the programmer parameters for
'        temperature profile.
'
'
'        Calling module No. 1
'
        a$ = "R"
        p$ = "S"
        decimal$ = "0"
        module& = 1
        CALL Commands(a$, p$, decimal$, module&)
'
'        Calling stage No. 1
'
        a$ = "R"
        p$ = "A"
        CALL Commands(a$, p$, decimal$, module&)
'
'        Setting the ramp temperature.
'
        a$ = "R"
        p$ = "B"         '  Parameter name.  B  for  ramp temperature.
        decimal$ = "0"
        CALL Commands(a$, p$, decimal$, ramp.temp&)
END SUB


SUB RunProgram
    a$ = "R"
    p$ = "K"
    num& = 21
    decimal$ = "0"
    CALL Commands(a$, p$, decimal$, num&)
END SUB


SUB TimeSetting
```

```
'
'       Subroutine to set the programmer parameters for
'       temperature profile.
'
'
'       Calling module No. 1
'
        a$ = "R"
        p$ = "S"
        decimal$ = "0"
        module& = 1
        CALL Commands(a$, p$, decimal$, module&)
'
'       Calling stage No. 1
'
        a$ = "R"
        p$ = "A"
        CALL Commands(a$, p$, decimal$, module&)
'
'       Setting the ramp time.
'
        a$ = "R"
        p$ = "C"          ' Parameter name.  C  for ramp time.
        decimal$ = "2"
        CALL Commands(a$, p$, decimal$, dt&)

END SUB
```

APPENDIX F

DATA FILE FOR SHRINKAGE RATE LIMIT 10 µm/mm/h

Firing time in h	Given temp by program in °C	Shrinkage in µm/mm	shrinkage rate in µm/mm/h	Current height in mm	Amount of contraction mm	Actual temp. in furnace in °C
0.00	612.00	-6.761	-5.709	2.107	7.953	610.000
0.13	617.00	-6.196	4.585	2.162	7.898	612.000
0.27	629.00	-6.177	0.117	2.227	7.833	632.000
0.40	639.00	-6.147	0.220	2.284	7.776	639.000
0.53	649.00	-6.173	-0.198	2.335	7.725	649.000
0.67	658.00	-5.837	2.522	2.399	7.661	659.000
0.80	669.00	-5.833	0.015	2.459	7.601	671.000
0.93	679.00	-5.970	-1.026	2.507	7.553	679.000
1.07	687.00	-6.141	-1.275	2.543	7.517	688.000
1.20	695.00	-5.669	3.548	2.612	7.448	696.000
1.33	707.00	-6.249	-4.367	2.662	7.398	709.000
1.47	714.00	-6.170	0.616	2.718	7.342	713.000
1.60	724.00	-6.514	-2.580	2.770	7.290	725.000
1.73	731.00	-6.400	0.865	2.820	7.240	731.000
1.87	740.00	-6.433	-0.249	2.875	7.185	742.000
2.00	749.00	-6.452	-0.139	2.933	7.127	750.000
. . . .	. . . .	. . . .	. . . .	. . . .	. . . .	. . . .
. . . .	. . . .	. . . .	. . . .	. . . .	. . . .	. . . .
19.73	1072.00	-190.346	-17.683	-2.380	12.440	1079.000
19.87	1075.00	-191.442	-4.850	-2.385	12.445	1072.000
20.00	1084.00	-193.128	-11.711	-2.380	12.440	1088.000
20.13	1086.00	-193.363	0.504	-2.360	12.420	1084.000
20.27	1099.00	-195.602	-16.893	-2.346	12.406	1106.000
20.40	1102.00	-196.128	-0.636	-2.327	12.387	1099.000
20.53	1116.00	-197.532	-10.406	-2.288	12.348	1122.000
20.67	1118.00	-198.158	-2.636	-2.289	12.349	1116.000
20.80	1130.00	-199.394	-8.747	-2.245	12.305	1136.000
20.93	1135.00	-199.790	-1.224	-2.212	12.272	1133.000
21.07	1149.00	-201.216	-10.447	-2.171	12.231	1155.000
21.20	1152.00	-201.456	0.307	-2.149	12.209	1149.000
21.33	1165.00	-202.387	-7.046	-2.101	12.161	1172.000
21.47	1173.00	-203.086	-3.820	-2.068	12.128	1172.000
21.60	1185.00	-203.785	-4.462	-2.019	12.079	1188.000
21.73	1196.00	-203.890	0.123	-1.960	12.020	1199.000
21.87	1205.00	-203.920	-0.254	-1.920	11.980	1216.000

APPENDIX G

Equations for the stress-strain analysis and numerical calculations

The domain of an ellipsoidal inclusion is bounded by

$$\frac{x_1^2}{a_1^2}+\frac{x_2^2}{a_2^2}+\frac{x_3^2}{a_3^2}=1 \tag{G.1}$$

where a_1, a_2 and a_3 are the principal axes of the ellipsoid and coincide with the x_1, x_2 and x_3 axes, respectively. The Eshelby's tensor $S_m=S_{ijkl}=S_{jikl}=S_{ijlk}$

For the case of sphere particles

$a_1=a_2=a_3$

$$S_{1111}=S_{2222}=S_{3333}=\frac{7-5\nu}{15(1-\nu)} \tag{G.2}$$

$$S_{1122}=S_{2233}=S_{3311}=S_{1133}=S_{2211}=S_{3322}=\frac{5\nu-1}{15(1-\nu)} \tag{G.3}$$

$$S_{1212}=S_{2323}=S_{3131}=\frac{4-5\nu}{15(1-\nu)}$$

The S is composed of the hydrostatic and deviatoric components as

$$S=(\alpha,\beta) \tag{G.5}$$

The α and β values are

$$\alpha=\frac{1}{3}*\frac{1+\nu}{1-\nu}$$
$$\beta=\frac{2}{15}*\frac{4-5\nu}{1-\nu} \tag{G.6}$$

For the case of circular cylinder

$a_1=a_2 << a_3=\infty$

$$S_{1111}=\frac{5-4\nu}{8(1-\nu)} \tag{G.7}$$

$$S_{2222}=\frac{5-4\nu}{8(1-\nu)}$$
$$S_{3333}=0 \tag{G.8}$$

$$S_{1122}=\frac{4\nu-1}{8(1-\nu)}$$
$$S_{2211}=\frac{4\nu-1}{8(1-\nu)} \tag{G.9}$$
$$S_{2323}=\frac{1}{4}$$

$$S_{2233}=\frac{\nu}{2(1-\nu)}$$
$$S_{3311}=0 \tag{G.10}$$
$$S_{1133}=\frac{\nu}{2(1-\nu)}$$

$$S_{3322}=0$$

$$S_{1212}=\frac{1}{16}*\frac{5-8\nu}{1-\nu} \qquad (G.11)$$

$$S_{3131}=\frac{1}{2}$$

The α and β values in this case are

$$\alpha=\frac{5-4\nu}{8(1-\nu)} \qquad (G.12)$$

$$\beta=\frac{4\nu-1}{8(1-\nu)}$$

Computer programme for calculating stress and strain

```
CLS
DIM EzeroS(i), NewzeroS(i), MewzeroS(i), BetazeroS(i), Bzero(i), Sigmaone(i),
Sigmazero(i)
Newzero = .34                  ' poisson's ratio of matrix
Newone = .22                   ' poissons's ratio of the particle
'Sigmay = 100                    ' Yield stress
h = 124                     ' work hardening rate
n = .23                     ' work hardening exponent
Ezero = 65.5 * 10 ^ 3          ' Young's modulus of Al  (matrxi)
Eone = 350 * 10 ^ 3            ' Youngs modulus of SiC  (particle)
'c = 0!
'c = .05
'c = .1
'c = .15
c = .23
'c = .28
'k = 1044.98'for l/d=8
k = 660    'for l/d=20
```

```
Mewzero = Ezero / 2 * (1 + Newzero)   ’ shear modulus of matrix
Mewone = Eone / 2 * (1 + Newzero)     ’ shear modulus of particle
OPEN "B:\diSiC10.dat" FOR OUTPUT AS #1

10 DATA .002, .01, .05, .1, .15, .2, .25, .3
READ absilonP(i)
’EzeroS(i) = 1 / (1 / Ezero + (absilonP(i) / (Sigmay + h * (absilonP(i) ^ n))))
                                                         ’ equation 1
’EzeroS(i) = 1 / (1 / Ezero + (absilonP(i) / (h * (absilonP(i) ^ n))))
EzeroS(i) = 1 / (1 / Ezero + (absilonP(i) / ((h * (absilonP(i) ^ n) + (k * (c *
absilonP(i)) ^ .5)))))
NewzeroS(i) = 1 / 2 - (1 / 2 - Newzero) * (EzeroS(i) / Ezero)
                                            ’ equation 2
MewzeroS(i) = EzeroS(i) / (2 * (1 + NewzeroS(i)))
                                              ’ equation 3
BetazeroS(i) = (2 / 15) * ((4 - 5 * NewzeroS(i)) / (1 - NewzeroS(i)))
                                           ’ equation 4
Bzero(i) = (BetazeroS(i) * (Mewone - MewzeroS(i)) + MewzeroS(i)) / ((c + (1 - c)
* BetazeroS(i)) * (Mewone - MewzeroS(i)) + MewzeroS(i))   ’ equation 5
’Sigmaone(i) = 1 / Bzero(i) * (Sigmay + h * (absilonP(i) ^ n))
’Sigmazero(i) = Sigmay + h * (absilonP(i) ^ n)
Sigmaone(i) = 1 / Bzero(i) * (h * (absilonP(i) ^ n) + (k * (c * absilonP(i) ^ .5)))
Sigmazero(i) = h * (absilonP(i) ^ n) + k * (c * absilonP(i) ^ .5)
’Sigmaone(i) = 1 / Bzero(i) * (h * (absilonP(i) ^ n))
’Sigmazero(i) = h * (absilonP(i) ^ n)
PRINT USING "####.### "; EzeroS(i); NewzeroS(i); MewzeroS(i); BetazeroS(i);
Bzero(i); Sigmaone(i); Sigmazero(i); absilonP(i)
 PRINT #1, USING "####.### "; absilonP(i); Sigmaone(i)’ ; Sigmazero(i); EzeroS(i);
NewzeroS(i); MewzeroS(i); BetazeroS(i); Bzero(i)
IF absilonP(i) = .3 GOTO 20
GOTO 10
20 END
```

APPENDIX H

PUBLICATIONS

1. D. Huda, M.A. El Baradie and M.S.J. Hashmi, "Metal matrix composite-Manufacturing aspects, part I", Journal of Materials Processing Technology, 37(1993) 513-528.

2. D. Huda, M.A. El Baradie and M.S.J. Hashmi, "Metal matrix composite-Materials aspects, Part II", Journal of Materials Processing Technology, 37(1993) 529-541.

3. D. Huda, M.A. El Baradie and M.S.J. Hashmi, "Compaction Behaviour of Metal Matrix Composite, Key Engineering Materials, Volumes 86-87 (1993), pp. 85-92.

4. D. Huda, M.A. El Baradie and M.S.J. Hashmi, "Manufacture and characterization of Aluminium Matrix Composite using Powder Metallurgy Route", editors-T. Chandra and A.K. Shingra, Proceedings of the International Conference of Advanced Composite Materials, University of Wollongong, Australia, Feb. 15-19, 1993, pp. 1029-1036.

5. D. Huda, M.A. El Baradie and M.S.J. Hashmi, "Development of a hardness model for MMCs (Al/Al_2O_3)", Journal of Materials Processing Technology, 44(1994) 81-90.

6. D. Huda, M. A. El Baradie and M.S.J. Hashmi, "Modelling for the compressive strength of Al-6061/SiC MMC's", Ed. M.S.J. Hashmi, Proceeding of the International Conference on Advances in Materials and Processing Technology (AMPT' 93), pp. 1131-1142. It is accepted for publication in the Journal of Materials Processing Technology.

7. D. Huda, M.A. El Baradie and M.S.J. Hashmi, "Analytical study for the stress analysis of Metal Matrix Composites", J. Mater. Process. Technol., 45 (1994) 429-434

8. D. Huda and M.A. El Baradie, "Application of Response Surface Methodology to the Optimization of Manufacturing Processes", Presented at a Seminar organized by The Institution of Engineers of Ireland, Mechanical and Manufacturing Division, 22nd Feb, 1994 and submitted for publication in IEI transaction.